Title

Fluorescence Lifetime Imaging for Intraoperative Diagnosis and Surgical Guidance of Oral Cavity and Oropharyngeal Cancer

Author

Weyers, Brent William

Publication Date

2022

Peer reviewed|Thesis/dissertation

Fluorescence Lifetime Imaging for Intraoperative Diagnosis and Surgical Guidance of Oral Cavity and Oropharyngeal Cancer

By

BRENT WILLIAM WEYERS

DISSERTATION

Submitted in partial satisfaction of the requirements for the degree of

DOCTOR OF PHILOSOPHY

in

Biomedical Engineering

in the

OFFICE OF GRADUATE STUDIES

of the

UNIVERSITY OF CALIFORNIA

DAVIS

Approved:

Laura Marcu, Chair

D. Gregory Farwell

Andrew Charles Birkeland

Randy Carney

Committee in Charge

2022

ABSTRACT

To achieve successful surgical oncology outcomes, surgeons must completely extirpate the full extent of a patient's cancer volume, both gross and microscopic. Currently, there is a lack of technology capable of providing surgeons with real-time feedback to quantify the extent of tumor; therefore, cancer may be missed, or surgeons may potentially compromise benign tissue. This research investigates whether Fluorescence Lifetime Imaging (FLIm) can optimize upper aerodigestive oncologic surgery through real-time surgical margin delineation. One hundred patients were evaluated, comprising N=45 patients with oral cavity cancer and N=55 patients with cancer of the oropharynx.

This work first demonstrates the series of methodologies, tools, and techniques developed to acquire intraoperative FLIm data and validate against gold-standard histopathology. Next, the ability of FLIm to demarcate primary tumors of the oropharynx was investigated for an initial N=10 patient cohort of tonsil tumors. In this study, FLIm demarcated the full extent of all patients' cancers; however, the best benign vs. tumor contrast originated from multivariate analysis of all FLIm time-resolved and spectral intensity parameters. To this end, a random forest classifier method was used to integrate multivariate FLIm parameters from an N=55 patient dataset comprising conventional primary tumors and leveraged to demarcate occult primary tumors of the oropharynx for a cohort of N=7 patients. This work concludes by investigating sources of FLIm data variability across all patients, such as tumor characteristics (e.g., p16 status), patient age, lymphoid tissue, high-grade dysplasia, and local anesthetic use. A preliminary demonstration of FLIm's ability to identify positive surgical margins *in vivo* within a patient's surgical cavity is also illustrated.

Collectively, this original research demonstrates the feasibility for FLIm to intraoperatively demarcate carcinoma during upper aerodigestive oncology procedures, therefore motivating ongoing investigation to materialize this technology towards an intraoperative diagnostic modality.

Table of Contents

LIST OF FIGURES

Appendix Figures

LIST OF TABLES

Appendix Tables

ACKNOWLEDGEMENTS

The completion of this dissertation has truly been a transformative process. This interdisciplinary research effort is the product of numerous collaborations with fellow biomedical engineering colleagues, experts in machine learning algorithm development, pathologists, clinical research coordinators, and surgeons in the Department of Otolaryngology – Head and Neck Surgery. The experience of being at the forefront of healthcare to design, evaluate, and iterate on impactful clinical technology has been a fulfilling and rewarding process. This dissertation, and associated publications, would not have been possible without the support and guidance from my mentors, colleagues, family, and friends.

First and foremost, I would like to thank Dr. Laura Marcu for hosting me in her talented laboratory group and for providing me with the resources and infrastructure to succeed in my graduate career. At the time of joining her lab, Dr. Marcu entrusted me with her most valued project, which under an R01 grant in collaboration with Intuitive Surgical, aimed to evaluate the diagnostic potential of Fluorescence Lifetime Imaging (FLIm) to diagnose head & neck cancer. This work resulted in the largest known clinical FLIm database in the world, featuring *in vivo* and *ex vivo* data from a diverse patient population, each with various manifestations of cancers and etiologies. The acquisition of this magnitude of data resulted in 521 FLIm scans (*in vivo, ex vivo* mucosa, *ex vivo* deep margin, and *in vivo cavity resection*), 15.23 hours of FLIm imaging time, 1,250 H&E slices to annotate and coregister *in vivo* and *ex vivo*, and 1,500,000 spectroscopic datapoints. This work took five years of extensive organization, coordination, communication, and collaboration! I am incredibly grateful to Dr. Marcu for providing the appropriate structure in her laboratory through personnel, resources, meetings, and funding to set me up for success in this endeavor. Dr. Marcu also played a substantial role in my personal career development, allowing me to attend leading conferences in my field of study such as SPIE Photonics West. This also includes two international conferences in Bern, Switzerland and Jena, Germany.

I am grateful to the patients who participated in our research to advance this investigational technology. The willingness of the patients to add this additional research to their procedure took courage, compassion for others, and demonstrated the utmost kindness, as their participation promoted technological advances in healthcare which may one day lead to better outcomes for future generations of oncology patients.

This research benefited from the unwavering support and effort of the clinical team who collectively made our data collection possible. Angela Beliveau and Randev Sandhu in the Department of Otolaryngology – Head & Neck Surgery worked tirelessly to screen potential patients for our study and coordinate their full consent process. Additionally, they provided our research team with all necessary pathology reports, clinical files, institutional review board (IRB) certifications, and other documents needed to make this research possible. I am truly grateful for the members of our surgical research team who welcomed me to join them for their oncology cases and worked with me directly in the operating room to acquire our data from human patients. These surgeons include Drs. Andrew C. Birkeland, D. Gregory Farwell, Arnaud F. Bewley, and Marianne Abouyared. In addition, all members of the surgical team worked closely with me to interpret our data and provide outstanding intellectual contribution in our data collection methods and in our manuscripts. Dr. Dorina Gui in the Department of Pathology and Laboratory Medicine served as the primary pathologist for the study and performed thorough histopathology annotations on hundreds of H&E slides. Together, our clinical team cooperated in this research endeavor with outstanding synergy, and undeniably played a key role in the success of this work.

The FLIm instrument used in this study resulted from a culmination of many contributors who came before me. I would like to thank all past and present Marcu Lab members for their various contributions related to the lab's infrastructure and related support network thereof. I would like to thank my colleagues Julien Bec, Alba Alfonso-Garcia, Sukhkaran Aulakh,

Tianchen Sun, Xiangnan Zhou, Athena Tam, and Roberto Frusciante, who each provided intellectual contributions, guidance, mentorship to this work. I am highly appreciative of our research group for allowing me to draw upon their expertise during this research investigation.

Our graduate coordinator, Christal Wintersmith, was always willing to assist in any area of my educational pursuits here at UC Davis. She was always open to providing me with support, both personal and academic. She undeniably played an essential role in my educational development and success in the program.

I am grateful for my dissertation committee members, Drs. Laura Marcu, Randy Carney, D. Gregory Farwell, and Andrew C. Birkeland. All committee members were closely engaged in my research over the years and provided me with guidance and new research ideas. I am indebted to all their mentorship and support in this journey.

Finally, I would like to thank my family and friends who supported me through every step of this adventure. Being the first in my family to attend graduate school and earn a Ph.D. has been quite an endeavor and required the ability to adapt and overcome various challenges, among which COVID-19 was the most prominent. I would like to thank my parents, Richard and Jill Weyers, my brother, Grant Weyers, and extended family, for keeping me happy and feeling loved. Lastly, to my beautiful, outstanding wife, Sarah Weyers, who I met in graduate school. Having been a graduate student herself, Sarah experienced the Ph.D. process with me and supported me in every step of the way. I did not know how rewarding and rich life was until I met her! Thank you for your love and support each and every day. I look forward to our future and the family we will build together!

PREFACE

Over the last decade, Fluorescence Lifetime Imaging (FLIm) has demonstrated promise for differentiating benign tissue from cancer in several oncology applications, ranging from laboratory settings with murine and porcine tumors, to *ex vivo* analysis of surgically excised human cancer specimens, to more recently *in vivo* human patient analysis.[1,2] Although not an exhaustive list, recent reported oncology applications of FLIm range from breast cancer surgery, neurosurgery, head & neck cancer, and atherosclerosis, among others.[2] FLIm technology enables non-invasive optical evaluation of tissue based on the strong fluorescence emission from endogenous tissue fluorophores. The technology can be deployed in real-time, does not require the administration of exogenous contrast, and exhibits sensitivity to numerous cancer-induced microenvironment changes; this includes pH, tissue oxygenation, metabolism, and structural protein composition, among others.

Preliminary research suggests that FLIm can support broad diagnostic quantitation within a wide range of surgical oncology disciplines.[2] The original research herein focuses on surgical guidance of head & neck (H&N) cancer as a key application area. FLIm technology is well-suited for evaluating H&N cancer, as greater than 90% of cancers of the oral cavity (e.g., lips, dorsal tongue, and floor of mouth) and oropharynx (base of tongue and palatine tonsil) present in the epithelized mucosa (surface tissues), which is within the approximate 250 μm penetration depth of FLIm's ultraviolet (UV) excitation laser.[3,4]

There are six core research objectives/questions investigated: (1) In order to benchmark FLIm results against the gold standard of hematoxylin and eosin (H&E) histopathology, can a series of custom-developed tools, methodologies, and techniques be developed to associate ground truth histopathology to optical FLIm measurements acquired over surgical regions of the oral cavity and oropharynx (ranging from 2-10 cm)? (2) In a first study investigating the use of FLIm for *in vivo* surgical guidance of oropharyngeal cancer, can the technique successfully demarcate the entire extent of all patients' cancer using time-resolved and spectral intensity

features? (3) Can multivariate FLIm metrics be systematically integrated into a random forest machine learning classifier and leveraged to enhance the prediction of cancer probability? (4) For rare tumor cohorts that evade surgical detection after exhaustive clinical (absence of visual cues and palpation), radiographic (negative PET, CT, MRI findings), and surgical evaluation (directed biopsies of suspicious lesions), can FLIm support the localization of the primary tumor site and correctly identify uninvolved benign functional tissue? (5) What roles, if any, do surgical conditions (e.g., local anesthetic use), nuanced tissue characteristics (e.g., lymphoid tissue and high-grade dysplasia), cancer characteristics (e.g., HPV-mediated vs. non-HPV-mediated cancer), and patient medical characteristics (e.g., patient age) have on FLIm data? Finally, (6) can *in vivo* positive surgical margins presenting in electrocauterized deep margin be detected with FLIm? Objectives 1-4 are investigated in detail, whereas the investigation of objectives 5-6 are limited in scope and serve as proof-of-concept due to a smaller cohort of patients available for analysis within these two research aims. Collectively, these objectives serve to establish the validation and rigorous assessment of FLIm's ability to demarcate tumors across a large array of pathologies and conditions afflicting H&N anatomy.

Chapter 1 serves as background for this work and provides and overview of the clinical need for intraoperative tumor-margin decision-making, discusses the anatomy of the oral cavity and oropharynx, reviews the characteristics of head and neck cancer, and presents the current practices to diagnose and surgically manage H&N cancer. The chapter concludes with a review of current progress made by optical technologies investigated for H&N surgical guidance (exempting time-resolved autofluorescence, which is presented in *chapter 2*).

Chapter 2 begins by presenting the physical principles of fluorescence, introduces autofluorescence, and discusses the mechanisms of autofluorescence-based contrast in H&N cancer. Next, a review of all significant pre-clinical and clinical literature to date for *in vivo* surgical guidance using time-resolved autofluorescence techniques is featured. The chapter

concludes with a discussion of key next steps in research to advance this technology in the surgical guidance space.

Chapter 3 discusses the methods developed to implement FLIm for surgical guidance in H&N cancer. This includes the FLIm hardware, computation of fluorescence lifetime, the FLIm data visualization approach, the workflow to account for motion in the data visualization approach, and the methodology for implementing machine learning classification to the database.

Chapter 4 presents the tools, methodologies, and techniques developed for associating tissue histopathology status (e.g., benign tissue, high-grade dysplasia, cancer) to intraoperative optical imaging measurements both *in vivo* and on surgically excised specimens. *Chapter 5* and *chapter 6* demonstrate the first use of FLIm for demarcating conventional primary and occult primary tumors of the oropharynx, respectively.

Chapter 7 investigates the collective linear discriminant analysis (LDA) classification of the full 100-patient dataset, and investigates the effect of biological variables, patient demographics, and surgical characteristics on the FLIm database. A preliminary analysis of FLIm used *in vivo* for identification of residual tumor volume in the surgical cavity of two patients is demonstrated. Finally, *chapter 8* concludes on the key research findings contributed from this original research and provides and outlook on the next steps to materialize FLIm towards an intraoperative diagnostic modality.

CHAPTER 1 | Background: Overview of Head & Neck Cancer, Current Approaches and Limitations in the Surgical Margin Assessment Process, and Review of Optical Technologies Investigated for Surgical Guidance

1.1 | The Clinical Need for Intraoperative Tumor-Margin Decision-Making

Cancer is a condition where cells defy standard growth regulatory mechanisms and exhibit sustained proliferation, therefore lacking the “altruistic” behavior characteristic of normal cells. The unrestricted multiplication of a single cell results in a tumor, which is a clone of cells identical to the original mutated cell. If a tumor mass is slow growing and does not infiltrate neighboring tissue, it is classified as a benign tumor. In contrast, tumor cells that multiply rapidly and form an invasive mass is characterized as a malignant tumor or cancer.

The Centers for Disease Control and Prevention (CDC) cites cancer as the second leading cause of death; estimates from 2020 suggest 1.8 million individuals in the United States were affected by cancer, and cited cancer to be the cause of 606,520 deaths.[5] Depending on the cancer type and severity, patients may be treated by chemotherapy, hormone therapy, immunotherapy, radiation therapy, targeted therapy, and surgery.[6] For solid tumors that are contained in one specific area, surgery is typically the favored treatment option. In surgical oncology, the goal is to completely remove the full extent of the tumor so that only benign tissue remains.[6] Surgical robotics over the last 20 years have become increasingly used in cancer surgery, enabling less invasive access to regions of interest, such as in colorectal cancer, thoracic surgery, and oropharyngeal cancer.[7]

During the tumor excision process, a surgeon’s primary goal and challenge is to completely eradicate cancer - both gross and microscopic.[8] A positive surgical margin (PSM) occurs when the complete removal of cancer is not achieved and cancerous cells remain at the edge of the resection specimen. A study from 2018 reporting on PSM trends from the *National Cancer Database* (NCDB) ranked the surgical fields with the highest prevalence of PSMs, with the top five being: (1) ovarian – 35.00%, (2) prostate – 21.03%, (3) oral cavity – 12.75%, (4) thyroid – 11.52%, and (5) bladder – 9.46%.[9] Despite outstanding surgical advances over the

last two decades, PSM rates continue to remain high; thus, surgeons are faced with an important dilemma of preserving benign functional tissue, while being appropriately aggressive with margins to ensure that no cancer cells remain after surgery. It is well understood that PSMs are highly predictive of cancer recurrence; thus, surgeons must corroborate their assessments of margins by intraoperative biopsies and pathologist-interpreted frozen sections acquired from surgically excised tissue.

Currently, there is a lack of technology capable of providing surgeons with real-time feedback to quantify the extent of tumor, posing two core problems: (1) cancer may be missed and result in reoccurrence, or (2) surgeons may be too aggressive with resection margins compromise benign tissue, resulting in loss of function and poor patient cosmesis. The prevalence of PSMs, and challenges associated with intraoperative decision-making, motivates the search for novel technology that aids surgeons in quantifying the extent of tumor. While this clinical need is shared across the many surgical oncology disciplines, the original research herein focuses on a specific application area, namely Head & Neck (H&N) cancer. FLIm was specifically investigated due to promising results of the technique achieved over the last decade; this includes various surgical oncology fields, such as breast cancer, brain cancer, prostate cancer, and additionally the detection of atherosclerosis.[2]

Herein, the ability of Fluorescence Lifetime Imaging (FLIm) to enhance intraoperative detection and delineation of tumor margins of the oral cavity (e.g., dorsal tongue) and oropharynx (e.g., palatine tonsils and base of tongue) was investigated to establish proof-of-concept for the technique. FLIm measurements were acquired on 100 patients undergoing upper aerodigestive oncologic surgery within the operating pavilion at the UC Davis Health System. The results presented herein elucidate the first scientific knowledge of FLIm applied *in vivo* for human oncology research of oropharyngeal cancers, as well as surgical guidance studies using time-resolved autofluorescence in both the oral cavity and oropharynx.

1.2 | Anatomy of the Oral Cavity and Oropharynx

The anatomy of the Head & Neck (H&N) is complex because many different functional structures are in close proximity to each other.[10] This includes elements of the digestive, nervous, respiratory, lymphatic, and endocrine systems, often within millimeters of one another.[10] The scope of this research investigation is restricted to the application of FLIm to the oral cavity and oropharynx, thus other anatomical locations of the H&N, such as the nasopharynx and larynx, are not discussed here.

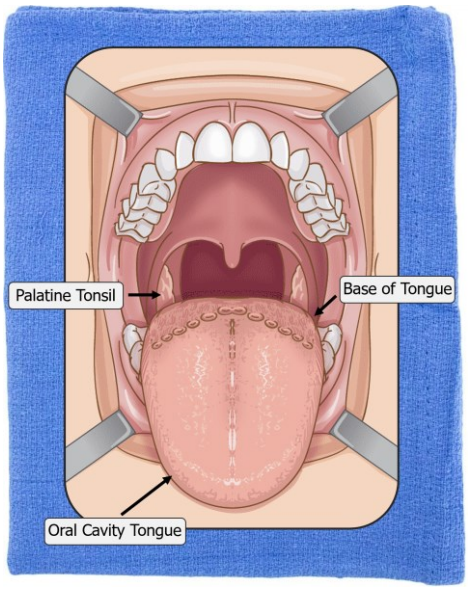

Figure 1: Simplified representation of oral cavity and oropharynx (superior) anatomy. The palatine tonsils and base of tongue comprise tissues of the oropharynx, which are composed of lymphatic tissue aggregates. The anterior 2/3rds of the oral tongue lies within the oral cavity and is a muscular organ with taste buds, nerves, arteries, and numerous projections of the mucous membrane (papillae). The figure is adapted with extensive modification from Gregory J., reference [11].

The oral cavity includes the lips, gingiva (gums), buccal mucosa (lining inside the cheeks and lips), the floor of mouth (under the tongue), the hard palate (bony top of mouth), the retromolar trigone (oral cavity subsite consisting of mucosa posterior to the last mandibular molar), and front two-thirds of the tongue.[10] The oropharynx is the middle part of the pharynx (hollow tube that starts behind the nose and leads to the esophagus) and includes the tonsils, the base of tongue, and the soft palate (back of the mouth).[10] *Figure 1* demonstrates a simplified

representation of the oral cavity tongue region, base of tongue region (oropharynx), and palatine tonsil region (oropharynx).

1.3 | Characteristics of Head & Neck Cancer

H&N cancer, of which oral cavity and oropharyngeal cancer are subsets, represents the sixth most common cancer worldwide.[12,13] In 2021, it was estimated that H&N cancer comprised 54,010 new cases of cancer in the United States, and therefore represented 2.8% of all new cancer cases.[14] Each year, oral cavity and oropharyngeal cancers are directly attributed to an estimated 10,850 deaths and thus represent a significant cause of death.[14] These cancers are most frequently diagnosed among people aged 55-64, and they afflict men in greater proportion than women.[14] Approximately 85% of these cancers (worldwide) are associated to heavy tobacco use and alcohol,[15–17] however tobacco-related carcinogenesis is slowly declining due to decreased global use of tobacco.[18,19] Recently, strong associations of oropharyngeal cancer to human papilloma virus (HPV), with clearly increasing incidence, have been reported.[20,21] The presentation of positive HPV status has been strongly linked to oral-sex exposure, where a latency of 10 to 30 years has typically been reported following the presentation of HPV-mediated oropharyngeal lesions.[18,22] HPV-mediated tumors aberrantly overexpress p16 biomarkers, thus p16 immunohistochemistry is recommended for determining HPV-associated etiology.[23]

Most H&N cancers present in patients *de novo*,[20] however precancerous lesions of the mucosal lining such as leukoplakia, erythroplakia, and high-grade dysplasia may progress into invasive cancers.[24] More than 90% of oral and oropharyngeal cancers of the head and neck are squamous cell carcinomas (SCC).[3,4] Head & neck squamous cell carcinoma (HNSCC) originates from squamous cells, which are thin, flat, surface cells that comprise the epithelized mucosa of the oral cavity and oropharynx.[25] Because HNSCC originates from one cell type (squamous epithelial cells) in the mucosal linings of the oral cavity, oropharynx, larynx, and

hypopharynx, one may hypothesize this cancer presents with relatively homogonous characteristics (e.g., morphology, metabolic characteristics) across patients.[20] Interestingly, there is marked heterogeneity of the tumors arising in the oral cavity and oropharynx,[20,26] attributed to the complex interplay of etiologies and the significant extent of molecular changes driving carcinogenesis.[20] The high degree of HNSCC cellular heterogeneity enables tumor cells to reverse lineage commitment to either proliferative or quiescent stages due to complex cell populations with various stages of differentiation.[27]

Conventional SCC is characterized by squamous differentiation (typically presenting as keratinization) and invasive growth which disrupts the underlying basement membrane.[28] The basement membrane marks the histological demarcation between the surface stratified epithelia and the underlying mesenchymal component.[27] SCC is graded into 3 classes: (1) well-differentiated SCC which resembles normal squamous mucosa, (2) moderately-differentiated SCC which displays nuclear pleomorphism, reduced keratinization, and atypical mitoses, and (3) poorly-differentiated SCC comprise immature cells, substantial atypical mitoses, minimal keratinization, and strong immunopositive cytokeratin markers.[28]

Verrucous carcinoma and basaloid SCC represent two additional commonly encountered variants of SCC. Verrucous carcinoma is a non-metastasizing variant of well-differentiated SCC, presenting with an exophytic, slowly-growing, warty tumor, with pushing rather than infiltrative margins.[28] These tumors impart a pronounced inflammatory response and impart abundant epithelial keratosis.[28] Alternatively, basaloid SCC is a high-grade variant of SCC composed of both basaloid and squamous components.[28] These tumors grow rapidly, are aggressive, and exhibit poor prognoses. The basaloid component of these cancers present with small packed cells with hyperchromatic nuclei without nucleoli, and scant cytoplasm.[28] Basaloid SCC requires multimodality treatment, including radical neck dissection surgery, radiotherapy,

and chemotherapy.[28] Although other H&N cancer subtypes exist, they represent atypical subsets of H&N cancer.[28]

1.4 | Current Diagnostic and Surgical Management Practices for H&N Cancer

Adequate intraoperative delineation of cancer is the key factor for long-term survival of patients diagnosed with oral and oropharyngeal cancer.[29] This requires rapid evaluation of the extent of molecular changes (neoplastic area) of the epithelial surface (mucosa). The preoperative diagnosis of HNSCC includes all, or a combination of: (1) a thorough review of medical history and physical examination,[26] (2) radiologic and non-ionizing imaging including computed tomography (CT), magnetic resonance imaging (MRI), ultrasound (US) and/or positron emission tomography (PET),[26] and (3) fine-needle aspiration biopsy, cited as a highly sensitive, specific, and accurate method for preliminary histological diagnosis.[26,30]

The complete surgical resection of tumors presenting in the oral cavity and oropharynx is the preferred method of cancer treatment. Adequate delineation of surgical margins in real-time and complete resection of cancer is imperative to maximize patient survival.[29] The surgical excision of oral cavity cancer (e.g., oral cavity tongue, lips, gums, etc.) is typically performed by hand, while oropharyngeal cancers (e.g., base of tongue, palatine tonsils, etc.) are generally resected via transoral robotic surgery (TORS) platforms. TORS, which has become increasingly utilized over the last few decades in otolaryngology, confers many advantages compared to conventional endoscopy procedures; this includes deeper access to anatomical sites which enables precise operation in tight spaces without a large open incision, improved patient functional outcomes, and enhanced dissection ability of lesions and neoplastic growths.[31]

The most routinely employed methods for intraoperative diagnosis include white light visualization, tactile feedback, and histopathologic assessment via biopsy; however, these traditional approaches present significant intraoperative surgical challenges.[32] For both TORS and non-robotic surgical procedures, the reliance on frozen section analysis introduces long

procedural waiting times, sampling error, the inability to provide continuous assessments of pathology margins, invasiveness associated with biopsies, and the potential for interpretative errors.[33] With respect to TORS in particular, the robotic platform eliminates a surgeon's ability to sense tissue and bone resistances,[31,34,35] and thus results in a loss of haptic feedback. This limitation has been cited to make TORS procedures more challenging.[34,35] Although informative, the reliance on white light visualization and tactile feedback to perform diagnosis is a dated and imprecise technique which also introduces the potential for subjectivity among healthcare practitioners.

At the present, positive surgical margins are found in up to 30% of patients at final histopathology approximately 1 week after the surgery, which is a percentage that has not changed over the past 30 years.[36–39] The disadvantages associated with the current intraoperative gold-standards for oral cancer and oropharyngeal diagnosis motivates the development of real-time and non-invasive technology to circumvent the shortcomings of current methods and improves diagnostic quantitation.

1.5 | Review of Optical Technologies Investigated for H&N Cancer Delineation (Exempting Time-Resolved Autofluorescence)

Due to the nature of optical technology penetration depths, which range from the order of the μm scale for ultraviolet wavelengths and millimeter scale for infrared wavelengths, such technologies are well-suited for interrogation of SCC (surface presenting tumors) for diagnosis and surgical guidance. A brief review of the key optical technologies investigated to date for H&N surgical guidance is provided here, with a summary featured in *tables 1 & 2*. These modalities include: (1) high resolution microendoscopy (HRME), (2) narrow band imaging (NBI), (3) Raman spectroscopy, (4) optical coherence tomography (OCT), (5) exogenous targeted fluorescence imaging (TFI), (6) exogenous non-molecularly targeted fluorescence imaging, and intensity-based endogenous fluorescence (IAF). An in-depth description of foundational time-resolved autofluorescence research is presented in *section 2.3.2*.

Beyond this list, other diagnostic adjuncts have been evaluated and reported, however have yielded limited success for diagnosis and surgical guidance. This includes vital tissue staining (toluidine blue),[40] brush cytology,[41] salivary tests,[42] and other approaches such as chemiluminescence.[43] These diagnostic adjuncts, as well as *ex vivo* studies, are not discussed here.

1.5.1 High Resolution Microendoscopy (HRME)

HRME provides microscopic images of cellular architecture and has been coined an "optical biopsy." [44,45] This technique relies on the transmission of light from light-emitting diodes (LED) transmitted through a fiber-optic bundle directly introduced via direct contact to mucosal tissue. This technique has the potential to excite endogenous fluorophores with the LED light, however typically is combined with superficially applied fluorophores such as proflavine, a nucleus-targeting contrast agent.[45] Like the LED illumination, emitted light is collected back to the fiber-optic bundle, where each optical fiber serves as individual pixels to the generated image rendered by a charge-coupled device (CCD) camera.[45] Histological features such as nuclear size, nuclear crowding, cellular pleomorphism, and nuclear-to-cytoplasm ratio is used to differentiate benign tissue from cancer.[45] The image resulting from the HRME system appears as cells with bright nuclei on a dark background. In HRME images, benign tissue is identified as cell nuclei appearing as bright discrete dots with even distribution, as opposed to neoplastic tissue which presents chaotic nuclear arrangement and enlarged nuclei.[45–47]

1.5.2 Narrow Band Imaging (NBI)

NBI is an optical image enhancement technology that visualizes capillaries of the mucosal surface, and veins within submucosal layers.[45] NBI wavelengths are within the visible spectrum, offering enhanced penetration depth compared to Ultraviolet-based imaging approaches. This technology narrows the bandwidth of illumination light within the absorption spectrum of hemoglobin, emitting blue light (400-430 nm) and green light (525-555 nm) to approximately match the peaks of absorption wavelengths of hemoglobin to enhance the

visualization of microvascular patterns.[45] The blue light has shorter wavelength with shallow penetration to highlight the superficial vessels, while the green light with longer wavelength penetrates deeper to illuminate underlying vessels.[45] Because neoangiogenesis is an important feature of neoplastic transformation, it is expected that visualization of vascular architecture can aid in the identification of pathological tissue.[45,48,49]

1.5.3 Raman Spectroscopy (RS)

Raman spectroscopy (RS) is a vibrational spectroscopic technique which detects variations of chemical components through interrogating a sample's "molecular fingerprint."[45] C.V. Raman in 1928 discovered that vibrations of intramolecular bonds caused light to scatter as a result of absorption or release of energy; this phenomena was coined Raman scattering, and was able to be captured and measured to form a spectrum.[45] A Raman spectrum contains specific and characteristic peaks assigned to a corresponding molecular structure and biochemical composition within imaged specimens.[50]

1.5.4 Optical Coherence Tomography (OCT)

OCT is a non-invasive technology capable of high-resolution imaging. OCT generates cross-sectional depth resolved two-dimensional and three-dimensional images in a method analogous to ultrasound A-scan and B-scan images, but using light rather than sound.[51] Magnitude, polarization, phase, and frequency shift of partially time-coherent light backscattered or back reflected from the sample is used as the basis to create the OCT image.[51] In biological tissue, water and melanin predominantly limit the transmission of OCT-based light.[51] Water absorption is low between ~280 nm and ~1,100 nm (except for an absorption peak at ~970 nm), whereas melanin absorption continuously decreases with increasing wavelength from the Ultraviolet to Infrared spectrum.[51]

1.5.5 Exogenous Targeted Fluorescence Imaging (TFI)

Exogenous contrast agents can be sub-divided into those which are targeted and those which are non-targeting (passive). *Targeted Fluorescence Imaging* (TFI) utilizes a targeting

fluorescence probe to delineate neoplastic tissue in real-time, typically consisting of a cancer targeting moiety and a conjugated fluorescent moiety.[52] TFI probes use several mechanisms to localize to neoplastic tissue, where a fluorescing modality is typically coupled to an active targeting modality with the corresponding mechanisms of action: (1) the targeting moiety binds to cancer cell receptors or is internalized into the cancer cell, with the fluorescent moiety subsequently fluorescing to highlight the cancer cells; (2) quenched probes can accumulate into cancer tissue, where cancer-specific enzymes (e.g., matrix metalloproteases) can de-quench the probe to enable detectable fluorescence signal; (3) a combination of #1 & #2; or (4) a targeting moiety binds to the neoangiogenesis related components, where the fluorescent moiety is subsequently excited and fluoresces.[45,53] Once the TFI probes accumulate in neoplastic tissue, an external light source (typically NIR excitation) is used to excite the fluorescing moiety and translate an image onto a CCD camera.

Cancer overexpresses epidermal growth factor receptor (EGFR); given that EGFR antibodies Cetuximab and Panitumumab are FDA approved, these antibodies are typically selected as an active targeting modality to couple with fluorescing modalities. NIR excited Cetuximab-IRDye800CW and Panitumumab-IRDye800CW are recently developed cancer specific probes which couple EGFR antibodies to IR excited dyes, however these agents are currently undergoing investigational use for FDA approval and require controlled lighting.[45]

1.5.6 Exogenous Non-Molecularly Targeted Fluorescence Imaging

An excellent example of a non-targeting fluorescent agent is indocyanine green (ICG), an FDA approved NIR fluorescent dye. This agent is commonly used in in perfusion imaging and in robotic surgery.[45,54] ICG localizes predominantly to tumor due to increased vascular endothelial permeability of the tumor microenvironment, where ICG is mainly bound to plasma proteins and therefore remains predominantly in the intravascular space.[55] 5 aminolaevulinic acid (ALA) induced protoporphyrin IX (the photosensitizing agent) is another notable example. 5-ALA is a naturally occurring intermediary in the heme synthetic pathway.[56] 5-ALA is

metabolized at the tissue level to the active compound protoporphyrin IX and accumulates within cells after exogenous ALA administration, resulting from low (compared to healthy tissue) ferrochelatase activity, the enzyme responsible for conversion of protoporphyrin IX to heme.[56]

1.5.7 Intensity-Based Endogenous Fluorescence (IAF)

The FDA approved VELscope has a long history of use for the early detection of oral neoplasia, and is among the most commercially recognized devices deployed for intensity-based autofluorescence evaluation.[32,43,45,57,58] Although these devices rely on the shallow penetration (<400 μm) of UV-VIS excitation light, it has been shown that they can detect changes in the epithelium with high sensitivity.[59] This device emits blue light between 400 and 460 nm wavelengths to excite endogenous fluorophores. After illumination, healthy tissue appears pale green when viewed through a selective long-pass filter, whereas abnormal tissue shows autofluorescence loss and appears as fark areas in contrast to surrounding tissue. Another similar implementation to VELscope is Identifi. Identafi is a multi-spectral device that incorporates white light, violet light, and green-amber light. The white light is for conventional oral examinations, the other two lights are designed to be used sequentially to facilitate examinations. Similar to VELscope, the violet light with 405 nm wavelength utilizes the autofluorescence loss phenomenon to distinguish neoplastic tissue from normal mucosa. Akin to NBI, the green-amber light with 545 nm wavelength approximately matches the peaks of absorption wavelengths of hemoglobin, which may facilitate the visualization of neoangiogenesis.

Table 1. Working Principles of Optical Techniques Investigated for H&N Cancer Surgical Guidance.

Technique	Resolution & Penetration Depth	Advantages	Disadvantages
High Resolution Microendoscopy **(HRME)**	Field-of-View (FOV): 330 µm – 1,400 µm Spatial Resolution: 4.0 – 4.5 µm.[60,61] Time resolution: 10-15 FPS.[45,62,63] Penetration Depth: 50 – 100 µm.[45]	• Simple instrumentation (no complex light sources, moving parts, or scanning mirrors).[45] • Real-time.	• Sensitivity and specificity depend on contrast agent.[45] • Requires exogenous contrast. • Proflavine, the most commonly used HRME contrast agent, is not FDA approved[45] and confounds imaging within heavily keratinized mucosa.[46] • Simplicity of HRME precludes optical sectioning.[45] • Shallow penetration depth. • Small FOV creates sampling error akin to biopsies.
Narrow Band Imaging (**NBI**)	Field-of-View: ~3 mm x 3 mm.[64] Spatial Resolution: ~10 µm when in contact with tissue.[64] Penetration Depth: < 1 mm for visualizing capillaries by blue light (400 – 430 nm) & < 2.5 mm for visualizing veins by green light (252-555 nm).[65]	• No exogenous contrast. • Reveals vascular and mucosal patterns.[48] • Easy to implement, user-friendly, widely available.[48] • Real-time implementation.	• User training needed to correctly interpret findings.[48] • Variability across users in interpreting findings.[48] • Vascular architecture is investigated for diagnosis, however vascular patters are affected by keratinization,[66] lymphatic tissue,[66] epithelial thickness,[66] benign lesions,[67] inflammation,[67] and sites of previous surgery.[67]
Raman Spectroscopy **(RS)**	Field-of-View: 0.85 ± 0.01 µm & Focal Imaging Depth: 5.05 ± 0.11 µm at 1,064 nm laser excitation.[68]	• Autofluorescence virtually eliminated with IR laser excitation.[69] • High SNR permits robust chemometric methods to be applied.[69] • Rapid, quantitative, molecularly specific, and objective.[69]	• Still in early stages for clinical adoption and commercialization.[70] • Technical limitations, including the need for controlled lighting, slow acquisition speed, and potential for sampling error. • Choice of wavelength impacts Raman scattering efficiency.[71]
Optical Coherence Tomography **(OCT)**	Spatial Resolution: 0.88 – 2.19 µm, aperture dependent,[51] using super resolution and deconvolution techniques.[72,73] Spatial resolution is dependent on aperture. Penetration Depth: ~2 to 3 mm aperture independent.[51]	• Highly investigated and commercially adopted, especially in ophthalmology.[51] • Technique prioritizes use of NIR, thereby exhibiting enhanced penetration depth (compared to UV and visible-based optical modalities). • Good depth of penetration.	• Penetration depth depends on wavelength and sample absorption and scattering properties.[51] • Motion artifacts in densely sampled tissue volumes.[74] • Long acquisition times to acquire data over large tissue areas.[74] • Structure-altering tissue conditions, such as dysplasia, may confound diagnosis.

Table 1 (Continued). Working Principles of Optical Techniques Investigated for H&N Cancer Surgical Guidance.

Technique	Resolution & Penetration Depth	Advantages	Disadvantages
Exogenous Targeted Fluorescence Imaging **(TFI)**	Spatial Resolution: Varies, ~ 21 µm.[75] Penetration Depth: ~5 mm using IRDye 800 CW Ex. 774 nm Em. 789 nm.[65]	• Targeting antibodies (e.g., EGFR), are well studied and exhibit ideal pharmacokinetic features, biodistribution, pose limited side-effects, and demonstrate low potential toxicity.[76] • Most fluorescent probes are NIR excited, enabling greater penetration depth and enhances tumor to background signal.	• Many current fluorescing probes are still in preclinical and early clinical investigation stages.[45] • Intra-tumor phenotype heterogeneity can impact sensitivity. Certain populations of tumors may downregulate the expression of cancer cell-surface antigens due to immune suppression or tumor internal coordination.[77] • Requires controlled lighting.[77] • Exogenous contrast.[77] • Reliance on a rather qualitative interpretation of fluorescence emission.[77] • Scattering, absorption, and autofluorescence properties may create low tumor signal-to-background ratio and obscure the invasive tumor front.[77]
Exogenous Non-Molecularly Targeted Fluorescence Imaging	Spatial Resolution: 2.66 µm for NIR-fluorescence microscopy[78] and ~20 µm for scanning fiber endoscopy.[79] Penetration Depth: > 1 mm for PPIX at Ex. 409 nm, Em. 633 nm.[65] ~ 5 mm for Indocyanine Green (ICG) at Ex. 789 nm and Em. 814 nm.[65]	• 5-ALA and ICG are well studied with highly documented safety profiles. • Good depth of penetration for ICG. • Use of ICG and 5-ALA in current practice in various surgical oncology fields.[80]	• Probes are not molecularly targeted, thereby exhibiting reduced tumor specificity.[81] • Relies on the presence of leaky capillaries to distribute to tumor.[82] • Non-tumor specific and lacks specificity for early neoplastic lesions.[81] • Exogenous contrast takes additional time to prepare and administer to the patient.
Intensity-Based Autofluorescence **(IAF)**	Spatial Resolution: ~ 1 mm for VELscope. 0.73 µm confocal laser scanning fluorescence microscope.[59] Penetration Depth: < 400 µm for VELscope	• Real-time implementation. • Endogenous-based fluorescence (autofluorescence). • Ability to qualitatively identify tumor margins through autofluorescence loss.[45]	• Steady-state fluorescence intensity analysis is confounded by irregular tissue surfaces due to non-uniform excitation/ collection geometry.[1,83] • Confounded by the variable presence of endogenous absorbers (e.g., blood) in the operative field.[83] • Poor specificity.[45]

Abbreviations: *Ex.* = Excitation, *Em.* = Emission, *SNR* = Signal-to-Noise Ratio, *FOV* = Field-of-View, *NIR*= Near Infrared, *UV*= Ultraviolet, *EGFR* = Epithelial Growth Factor Receptor, *PPIX* = Protoporphyrin IX

Table 2. Review of Literature: Optical Modalities Investigated for Surgical Guidance in Human Patients *In Vivo*

Authors & Year	Experiment Conditions	Technique	Evaluated Pathology	Results
Miles BA, Patsias A, Quang T, et al. **2015** [84]	*In Vivo* Human **Phase I Trial** N=33 Patients	**HRME** for margin delineation ("optical biopsy" of 695 images") of cancer, margin, ipsilateral normal, and contralateral normal	SCC tumors of the oral cavity and oropharynx.	Accuracy: 95.1 ± 1.0% Sensitivity: 96% ± 2.5% Specificity: 95% ± 4.5%
Garofolo S, Piazza C, Del Bon F. et al. **2015** [85]	*In Vivo* Human **Research** N=82 Patients	**NBI** used for intraoperative evaluation of early glottic cancer of the oropharynx via TORS.	Lesions and carcinoma of the oropharyngeal glottis.	The rate of positive superficial margins was 3.6% with the use of NBI, and 23.7% without the use of NBI.
Tirelli G., Piovesana M, Gatto A. et al. **2016** [86]	*In Vivo* Human **Research** N=70 Patients	**NBI** used for intraoperative delineation of resection margins.	Oral cavity and oropharynx SCC.	Use of NBI reduced positive margin rate from 36.4% in the control group (N=44 patients) to 11.5% (N=26 patients) using NBI.
Malik A, Sahu A, Singh SP, et al. **2017** [87]	*In Vivo* Human **Research** N=99 Patients	**RS** used to demarcate zones of mucosa prone to cancer reoccurrence via field changes at the molecular level.	Oral cavity SCC.	Sensitivity: 80% Specificity: 29.7%
Sunny SP, Agarwal S, James BL, et al. **2019** [88]	*In Vivo* Human **Research** N=14 Patients	**OCT** (spectral domain) was intraoperatively used to assess oral squamous cell carcinoma margins.	Oral cavity SCC on buccal mucosa and tongue.	Sensitivity: 92.8% Specificity: 70.51%
Keulen S., Nishio N, Fakurnejad S, et al. **2019** [36]	*In Vivo* Human **Phase I Trial** N=20 Patients	**TFI** (open-field fluorescence imaging). EGFR antibody panitumumab conjugated to IRDYE800CW used.	Primary oral cavity SCC tumors.	All carcinoma delineated (100%). Average tumor-to-background ratio: 2.2 ± 0.4.
Keulen S., Nishio N, Fakurnejad S, et al. **2019** [89]	*In Vivo* Human **Phase I Trial** N=14 Patients	**TFI** (open-field fluorescence imaging). EGFR antibody panitumumab conjugated to IRDYE800CW used.	Oral cavity SCC (pre-resection, followed by deep margin).	Surgical decision-making was improved in N=3 cases (21.4%) and deep-margin tumor detected in N=10 (71.4%) of patients.
Cicciu M, Cervino G, Fiorillo L, et al. **2019** [90]	*In Vivo* Human **Commercial** (Review of 25 Manuscripts over 10 Years)	**AFI Imaging** (VELscope) Excitation wavelength: 400 nm – 460 nm	Oral cavity SCC	Mean Sensitivity: 70.19% Mean Specificity: 65.95%
Pan J, Deng H, Hu S, et al. **2020** [91]	*In Vivo* Human **Research** N=20 Patients	**ICG** (intravenously delivered) visualized by near-infrared fluorescence imaging.	Oral cavity SCC	ICG fluorescence visible in all tumors, with a tumor to background ratio of 1.45 ± 0.36 reported. PSMs detected in all two patients.

Abbreviations: *HRME* = High Resolution Microendoscopy, *NBI* = Narrow Band Imaging, *RS* = Raman Spectroscopy, *OCT* = Optical Coherence Tomography, *TFI* = Targeted Fluorescence Imaging, *ICG* = Indocyanine Green, *SCC* = Squamous Cell Carcinoma, *EGFR* = Epithelial Growth Factor Receptor, *PSM* = Positive Surgical Margin *AFI Imaging* = Autofluorescence Intensity Imaging

CHAPTER 2 | Physical Principles of Fluorescence, Autofluorescence Properties of Head & Neck Cancer, and Review of Foundational Research to Date

2.1 | Physical Principles of Fluorescence

Fluorescence is a form of luminescence, where luminescence is the emission of light from any substance, which occurs from electronically excited states.[92] Luminescence is partitioned into two categories based on the nature of the excited state as either fluorescence or phosphorescence.[92] When specific molecules absorb photons of appropriate energy, a cascade of photophysical events occur; depending on the molecule, this may include: (1) internal conversion and vibrational relaxation (resulting in energy loss in the absence of light emission), (2) fluorescence, (3) intersystem crossing, and (4) phosphorescence.[93] The lifetime of the excited state is defined as the average time a molecule spends in the excited state prior to return to the ground state.[1,92,93] The lifetime of photophysical processes, such as internal conversion, varies from tens of femtoseconds,[94,95] to nanoseconds for fluorescence,[93] and finally microseconds to seconds for phosphorescence.[95]

Fluorescence lifetime is considered a state function as it does not depend on initial perturbation conditions, such as duration of light exposure, excitation wavelength, fluorophore concentration, photobleaching, and is independent of fluorescence intensity.[93] Fluorescence is typically characterized by the absorption cross-section of the molecule, the coupled absorption and emission spectrum, the quantum yield (number of emitted photons over the total number of absorbed photons), and the lifetime (τ) of the fluorescence signal.[2]

Jablonski diagrams, demonstrated in *figure 2*, are useful representations that visually denote the processes of molecular absorbance and emission of light after applying photons to a particular molecule. The diagram is an energy diagram, arranged with energy on the vertical axis. Bold horizontal lines are representations of the limits of electronic energy states, and within each electronic energy state are multiple vibronic energy states that may be coupled with the electronic state. The use of straight and curved lines demonstrates transitions between

eigenstates that occur from exposure of a molecule to a particular wavelength of light. Only certain wavelengths of light are possible for absorbance, which are wavelength energies that match the energy difference between two different eigenstates of a particular molecule. 'S_0' represents the ground singlet state, 'S_1' is the first singlet state and 'S_2' is the second singlet state. Fluorescence occurs only from the transition from the limit of the 'S_1' vibrational state down to electronic energy levels of the ground state.

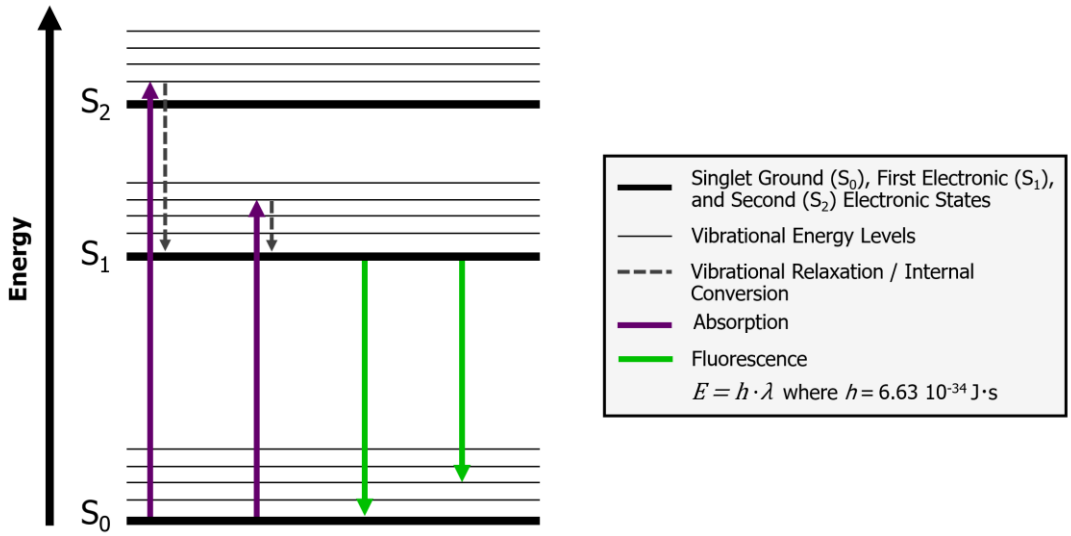

Figure 2: Simplified Jablonski diagram demonstrating the fluorescence photophysical process. Incident photons of appropriate energy promote electrons from the ground state (S_0) to an excited state (e.g., S_1, S_2). Fluorescence results from the transition from the lowest limit of the S_1 vibrational state down to vibronic energy states of S_0. Figure adapted with modification from reference [96].

Fluorescence typically occurs from aromatic molecules, where fluorescing substances are coined as "fluorophores." Many fluorophores can be found in nature (e.g., Quinine, Pyridine 1, Rhodamine B, Fluorescein, etc.) as well as in biological tissues (discussed in *chapter 2.3* in detail). Fluorescence lifetime varies between molecular species and is sensitive to environmental factors such as the conformation and binding state of the absorbing molecule, the temperature, the pH, or the solvent viscosity.[97] For fluorophores intrinsic to tissue, such dependencies can be used for probing tissue properties including composition, structure, and metabolic state.[1,58]

2.2 | Introduction to Autofluorescence

Autofluorescence is a term used to designate fluorescence that originates from specific endogenous (intrinsic) tissue fluorophores, thus representing a label-free optical phenomenon. As described previously in the context of a Jablonski diagram, autofluorescence is the radiative process that occurs after a molecule absorbs a photon (*figure 3A*) that promotes an electron from the ground state (S_0) to an excited state (S_1), resulting in an electron decay back to the ground state, which resulting in the emission a photon of lower energy (*figure 3B*). Due to the magnitude of possible vibrations and rotational energy levels within a molecule, resulting fluorescence occurs over a spectral range, denoted as the emission spectra in *figure 3C*. Correspondingly, fluorescence emission is of lower energy than the absorbed photons, which is referred to as Stokes shift (*figure 3C*). Single fluorophores exhibit mono-exponential lifetime decays, where the fluorescence lifetime corresponds to the value of 'τ' in $\mathrm{I(t)} = \frac{1}{e^{t/\tau}}\mathrm{I_0}$, which is the time it takes for $\mathrm{I} = \frac{1}{e}\mathrm{I_0}$ (*figure 3D*). Typically, the lifetime of endogenous fluorophores ranges from 0.1-7 nanoseconds.[93]

Intrinsic tissue fluorophores often present as aromatic molecules. Amino acids like tryptophan and tyrosine absorb and emit light in the ultraviolet (UV) range. Enzymatic cofactors Nicotinamide Adenine (Phosphate) Dinucleotide (NAD(P)H), Flavin Adenine Dinucleotide (FAD) and pyridoxal phosphate fluoresce in the visible range. Other molecules that fluoresce in the visible range include collagen, elastin, structural protein crosslinks, keratin, lipopigments and porphyrins. The fluorescence properties of these molecules and other tissue fluorophores are described in detail elsewhere.[93,96,98,99]

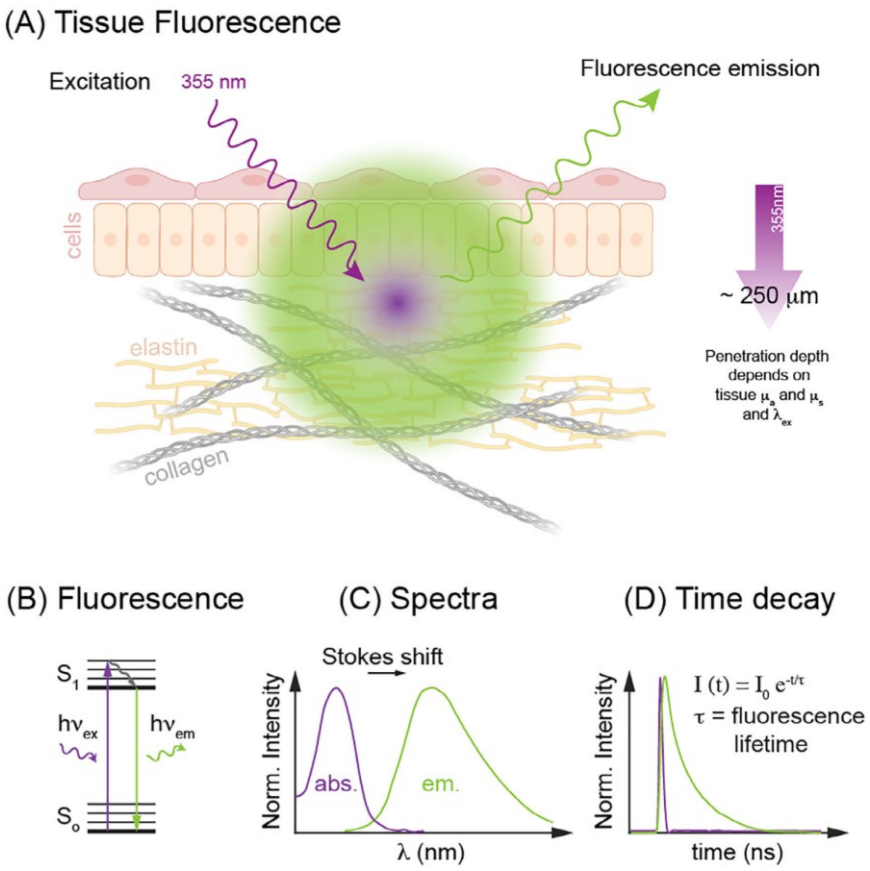

Figure 3: Representation of autofluorescence excitation-emission, spectra, and lifetime. (A) Schematic of light-tissue interaction, where incident excitation light results in the generation of fluorescence emission. The tissue penetration depth depends on the tissue scattering (μ_s) and absorption (μ_a) properties, which are wavelength (λ_{ex}) dependent. The longer the wavelength, the deeper light penetrates. (B) Simplified Jablonski diagram for fluorescence, where a photon ($h\nu_{ex}$) excites the electrons from the ground state (S_0) to an excited state (S_1). The radiative relaxation back to S_0 emits fluorescence photons ($h\nu_{em}$). (C) Absorption (abs.) and emission (em.) spectra featuring the Stokes shift. (D) Temporal intensity decay of the fluorescence emission characterized by the fluorescence lifetime (τ) following an excitation pulse. Figure reproduced with permission from Alfonso-Garcia A., et al. reference [2].

Collagen, NAD(P)H, FAD, and porphyrins are recognized as the main contributors to head and neck cancer autofluorescence emission due their prevalence and high quantum yield in oral cavity and oropharyngeal tissues.[1] The excitation, emission, and lifetime properties of these fluorophores are summarized in *table 3*.

Collagen is the most abundant protein in the body, making up nearly half of the total body protein by weight.[100] This protein forms flexible, but nonelastic fibers, that provide tensile strength to tissue, thereby imparting resistance to longitudinal stress.[100] In the oral mucosa, collagen forms the structural network of the connective tissue component and is present in fibrillar form.[101] The lamina propria beneath the stratified squamous epithelium is the fibrous

tissue layer that contains collagen in oral mucosal tissues.[101] There are two different collagen types in oral mucosa: (1) type III and type IV collagen, representing a loose reticular network, comprising the upper connective stroma (lamina propria) and (2) collagen type 1 and type 3, present in a ratio of 4:1, in deeper stroma.[101] Collagen type I and III are the major fibrillar components, presenting in a ratio of 4:1 in the submucosa. Collagen fiber organization and size vary topographically in the oral mucosa.[101]

Table 3. Excitation, Emission, and Lifetime Characteristics of Collagen, NAD(P)H, FAD, & Porphyrins.

	Excitation (nm)	Emission (nm)	Lifetime (ns)
Collagen	280-350 [102]	370-440 [102]	≤5.3 [93]
NAD(P)H (Free)	300-380 [103]	450-500 [103]	0.3 [103]
NAD(P)H (Protein Bound)	300-380 [103]	450-500 [103]	2.0−2.3 [103]
FAD (Free)	420-500 [103,104]	520-570 [103,104]	2.91 [103,104]
FAD (Protein Bound)	420-500 [105]	Very Weak 520-570 [105]	<0.01 [105]
Protoporphyrin IX	400-450 [103,106]	635,710 [103,106]	Range: 2-3 (dimers) [1] 10-12 (monomers) [1]

Abbreviations: *NAD(P)H* = Nicotinamide Adenine (Phosphate) Dinucleotide, *FAD* = Flavin Adenine Dinucleotide

The fluorophores within collagen molecules are the fluorescent amino acids phenylalanine and tyrosine, pyridinoline crosslinks, and specific glycation end products such as pentosidine.[107] Nearly half of the fluorescent components are from the pyridinoline crosslinks, which account for 5% of all amino acids in a collagen molecule.[107] It is observed that increased crosslinking results in increased fluorescence lifetime; because there is an accumulation of fluorophores within crosslink sites, changes to fluorescence lifetime of collagen can be linked to changes to crosslinking.[107]

The reduced form of Nicotinamide Adenine Dinucleotide (NADH) and its phosphate derivative (NADPH) are key fluorescent molecules in the metabolic network, along with Flavin Adenine Dinucleotide (FAD).[93] Together, NAD(P)H and FAD play ubiquitous roles in cellular glycolysis, the citric acid cycle, and oxidative phosphorylation.[93,100] The fully oxidized form of

NAD(P)H, $NAD(P)^+$, and the fully reduced form of FAD, $FADH_2$, are non-fluorescent forms of these redox cofactors.[93] It should be noted that the intensity and lifetime of NAD(P)H strongly depends on the microenvironment, where NAD(P)H has a mean fluorescence lifetime of 2.3-3.0 ns when bound to protein, and a short lifetime ~0.3-0.4 ns when in free form.[108,109] Metabolic shifts in cellular processes, such as cells predominantly undergoing glycolysis vs. oxidative phosphorylation, drives a shift in the ratios of the protein-bound NAD(P)H fractions, and oxidative and reduced ratios of FAD and NAD(P)H, thereby driving marked changes in autofluorescent intensity and lifetime.

Porphyrins represent among the longest emission wavelength of all naturally occurring fluorophores, fluorescing in the reddish-orange range.[93] Protoporphyrin IX (PPIX) has been reported as a key fluorophore in cancer diagnostics, where enzymatic differences between tumor and normal cells culminate in higher PPIX concentration in cancer.[1] Although promising, PPIX has been less studied and has reduced quantum yield compared to that of collagen, NAD(P)H, and FAD.

2.3 | Autofluorescence Properties of H&N Cancer – Mechanisms of Contrast, Review of Foundational Research to Date, and Expected Outcomes

2.3.1 Head and Neck Cancer Drives Changes in Autofluorescence Properties – An Explanation from a Physiological Standpoint

In the 1920s, Otto Warburg demonstrated that cancer cells are highly glycolytic compared to normal cells, which favor the much more efficient oxidative phosphorylation pathway. This phenomena was coined the *Warburg Effect*, where reductive glycolysis was demonstrated as the prevailing cancer cell metabolic pathway.[110,111] While current knowledge demonstrates this effect is not as binary as originally thought, this effect generally holds true for many cancer cell populations. Recent findings suggest that tumors demonstrate some degree of metabolic plasticity, and depending on the conditions, can switch between glycolysis and oxidative phosphorylation (although cancer prefers the glycolytic pathway due to the production of metabolic intermediates which promote tumor progression).[112] HNSCC has been previously demonstrated to follow the general principles of the Warburg effect. A transition of cell populations to glycolysis under the *Warburg Effect* demonstrates considerable changes to the balance of NAD+/NAD(P)H and FAD/$FADH_2$.

Tumors are complex structures with malignant cancer cells embedded in vasculature and surrounded by a dynamic tumor stroma.[113] The tumor microenvironment acts similarly to the inflammatory response of healing wounds, in that it promotes angiogenesis, turnover of the extracellular matrix (ECM), and is characterized by tumor cells with marked motility.[113,114] Matrix metalloproteinases (MMPs) regulate a variety of physiological processes and signaling events, therefore representing key roles in the molecular communication between tumor and stroma.[113] MMPs form a family of proteases which are associated with a variety of tumor-driven processes, including: (1) tumor invasion and intravasation, (2) angiogenesis, (3) regulation of inflammation, and (4) the metastatic niche.[113] It is known that HNSCC tumors mediate the activity of collagenases.[115] Other studies have demonstrated that cancer associated fibroblasts within squamous cell carcinomas can regulate collagen cross-linking,[116] which, synergistically with

MMPs, influences the invasive properties of tumor cells. Suitably, MMPs associated with tumor progression alters fluorescence lifetimes (decreases lifetime due to reduced crosslinking) and intensities (decreases intensity of the fluorescent amino acids phenylalanine and tyrosine due to cleavage), thereby imparting a mechanism for autofluorescence contrast between benign tissue and cancer.

A unique feature of cancer is an acidic tumor microenvironment, which is recognized to drive cancer somatic evolution and disease progression.[117] The tumor acid/alkaline balance is regulated through a complex interplay between cellular carbon metabolism and acid removal mediated by abnormal tumor-associated vessels, interstitial fluid buffering, and transport proteins.[117] The pH of extracellular fluid in healthy tissues is tightly regulated between 7.35 – 7.45, which is important to sustain normal physiology and cellular metabolism.[117] Conversely, the extracellular fluid pH neighboring cancer cells is acidic, between 6.3 – 7.0, which demonstrates the dysregulation of the acid-base homeostatic mechanisms which are observed within solid tumor microenvironments where hypoxic conditions and high respiration (e.g., excess CO_2 production creating carbonic acid) conditions dominate.[114,117] Because pH is known to alter fluorescence lifetime,[108] it is expected that the acidic tumor microenvironment plays a role in lifetime-based contrast for endogenous fluorophores. This result was confirmed for endogenous FAD in HeLa cells, when the fluorescence lifetime of FAD was measured at different intracellular pHs.[118] It was found that increased (more basic) intracellular pH resulted in decreased average fluorescence lifetime of FAD in these cell cohorts.[118] Interestingly, when FAD was isolated and placed in buffer solution, the lifetime did not change with pH when exposed to a pH range of 5-9.[118] This result confirmed that interactions between FAD and surrounding functional groups in a protein depend on intracellular pH, which promotes pH-induced change in the non-radiative decay rate, and thus lifetime, of FAD in HeLa cells.[118] An analogous result was observed with NAD(P)H in HeLa cells, where the average fluorescence

lifetime of NAD(P)H became shorter monotonically as intracellular pH increased in a range from pH 5 to pH 9.[118]

The effect of temperature on fluorescence lifetime is an important consideration, particularly when interrogating excised tissue for fluorescence lifetimes in diagnostic applications, where excised tissue is no longer maintained at normal body temperature (97.7–99.5 °F). Temperature affects bond rotation rate constants, where increased temperature increases the bond rotation rate, which in turn decreases the fluorescence lifetime.[93]

2.3.2 Review of Significant Pre-Clinical and Clinical Autofluorescence Research Findings to Date in H&N Oncology Research

This section focuses on a review of the foundational time-resolved autofluorescence research conducted in the H&N oncology research space, both in laboratory and clinical settings. *Table 4* provides an overview of foundational pre-clinical and clinical research conducted to date (exempting completed research within this scope of original research herein) for head & neck oncology. As the focus of this work is based on intraoperative margin evaluation, literature focused on *ex vivo* is not discussed. We remark however that promising *ex* results using autofluorescence have been demonstrated, including recent work (March 2022) by Maie St. John et al.[119]

Table 4. Foundational Time-Resolved Autofluorescence Research in Head & Neck Oncology.

Authors & Year	Experiment Conditions	Evaluated Pathology	Technique	Ex. & Em. λ and Fluorophores	Results
Chang CL, You C, Chen HM, et al. **2004** [120]	***In Vivo*** **Human** Patients (N=33 Oral Cavity Lesions)	Benign, Leukoplakia, Verrucous Hyperplasia, Dysplasia, & SCC	TCSPC Spectra	Ex: 410 nm Em: 630 nm (PpIX)	$LT_{Benign}<LT_{SCC}$ & $LT_{Benign}<LT_{Dysplasia}$
Chen HM, Chiang CP, You C, et al. **2005** [121]	***In Vivo*** **Human** Patients (N=55 Oral Cavity Tongue & Mouth Lesions)	Benign, Hyperplasia, Dysplasia, Verrucous Hyperplasia	TCSPC Spectra	Ex: 410 nm Em: 630 nm (PpIX)	LT Resolved Benign Epithelium, Hyperplasia, and Dysplasia
Sun Y, Phipps J, Elson DS, et al. **2009** [83]	***In Vivo*** **Hamster** (Buccal Pouch)	Benign, Dysplasia, *In Situ* SCC, SCC	Endoscopic FLIm via Gate Intensified CCD Camera	Ex: 337 nm, Em_1: 390/70 nm (Collagen) Em_2: 450/65 nm (NADPH)	Collagen Intensity Decreased in Cancer Relative to Benign & NADH LT Decreased for Cancer
Farwell DG, Meier JD, Park J, et al. **2010** [122]	***In Vivo*** **Hamster** Oral Cavity	Benign, Dysplasia, *In Situ* SCC, SCC	TRFS Spectra	Ex: 377 nm Em: 360-650 nm at 5nm Intervals 390 nm (Collagen) 460 nm (NADPH) 633 nm (Porphyrin)	$LT_{Benign}>LT_{Cancer}$ at 460 nm. Combined LT and IR Resulted in Better Discrimination Performance
Jo JA, Applegate BE, Park J, et al. **2010** [123–125]	***In Vivo*** **Hamster** Oral Cavity	Benign, SCC	FLIm & OCT (Multimodal)	FLIm Ex: 355 nm Em_1: 390/40 nm (Collagen), Em_2: 452/45nm NADPH, Em_3: 550/40 nm FAD	Multimodal Evaluation Improved Discrimination vs. Single-Modality
Sun Y, Phipps JE, Meier J, et al. **2013** [126]	***In Vivo*** **Human** 10 Patients 26 Sites Buccal Mucosa	Benign, SCC	Endoscopic FLIm	Ex: 337 nm Em: 460/50 nm (Combination of Collagen & NADPH)	$LT_{SCC} < LT_{Benign}$ $INT_{SCC} < INT_{Benign}$
Fatakdawala H, Poti S, Zhou F, et al. **2013** [127]	***In Vivo*** **Hamster** Buccal Pouch	Benign, Precancerous Lesions, SCC	Multimodal FLIm, PAI, & UBM	FLIm Ex: 337 nm Em_1: 390/40 nm, (Collagen) Em_2: 450/45 nm, (NADPH) Em_3: 542/50 nm (FAD) Em_4: 629/53 nm (Porphyrins)	Benign, Precancer Lesions, and SCC Distinguished with Average LT. PAI Detected Higher Vascularization within Tumor. UBM Improved FLIm Discrimination

Table 4 (Continued). Foundational Time-Resolved Autofluorescence Research in H&N Oncology.

Authors & Year	Experiment Conditions	Evaluated Pathology	Technique	Ex. & Em. λ and Fluorophores	Results
Pande P, Shrestha S, Park J, et al. **2016** [128]	***In Vivo*** **Hamster** Buccal Pouch	Benign, Precancerous Lesions, SCC	Multimodal FLIm and OCT	FLIm at Ex: 355 nm Em_1: 390/40 nm, (Collagen) Em_2: 452/45 nm, (NADPH) Em_3: 600/125 nm (FAD & Porphyrins)	Automated Quantitative Image Analysis of 3D FLIm and OCT. Classification Accuracy of Both Modalities: 87.4%; FLIm Only: 83.4%
Malik BH, Lee J, Cheng S, et al. **2016** [129]	***In Vivo*** **Hamster** Buccal Pouch	Benign, Low grade Dysplasia, High Grade Dysplasia	FLIm	Ex: 355 nm Em_1: 390/20 nm (Collagen), Em_2: 450/22.5 nm (NADPH) Em_3: 500 nm/20 nm (FAD)	$LT_{Benign} > LT_{SCC}$ For Collagen and NAD(P)H
Gorpas D, Davari P, Bec J, et al. **2018** [130]	***In Vivo*** **Human** Oral Cavity Mucosa	Oral Lichen Planus (OLP)	TRFS Spectra	Ex: 337 Em_1: 390/40 nm (Collagen) Em_2: 466/40 nm (NADPH) Em_3: 542/50 nm (FAD) Em_4: 629/53 nm (Porphyrins)	LT_{OLP} Collagen, NADH, & FAD < LT_{Benign} Collagen, NADH, & FAD
Lagarto JL, Phipps JE, Faller L, et al. **2018** [131]	***In Vivo*** **Swine** Tonsil, Base of Tongue, Soft Palate	Electrocautery Effects on Mucosal Tissue	FLIm Integrated into Da Vinci Si Transoral Robotic Surgical Platform	Ex: 355 nm Em_1: 390/40 nm (Collagen) Em_2: 470/28 nm (NADPH) Em_3: 542/50 nm (FAD) Em_4: 629/53 nm (Porphyrins)	FLIm Incorporated into TORS. Aiming Beam Augmented Data. Distinct FLIm Signatures w/ Electrocautery. Temporal Dependence of Electrocautery
Jo JA, Cheng S, Cuenca R, et al. **2018** [132,133]	***In Vivo*** **Human** Oral Cavity Lesions	Benign, High Grade Dysplasia, SCC	FLIm Endoscope	Ex: 355nm Em_1: 390/20 nm (Collagen), Em_2: 452/22.5 nm (NADPH), Em_3: ~500 nm (NADPH/FAD)	$LT_{Benign} > LT_{scc}$ $INT_{Benign} > INT_{scc}$
Gorpas D, Phipps J, Bec J, et al. **2019**	***In Vivo*** **Pig & Human** Oropharynx	Benign, SCC, SCC with Lymphoid Tissue Background	FLIm Integrated into Da Vinci Si	Ex: 355 nm Em_1: 390/40 nm (Collagen) Em_2: 466/40 nm (NADPH) Em_3: 542/50 nm (FAD) Em_4: 629/53 nm (Porphyrins)	First Demonstration of FLIm in the Human Oropharynx. Benign Tissue, SCC, and SCC Over Lymphoid Tissue Resolved with Multi-Spectral LT Plots

Abbreviations: *Ex.* = Excitation, *Em.* = Emission, *λ* = Wavelength, *SCC* = Squamous Cell Carcinoma, *LT*= Lifetime, *TCSPC*= Time Correlated Single Photon Counting, *CCD* = Charge Coupled Device, *UBM* = Ultrasound Backscatter Microscopy *TRFS* = Time Resolved Fluorescence Spectroscopy, *PAI* = Photoacoustic Imaging, *PPIX* = Protoporphyrin IX, IR = Intensity Ratio *TORS* = Transoral Robotic Surgical Platform

* *Table excludes research conducted under the purview of the present research investigation.*

As demonstrated in *table 4*, the first published study regarding autofluorescence lifetime measurements on human subject oral carcinogenesis was reported in 2004, where a time-correlated single-photon counting system (TCSPC) system was used to study the temporal profile of Protoporphyrin IX (PpIX) as an indication of carcinogenesis *in vivo*.[120] Among 33 human patient oral cavity tissues assessed, normal tissue was found to have a significantly shorter (PpIX) lifetime than tissue characterized by dysplasia and cancer, thus demonstrating the preliminary feasibility of autofluorescence for the demarcation of dysplasia and tumor tissue.[120] Further studies by this group in 2005 on a 55 human subject cohort substantiated their preliminary findings, also demonstrating the ability to differentiate hyperplasia from normal epithelium by PpIX autofluorescence.[121]

In 2009, using an endoscopic FLIm instrument with a gate intensified CCD camera, Sun et al. published first multi-spectral assessment of oral cancer, where collagen (390/70 nm) and NADH (450/65 nm) autofluorescence was leveraged to differentiate normal tissue from dysplasia, carcinoma in situ, and squamous cell carcinoma *in vivo* on hamster buccal pouch models.[83] Collagen intensity and lifetime was found to decrease for cancer relative to healthy tissue.[83] A study in 2010 used time resolved fluorescence spectroscopy (TRFS) was used to detect oral carcinoma in hamster buccal pouch models.[122] Healthy tissue, dysplasia, carcinoma *in situ*, and invasive carcinoma were evaluated using autofluorescence spectra of collagen, NAD(P)H, and porphyrins.[122] Sensitivity and specificity were calculated using spectral ratio, average lifetime, and use of a zero-order Laguerre fitting coefficient to the temporal profile.[122] Superior results were achieved with respect to sensitivity and specificity when using spectral ratio, average lifetime, and the zero-order Laguerre fitting coefficient together.[122] A sensitivity of 76.5% and specificity of 96.2% was achieved.[122]

An independent study in 2010 by Jo et al. introduced the first multimodal FLIm-OCT device for the characterization of oral cavity cancer;[124] collective findings using this instrument

on hamster cancer models *in vivo* demonstrated that multimodal evaluation of cancer and healthy tissue improved discrimination capacity by improving both sensitivity and specificity.[123–125] A subsequent 2013 study by Fatakdawala et al. coupled multimodal FLIm, photoacoustic imaging (PAI) and ultrasound backscatter microscopy (UBM) to distinguish normal tissue from precancerous and carcinoma tissue in hamster buccal pouch models.[127] The authors noted the improvement which multimodal approaches confer to FLIm, where the highest sensitivity and specificity was reported when FLIm was used in combination with the other imaging modalities for healthy vs. cancer differentiation. Pande et al. further substantiated these findings with their own multimodal FLIm-OCT implementation.[128]

In 2016, promising results were reported for the *in vivo* detection of oral carcinogenesis for hamster cheek pouch models, where collagen, NADH, and FAD were used to differentiate between normal tissue, benign lesions, low-grade dysplasia, and high-grade dysplasia with statistical significance.[129] Also in 2016 Jo et al. demonstrated the first use of automated quantitative image analysis of 3D FLIm and OCT for the automated diagnosis of oral cavity cancer, which was an essential first step towards automated diagnostic algorithms on autofluorescence in this research area. In 2017, TRFS was used to detect oral lichen planus *in vivo* in human subjects, with collagen, NADH, and FAD leveraged as the primary fluorophores for time-resolved contrast.[130] In 2018, the effect of electrocautery on ms-FLIm for live Yorkshire pigs was investigated.[131] BOT, tonsil, tonsil-soft palate intersection, and tongue were evaluated.[131] This work discovered distinct redox ratios and FLIm signatures appear with electrocautery, with an apparent temporal dependence following cauterization to restore fluorescence back towards the non-cauterized baseline.[131] Other work in 2018 used ms-FLIm for detection of dysplasia, oral cancer, and benign lesions.[132,133] Optical redox ratio, collagen intensity, FAD intensity, and NAD(P)H lifetime were most informative in differentiating

conditions.[132,133] Finally in 2019, multispectral-TRFS was integrated into the da Vinci surgical system, with its functionality validated in swine and human patients.[134]

2019 was a remarkable year for the intraoperative translation of FLIm for intraoperative surgical guidance as Gorpas et al. worked with Intuitive Surgical to integrate multi-spectral FLIm into the da Vinci surgical system.[135] The validation of this transoral robotic surgery integration was reported on both swine (n=3) and human (n=4) patients.[135] Results were also published on the effect of electrocautery on ms-FLIm for live Yorkshire pigs using this da Vinci surgical platform.[131] This integration into the da Vinci opened up a new and previously unexplored research area for FLIm, oropharyngeal cancer, as these deeper and harder to access cancers (palatine tonsil, lingual tonsil, base of tongue, etc.) require the use of TORS for resection.

2.3.3 The Next Steps to Progress Autofluorescence Research & Instrumentation Towards Devices Suitable for Diagnosis and Surgical Guidance

Significant human-based time-resolved autofluorescence studies conducted to date have primarily focused on the feasibility of FLIm for intraoperative diagnosis. These studies have typically characterized only one cancer type or anatomical site at a time, and many of these studies have used measurements on contralateral healthy tissue for juxtaposition to cancer measurements. Performing comparisons based on contralateral sites however does not establish feasibility for intraoperative surgical guidance since measurements within the heathy-tumor interface must be explored. Current studies have solely focused on oral cavity cancer (e.g., tongue, lips, floor of mouth, gingivae), but many have not explored deeper and harder to access anatomical cancers, such as the oropharynx (e.g., palatine tonsil, base of tongue, lingual tonsils). Previous studies have not characterized how fluorescence lifetimes and intensities change with distance from cancer tissue, and if there is a gradient of transitions in FLIm data, or a discrete change in fluorescence at the tumor-healthy interface. Other physiological conditions which may impact FLIm measurements, such as ulceration, necrosis, and dysplasia have been sparsely investigated.

Previous research has not characterized how other major factors such as heavy smoking and tobacco use, tissue damage from mastication forces, and other factors alike impact oral tissue autofluorescence. In particular, chronic smoking and chewing tobacco use is known to change pigmentation and thickness of the oral epithelium,[136] increase keratin formation,[136] alter cellular metabolism and gene expression,[137] change collagen properties,[138] and create other conditions such as inflammation.[139] Such dramatic alterations of the epithelium due to tobacco use are within the purview of fluorescence lifetime and intensity-based alterations, and are thus essential to characterize in order to assess the impact of smoking and non-smoking populations on fluorescence lifetime research.

With respect to anatomy, the tissues of the oral and oropharyngeal cavity vary in structure, function, and metabolism, yet the majority of FLIm research to date has done little to elucidate the autofluorescence differences among disparate anatomies and has typically grouped measurements at all anatomical locations under one analysis for studies based on multiple anatomic sites. To cite a specific scenario, consider the shallow penetration depth of FLIm (<250 μm); it is expected that tissues with varied epithelial thicknesses should confer differences in FLIm signal since the lamina propria and basement membrane will provide enhanced autofluorescence signal contributions for tissues with small epithelial thicknesses. Normal values for epithelial thickness within oral cavity tissues vary from 106 μm ± 25 μm at the floor of mouth, 216 μm ± 59 μm for the oral cavity tongue, and 294 μm ± 68 μm in the buccal mucosa.[140] Interestingly, inflammatory responses,[141] hyperplasia,[142] dysplasia,[142] and cancer[142,143] have been associated with increased epithelial thickness; all of which should drive changes in autofluorescence signal.

Due to the sensitivity of autofluorescence to chemical and physical factors,[108] it is expected that fluorescence lifetime and intensity measurements will vary at different anatomical locations as epithelial thickness[140], collagen content,[144] metabolism, and other factors will vary.

The evaluation of oral autofluorescence has traditionally grouped all cancer types together, however different oral cancer types in theory should exhibit significant autofluorescence differences due to different malignancy levels, different mechanisms of action, disparate metabolic properties, and varied cell morphologies. The extent of contrast achievable within a patient and the degree of variation among patients have not been quantitatively evaluated. Suitably, there is great opportunity to further characterize FLIm's diagnostic potential of oral cavity and oropharyngeal cancer, which is an essential next step in the realization of this method for intraoperative use in tumor margin mapping and diagnosis.

To continue to advance FLIm past initial feasibility stages with the eventual goal of clinical diagnostic use, an essential next step is to rigorously evaluate if FLIm-derived lifetime and intensity ratio parameters can be always found and used as a means of generating significant intrapatient contrast between healthy tissue and cancer, irrespective of experimental situations. For FLIm to be widely implemented for universal diagnosis, it is essential to understand if certain tissue anatomies, cancer types, medical histories (such as tobacco use), or imaging contexts (*in vivo* vs. *ex vivo*) yield poor contrast. Such results will inform on FLIm's overarching diagnostic potential and identify patient cohorts, and other factors, which yield poor contrast and perhaps require alternative techniques for performing robust diagnosis.

Another important aspect of future work in this area is to elucidate overarching FLIm-derived parameters (e.g., average lifetimes and intensity ratios) for healthy tissue, dysplasia, and cancer, and to evaluate the degree of interpatient variability. It will be important to study the impact of imaging conditions (anatomical tissue type, *in vivo* vs *ex vivo* imaging, patient medical history, etc.) on these trends to understand common ground which will enable universal diagnostic use. Collectively, this work will rigorously evaluate the diagnostic efficacy of FLIm, study the impact of experimental situations and imaging conditions on FLIm-based contrast, and provide a comprehensive overview of the associated FLIm lifetime and intensity trends thereof.

This work additionally serves as feasibility for investigation of other techniques, such as machine learning.

2.3.4 Expected Autofluorescence Trends Associated with Pathology

Figure 4 graphically summarizes the hypothesized fluorescence lifetime, fluorescence intensity, and predicted changes to mucosal thickness with inflammation, dysplasia, and cancer.

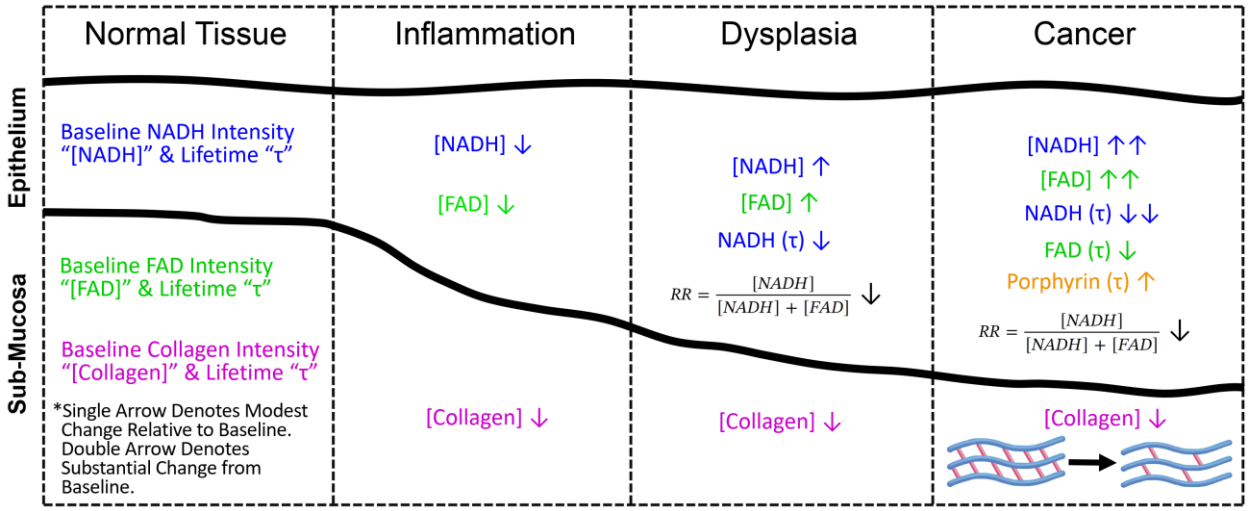

Figure 4: Expected autofluorescence outcomes predicted with the onset of pathology. Published studies demonstrate that epithelial thickness of oral mucosa increases with inflammation, dysplasia, and cancer, which results in reduced collagen autofluorescence intensity.[59,129,145,146] Dysplasia and cancer drive a shift towards shorter NAD(P)H lifetimes,[129,130,146] decreased redox ratio, defined as CH2/[CH2+CH3],[145] increased NAD(P)H intensity,[59,129,145] and increased FAD intensity.[129,146] Cancer additionally drives a decrease in FAD lifetime,[130] and an increase in Porphyrin lifetime.[120,146] Figure concept motivated from reference [146].

Previously reported oral cavity autofluorescence research demonstrates that inflammation decreases NAD(P)H,[146] FAD[146] and collagen intensity relative to baseline benign tissue values.[59,145,146] Dysplasia has been shown to increase NAD(P)H,[59,129,145] FAD,[129,146] and porphyrin intensities,[120,146] decrease NAD(P)H lifetime,[146] decrease redox ratio,[145] and decrease collagen autofluorescence intensity.[59,120,129,145] Oral cancer demonstrates substantial increases in NAD(P)H[59,145] and FAD intensities,[129,146] a significant decrease in NAD(P)H lifetime,[129,130] an increase in porphyrin lifetime,[120,146] a decrease in FAD lifetime,[130] a decrease in collagen intensity,[59,129,145] and a decrease in the redox ratio.[145]

CHAPTER 3 | Method for Implementing FLIm for Surgical Guidance of H&N Cancer: Instrumentation, Data Visualization, and Classification Approach

3.1 | FLIm Instrumentation & Computation of Analytical Parameters (Spectral Intensity Ratio, Average Lifetime, and Phasor Analysis)

3.1.1 Description of Hardware

Fluorescence Lifetime Imaging (FLIm) hardware and analytical approaches vary depending on the scale of measurement (e.g., microscopic vs. mesoscopic assessments) and implementation (e.g., microscopy vs. point-scanning). From a hardware standpoint, autofluorescence can be evaluated through both spectral intensities, as well as through time-resolved characteristics of autofluorescence temporal dynamics. Single-photon and two-photon excitation setups are common, and the emission spectrum evaluated varies, hence the endogenous fluorophore emission spectrum of interest is tailored to capitalize on the intended fluorophore target. These devices may be implemented in various fashions, such as benchtop devices (e.g., microscopy), endoscopes, and point-scanning methods. The preprocessing requirements, approach to analysis (such as time or frequency domain FLIm), and other analytical models also change depending on the implementation and number of fluorophores evaluated. The discussion of all implementations are outside the scope of this research investigation and are detailed extensively elsewhere.[1,2,96] However, the FLIm instrumentation used to acquire intraoperative data within the context of this research is presented in detail in the following section.

The clinical system used for data acquisition is a custom-built, fiber optic-based, multi-spectral, point-scanning, pulse-sampling FLIm system. This device was developed for rapidly acquiring intraoperative data across multiple centimeter tissue scales and was designed to augment computed fluorescence lifetime data over surgical images in real-time.[134] This instrument employs a 355 nm micro Q-switched pulsed laser (0.6 ns FWHM pulse width, 120 Hz repetition rate; STV-02E-1x0, Teem Photonics, France) delivered through a 365 μm core diameter multi-mode fiber imaging probe designed for surgical oncology applications. The same

fiber optic was used to collect the autofluorescence emanating from the tissue regions evaluated. The fiber's proximal collection end is coupled to a wavelength selection module (WSM) which features a set of four dichroic mirrors and bandpass filters (i.e., CH1: 390 ± 20 nm; CH2: 470 ± 14 nm; CH3: 542 ± 25 nm; and CH4: 629 ± 26.5 nm) used to spectrally resolve the autofluorescence signal. These spectral bands were tailored to capitalize on the autofluorescence emission maxima of endogenous fluorophores previously reported as the main contributors to head and neck cancer autofluorescence emission, specifically collagen, NAD(P)H, FAD, and porphyrins.[1] The optical signal from each spectral band is time-multiplexed onto a single microchannel plate photomultiplier tube (MCPPMT, R3809U-50, 45ps FWHM, Hamamatsu, Japan), amplified (AM1607-3000, Miteq Inc., Hauppauge, NY), and time-resolved by a high sampling frequency digitizer (12.5 GS/s, 3GHz, 8-bit, 512 Mbytes, PXIe-5185, National Instruments, Austin, TX, USA) at 80 ps time intervals.

In the pulse sampling approach, short (sub-nanosecond) and intense (~0.1-10 μJ) excitation pulses generate a large amount of fluorescence photons that are detected by a high-bandwidth photodetector.[147,148] A fast digitizer measures the resulting electrical transient signal with a resolution of tens of picoseconds, and full fluorescence intensity decays are recorded within a few microseconds. With this implementation, room illumination has a negligible effect on the fluorescence signal (a large number of fluorescence photons generated within a nanosecond) that can be even further minimized by low-frequency filtering.[131,135,149] Other groups have adapted the basic concept of this instrument[125,150,151] to make it compatible with galvanometer scanners for *in vitro* and *in vivo* tissue diagnosis with hand-held endoscopes[152] or through scanning microscopy.[125]

To determine the spatial location of each FLIm point measurement, a 455 nm continuous-wave diode-laser aiming beam (TECBL50G-440-USB, World Star Tech, Canada) was integrated into the WSM of the FLIm system to highlight the location where FLIm point

measurements were acquired to facilitate image reconstruction.[135] This aiming beam is delivered through the same optical path used to excite tissue autofluorescence. The amplifier of the instrument is AC coupled with a cut off frequency of 10 kHz to filter out any signal contribution from the aiming beam and other sources of light, such as lights in the operating room. The position of the measurement location is determined by localizing the aiming beam within a 2-dimension white light image of the tissue specimen (captured by the camera integrated into the da Vinci system). This localization is performed by transforming the image into the hue saturation value (HSV) color space, thresholding the hue and saturation channels, and performing a series of morphological operations to isolate the center of the beam. By performing aiming beam segmentation in parallel with the deconvolution of autofluorescence decay signals, FLIm parameter visualizations can be generated.

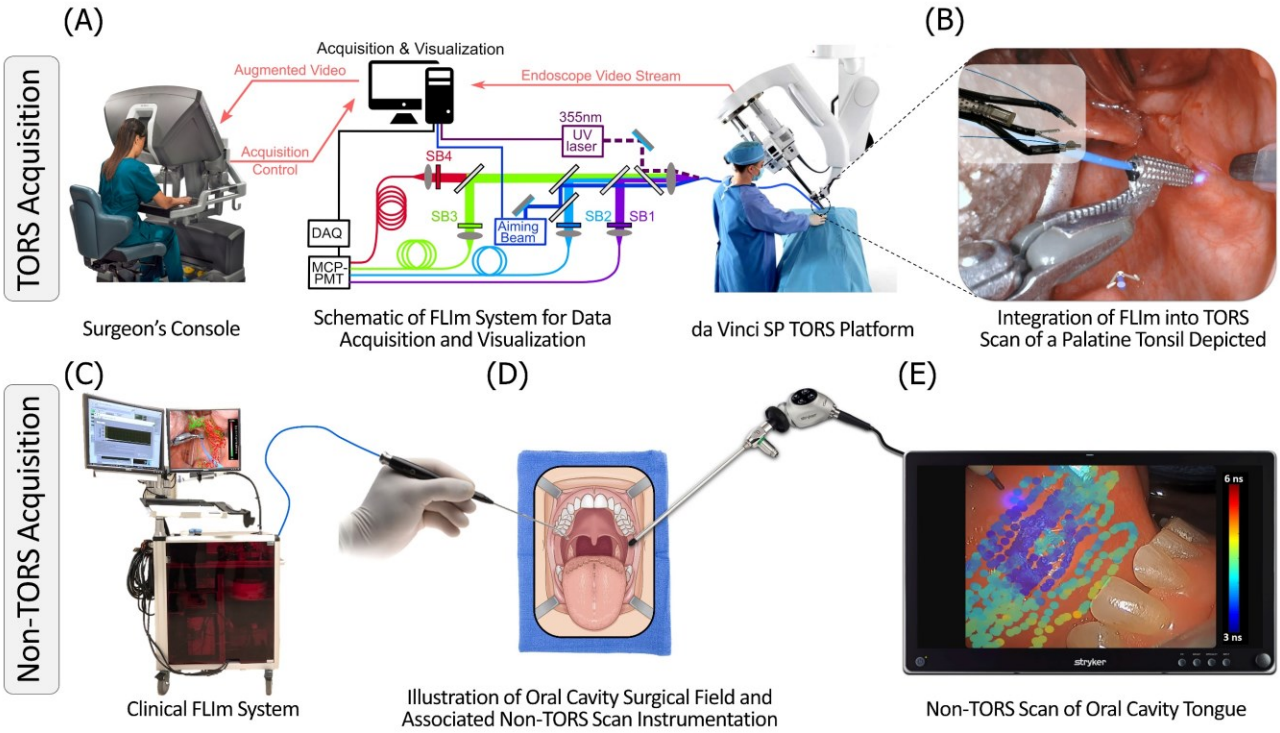

Figure 5: Clinical FLIm instrumentation and corresponding integration into surgical procedures of the oropharynx (TORS acquisition) and oral cavity (non-TORS acquisition). (A) Visual schematic of the of the FLIm instrument, integration of the FLIm video stream into the TORS platform for surgical control, and multi-mode fiber optic integration into the da Vinci SP. (B) Photograph of the FLIm probe with a 3D printed stainless steel grasper being maneuvered by the da Vinci SP's Maryland graspers to conduct an *in vivo* scan of a patient's palatine tonsil. (C) Photograph of clinical FLIm system, comprising components of the FLIm schematic in title A within the encasing. (D) Rendering of an *in vivo* scan of a patient's oral cavity, where the FLIm fiber optic is held by hand with a 5 French Omniguide laser handpiece and the surgical region is visualized with a Stryker 0^0 endoscope. (E) Augmented FLIm rendering of SB2 lifetime data (associated primarily with the metabolic cofactor NAD(P)H), where the jet map between blue to red represents fluorescence lifetimes of 3 ns to 6 ns respectively.

Figure 5 visually demonstrates the custom-built FLIm instrumentation used in this study and shows the corresponding integration into H&N surgical procedures. For surgical procedures of the oropharynx, FLIm was integrated into the da Vinci Si/SP surgical system, illustrated in *figures 5A* and *5B* respectively. *Figure 5C* presents a photograph of the actual clinical FLIm device. For oral cavity cancer procedures, FLIm was integrated into the clinical workflow using a handheld Omniguide laser handpiece and a Stryker endoscope for surgical field visualization and is illustrated in *figures 5 D-E* respectively.

3.1.2 FLIm Preprocessing Requirements

Time-domain FLIm instrumentation records fluorescence emission pulses at distinct wavelengths or wavelength bands. Absolute fluorescence intensity and intensity decay parameters can be extracted from the measured fluorescence pulses in multiple ways. Since the physical representation of the fluorescence emission decays follows a mono-exponential (single fluorophore) or multi-exponential (multiple fluorophores as found in tissue) function, fitting the intensity decay to a multi-exponential curve is an intuitive solution. However, this method is computationally intensive, slow, and not well suited for typical biological samples where the number of fluorescent species is large and unknown. Fast computational methods that do not require *a priori* assumptions on the number of fluorescent species is preferred to extract FLIm parameters. A large number of algorithms have been proposed for FLIm data analysis and are summarized elsewhere.[99] Here, the discussion is focused on methods used to process clinical FLIm data in this original research.

A schematic of the data pre-processing steps for the multispectral FLIm system is illustrated in *figure 6*. Fluorescence from four spectral bands is temporally multiplexed onto a single MCP-PMT detector. The raw waveforms are therefore a concatenation of the fluorescence signal from each spectral band (*figure 6A*). Averaging the waveforms over multiple pulses improves the signal-to-noise ratio (SNR). The fiber probe introduces a non-negligible background from fluorescence generated at the proximal end, within the length of the fiber-optic cable, and at the distal end of the fiber; this effect is most noticeable in the first spectral band illustrated in *figure 6B*. Only the distal-end background temporally overlaps with the sample fluorescence signal, reducing the dynamic range of the system. The fiber background is subtracted from the raw waveform (*figure 6C*). After background subtraction, the sample fluorescence is truncated to isolate the decay waveform corresponding to each spectral band (*figure 6D*). The truncated waveform (*figure 6D*) and the measured instrument response function

iIRF (*figure 6E*) are used to estimate the fluorescence impulse response function fIRF (*figure 6F*).

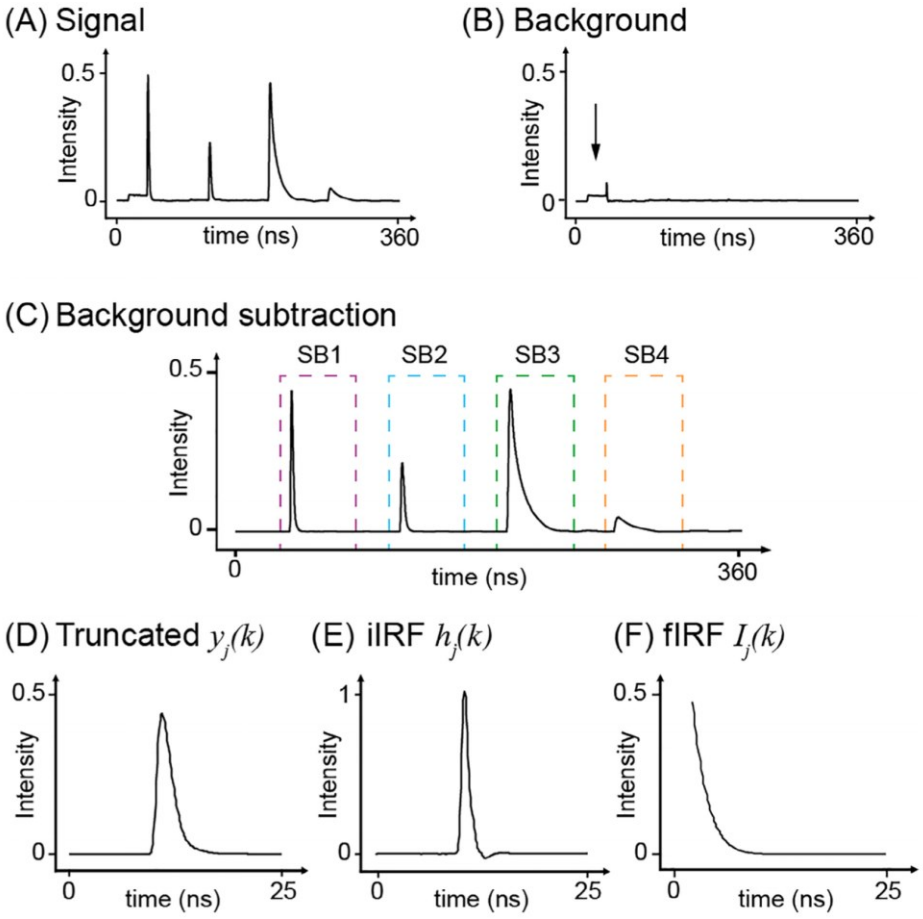

Figure 6: Data processing workflow for time-domain FLIm using pulse sampling methods. (A) Raw waveform signal. (B) Fiber background. (C) Background subtracted from the signal. Each box outlines the signal in one spectral band (*j*). (D) Truncated signal $y_j(k)$. (E) Instrument impulse response function (iIRF) $h_j(k)$. (F) Deconvolved fluorescence impulse response function (fIRF) $I_j(k)$ from which to extract intensity and lifetime parameters. Figure reproduced with permission from Alfonso-Garcia A, et al. reference [2].

3.1.3 Calculation of Fluorescence Lifetime Using the Laguerre Approach

Both the fluorescence system (tissue) and the instrument system are assumed to be linear time invariant systems, such that they are entirely characterized by their impulse response functions.[153] The fluorescence signal is assumed to be multi-exponential.[153] The measured signal as a function of time '$y(t)$', is a convolution of the fluorescence impulse response function (fIRF) '$h(t)$', with instrument response function (iIRF) '$I(t)$' (*equation 1*).[153]

$$y(t) = I(t) * h(t) \qquad \text{(Eq. 1)}$$

Thus, for linear, shift-invariant systems, the following holds:

$$Y(f) = I(f)H(f) \quad \text{(Eq. 2)}$$

Where translating this to the discrete time representation, for a sampling interval of δt, with sampling time points $t_i = i\delta t$ and $i = 0,\ldots, N\text{-}1$ over a total of N sampling points gives:

$$y(k) = \sum_{i=0}^{k} I(k-i) \cdot h(k) + \varepsilon_k \quad \text{(Eq. 3)}$$

for $k = 0, \ldots, N\text{-}1$, where additive white noise at time point t_k is ε_k. The iIRF is measured using a fluorescent dye with a very short lifetime (~30 ns), which in this case is 2-[4-(Dimethylamino)-styryl]-1-methylpyridinium iodide (2-DASPI).

The goal is to estimate fIRF, denoted as $h(k)$, from measured iIRF $I(k)$ and time-resolved fluorescence signals $y(k)$.[153] Here, fIRF $h(k)$ is parameterized by decomposition onto an ordered set of discrete time Laguerre functions where α = 0.9 is used for scale and L=12 expansion coefficients are used as previously reported and demonstrated in *equation 4*.[153]

$$h(k) = \sum_{l=0}^{L-1} c_l b_l(k;\alpha) \quad \text{(Eq.4)}$$

where $L=12$, $\alpha = 0.9$ and $b_l =$

$$b_l(k;\alpha) = \alpha^{(k-l)/2}(1-\alpha)^{1/2} \sum_{i=0}^{l} (-1)^i \binom{k}{i} \binom{l}{i} \alpha^{l-i}(1-\alpha)^i \quad \text{(Eq.5)}$$

The c_l is the lth expansion coefficient, α is a basis parameter, and L is the total number of Laguerre Basis Functions (LBFs) $b_l(k;\alpha)$. Constrained least squares deconvolution is used to estimate the deconvolved decay function $\hat{h}(k)$ as previously described.[153] This yields *equation 6*:

$$\hat{h}(k) = \sum_{l=0}^{L-1} \hat{c}_l b_l(k;\alpha) \quad \text{(Eq.6)}$$

Average lifetime τ_{avg} was calculated from the mean lifetimes from individual exponential components weighted by their fractional contributions for *N* equal sampling time points,[153] such that estimation of the average lifetime is denoted as:

$$\hat{\tau}_{\text{avg}} = \frac{\delta t \sum_{k=0}^{N-1} k\hat{h}(k)}{\sum_{k=0}^{N-1} \hat{h}(k)} \quad \text{(Eq.7)}$$

3.1.4 The Phasor Approach to Fluorescence Lifetime

A phasor is a frequency domain representation of fluorescence lifetime evaluated at a particular frequency. The phasor analysis approach to fluorescence lifetime analysis consists of the transformation of the fluorescence decay histogram I(t) into its sine and cosine components.[154] Data in this type of analysis is displayed in a polar plot (phasor plot) and does not require fitting thorough exponential decays, therefore allowing each phasor datapoint to be independent of the number of exponentials needed to determine its decay.[154,155] Phasor plots represent each decay with two coordinates; 'phase' and 'modulus' are used in polar coordinates, and in cartesian coordinates, 'g' and 's,' represented by *equation 8* and *9* respectively, are used.[156] The 'g' and 's,' correspond to the real and imaginary parts of the Fourier transformation respectively, and are a projection of the polar coordinates into the coordinate axes.[156]

$$g_i(\omega) = \frac{\int_0^\infty I(t)\cos(n\omega t)\,dt}{\int_0^\infty I(t)\,dt} \quad \text{(Eq.8)}$$

$$s_i(\omega) = \frac{\int_0^\infty I(t)\sin(n\omega t)\,dt}{\int_0^\infty I(t)\,dt} \quad \text{(Eq.9)}$$

Here, 'ω,' equals 2πf and 'n' is the harmonic frequency (typically between values of 1 to 5).[157] In the frequency domain, phasor points are defined by phases (φ) and modulations (*m*) as represented in *equations 10* and *11*.[157]

$$g_i(\omega) = m\cos(\phi) \quad \text{(Eq.10)}$$

$$s_i(\omega) = m\sin(\phi) \quad \text{(Eq.11)}$$

The values of '$g_i(\omega)$' and '$s_i(\omega)$' are regarded as coordinates of vectors with an origin at (0,0). Phasors are normalized such that the coordinates do not have units. The horizontal axis of the phasor plot is used for the 'g' cosine transform with values between 0 and 1, and the vertical axis is for the 's' sine transform, which has values between 0 and 0.5.

Phasors follow normal vector algebra, where their coordinates can be added or subtracted. Phasor analysis is advantageous in the sense that no *a priori* knowledge or assumption are needed to be made about the number of fluorescent species and lifetime characteristics within a given system.[154,158] The 2D graphical view of lifetime distributions enable rapid visual distinguishing of where fluorescence populations lie, which can enabled enhanced identification of patters and trends in autofluorescence data. *Figure 7A* demonstrates the derivation of the real 'g' and imaginary 's' parts of the phasor from the time domain to yield the frequency domain representation g(ω) and s(ω). *Figure 7B* depicts a universal phasor plot, where the real component 'g' occupies the horizontal axis, and the imaginary component 's' represents the vertical axis.

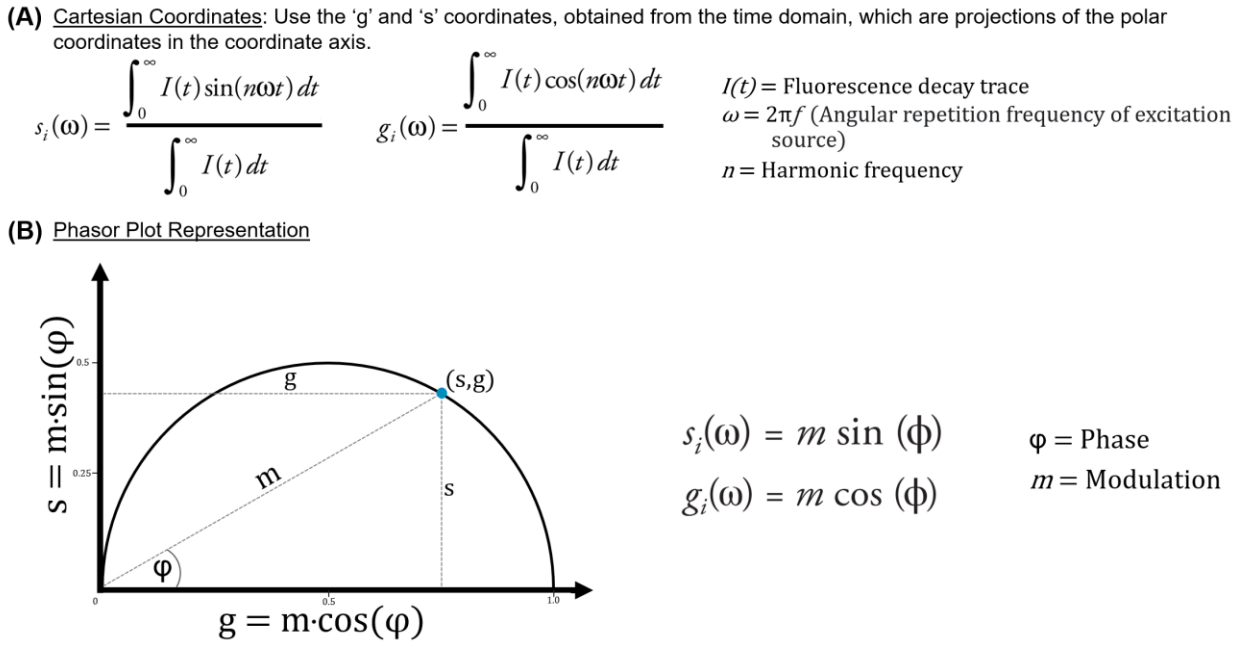

Figure 7: Mathematics and visual overview of the phasor approach. (A) Derivation of the real 'g' and imaginary 's' parts of the phasor from the time domain to yield $g_i(\omega)$ and $s_i(\omega)$. (B) Representation of the phasor plot with components phase (φ) and modulation (m) which determine phasor coordinates 's' and 'g.' Figure concept inspired from reference [159].

Phasor analysis can be performed with any harmonics of the original modulation frequency.[154] Without changing the lifetime value, the use of different harmonics changes the location of the corresponding phasors in plots because the phase (φ) and modulation (*m*)

change with different harmonics.[154] Evaluating phasor data at different harmonics may be useful, particularly when separate phasors belong to different species that may overlap in the first harmonic, but may be separated at higher harmonics.

Figure 8 outlines essential properties of phasor plots. *Figure 8A* demonstrates that phasor points which lie on the general phasor semi-circle represent a single-lifetime fluorophore characterized by a mono-exponential decay. Phasors characterized by multiple fluorescent species represents a complex, which exists as a linear combination of individual phasors of single-lifetimes species (*figure 8B-D*). Connecting these individual phasors on the semicircle yields a convex set inside the semicircle, thus a species of multiple lifetime components must lie inside the semicircle.[159] A qualitative rendering of how a bi-exponential fluorophore mixture contributes to an overall intensity waveform with lifetime 'τ,' and the relationship in the phasor domain, are demonstrated in *figure 8E* and *8F* respectively. Lastly, *figure 8G* demonstrates how evaluating phasor plots at different harmonics may add value in differentiating phasors that belong to different species (e.g., benign vs. cancer).

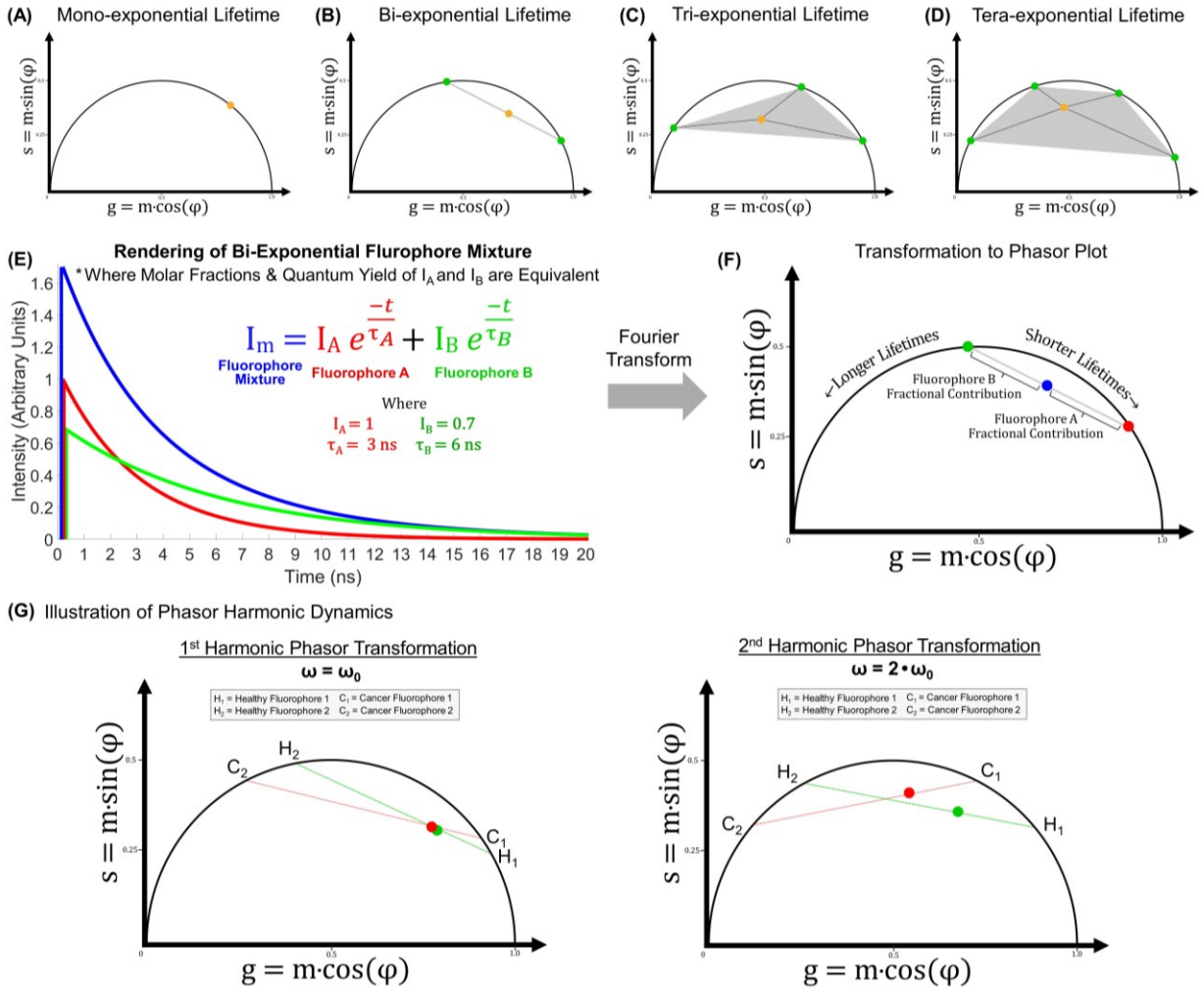

Figure 8: Characteristics of phasor plots and introduction to phasor harmonics. (A) Representation of a single fluorescent species with lifetime τ, which results in the phasor (orange dot) lying on the universal semi-circle. (B) Illustration of a bi-exponential fluorescing species with lifetime τ_1 (one of the green dots) & τ_2 (the other green dot) which results in the phasor (orange dot) lying within the semi-circle. (C) & (D) represents tri-exponential and tera-exponential lifetimes respectively where the phasor lies within the polygon area, serving as a linear combination of the fluorescing species. (E) Rendering of a bi-exponential fluorophore mixture intensity curve (I_m) consisting of contributions from fluorophore I_A and I_B, and (F) the resulting illustration of influence on the phasor plot, where the phasor resulting from the fluorophore mixture (blue) is a linear combination of fluorophore A (red) and fluorophore B (green). (G) Representation of phasor harmonics where phasors from different populations (e.g., benign tissue vs. cancer) may overlap at certain harmonics, but at alternate harmonics, may enable enhanced separation of the data. Figure parts A-D adapted from reference [158], part F from [160], and part G from [154].

3.2 | Visualization of FLIm Data: Augmentation and Accounting for Motion

An important feature of the intraoperative data collection effort is the ability to augment FLIm data in real-time over surgical regions of interest. *Figure 9* demonstrates the data output from a non-TORS FLIm scan over tongue SCC, where blue values represent Channel 2 average lifetimes values in the 3 ns range, and orange-red values in the 6 ns range. In this example, the blue values indicated the region of cancer.

Figure 9: Rendering of augmented FLIm data on tongue SCC visualized by a non-TORS endoscope. Channel 2 lifetime (associated to NAD(P)H) is displayed on a jet map color scale, where blue values represent lifetimes in the 3 ns range, and orange-red values representing lifetimes toward the longer 6 ns range.

An important aspect of FLIm data visualization is the need to account for surgical motion when augmenting data. Accounting for surgical motion not only directly affects the proper visualization of augmented FLIm features on tissue, but also the validation of results. For example, accounting for surgical is needed to maintain the correct registration of optical imaging measurements to ground truth histopathology. In this validation process, a single frame (720x1280 resolution), entitled the 'reference frame,' is selected for H&E annotation from a given surgical FLIm scan video. Histopathology is coregistered to that reference frame (as demonstrated in *figure 10*); this registration of histopathology enables annotated pixel coordinates of the 720x1280 pixel image to serve as the ground truth to FLIm datapoints acquired at tracked coordinates (obtained from the aiming beam). When motion occurs, the

coordinates of augmented data no longer match the native tissue location in the reference frame; correspondingly, without compensating for motion, the acquired datapoints do not reflect the correct histopathologic validation.

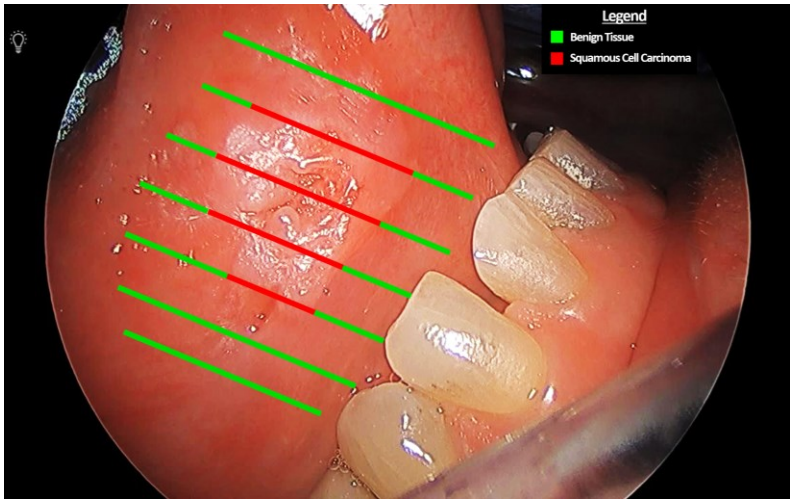

Figure 10: Illustration of histopathology registered in the oral cavity to a surgical reference frame. Histopathology is used as the gold-standard in the validation (corroboration) of FLIm data to pathology status.

Figure 11 demonstrates a visual example of the effect of motion on static augmented coordinates. In this example, the reference frame is illustrated on the left, with the locations of acquired measurements marked ‘green.’ The frame on the right represents a subsequent video frame after the occurrence of motion. For the frame on the right, ‘green’ measurements correspond to static augmented values which did not account for motion, whereas measurements marked in ‘yellow’ represent the correct locations augmented values should have adjusted to following the occurrence of motion. Without motion correction, the deviation of the augmented coordinates from the reference frame would not be accounted for, thus the original measurements (depicted green on the right image) would not reflect the appropriate coordinate adjustment after motion. Suitably, it is recognized that if motion is not accounted for in the analysis process, association of FLIm datapoints to histopathology status would be potentially inaccurate.

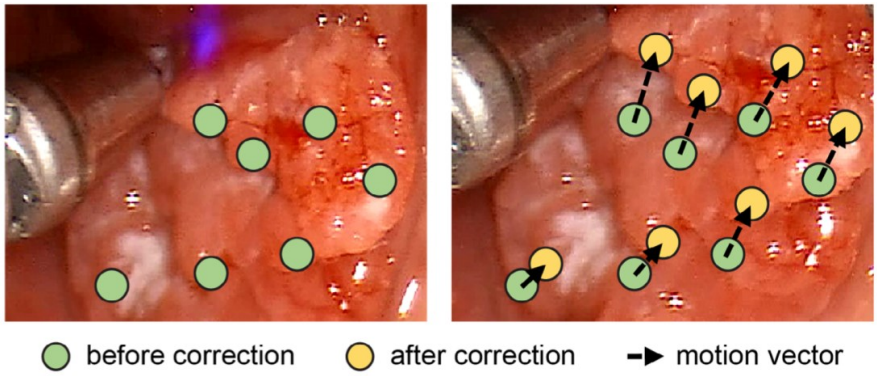

Figure 11: Graphical demonstration of motion correction concept applied to intraoperative data. The left image represents the reference frame, where the right image represents the surgical video seconds after with motion. The 'green' points of the right image reflect uncorrected augmentation, and 'yellow' points denote motion correction applied to the data. Figure reproduced with permission from Marsden M, et al. reference [161].

Beyond validation of the FLIm data, motion additionally impacts visualization of the augmented FLIm image. Consider the previous *figure 9* which demonstrates a non-TORS FLIm scan of an oral cavity tongue tissue. If motion occurs during this FLIm scan, the augmented values will not shift without an appropriate coordinate transformation that accounts for motion.

To address this challenge, a workflow was conceptualized to estimate and account for motion; this workflow is represented at a high level in *figure 12*. This process includes: (i) obtaining coordinates from the FLIm aiming beam, (ii) estimating motion between a previous (I_{t-1}) and current frame (I_t), and (iii) renewing the prior frame's (I_{t-1}) coordinates to the current frame's (I_t) coordinates. The reference frame selected for annotation is regarded as frame (I_t) in *figure 12*, therefore the coordinates of prior frames (I_{t-1}, I_{t-2}, I_{t-3}, etc.) and subsequent frames (I_{t+1}, I_{t+2}, I_{t+3}, etc.) are renewed to the reference frame's (I_t) coordinates. Suitably, tissue motion estimation and aiming beam position correction was performed on a frame-by-frame basis during FLIm acquisition.

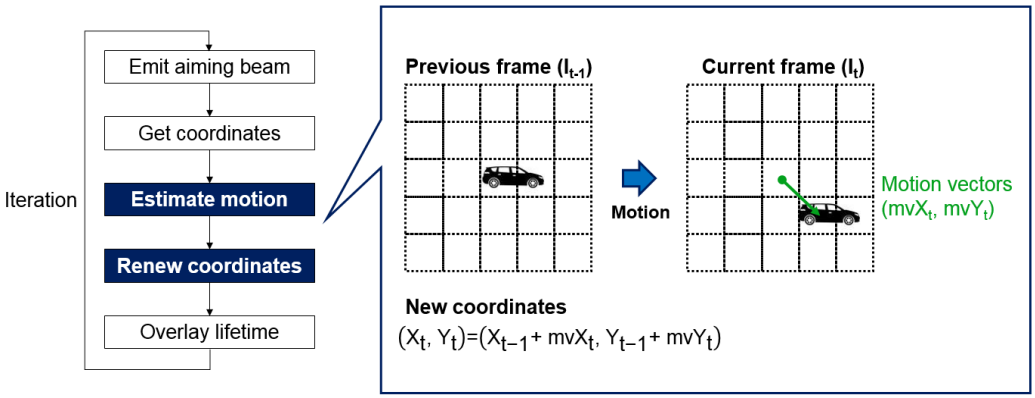

Figure 12: High-level overview of the motion correction workflow. Coordinates from a prior frame (X_{t-1},Y_{t-1}) are associated to coordinates of the present frame (X_t,Y_t) through motion vectors mv_x and mv_y for X_{t-1} and Y_{t-1} respectively. This renews coordinates following the occurrence of motion, where the revised coordinates are relative to a given frame chosen as a reference for histopathological labeling.

In vivo FLIm scans enable locally correlated motion patterns to be observed across tissue surfaces with gradual motion between frames. Informed by this observation, motion estimation was performed using adaptive root pattern search (ARPS) block-matching,[162] which allows for efficient and accurate estimation of local motion vectors. Block-matching, demonstrated in *figure 13*, was selected over feature matching methods[163,164] for motion estimation due to the presence of visually homogeneous tissue regions in the oral cavity and oropharynx lacking in strong landmarks. These homogeneous regions can be more accurately tracked by comparing image patches (i.e., block-matching) rather than individual interest points.

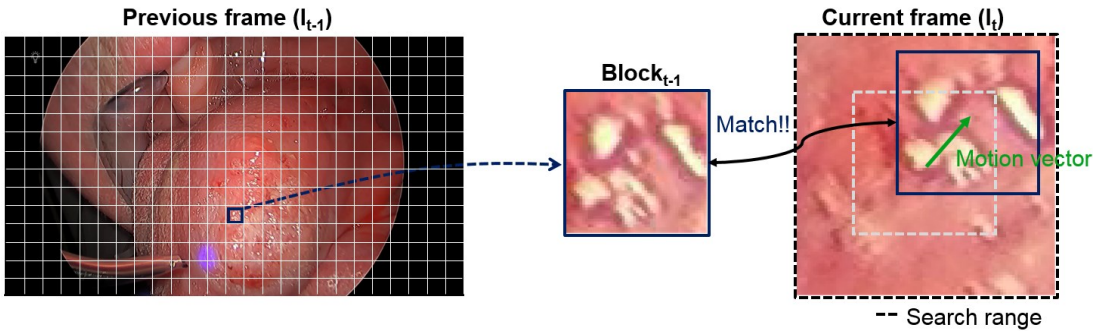

Figure 13: Illustration of block matching process for computing motion vectors. Individual macroblocks of the divided 720 x 1280 pixel image of a previous frame I(t-1) are compared to a current frame I(t) motion vectors mv_x and mv_y for X_{t-1} and Y_{t-1} such that $(X_t,Y_t) = (X_{t-1}+mv_xX_t, Y_{t-1}+mv_yY_t)$. Figure reproduced with permission from Marsden M, et al. reference [161].

When using the image block-matching method, the variable presence of surgical instruments such as suction tools, robotic instrument arms, and the scanning fiber probe itself imparted challenges when using visual differences across frames to track motion. The

instruments themselves both occluded visualized tissue and represented a change to visualized features in subsequent frames. An example of this is shown in *figure 14*.

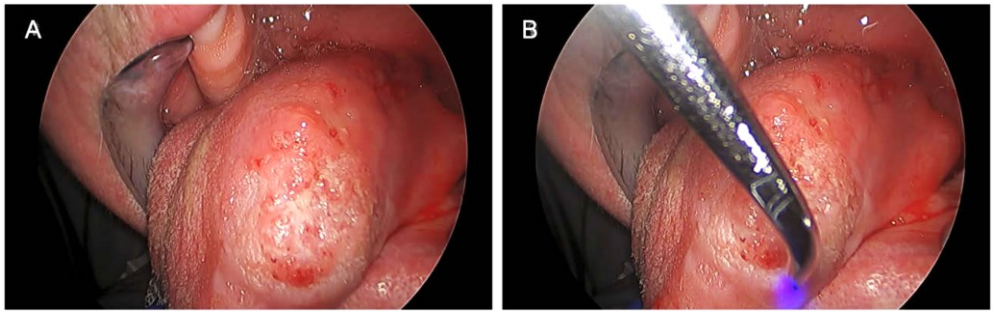

Figure 14: Illustration of surgical instrumentation occlusions on surgical field while scanning. (A) Surgical field before occluding instrument blocks the surgical image and (B) non-TORS FLIm scanning sheath blocking a portion of the surgical field. Such occlusions create challenges in the adaptive root pattern search (ARPS) block-matching process. Figure reproduced with permission from Marsden M, et al. reference [161].

To account for the effect of instrumentation in the block matching process, a U-Net convolutional neural network (CNN) architecture[165] was used to train a segmentation model to isolate aiming beam contributions to the surgical video and create an instrument segmentation mask. The details of the developed CNN approach are reported in detail elsewhere.[166]

At a high level, *figure 15* demonstrates and overview of the motion estimation and correction process. This includes segmenting the aiming beam, creating an instrument segmentation mask, estimating motion vectors, and updating FLIm coordinates to maintain an appropriately augmented surgical field-of-view. This developed algorithm was implemented in Matrix Laboratory (MATLAB).

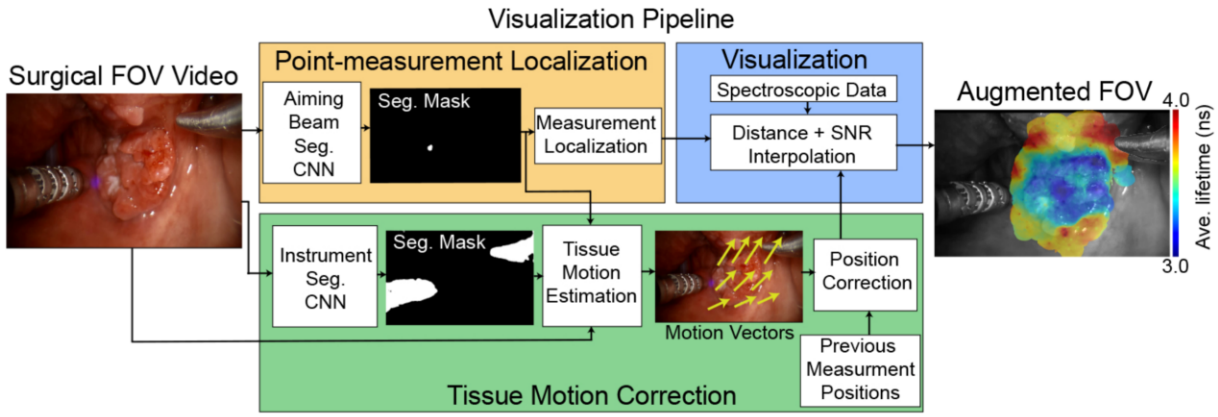

Figure 15: Overview of FLIm point-measurement motion correction procedure. Video frames of the FLIm scan were acquired with an external Stryker endoscope for oral cavity cases and integrated da Vinci SP camera for TORS procedures of the oropharynx. Point-measurement localization (orange) was performed by segmenting the aiming beam emitted from the fiber optic using a U-Net CNN. Tissue motion correction (green) was performed by segmenting the surgical instruments using a U-Net CNN to exclude these regions from tracking. Motion estimation via an optimized block-matching approach was then applied. Point-measurement position correction was performed on a frame-by-frame basis for previous measurement locations using the estimated motion vectors. Data visualization (blue) was then performed by generating an augmented overlay using measured spectroscopic data (e.g., average fluorescence lifetime for a specific spectral band) for all point-measurements acquired. Marsden M, et al. reference [161].

As demonstrated in *figure 16,* to perform the block matching process, each video input frame was divided into non-overlapping 32 × 32-pixel macroblocks (MBs), corresponding to 2.5% of the overall image width. Prior to motion estimation for a given frame, a region-of-interest for motion correction was first selected in terms of MBs based on prior aiming beam segmentation locations. Second, occluded MB tissue regions were detected for each frame using a previously developed surgical instrument segmentation CNN[167] before being excluded from direct motion estimation. This step prevents motion from surgical instruments affecting motion estimation for the underlying tissue. ARPS motion estimation was then performed. A set of motion vectors were estimated for each frame, allowing for previously estimated aiming beam positions to be refined through a position correction step using these motion vectors.

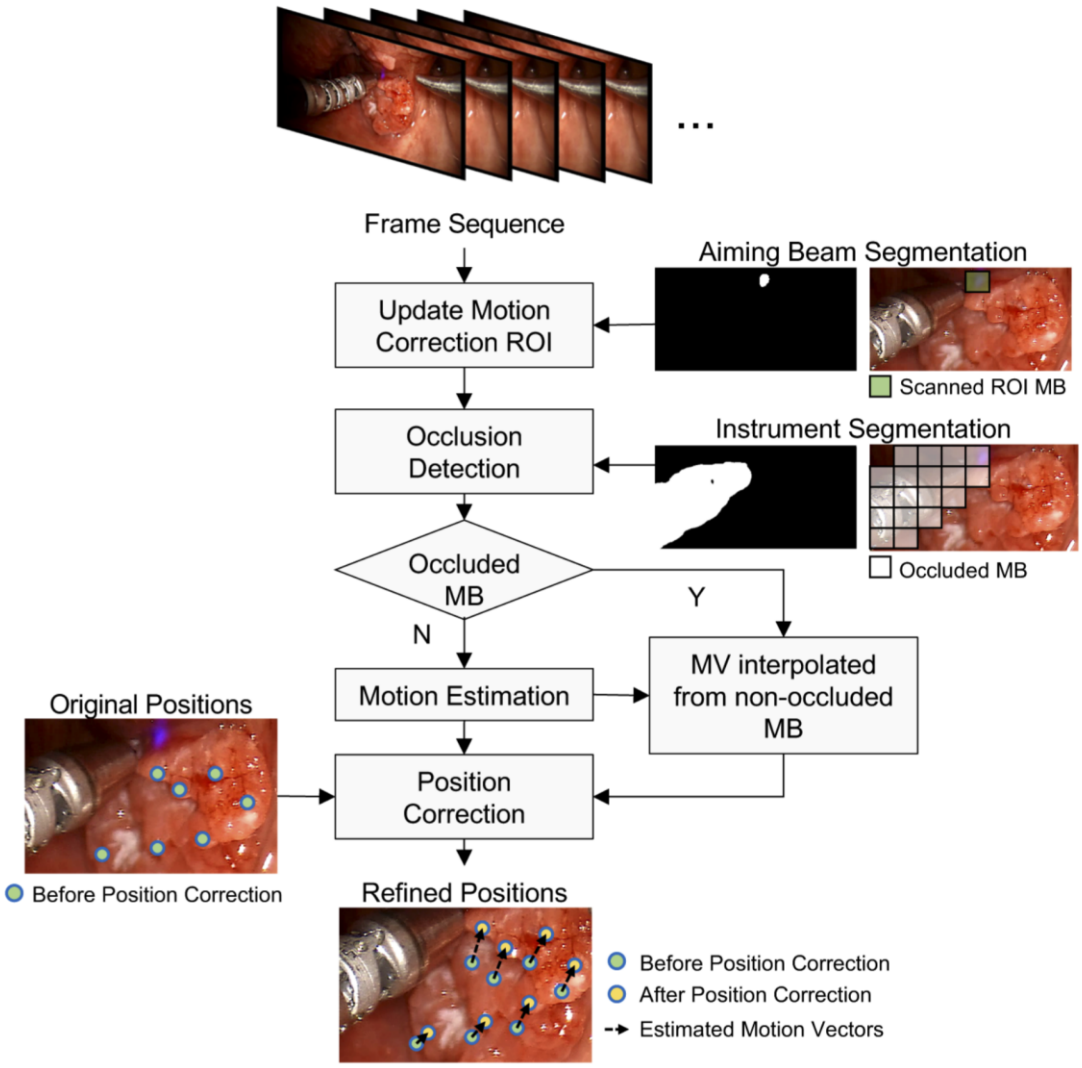

Figure 16: Method for motion estimation in FLIm data by ARPS macroblock matching. First, the motion correction ROI was updated based on the scanned tissue region to remove redundant processing. The size of this ROI increases over the course of a given FLIm run as more tissue surface is scanned. In practice, only a small portion of the surgical FOV is scanned and included in this ROI, limiting the computational demands. Then, tissue occlusion was detected using a surgical instrument segmentation CNN to prevent errors due to instrument motion. Adaptive rood pattern search (ARPS) block-matching was then performed to estimation local motion vectors. If a given macro-block was occluded, motion vectors were interpolated from neighboring macroblocks included in the ROI. With an estimated set of motion vectors for a given frame, position correction was performed for prior FLIm point-measurements to ensure an accurate visualization is subsequently generated. Figure reproduced with permission from Marsden M, et al. reference [161].

If a given MB was occluded, motion vectors were interpolated from the 3 nearest non-occluded MBs through a weighted average inversely proportional to the distance between blocks. It was required that all 3 MBs used for vector interpolation lied within a 5-MB radius of the occluded macroblocks, otherwise no motion vector interpolation was performed. The rationale for applying motion vector interpolation stems from the observation that tissue motion

within a local region is largely homogeneous. With an image width of 1280 pixels employed the 32 × 32 macroblock size corresponded to 2.5% of the overall image width. Calculating local motion vectors across a full video sequence also allows for estimated measurement positions to be translated via vector summation to any desired reference frame for histopathologic corroboration.

3.3 | Machine Learning Classification Method

Each acquired FLIm datapoint yields multiple optical parameters for analysis; this includes 4 computed average fluorescence lifetimes, 4 spectral intensity ratio parameters, and 12 Laguerre expansion coefficients per channel (48 total). Additionally, the raw spectral fluorescence decay curve can be analyzed as an additional analytical input in deep learning approaches, such as convolutional neural networks. *Figure 17* graphically demonstrates the magnitude of data obtained from a single FLIm measurement.

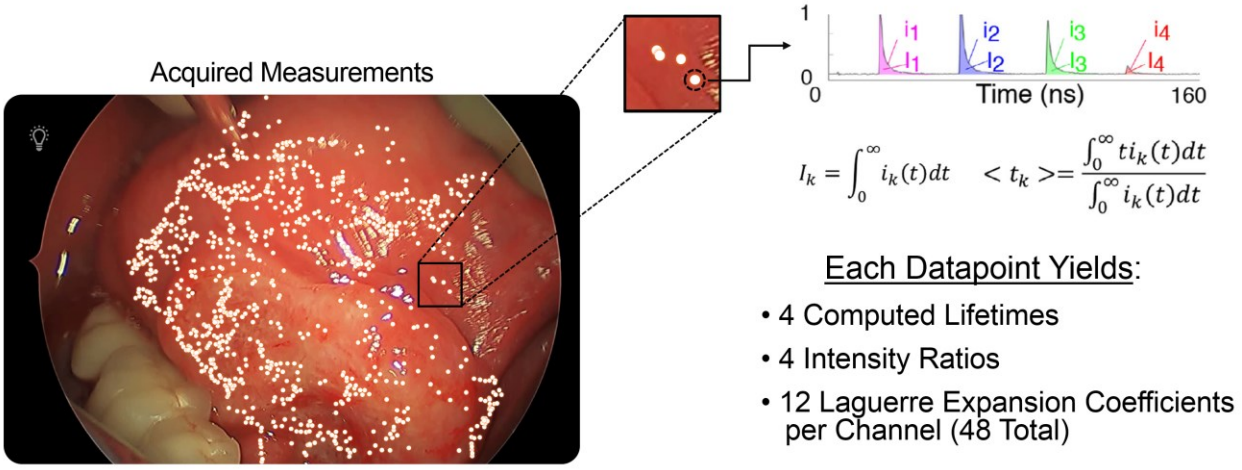

Figure 17: Demonstration of multi-parametric FLIm data obtained from individual measurements. Each second of FLIm scanning yields 30 datapoints (averaged 4 times from 120 Hz excitation laser repetition rate). Each datapoint is associated with the illustrated 4-waveform fluorescence decay. Deconvolution of these waveforms, and associated computation of intensity ratio and lifetime, gives rise to 1 computed lifetime, 1 intensity ratio, and 12 Laguerre expansion coefficients per channel. When analyzing channels 1-3, this yields 42 total parameters, and for channels 1-4, 56 total parameters are available for analysis.

While univariate (single-parameter) analysis may be informative in the tumor delineation process, the inherent value of multi-parametric analysis of intraoperative fluorescence lifetime imaging has been demonstrated by our group in several studies;[2,168,169] it is understood that

leveraging multiple possible sources of FLIm-derived optical contrast achieves superior benign vs. cancer discrimination, than single-parameter analysis alone. To this end, a random forest classification method which leverages multi-parametric FLIm parameters to predict cancer probability was reported our study by Marsden et al.[169] The following discussion within this section will elaborate on pertinent details of the developed approach.

In this original work, a random forest classifier[170] was trained using lifetime, intensity ratio, and Laguerre coefficient parameters from channels 1-3, yielding 42 parameters in total for each acquired FLIm datapoint measurement. Channel 4 was not analyzed due to low signal-to-noise ratio (SNR) data. Patient FLIm data associated via histopathology to benign tissue and cancer was used to train the random forest classifier. Data associated with dysplasia was omitted from training and was used for evaluation purposes only. An initial 53-patient dataset was used to train and evaluate the classifier in *section 3.2*, and then later a full 100-patient database evaluation was performed in section *4.2*. *Figure 18* demonstrates the high-level process for annotating histopathology on surgical images and selecting FLIm point-measurements in classifier training data. Measurements acquired outside of H&E demarcated regions were considered benign from the absence of findings in patient radiology (PET, CT, MRI, and ultrasound where applicable). An overview of random forest classifier training, probability of cancer output, and validation is demonstrated in *figure 19*.

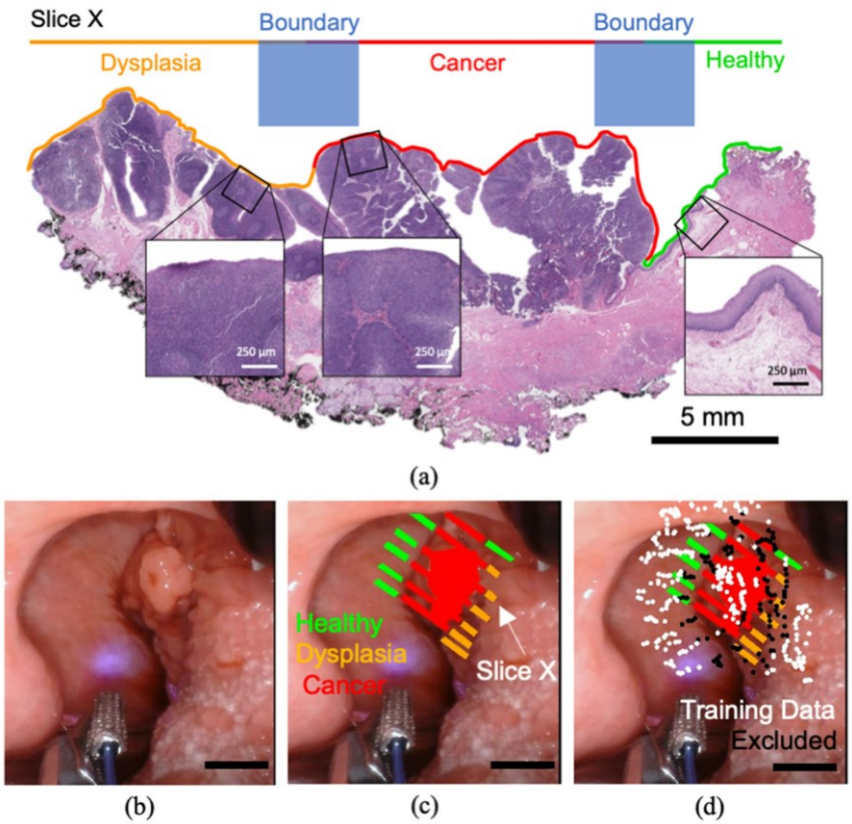

Figure 18: Tissue annotation and training data selection process. (a) The ground truth for classifier training was derived directly from histopathology via H+E staining. Each annotated slice was coregistered with white light images of the specimen (*in vivo* and *ex vivo*), (b) Surgical FOV for *in vivo* imaging of a given specimen and (c) Corresponding registration of pathology (in vivo). Homogenous regions of a single tissue label (healthy, cancer, dysplasia) were annotated in a region-based fashion. (d) Point measurements centered at a boundary between disparate tissue conditions, specifically within a 15-pixel radius of multiple tissue labels (approx. 2.0 mm), were excluded from classifier training due to their ambiguous ground truth. The scale bar for white light images corresponds to 5 mm. Reproduced with permission from Marsden, M, et al. reference [169].

An ensemble size of 100 was selected for the random forest supervised machine learning algorithms, as ensemble sizes greater than 100 did not improve performance further, as demonstrated my Marsden et al.[169] Classifier training and evaluation comprised a leave-one-patient-out scheme. A binary assessment of cancer probability was then output from the classifier, where validation of the prediction was performed by histopathology.

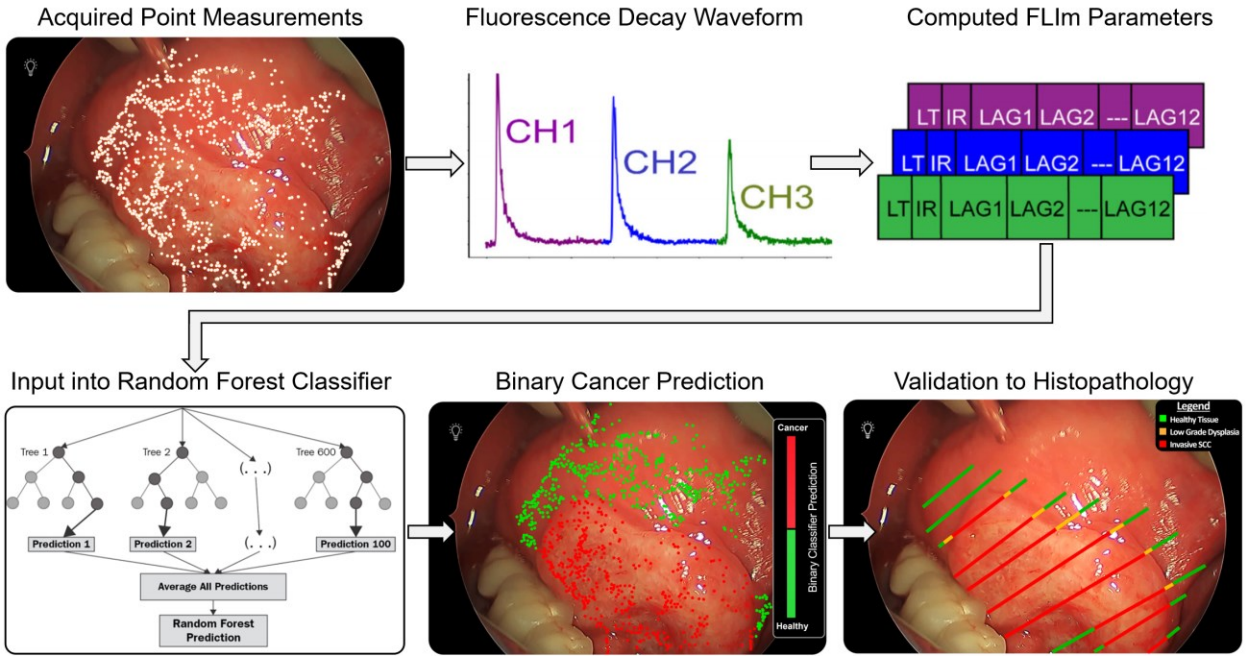

Figure 19: Overview of random forest classifier training, probability of cancer output, and validation. Acquired FLIm point measurements each yield a multi-channel fluorescence decay waveform. The waveforms from channels 1-3 are used in further analysis, whereas channel 4 is omitted due to poor SNR. Laguerre deconvolution and FLIm parameter extraction gives rise to 1 average lifetime, 1 intensity ratio, and 12 Laguerre coefficients per channel, thus 42 total parameters for analysis per FLIm measurement. These metrics are input into a random forest classifier for training and evaluation using a leave-one-patient-out scheme. The output of the classifier enables a binary prediction of cancer probability. Finally, the results of the predicted binary output can be validated against histopathology to compute the true positive vs. false positive rate of the data. The area under the curve, designated as ROC-AUC, enables quantification of the extent of classification accuracy. Random forest figure tile adapted from reference [171].

A receiver operator characteristic area-under-the-curve (ROC-AUC) approach was used to classify the true-positive-rate (TPR) vs. false-positive-rate (FPR) of the classifier output when validated to histopathology. The computation of TPR (sensitivity), specificity, FPR, and ROC-AUC is demonstrated in *equations 12-15* respectively.

$$\text{TPR / Recall / Sensitivity} = \frac{\text{True Positive (TP)}}{\text{True Positive (TP)} + \text{False Negative (FN)}} \quad \text{(Eq.12)}$$

$$\text{Specificity} = \frac{\text{True Negative (TN)}}{\text{True Negative (TN)} + \text{False Postive (FP)}} \quad \text{(Eq.13)}$$

$$\text{FPR / 1-Specificity} = \frac{\text{False Positive (FP)}}{\text{True Negative (TN)} + \text{False Positive (FP)}} \quad \text{(Eq.14)}$$

$$\text{ROC-AUC} = \int_{x=0}^{1} TPR\left(FPR^{-1}(x)\right)dx \quad \text{(Eq.15)}$$

Figure 20 graphically illustrates an ROC-AUC plot and performance as a function of data class overlap. As illustrated *in figure 20B*, the best-case scenario is when the ROC-AUC of an LDA output is high (toward a value of 1.00), which indicates that benign and cancer data can be completely separated in linear space through an optimized decision boundary. An ROC-AUC of 0.70 (*figure 20C*) signifies data with significant overlap and is typically regarded in the classification field as the minimum ROC-AUC value to indicate that two data classes can be adequately separated. As represented in *figure 20D*, an area-under-the-curve value of 0.50 is the worst-case scenario, where the level of true decisions (TP & TN) approximately match the level of false decisions (FP & FN), indicating no discrimination. Values < 0.50 demonstrate reversed assessment of the negative and positive classes.

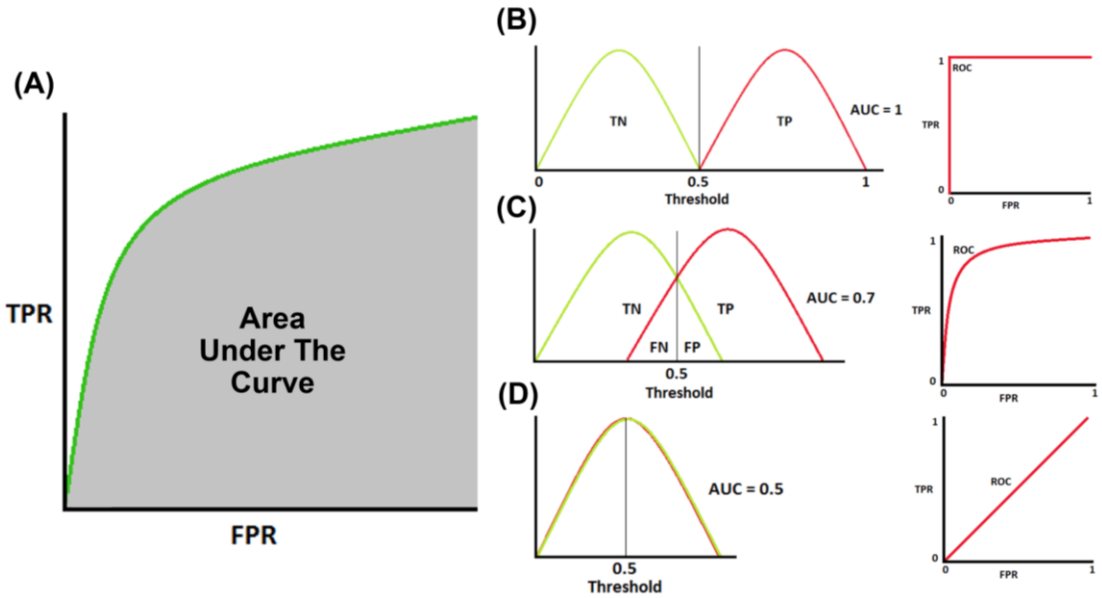

Figure 20**:** Illustration of receiver operator characteristic area under the curve (ROC-AUC) computation and performance as a function of data class overlap. (A) Illustration of the receiver operator characteristic curve with corresponding area under the curve (gray) taken as the computation of true positive rate (TPR) and false positive rate (FPR), with the computation demonstrated in *equations 12 and 14* respectively. (B) Rendering of ROC-AUC performance with an area under the curve of 1.00 when there are no false positives or false negatives and only correctly classified true negatives and true positives after optimization of the decision boundary. (C) Illustration of reduced ROC-AUC performance (0.70) when significant overlap between the data classes yields false positive and false negative misclassification. An area under the curve of 0.70 is regarded as the minimum in the classification field to designate adequate classification performance. (D) When there is complete overlap between the two data classes (i.e., benign and cancer tissue), there is no separability of the data, imparting an equal TRP and FPR, which yields an area-under-the-curve of 0.50.

CHAPTER 4 | Tools, Methodologies, and Techniques for the Coregistration of Tissue Histopathology to Intraoperative Optical Imaging Measurements

This study protocol was inspired upon identifying key challenges in the clinical validation of optical imaging technologies, where experimental measurements must be linked to a ground-truth, namely histopathology-derived tissue labels (e.g., benign tissue, dysplasia, cancer). By way of context, optical technologies have become increasingly investigated in clinical settings for diagnosis and surgical guidance. Histopathology serves as the gold standard for identifying disease, where hematoxylin and eosin (H&E) stained slides are most typically used for oncologic diagnosis. The association of experimental measurements to histopathology presents an ongoing challenge when performing clinical research; to gain traction in rigorously vetting the diagnostic potential of optical technologies, there must be an accurate link between acquired data and ground-truth tissue labels. Registration errors are detrimental when developing classification algorithms, which require adding the correct tissue label to optical data used for training and evaluating performance. Despite the importance of accurate registration, few studies enumerate their methods used for performing tissue labeling and how potential registration errors are accounted for (if at all). These limitations accordingly impact the reproducibility of such research and devalues the accuracy of the optical technique's performance.

This study protocol begins by elucidating various sources of registration error that may occur when establishing the histopathologic validation of intraoperatively acquired optical imaging measurements. Thereafter, this protocol codifies the various methodologies developed to control for these potential sources of error. Additionally, custom-built tools to perform labeling of surgical images and corresponding data extraction are provided. This work was developed within the context of investigating a custom-built Fluorescence Lifetime Imaging (FLIm) device for head & neck cancer surgical guidance, however it is noted that this protocol can be extrapolated to research involving other optical imaging modalities based on histopathologic

validation, and even methods that require localized registration of assays to tissue (e.g., molecular analysis based on tissue microarrays).

4.1 | Abstract

Background: Optical diagnostic technologies have become increasingly investigated in the clinical space for diagnosis and surgical guidance. These technologies interrogate tissue with light and generate contrast based on intrinsic optical properties. Histopathology serves as the gold standard for identifying disease, however the process for correctly associating optical data to histopathology-derived tissue labels (e.g., benign tissue, dysplasia, lymphoid tissue, cancer) remains a key challenge. It is acknowledged that registration errors negatively affect the validation of optical technologies, and in turn, affects the reproducibility of results. Considering this challenge, the protocol herein strives to elucidate various sources of registration error and codifies the various methodologies and tools developed to enhance histopathologic corroboration to optical imaging measurements.

Methods: Methodologies to account for common sources of registration error, and tools to assign labels to optical imaging data, were developed. This includes: (1) procedures for digital annotation of histologic grossing processes, (2) a customized tool for pathologists to digitally annotate histopathology sections, (3) processes to account for tissue deformation, (4) denoting tissue labels on ex vivo specimen images, (5) demarcating tissue excision margins on in vivo reference images, (6) identifying and matching of anatomical landmarks of reference images between ex vivo tissue and in vivo pre-resected tissue, (7) methodology for transferring ex vivo tissue labels to in vivo pre-resected tissue, and (8) a custom-developed MATLAB tool to perform histologic labeling of surgical images, and subsequent extraction of labeled data.

Discussion: This study protocol proposes solutions to account for sources of data labeling errors, provides tools to the scientific community for labeling optical data based on their localization in the surgical image, and facilitates clinical validation of the technology. While this

work was developed within the context of a Fluorescence Lifetime Imaging (FLIm) device investigated for head & neck cancer surgical guidance, this protocol can be extrapolated to other optical imaging modalities and oncology investigations involving histology labeling.

4.2 | Introduction: Current Challenges and Opportunities to Improve Histopathology Registration in Clinical Optical Imaging Research

Optical technologies have become increasingly investigated for their role in surgical oncology.[2] Advancements in instrumentation, computational capacity, and enhanced analytical methods have enabled these technologies to transition from bench-top instruments towards modalities suitable for clinical research in patients.[2] The working principle of optical instruments is to interrogate tissue with light, thereby generating contrast based on optical properties (e.g., reflection, scattering, absorption, autofluorescence). These technologies thereby obtain information about tissue characteristics (e.g., composition, morphology, biochemistry, microvasculature), which can be achieved through inherent tissue and molecular properties, or by the application of exogenous agents. Some prominent technologies in clinical investigation include optical coherence tomography, Raman spectroscopy, narrow-band imaging, high-resolution microendoscopy, targeted fluorescence imaging, intensity-based fluorescence imaging, and fluorescence lifetime imaging (FLIm).

To evaluate the diagnostic performance of optical instruments, it is essential to associate optical parameters to ground-truth tissue characteristics. In surgical oncology, the gold-standard to evaluate tissue pathology status is through histologic analysis of either biopsies or surgically excised tissue sections. More recently, immunohistochemistry and molecular analysis are emerging as additional accepted standards, alongside histopathology. The histologic stain, hematoxylin and eosin (H&E), is most commonly used for characterizing pathology. Upon reviewing H&E sections, a pathologist can then determine ground-truth tissue labels (e.g., benign tissue, reactive changes, dysplasia, ulceration, cancer, and other pathologic features).

A key challenge in demonstrating the diagnostic value of optical technologies is the spatial registration of tissue pathology to the location where optical data was recorded.[172] This is essential for the labeling the optical parameters in relationship with local pathology as accepted in medical practice. Inaccurate spatial registration of tissue pathology to optical data limits the ability to thoroughly investigate the performance of an optical technique, thereby impacting the development of classification algorithms and limits the reproducibility of the research. The challenges associated with correlating histopathology to optical measurements are well documented,[2,172,173] and also affect radiology-based imaging techniques (e.g., magnetic resonance imaging,[174,175] positron emission tomography,[175] and ultrasound,[176] among others).

Error in tissue pathology registration is acknowledged to originate from three primary sources: (1) during surgical excision, (2) during the tissue fixation process, and (3) when reporting tissue labels identified from H&E back onto the gross specimen.[174] The tissue removal process itself creates deformation of resected tissue relative to its *in vivo* conformation. Devascularization imparted by surgical resection results in the loss of blood volume and internal fluids, thus in parallel with sample dehydration, results in tissue shrinkage.[174] Electrocautery, which leads to protein coagulation, may additionally contribute to tissue deformation. In addition, the process of tissue sample preparation for histology involves formalin fixation, which results in tissue shrinkage and distortion. When linking histopathology-derived labels to intact tissue, the lack of clearly defined landmarks (distinct features on the tissue specimen) may lead to misorientation and misalignment of the location of gross sections. Other potential sources of registration error are outlined in detail elsewhere by Alyami W. et al.[174]

4.2.1 Application to Clinical Fluorescence Lifetime Imaging (FLIm) Research

While investigating FLIm's diagnostic performance in H&N surgical oncology procedures, our group experienced the need to develop robust histopathological registration methods that enable corroboration of FLIm parameters with histopathologic findings. As such,

solutions to mitigate opportunities for spatial registration error are needed. Here we report a variety of tools and techniques created in MATLAB to perform histopathologic labeling of surgical images, link optical data to tissue histological features at the surgical resection margins, and subsequently perform labeled data extraction. Collectively, this work seeks to call attention to sources of registration errors and acknowledge their impact on the optical imaging field while providing tools to the scientific community to improve registration accuracy.

4.3 | Methods and Design

4.3.1 Study Design

This protocol was developed in support of establishing the relationship between the FLIm data obtained from surgical resection margins *in situ* and the corresponding histopathologic features of tissue removed during surgical procedures. This study involved a cohort of 100 patients, where study participants presented with tumors of either the oral cavity (e.g., tongue) or oropharynx (e.g., base of tongue and tonsil). Under Institutional Review Board (IRB) approval, research was conducted on patients, and/or with their surgically excised specimens, only after receiving informed consent. All research was performed and supervised within the University of California, Davis Tertiary Academic Medical Center.

The study protocol developed herein applies to ongoing and future studies concerned with establishing FLIm as a tool for real-time intraoperative guidance of H&N cancer. While this work was developed within the context of a Fluorescence Lifetime Imaging (FLIm) device investigated for head & neck cancer surgical guidance, this protocol can be extrapolated to other imaging modalities and oncology investigations involving histology labeling of optical imaging data.

4.3.2 Overview of the Data Collection, Coregistration, and Data Analysis Process

Figure 21 presents an overview of the FLIm data collection, registration of histopathology to tissue both *ex vivo* and *in vivo*, and the analysis process. This includes: (21A) recruitment of patients, (21B) data acquisition *in vivo*, (21C) data acquisition *ex vivo*, (21D)

annotations of locations of where tissue is surgically grossed, (21E) digital annotation of tissue labels (e.g., benign, dysplasia, cancer) on H&E sections by a pathologist, (21F) registration of H&E tissue labels to the *ex vivo* specimen, (21G) creation of a surgical outline and landmark matching *in vivo*, (21H) registration of *ex vivo* tissue labels *in vivo*, (21I) the annotation of registered tissue labels from surgical images using a custom-built tool, (21J) the creation of a ground truth data mask to corroborate localized point spectroscopic FLIm measurements to tissue labels, (21K) data extraction, and finally (21L) data analysis. Each step is described in detail in the following sections.

4.3.3 In Vivo and Ex Vivo Data Collection

FLIm data was acquired during cancer removal procedures performed either by hand for oral cavity cancer procedures, or by transoral robotic surgical platforms, namely the da Vinci SP, for oropharyngeal cancer. This surgical integration was demonstrated in our prior work.[134] Following informed consent, the patients (*figure 21A*) were anesthetized, intubated, and prepared for surgery as part of routine standard-of-care for their surgical procedure. The *in vivo* FLIm scan was conducted on the tumor epithelial surface and the surrounding uninvolved benign tissue (*figure 21B*) as identified by the surgeon. Throughout the duration of the scan, FLIm datapoints were localized as pixel coordinates within the surgical white light image. FLIm datapoint localization was achieved by segmentation of a continuous wave 455 nm aiming beam, which generated visible blue illumination at the location where data was acquired. Upon completing the scan, the surgeon proceeded with *en bloc* excision of the tissue suspected of cancer. An *ex vivo* FLIm scan was then performed on the surgically excised specimen (*figure 21C*).

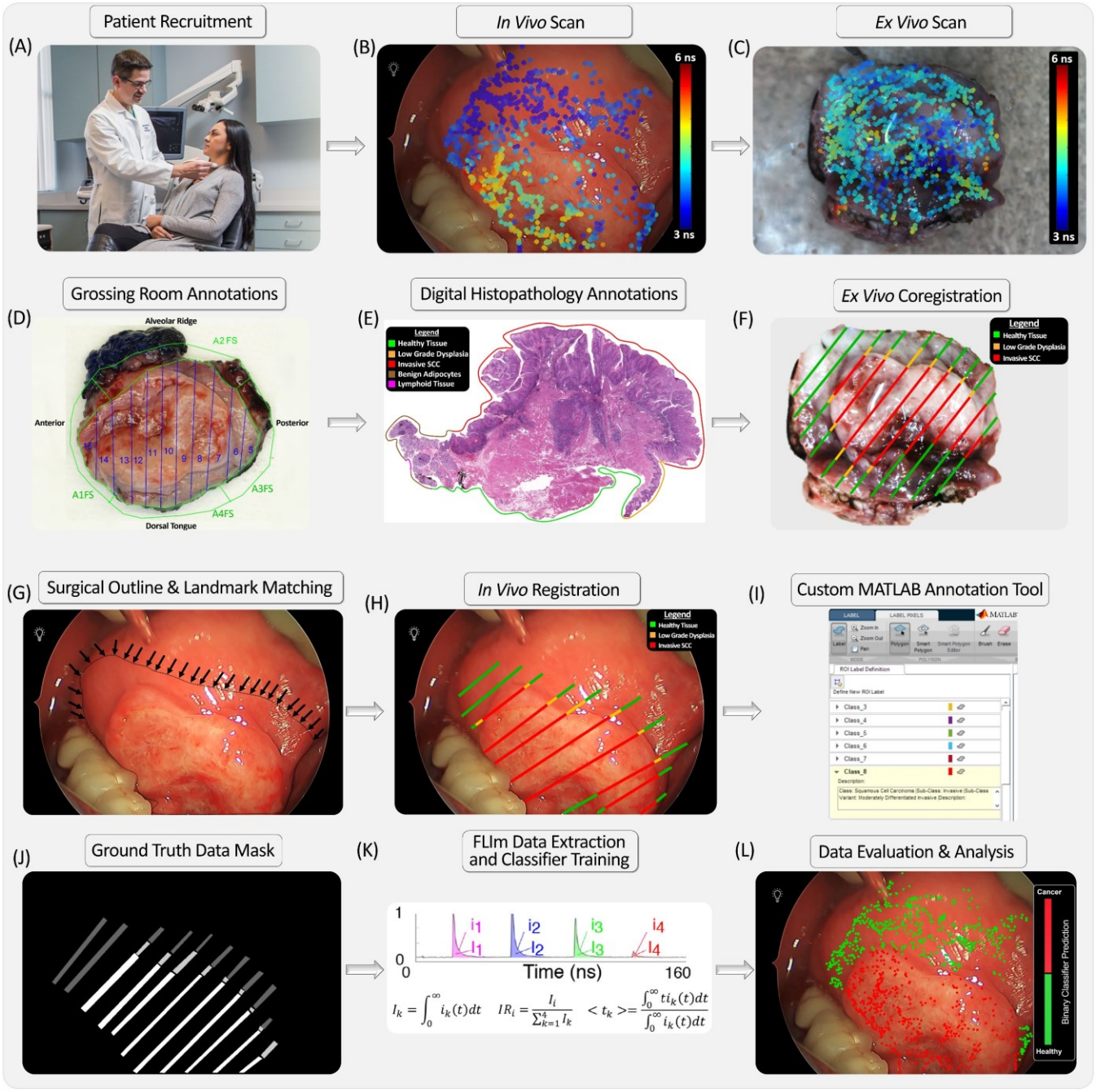

Figure 21: Overview of data collection, coregistration, and data analysis process. (A) Patients were recruited in the research study after obtaining their informed consent. After patients were prepared for surgery, an intraoperative FLIm scan was conducted (B) *in vivo* and with (C) the surgically excised specimen *ex vivo*. (D) Annotations were obtained of the surgical grossing process to facilitate H&E registration to the excised tissue. (E) A pathologist digitally annotated H&E to create tissue labels (e.g., benign tissue, dysplasia, cancer). (F) Tissue labels were next registered to the *ex vivo* specimen. (G) A surgical resection outline was created using videos of the surgical procedure and used in combination with tissue features to perform registration between *in* vivo and *ex vivo* images and (H) transfer the labels to the in vivo image. (I) Labeled surgical images were annotated using a MATLAB annotation tool to create a (J) data mask containing tissue labels. (K) For each optical measurement, FLIm time-resolved and spectral intensity parameters were extracted, as described elsewhere.[153] (L) Labeled FLIm data was used to develop classifiers using a leave-one-patient-out validation scheme.[169]

4.3.4 Surgical Grossing Annotation Process

Following FLIm scanning, the excised specimens were transferred to a pathology grossing room. As part of standard-of-care, the intact specimens were inked with tissue marking dyes (cationic charged ink, Fisher Scientific, USA) according to anatomic orientations designated by the surgeon (e.g., superior, inferior, anterior, posterior). This marking enables orientation of the excised tissue samples sent to the histopathology laboratory. The dyes are specifically formulated to be visible on frozen and permanent H&E sections. After inking, the tissue specimen was serially grossed to generate tissue slices, which were then formalin-fixed, paraffin embedded, sectioned, and stained to create H&E slides for pathology interpretation. The locations where gross tissue slices were obtained (cut lines) were annotated on a pre-grossed image of the ex vivo specimen; this step ensured that the locations of gross slices submitted for H&E staining could be directly traced back to the original location of the surgical specimen (*figure 21D*). All H&E slides were then scanned for digital microscopy retrieval at 0.5 µm / pixel resolution using a Aperio Digital Pathology Slide Scanner (Leica Biosystems, United States).

4.3.5 Pathologist Digital Annotation Process

A pathologist (DG), who was agnostic to FLIm data, digitally annotated scanned H&E slides using Aperio Imagescope. Tissue labels were assigned according to histologic features observed within 250 µm of the tissue's epithelial surface, in addition to the deep margin (*figure 21E*). The following tissue labels were used: (1) benign tissue, (2) carcinoma, (3) low-grade dysplasia, (4) high-grade dysplasia, (5) lymphoid tissue, (5) inflammation, (6) reactive tissue, and (7) ulceration.

4.4 | Registration of H&E Sections to Ex Vivo Specimens

Figure 21F demonstrates the resulting tissue labels associated to the excised specimen. The *ex vivo* coregistration process is described in detail in *figure 22*. To register tissue labels from bread-loafed H&E sections to an *ex vivo* specimen, digitally annotated H&E sections were

first measured by Aperio Imagescope's automated pixel to distance conversion (*figure 22A*). In *figure tile 22A*, green annotations correspond to benign tissue labels, orange to low-grade dysplasia, and red to cancer. *Figure 22B* depicts all grossed tissue slices for a given specimen. Each digital H&E section and image of the gross slice were placed on a PowerPoint slide, and the background was removed from both images. The H&E section and gross slice were spatially overlaid and made semi-transparent to compare images. The tissue ink on the H&E section and gross slice were used to verify the correct orientation (i.e., left vs. right, up vs. down). After verifying the orientation, both the fixed section (*figure 22A*) and the gross slice (*figure 22B*) were measured, and their dimensions compared. Small discrepancies were expected due to folding and/or absence of some areas of the fixed section. This was confirmed by identifying landmarks visible on both the fixed and gross sections. Once the H&E section and gross slice pictures were matched, the tissue labels from the H&E were replicated onto the gross slice. This process was performed by using the dimensions obtained from the tissue H&E section and gross (macroscopic) slices and comparing differences in both morphology (e.g., tissue bending) and dimensions (e.g., tissue shrinkage). Slice A7 is illustrative of a H&E section which closely matches the morphology and dimensions of the gross slice; accordingly, little to no adjustment was needed to transfer the H&E tissue labels. Slice A12 alternatively demonstrates significant bending and compression of the H&E section relative to the gross slice, therefore requiring adjustments to transfer tissue labels from H&E sections to the gross slices. In the next step, as shown in *figure 22C*, digital annotations (designated by gray bars) were overlaid on the locations of the pre-grossed specimen where gross slices were obtained. The process for comparing spatial discrepancies was then performed analogously between the gross slices (figure 2B) and the matching locations on the intact surgical specimen (*figure 22C*), resulting in the transfer of the gross slice tissue labels to the *ex vivo* specimen image (*figure 22D*).

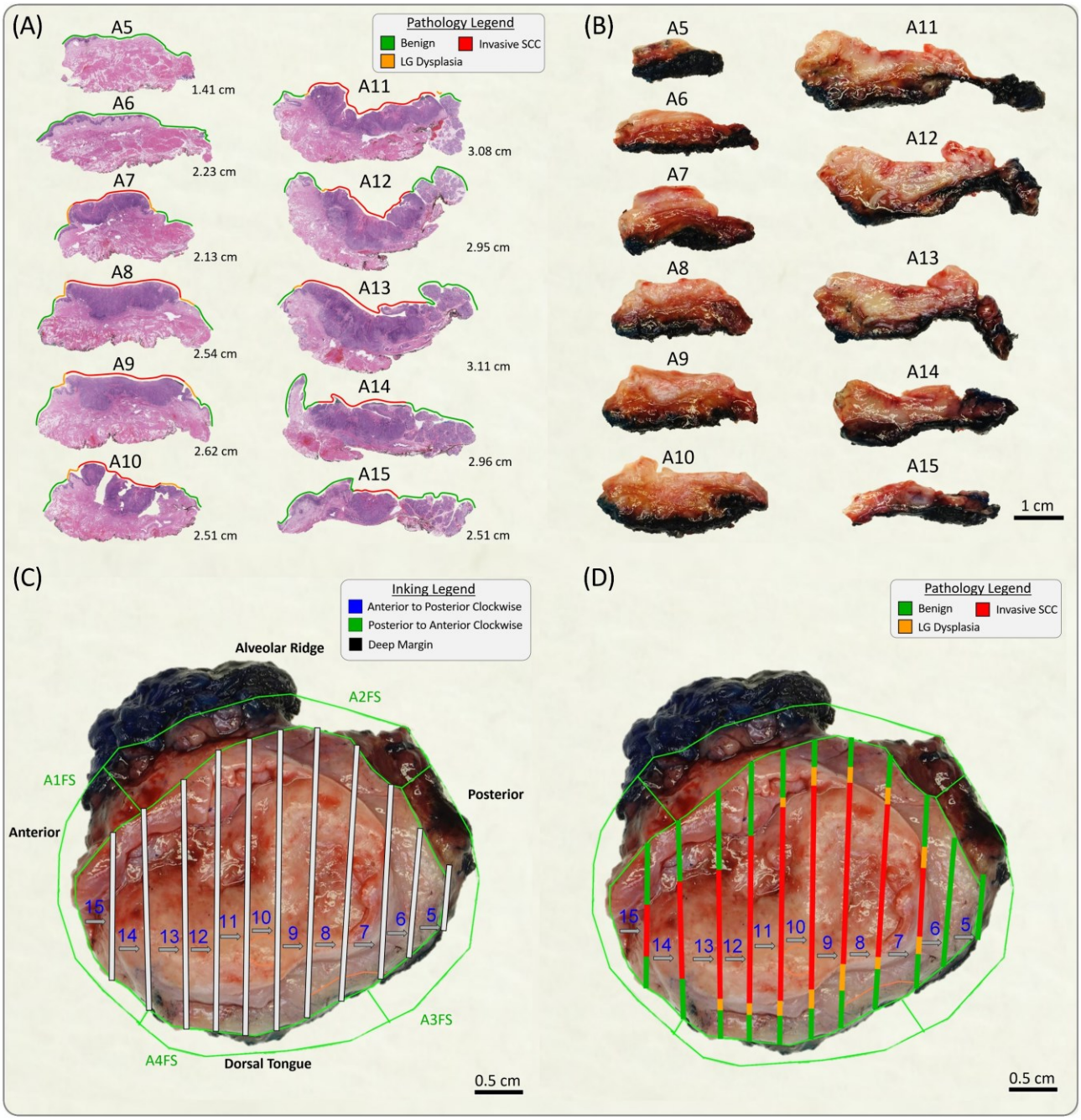

Figure 22: Process for registering serial sectioned H&E sections onto the intact *ex vivo* surgical specimen. The intact surgical specimen (tile C) is cut into gross sections (tile B), each section is formalin-fixed, paraffin embedded, sectioned, and stained to create H&E slices (tile A) before examination by the pathologist. (A) H&E-stained slides were scanned and digitally annotated by a pathologist (DG) to create tissue labels corresponding to features (e.g., benign tissue, dysplasia, cancer) of the epithelial tissue surface. In the figure, benign tissue is indicated by green tissue labels, low-grade dysplasia by orange labels, and cancer by red labels. (B) H&E tissue labels were transferred onto the gross sections; when transferring tissue labels, adjustments were made to account for differences in morphology (e.g., bending) and dimensions (e.g. shrinkage) between H&E sections and gross sections. (C) During the process of surgically grossing the surgical specimen in the pathology room, gray bars were digitally overlaid over the intact specimen image to indicate the regions where gross slices were obtained. Tissue labels mapped onto the gross sections (tile B) were transferred to the intact gross specimen (tile C) in the same process that accounts for morphological and dimensional variations, resulting in (D) tissue labels coregistered to the *ex vivo* specimen.

4.5 | Registration of H&E In Vivo

4.5.1 In Vivo Reference Frame Selection and Surgical Outline Delineation

Figure 21G illustrates an in vivo surgical outline, which is used to determine the boundaries where an intact gross specimen was excised. To create this outline, a key initial step is to identify a reference frame from the data acquisition video where the surgical field-of-view is not obstructed. Using images of the patient's surgical cavity and recorded video of the surgical procedure, the surgical outline is then marked on the in vivo reference image. Landmarks were next identified between the in vivo reference image (*figure 21G*) and ex vivo image (*21F*) to facilitate in vivo registration.

4.5.2 In Vivo Registration Process

When performing *in vivo* registration, it is essential to account for deformations of the *ex vivo* specimen relative to the *in vivo* tissue conformation. *In vivo* tissue is under various elastic and geometric influences; upon surgical excision, changes in tissue morphology (e.g., tissue folding, twisting) and dimensional changes (e.g., shrinkage due to fluid loss) occur. *Figure 21H* demonstrates the result of mapping tissue labels from an *ex vivo* specimen *in vivo*; the process for performing this registration is detailed in *figure 23*. Tiles A-C of the figure demonstrate the process for outlining boundaries of the surgical region on base of tongue tissue in a patient case study. Using the reference image (*figure 23A*) and the surgical electrocautery outline (*figure 23B*) derived from intraoperative videos, the surgical outline was annotated on the pre-resected tissue reference frame (*figure 23C*). *Figure 23 D-G* demonstrates a second case study of oral tongue tissue where the surgical outline was demarcated on a reference image (*figure 23D*) and used in combination with landmarks (*figure 23E*) and the *ex vivo* specimen to create tissue labels within the *in vivo* reference image (*figure 23F*). These landmarks were used to assess orientation, compression, and expansion of the tissue in the registration of the tissue labels. Upon completing the registration process, the results of FLIm scan classifier output can be validated against ground-truth tissue labels (*figure 23G*).

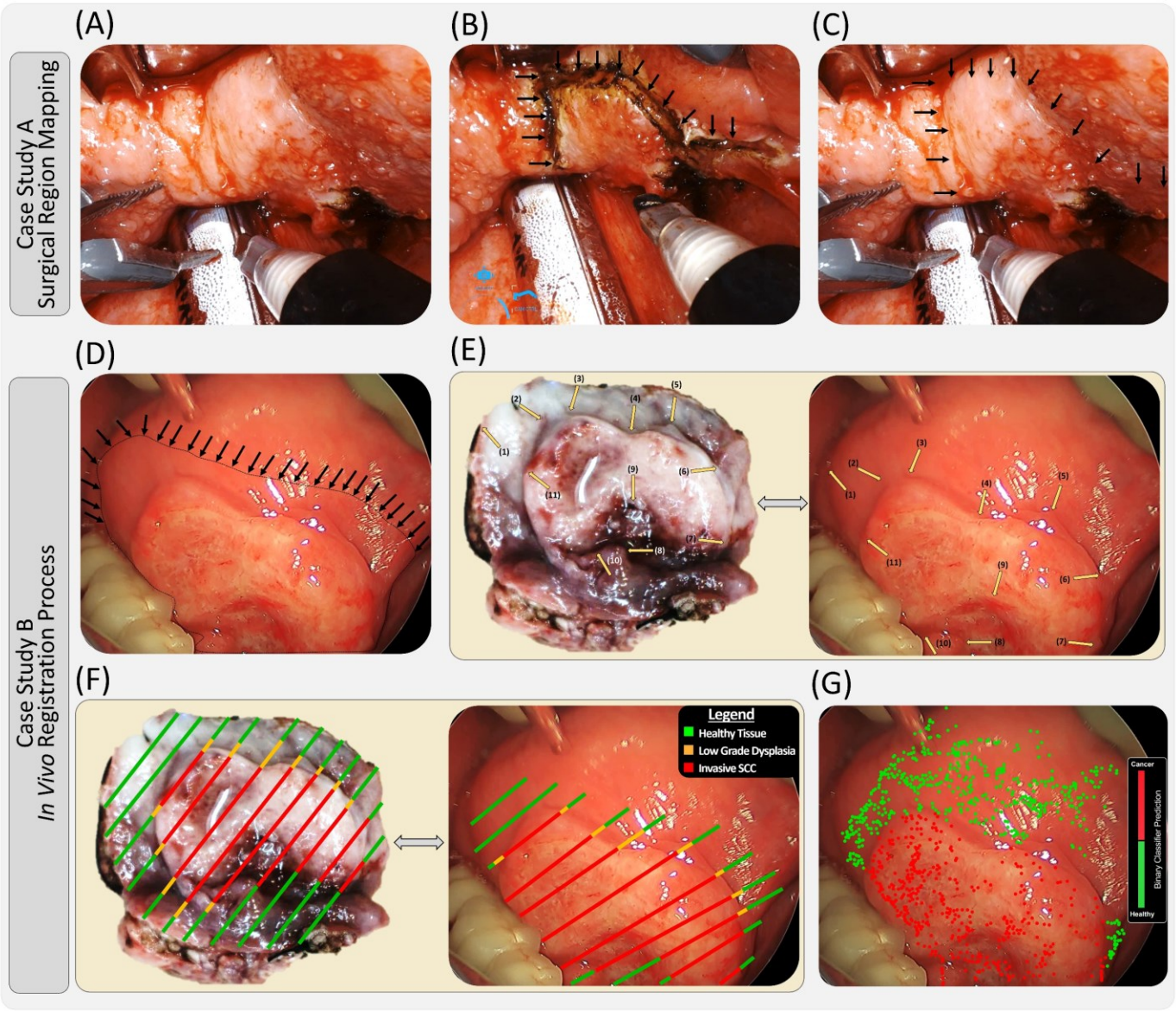

Figure 23: Transfer of labels from an *ex vivo* tissue image to the *in vivo* tissue image. Parts A-C present a case study, which demonstrates the creation of a surgical outline on the in vivo surgical image, which aids in transferring the labels overlaid on the *ex vivo* specimen to the *in vivo* surgical image. (A) Surgical field of view where FLIm scan was conducted prior to surgical excision. (B) Photograph of intraoperative surgical excision process. Here, a video of the entire surgical process is obtained and a key image that demonstrates the excision boundary was selected to determine the surgical outline. (C) The excision outline is then demarcated on the reference image. Parts D-G present a second case study (different patient, presented in figure 2) where the *in vivo* registration process is performed after determining the surgical outline, demarcated by black arrows on the FLIm reference image (tile D). (E) Key landmarks identifying clearly visible features, of which 10 are denoted, are identified on the *ex vivo* image and used to match to landmarks *in vivo*. (F) Landmarks are used to facilitate the coregistration of the *ex vivo* specimen image to the *in vivo* image and transfer associated histopathology labels. Notice that some *ex vivo* features are not visible near the teeth region *in vivo*, particularly the low-grade dysplasia region, and are thus omitted from the reference frame. (G) Finally, after transferring histopathology labels to the *in vivo* image, the FLIm data itself was labeled based on the point-measurement location and data from the patient was analyzed. An example of the binary random forest machine learning classifier output is demonstrated in (G). Using a leave-one-patient-out classification scheme (presented in detail elsewhere),[169] the classifier predicted cancer where datapoints are red, and benign tissue where datapoints are green.

4.6 | Histopathology Annotation Tool and Ground Truth Data Mask

A MATLAB annotation tool (*figure 21I*) was developed to create a label mask (*figure 21J*) using registered tissue labels from *ex vivo* (*figure 21F*) and *in vivo* (*figure 21H*) reference images. The label mask allows tissue labels to be annotated in a pixel space. Correspondingly, the annotated pixels are used to label optical spectroscopic data for which the measurement location is known in the white light pixel space. Due to the potential value of this tool for optical imaging researchers, the code, a user guide, and an example dataset is provided for researchers on *GitHub* (a provider of internet hosting for software development and version control). These resources are provided at the directory of bwweyers/Histopathology-Annotation-Tool. The characteristics of this tool are described in detail in the *GitHub* user guide; in brief, this tool (*figure 21I*) allows a user to create a series of tissue labels (e.g., lymphoid tissue, benign tissue, cancer) to annotate surgical reference images (*figure 21H* / *figure 24*). The tool allows for label sets to be saved, and then exported to a customized MATLAB image labeling workspace where coregistered surgical reference images can be annotated. The result of the completed label annotations results in a ground truth data mask, demonstrated in *figure 21J / figure 25*.

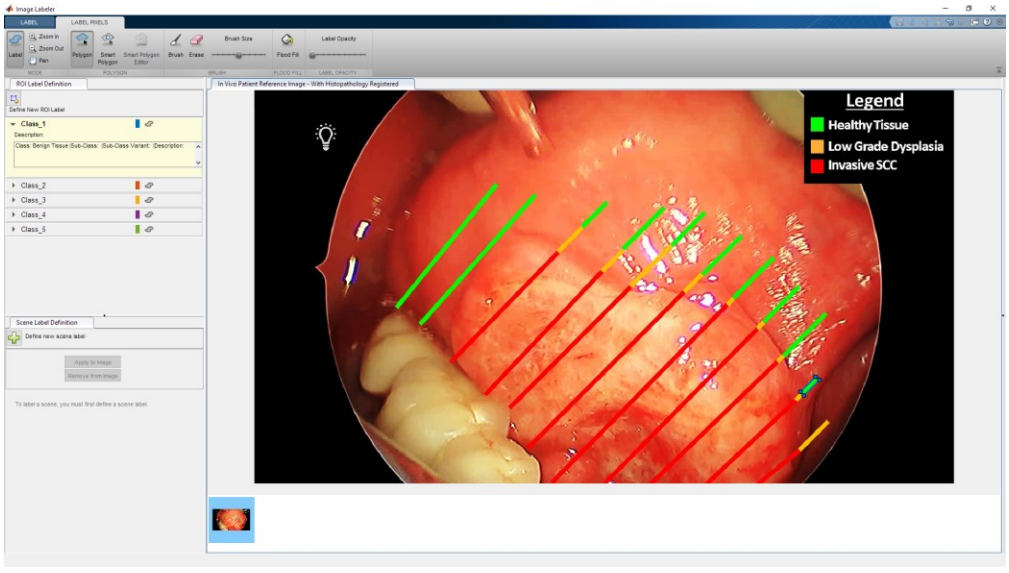

Figure 24*:* Histopathology annotation tool with reference image loaded in. This step is done prior to annotations being performed.

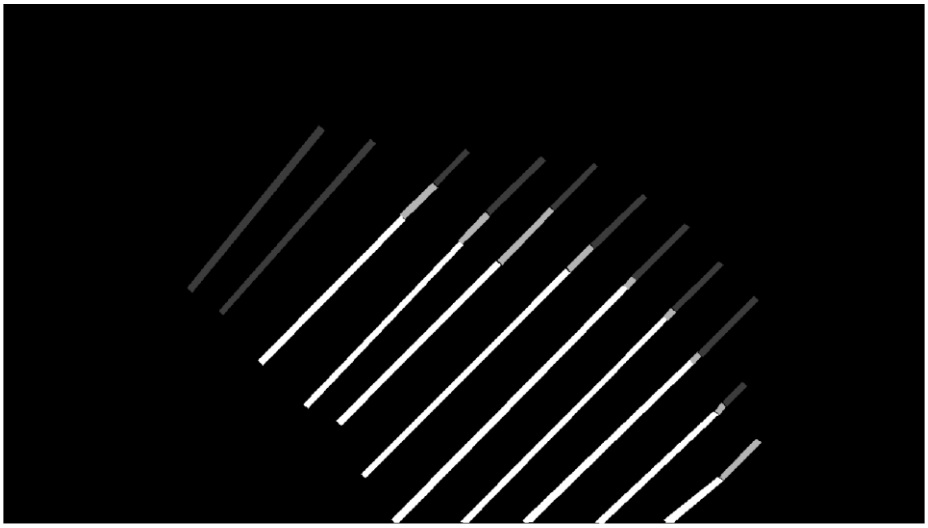

Figure 25: Demonstration of data pixel annotation mask. Depicted is a 720x1280 data annotation mask exported from the *Data Annotation Tool* using the *Test Dataset*.

By way of demonstration, consider the following: all surgical videos in this database were acquired with 720x1280 pixel resolution. FLIm spectroscopic point-measurements acquired during a surgical scan are assigned to coordinates in the 720x1280 pixel space to denote the location where the point-measurements were acquired. The annotated 720x1280 pixel reference image (with coregistered tissue labels) is imported into this tool for labeling. Assuming a label value of 1 is used for cancer, and 2 for benign tissue; the pixels in the 720x1280 label mask (*figure 25*) would have a value of 1 in correspondence to the locations of cancer identified in mucosal regions of the H&E slice. This mask would have a value of 2 in correspondence to benign tissue identified in regions of the H&E slice, and elsewhere a value of 0 where there is no annotation. This label mask can then be used as a filter to identify data obtained at coordinates in the 720x1280 pixel space and associate them with histopathology labels. If a datapoint was acquired at pixel [450, 700] with respect to the reference image, and the label mask contained a cancer annotation (pixel value of 1) at pixel coordinates [450,700], that datapoint would be labeled as cancer. This tool correspondingly allows for the rapid and versatile association of data coordinates to tissue labels for analysis.

4.6.1 FLIm Data Extraction & Analysis

The FLIm system acquires 30 averaged datapoints per second (120 Hz measurement speed, averaged 4 times).[153] Each spectral datapoint yields a plurality of FLIm-derived parameters (e.g., time-resolved and spectral intensity metrics, as demonstrated in *figure 12K*).[153] These parameters can be further incorporated into classification models to predict cancer probability. *Figure 21L* demonstrates the output of a random forest classification algorithm[169]. Coregistered tissue labels from the data mask (*figure 21J*) compared to data outputs (*figure 21L*) allows for analysis of FLIm metrics and evaluation classification performance.

4.7 | Discussion

Accounting for sources of registration error, and taking steps to mitigate inaccuracy, represents an ongoing challenge. When investigating the utility of optical technologies for clinical use, it is imperative to evaluate optical data accurately against the accepted gold-standard. It should be noted that the challenges related to correctly registering ground-truth histopathology not only affects researchers, but also presents challenges to operating surgeons.[177,178] In an attempt to improve the marginal control of oral cavity and oropharyngeal carcinoma, surgeons routinely perform frozen section analysis.[177] In scenarios where frozen sections are reported as positive, ensuring the correct location of where the frozen section was derived to facilitate re-excision of additional tissue is essential.[177] Considerations described within this protocol may prove useful to clinicians to aid in the accuracy of histopathologic corroboration of frozen sections in surgical settings. While the gold-standard for tissue pathology presented herein focuses on histopathology, other approaches which require local registration to tissue (e.g., molecular markers assessed via tissue microarrays) also bear relevance to the described registration considerations.

As identified by de Boer et al. in 2019, “[In the optical research field] there is only limited literature focusing on correlating optical measurements with histopathology, and when a method

for correlation the optical data to histopathology is described, the reported registration methods do not seem to correct for tissue deformation."[172] The key contribution provided by this protocol is the ability to codify all methods in one place to facilitate reproducibility and mitigate opportunities for registration error by drawing attention to primary scenarios where error is introduced. An additional key contribution is the tool and framework developed for performing labeled data extraction. Collectively, the dedicated resources herein seek to provide standardization of the coregistration process and articulate a structured approach to make this process as robust as possible with the currently available methods.

Multiple strategies to perform histopathology registration have been implemented by different researchers across the optical technology research space. To focus on autofluorescence-based research involving oral tissue, static measurements (where a probe is held in position) on a tissue location have most commonly been performed, followed by directed biopsies at the measured site, with subsequent pathologist interpretation.[120,122,130,179] Other studies, such as by Jo et al., have used a hand-held endoscope capable of scanning a small field-of-view (mm-scale) and directly registering to biopsy specimens.[128,132,133,152] Our approach to FLIm for intraoperative surgical guidance is significantly different in the sense that FLIm imaging occurs over large areas of tumor, on the order of multiple centimeters. For practical reasons (e.g., bleeding and tissue processing time), the collection of many small biopsies at distinct measurement locations cannot be performed. Therefore, histopathological validation must occur over the whole resected tissue. Accordingly, in this research, labeling of imaging data, in addition to data extraction, requires more extensive registration approaches compared to research involving direct validation via biopsy.

A predominant challenge in assessing the accuracy of the histopathology registration is the lack of quantitative measures to assess performance, therefore it is difficult to quantify the improvement of coregistration accuracy using the reported methods. This challenge originates

from the many qualitative and somewhat subjective tasks involved in the coregistration process (e.g., landmark identification, determination of compression or expansion artifacts, and reduced clarity of the *in vivo* surgical field of view when lighting or focus of the visualizing endoscope is not ideal). While not possible to directly assess the improvement in histopathologic registration accuracy which this study protocol confers, the developed approach has increased the degree of objective metrics that can be referenced to minimize potential error and facilitate more accurate registration.

Continuing to improve on the present histopathology registration effort by emphasizing more automated and quantitative approaches will be essential to further advance registration accuracy. Along these lines, a central limitation in the proposed protocol is the potential to introduce subjectivity across the various steps. In this context, integrating advances to feature matching software, such as those developed for facial recognition, will enable more precise optical registration and orientation based on subtle geographic and anatomic features. The addition of fiducial markers, such as ink and surgical clips, can additionally facilitate enhanced registration accuracy. Various other methods are actively being explored to aid in automated feature extraction. This includes extracting Fourier-based features, scale-invariant feature transformation based on difference of Gausians, extracting features from anatomical structures and tissue boundaries across images to create comparable scales, in addition to other automated landmark-based approaches.[180] While the best approach to improve present histopathology registration may require a combination of techniques to achieve accurate registration, it is clear that more sophisticated automated approaches is the key next step to achieve standardized registration with reduced variability across researchers. Through the incorporation of the described techniques, in parallel to advances in imaging technologies and spatial recognition software, the accuracy of future coregistration efforts and reproducibility of research will continue to improve.

CHAPTER 5 | Application of FLIm for Intraoperative Delineation of Primary Tumors of the Oropharynx: An Initial 10-Patient Feasibility Study

5.1 | Abstract

This chapter reports on the first use of FLIm to demarcate tumors of the oropharynx using TORS platforms. We first demonstrate that cancer in epithelial tissue diagnosed by histopathology can be differentiated from surrounding healthy epithelial tissue imaged *in vivo* prior to cancer resection and *ex vivo* on the excised specimen. Second, we study the fluorescence properties of tissue imaged *in vivo* at surgical resection margins (tumor bed). Fluorescence lifetimes and spectral intensity ratios were calculated for three spectral channels, producing a set of six FLIm parameters. Results from N=10 patients undergoing TORS procedures demonstrated that healthy epithelium can be resolved from cancer ($P < 0.001$) for at least one FLIm parameter. We also showed that a multiparameter linear discriminant analysis approach provides superior discrimination to individual FLIm parameters for tissue imaged both *in vivo* and *ex vivo*. Collectively, this work highlights the potential for FLIm to be developed into a diagnostic tool for clinical cancer applications of the oropharynx and serves as the preliminary basis for investigation of classification methods (e.g., machine learning) for real-time surgical decision-making. This technique could help to circumvent the issues posed by the lack of tactile feedback associated with robotic surgical platforms to better enable cancer delineation.

5.2 | Introduction

A first step in investigating the use of FLIm for surgical guidance of the oropharynx is to first demonstrate the ability to resolve benign tissue from cancer at a patient-level. Prior to this study, no reported studies demonstrate the use of FLIm *in vivo* to demarcate conventional primary tumors of the oral cavity. Accordingly, the goals of this study were to: (1) conduct FLIm measurements during TORS procedures involving oropharyngeal carcinoma, (2) to evaluate the effect of experimental procedures on FLIm data, and (3) to determine whether a combination of

FLIm-derived parameters can be always found and used as means of intrapatient diagnostic contrast irrespective of experimental situations.

Both univariate (i.e., single-parameter) and multivariate approaches involving FLIm spectral intensity and time-resolved features were investigated. For the multivariate approach, linear discriminant analysis (LDA) was used to incorporate all FLIm spectral intensity and time-domain fluorescence parameters to resolve benign tissue from cancer. FLIm data was evaluated both *in vivo* and *ex vivo* with the surgically excised specimens. This study additionally investigated FLIm characteristics of the *in vivo* surgical cavity.

5.3 | Materials & Methods

5.3.1 Integration of FLIm into TORS Instrumentation

The FLIm instrumentation and the corresponding integration into TORS is discussed extensively in *chapter 3.1.1*. In brief, to acquire data in this investigation, the FLIm system was coupled to the da Vinci Si Surgical System via a 5Fr EndoWrist Introducer, demonstrated in *figure 26*. *In vivo* pre-resection and cavity scans were performed by TORS, whereas *ex vivo* scans were performed by hand (*figure 26*).

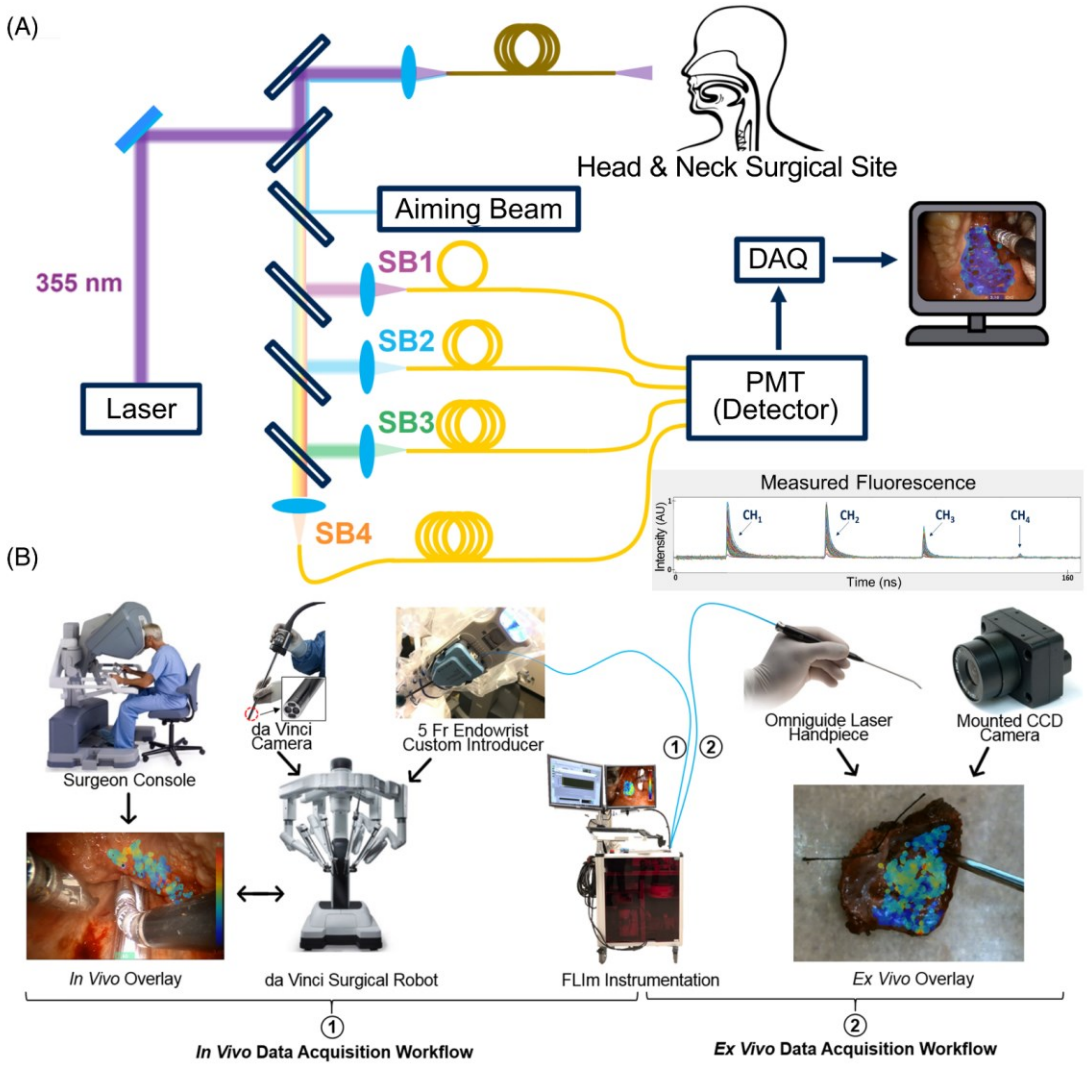

Figure 26: Illustration of FLIm integrated into TORS and clinical workflow. (A) Schematic of the custom-built FLIm system, featuring the excitation beam to generate autofluorescence, the aiming beam to spatially coregister data, and the four spectral channels to resolve fluorescence lifetime and spectral intensity. Also illustrated is an example of the measured fluorescence waveforms output from the four time-delayed spectral channels; the method for the detailed calculation of fluorescence lifetime and spectral intensities for each spectral channel is described by Liu et al.[153] (B) Integration of the FLIm system with the da Vinci surgical system in the OR workflow: (1) represents the *in vivo* workflow for both pre-resection and post-resection (cavity) analysis where the da Vinci surgical system (including the integrated camera) was leveraged to collect measurements, and (2) represents the *ex vivo* workflow used for resected specimen pathology assessments where an Omniguide Laser Handpiece was used to perform a hand-held scan visualized by a mounted camera. The surgeon console and da Vinci system images are adapted with permission from Intuitive Surgical Inc. Reproduced with permission from Weyers et al. reference [168].

5.3.2 Human Patients and Data Collection

Under institutional review board (IRB) oversight, 10 human patients undergoing upper aerodigestive oncologic surgery of the oropharynx were recruited for the study. The enrolled patients, along with their corresponding surgical locations, etiologies, and residual cancer status are enumerated in *table 5*.

Table 5. Overview of Patients, Afflicted Anatomical Tissues, Resulting Pathologies, and Residual Cancer Status.

Patient	Anatomy	Pathology	Residual Tumor
1	Lingual Tonsil	SCC	N/A
2	Palatine Tonsil	SCC	N/A
3	Palatine Tonsil	SCC	N/A
4	Palatine Tonsil	SCC	N/A
5	Palatine Tonsil	SCC	N/A
6	Palatine Tonsil	SCC	N/A
7	Palatine Tonsil	Basaloid SCC	N/A
8	Palatine Tonsil	SCC	N/A
9	Base of Tongue	Benign (No Cancer)	N/A
10	Palatine Tonsil	SCC	N/A

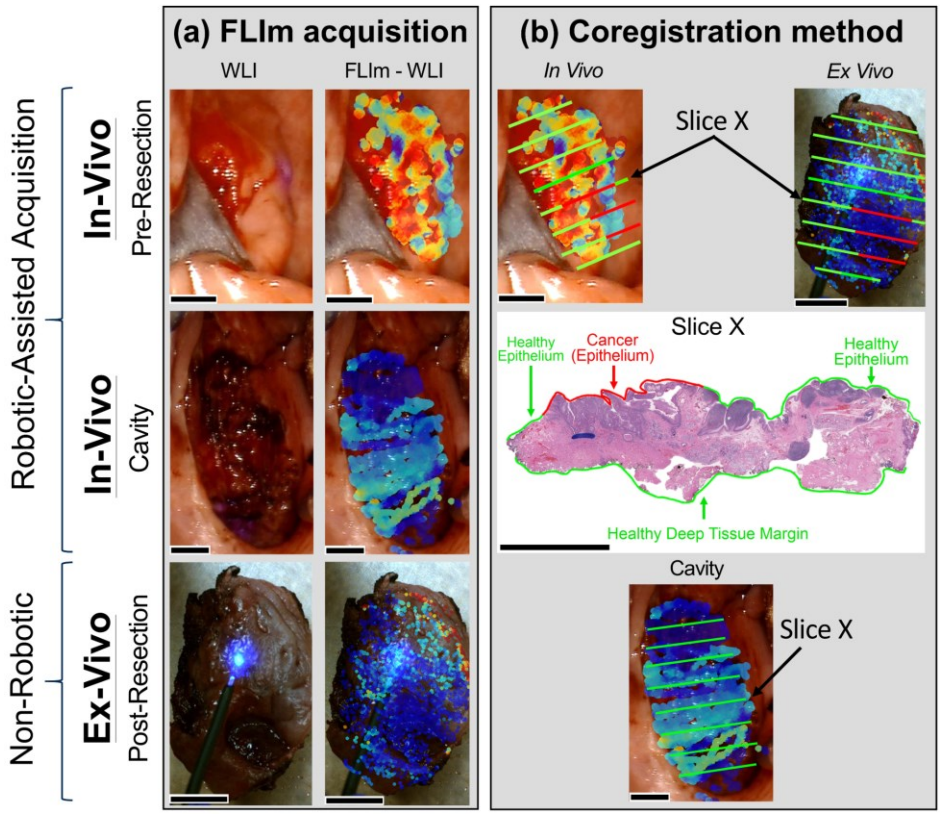

Figure 27: Coregistration of FLIm to tissue histopathology. (A) First, a surgical region of interest was identified *in vivo* by the operating surgeon. A FLIm scan was then performed at the surgical region of interest, in addition to benign peripheral tissue, to create and augmented FLIm image. *En bloc* tumor excision was then performed, and a FLIm scan of the surgical cavity and surgically uninvolved peripheral tissue was acquired. Thereafter, an *ex vivo* scan was performed on the excised specimen. (B) The surgically excised specimen was surgically grossed to create H&E sections. The pathologist annotated the corresponding histology, and the results were extrapolated onto the respective slice both *in vivo* and *ex vivo* as demonstrated in *chapter 4*. All scale bars represent 0.5 cm. Reproduced with permission from Weyers et al. reference [168].

Prior to robotic surgery, the EndoWrist instrument containing the fiber optic from the FLIm instrument was installed in the da Vinci surgical system and was placed inside the oral cavity of the patient under anesthesia. Surgeons identified the tissue areas of interest based on preoperative planning. FLIm measurements were then acquired by scanning the EndoWrist instrument over that region, as demonstrated in *figure 27*. FLIm data was collected *in vivo* prior to *en bloc* surgical excision, with the excised surgical specimen, and in the patient's surgical cavity *in vivo*. Peripheral benign tissue was also imaged within the *in vivo* pre- and post-resection scans. FLIm results were registered to histopathology for validation, as demonstrated in *chapter 4*. FLIm data deconvolution and data visualization was performed using the methods from *chapter 3*.

5.3.3 Data Annotation, Coregistration, and Preprocessing

FLIm measurements were coregistered to tissue annotations and analyzed only at regions directly guided by histopathology. Measurements near heterogeneous tissue conditions (i.e., boundaries between cancer and healthy tissue) were excluded by removing any measurement within a 10-pixel radius (~0.75 mm) of multiple disparate tissue conditions. A larger exclusion radius would remove a large quantity of data points from the analysis stage of this initial study. A SNR threshold of 30 dB was applied across all spectral channels. Outlier removal was performed prior to any univariate statistical analysis for each FLIm parameter using a median absolute deviation (MAD) filtering approach,[181] where parameter values ±2.5 MAD from their respective median were removed for each patient. This MAD filtering procedure was performed separately for *in vivo* pre-resection scans, *ex vivo* scans, and cavity scans. Spectral channel 4 was excluded from analysis due to the poor signal properties observed, thus six FLIm parameters were evaluated in this study: average fluorescence lifetime and spectral intensity ratio from spectral channels 1–3. Outlier removal and SNR filtering removed 0.5% and 2.5% of data points respectively.

5.3.6 Statistics and Discrimination Metrics

Statistical tests and discrimination metrics were implemented to quantify FLIm's ability to distinguish between benign tissue and cancer. Statistically, no assumptions of a normal distribution were made for acquired FLIm data, however, independence and equal variance were assumed; with these considerations, the Wilcoxon rank sum test, a non-parametric statistical method, was selected for statistical evaluation.[182,183] Receiver operating characteristic (ROC) and precision-recall curve analysis were performed for each FLIm parameter to calculate a set of discrimination metrics.

Once calculated for a given variable, area-under-the-curve (AUC) and average precision (AP) provide a comprehensive overview of its discriminative power. Average precision is influenced more by the performance of the positive class (e.g., cancer) and can highlight poor discrimination even if the dataset is imbalanced between classes (i.e., majority healthy), while AUC treats each class with equal importance. For each patient, analysis was performed separately for each imaging context (*in vivo* prior to tissue resection, *ex vivo* after tissue resection for the excised specimen, and within the *in vivo* surgical cavity).

5.3.7 Multiparameter Discrimination

LDA was used to investigate if a weighted linear combination of the six calculated FLIm parameters can provide better discrimination of tissue types than individual FLIm parameters. This analysis was performed separately for each patient and tissue context, as the focus of this work was on intrapatient sources of FLIm contrast, rather than the development of a generalized classifier. The LDA variable was calculated for each case by resubstitution validation (through singular value decomposition), minimizing the intraclass variance and maximizing the interclass variance. The optimized set of weights was applied to the FLIm data for a given scan before min-max scaling was performed, producing a set of LDA variables in the range of 0.0–1.0 for this scan, which are used to distinguish healthy tissue from cancer. AUC and AP were calculated for this LDA variable, allowing for a direct comparison with each individual FLIm

parameter in terms of discriminative power. The objective here was not to train a generalized classifier, but to compare single parameter and multiparameter tissue discrimination approaches within individual patients.

5.4 | Results

FLIm measurements acquired from patients (N=10) and subsequently analyzed generated a total of 42,777 FLIm data points coregistered with histopathology. 13,765 of these data points were associated to cancer and the remaining 29,012 to benign tissue. This dataset includes nine *in vivo* pre-resection scans, nine *ex vivo* specimen scans, and seven post-resection tumor bed scans. No positive surgical margins were identified in the resection tumor bed scans. Patient 9 did not have cancer; thus this patient was omitted from *figures 28* and *28*. *Table 5* summarizes the patient information involved in this study.

The patient case studies in *figure 28* and *figure 29* were selected for the following reasons: first, they highlight different levels of single parameter contrast (both *in vivo* and *ex vivo*) and show how limited contrast can be overcome through a multiparameter LDA approach, and second, distinct tissue conditions (i.e., levels of heterogeneity) are observed in the histopathology for each case. Each case study presents: (1) heat map visualizations of all six FLIm parameters with the associated AUC and AP score, (2) violin plots (a non-parametric data visualization method which includes both a box plot and a kernel density plot) for all six FLIm parameters with statistically significant change ($P < 0.001$) highlighted, (3) a heat map visualization of the multiparameter LDA variable along with AUC and AP score, and (4) registered histopathology.

Following the *in vivo* and *ex vivo* scan for each case, the FLIm profile of the surgical cavity scan is presented. For *in vivo* pre-resection and *ex vivo* scans, the aim was to evaluate whether neoplastic changes in epithelial tissue diagnosed by conventional histopathology can

be differentiated from surrounding healthy epithelial tissue, while for the post-resection cavity scan, the goal was to evaluate changes in optical parameters due to cauterization.

5.4.1 Case Study A

Case study A (*figure 28*) presents FLIm measurements for Patient 8. Statistically significant change ($P < 0.001$) was observed between tissue conditions for five FLIm parameters in the *in vivo* pre-resection scan and four FLIm parameters in the *ex vivo* post-resection scan. LDA improved both AUC and AP score for both scans compared to the best performing individual parameter in each case. For the *in vivo* scan, the use of the LDA variable improved AUC and AP by just 0.02 and 0.01 respectively, suggesting that when good single-parameter contrast is observed (i.e., AUC of 0.89) that a multiparameter approach (LDA) only results in marginal improvement. For the ex vivo scan, the use of the LDA variable improved AUC and AP by 0.04 and 0.01 respectively, these marginal improvements due to the already strong single parameter contrast observed (AUC of 0.74). A bimodal distribution was observed within the tumor bed for intensity ratio in CH1, CH2, and CH3, suggesting that distinct tissue conditions are present.

5.4.2 Case Study B

Case study B (*figure 29*) presents FLIm measurements for Patient 5. Statistically significant change ($P < 0.001$) is observed between tissue conditions for two FLIm parameters in the *in vivo* pre-resection scan and four FLIm parameters in the *ex vivo* post-resection scan. LDA improved both AUC and AP score in both scans compared to the best performing individual parameter in each case. For the *in vivo* scan, the use of the LDA variable improved AUC and AP by 0.11 and 0.12 respectively, highlighting the advantage of a multiparameter approach when single parameter contrast is not strong (i.e., AUC of 0.60). For the *ex vivo* scan, the use of the LDA variable improved both the AUC and AP by 0.11, once again highlighting the benefit of a multiparameter approach. A bimodal distribution is observed within the tumor bed

for average lifetime in channels 1–3 and intensity ratio CH1, suggesting heterogeneity within this region.

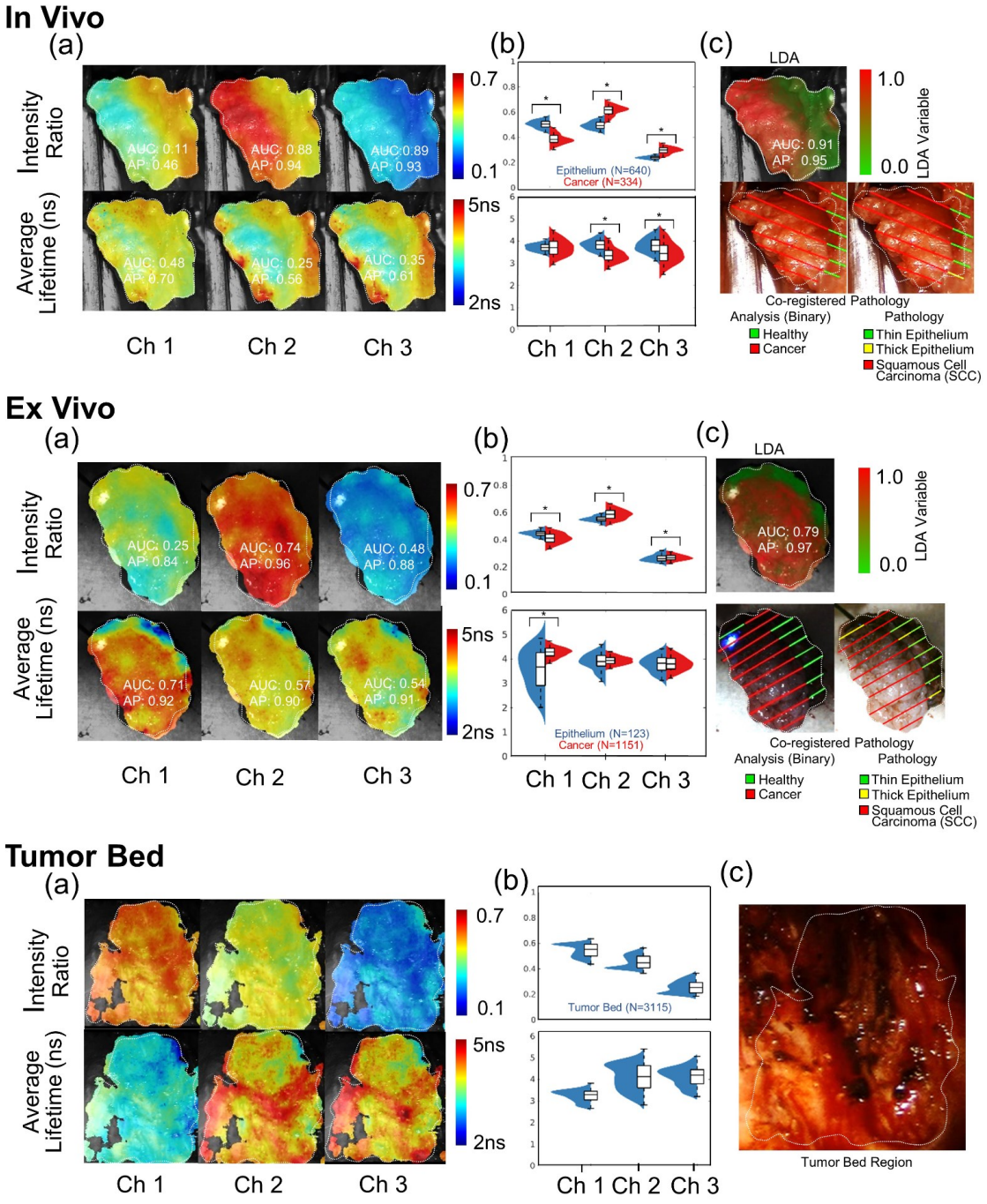

Figure 28: Case study A (Patient 8): Linear discriminant analysis on palatine tonsil. **Upper panel:** pre-resection *in vivo* scans. (a) Heat map visualizations and (b) violin plots of the six FLIm parameters (significance marked '*' for P<0.001). (c) Heat map visualization of the linear discriminant analysis (LDA). **Middle panel:** *ex vivo* scans. (a) Heat map visualizations and (b) violin plots for the six FLIm parameters. (c) Heat map visualization of the LDA variable **Bottom Panel:** surgical cavity scans. (a) Heat map visualization and (b) Violin plots for six FLIm parameters. (c) White light image of the tumor resection bed. Reproduced with permission from Weyers et al. reference [168].

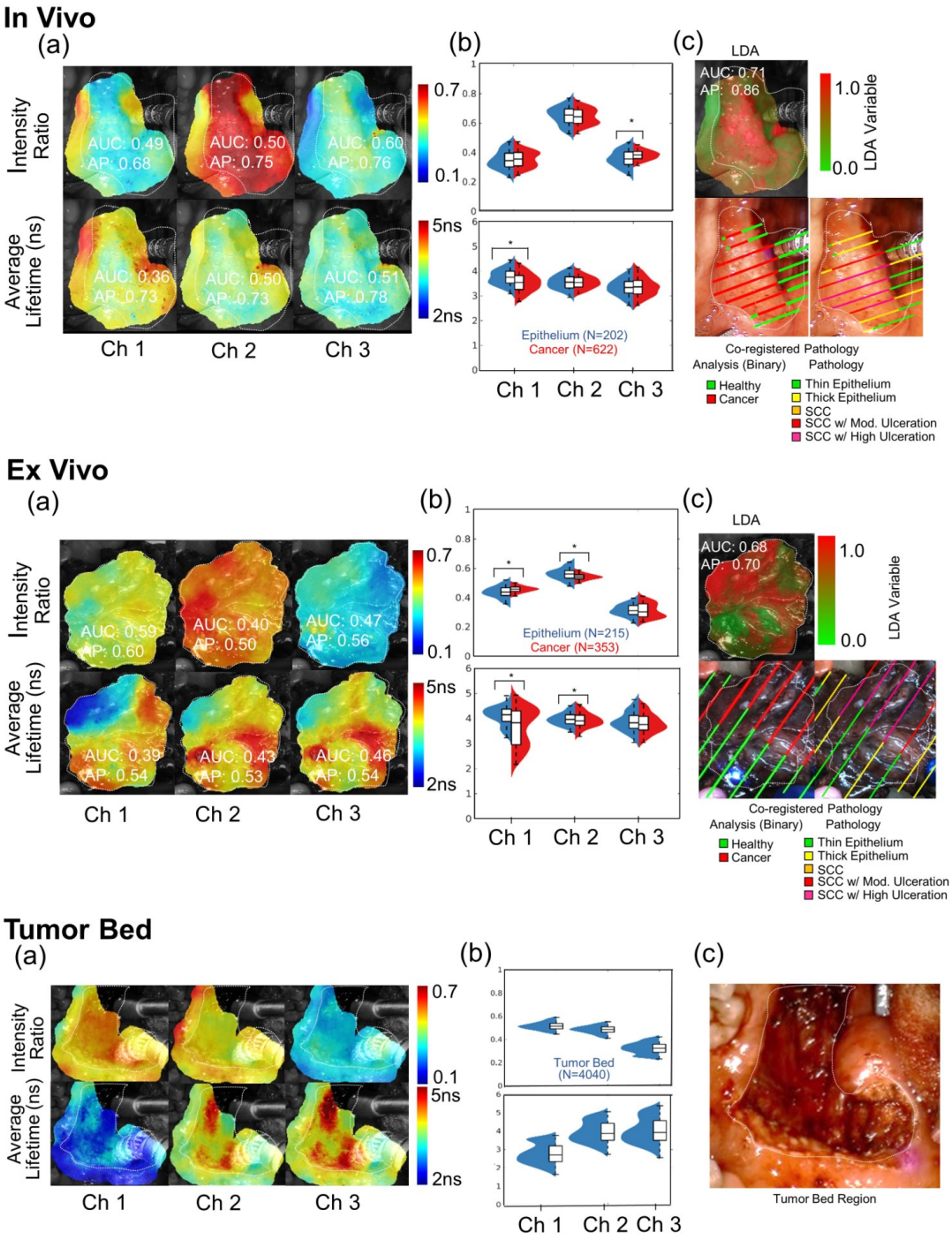

Figure 29: Case study B (Patient 5): Linear discriminant analysis on palatine tonsil. **Upper panel:** pre-resection *in vivo* scans. (a) Heat map visualizations and (b) violin plots of the six FLIm parameters (significance marked '*' for P<0.001). (c) Heat map visualization of the linear discriminant analysis (LDA). **Middle panel:** *ex vivo* scans. (a) Heat map visualizations and (b) violin plots for the six FLIm parameters. (c) Heat map visualization of the LDA variable **Bottom Panel:** surgical cavity scans. (a) Heat map visualization and (b) Violin plots for six FLIm parameters. (c) White light image of the tumor resection bed. Reproduced with permission from Weyers et al. reference [168].

5.4.3 ROC-AUC and Average Precision Comparisons at Patient-Level

Statistically significant change ($P < 0.001$) between healthy epithelium and cancer was observed for at least one FLIm parameter in all *in vivo* pre-resection scans and 8/9 *ex vivo* post-resection scans. A comparison of patient-level ROC-AUC scores for the *in vivo* pre-resection scans and *ex vivo* scans is presented in *figure 30*. The main sources of contrast among the six FLIm parameters varied among patients for each scan context. In all scans, the use of the LDA variable resulted in superior AUC score, with a 0.07 ± 0.03 mean increase observed for the in vivo pre-resection scans and a 0.06 ± 0.03 mean increase observed for the ex vivo post-resection scans. In terms of single parameter discriminative performance, the highest single parameter mean AUC was observed for CH3 intensity ratio in both scan contexts. A single parameter AUC score greater than 0.70 was observed for 6/9 *in vivo* pre-resection scan and 4/9 *ex vivo* post-resection scans.

A comparison of patient-level average precision for the in vivo and ex vivo post-resection scans is presented in *figure 31*. As observed for ROC-AUC analysis, the main source of contrast varies between patients for both scan contexts. The use of LDA resulted in a superior overall AP score, with a 0.08 ± 0.06 mean increase observed for the *in vivo* pre-resection scans and a 0.06 ± 0.03 mean increase observed for the *ex vivo* post-resection scans. In terms of single parameter discriminative performance, the highest single parameter mean AP was observed for CH3 intensity ratio in the in vivo pre-resection scans and CH1 intensity ratio for the ex vivo scans. A single parameter AP score greater than 0.70 was observed in 6/9 in vivo pre-resection scans and 3/9 ex vivo post-resection scans.

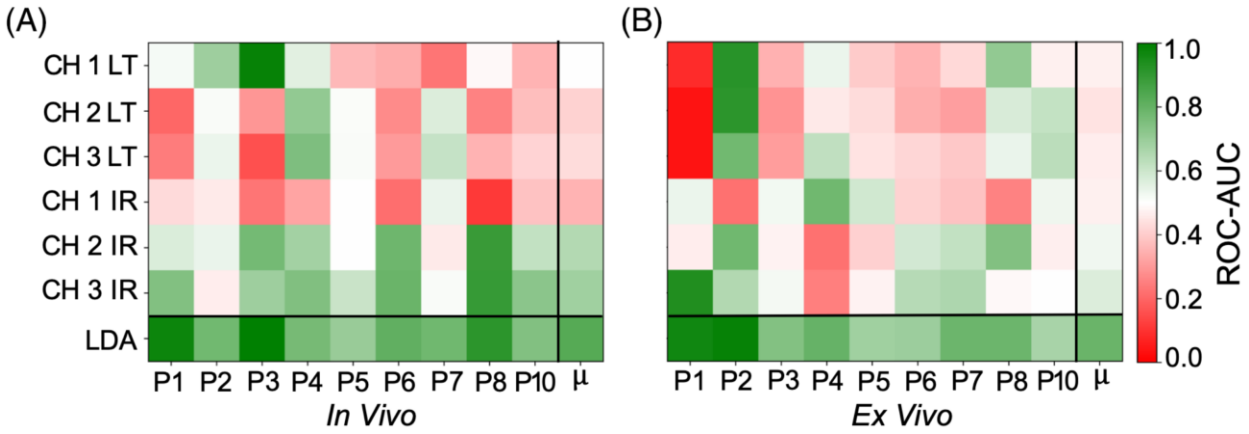

Figure 30: *In vivo* & *ex vivo* patient-level ROC-AUC performance. A comparison of patient-level ROC-AUC performance for (A) *in vivo* pre-resection scans and (B) *ex vivo* post-resection scans. μ corresponds to the mean performance for each parameter including the linear discriminant analysis (LDA) variable. For each scan type, use of the LDA variable resulted in superior AUC to the best performing signal parameter, with a 0.07 ± 0.03 mean increase observed for the in vivo pre-resection scans and a 0.06 ± 0.03 mean increase observed for the ex vivo scans. A single parameter AUC score greater than 0.70 was observed for 6/9 in vivo pre-resection scan, and 4/9 ex vivo scans. Reproduced with permission from Weyers et al. reference [168].

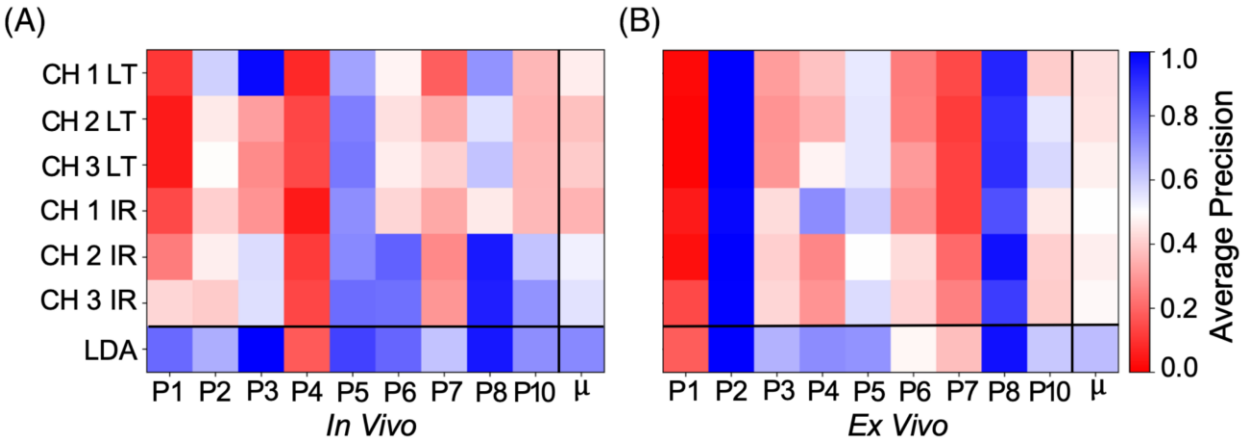

Figure 31: *In vivo* & *ex vivo* patient-level average precision. A comparison of patient-level average precision performance for (A) *in vivo* pre-resection scans and (B) *ex vivo* post resection scans. μ corresponds to the mean performance for each parameter including the linear discriminant analysis (LDA) variable. For each scan type, the use of the LDA variable resulted in superior AP to the best performing signal parameter, with a 0.08 ± 0.06 mean increase observed for the in vivo pre-resection scans and a 0.06 ± 0.03 mean increase observed for the ex vivo scans. A single parameter AP score greater than 0.70 was observed in 6/9 in vivo pre-resection scans and 3/9 ex vivo scans. Reproduced with permission from Weyers et al. reference [168].

5.4.4 Comparison of Healthy Epithelium in the Tonsil Region

Figure 32 illustrates the range of FLIm parameter values for all measurements of non-cauterized healthy epithelium taken in three distinct experimental contexts: *in vivo* pre-resection (n = 5,606 measurements), *ex vivo* post-resection (n = 7,252 measurements), and *in vivo* post-resection (peripheral to tumor bed) (n = 4,060 measurements). All measurements were performed for the tonsil region of the oral cavity (N=9). Data from any non-tonsil patient (i.e., Patient 9) is excluded from this analysis to restrict the focus to the same anatomy.

Due to the high number of measurements included in this analysis (n > 10,000), P values are not computed as these statistics are shown to always indicate significance as 'N' grows very large.[184] Alternatively, Cohen's d[185] effect size (ES) was computed to overcome this high sample size. Higher ES values are observed between healthy epithelium contexts for intensity ratio parameters compared to average lifetimes. Channel 3 has the smallest set of ES values between healthy epithelium contexts for both average lifetime and intensity ratio, indicating this channel's FLIm profile may be the most robust to these context changes. For average lifetime in channels 2 and 3, there is a small ES observed between pre-resection *in vivo* and post-resection peripheral tissue (*in vivo*), suggesting a consistent FLIm profile for these parameters before and after resection. For channel 1 average lifetime, a high ES is observed between healthy epithelium in all three imaging contexts, suggesting this parameter is less robust to these changes with respect to a healthy epithelium imaging context.

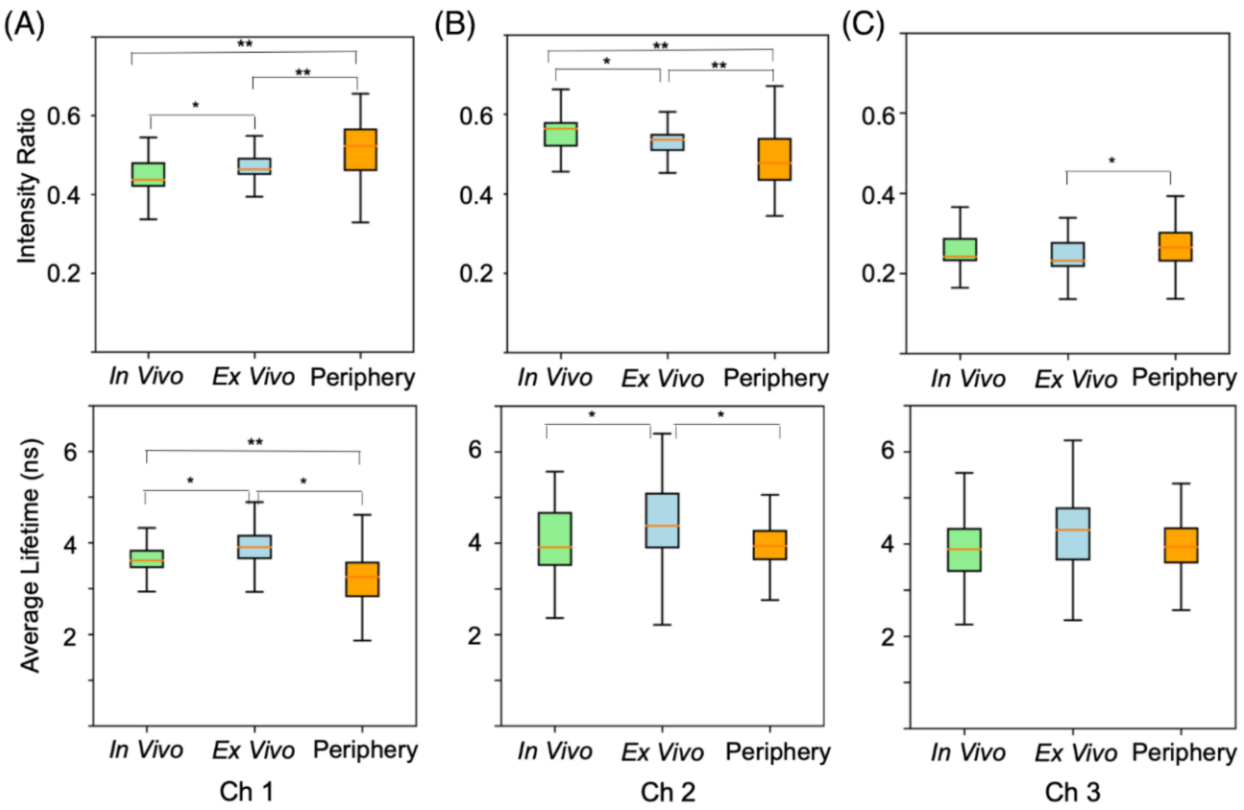

Figure 32: Comparison of univariate FLIm trends for healthy tissue by imaging context. Comparisons are made for all measurements of non-cauterized healthy epithelial tissue (tonsil regions, N=9 patients) acquired *in vivo* pre-resection (n = 5,606 measurements), *ex vivo* post-resection (n = 7,252 measurements), and *in vivo* post-resection (peripheral to tumor bed) (n = 4,060 measurements). Intensity ratios and average lifetimes for (A) CH1 fluorescence emission, (B) CH2 fluorescence emission, and (C) CH3 fluorescence emission. Cohen's d effect size (ES) is computed between imaging contexts. *ES > 0.5; **ES > 0.8. Reproduced with permission from Weyers et al. reference [168].

5.4.5 Comparison of Tumor Bed with Pre-resection Healthy Epithelium and Cancer

Average lifetime parameters observed in the tumor bed (n = 19,567) are compared with those observed pre-resection for both *in vivo* healthy epithelium (n = 6,151) and *in vivo* cancer (n = 3,760) across the entire 10-patient cohort. For channel 1 average lifetime an ES of 1.45 and 1.5 are observed respectively when comparing tumor bed with healthy epithelium and cancer, suggesting a consistent change for this parameter when compared to both tissues. Conversely, for average lifetime in channels 2 and 3, no ES value greater than 0.36 is observed when comparing tumor bed with healthy epithelium and cancer, suggesting a less prominent change for these channels.

5.5 | Discussion

The results collectively demonstrate FLIm-derived average lifetime and intensity ratio parameters can distinguish between benign oropharyngeal tissue and cancer. This work first investigated the use of FLIm to provide intrapatient contrast between healthy surface epithelium and cancer *in vivo* prior to resection, and *ex vivo* (*figures 28–30*). While the number of individual parameters able to resolve healthy tissue from tumor varies, for 9/9 *in vivo* pre-resection scans and 8/9 *ex vivo* scans, we show that at least one FLIm parameter shows statistically significant difference ($P < 0.001$) per patient between healthy epithelial tissue and cancer. The experimental context by which data was acquired (*in vivo* or *ex vivo*) and tissue heterogeneity appears to play a role in the number of parameters needed for discrimination. Overall, more parameters are needed for discrimination when more complex histopathological features were observed for a given patient.

This initial research highlighted that a weighted linear combination of all six FLIm parameters by LDA provides superior discrimination of tissue conditions in both scenarios. Intensity ratio parameters demonstrated superior discriminative power to average lifetimes, however average lifetime parameters did contribute to the performance of the LDA. The best FLIm-based diagnostic assessment was achieved *in vivo*. This first research objective identified a core challenge, which is that that reliable and consistent variables across patients need to be identified for robust diagnostic-decision-making. Due to the variability in reliable parameters for differentiating benign vs. cancer tissue, more advanced classification algorithms may benefit this work by identifying patterns in complex multivariate FLIm data which enable consistent cancer demarcation potential across patients.

Second, we evaluated the effect of electrocautery *in vivo* on FLIm properties (*figures 28 & 29*, bottom panel). Channel 1 lifetime within the electrocauterized surgical bed were significantly lower when compared to the values obtained for tumor measured *in vivo* pre-resection in the same patient. This trend was observed for all patients (CH1: ES of 1.45)

indicating that CH1 (associated with the fluorescence emission of matrix proteins) might be able provide a means of contrast if residual tumor is present. For CH2 and CH3, an ES of 0.15 and 0.29 was observed, indicating little effect. We also noted that the average lifetime values of healthy electrocauterized submucosa were also significantly lower relative to healthy epithelium (CH1: ES of 1.5).

Third, we investigated the effect of the surgical procedure and potential hemostasis on healthy epithelium (*figure 32*). The results indicate that FLIm parameters for healthy and cancer tissue changes with imaging context; this phenomena is expected due to the inherent sensitivity of endogenous fluorophores to their local microenvironment.[108] Biological tissue is under tremendous stress when it is surgically separated from the body,[186] particularly due to the loss of blood supply, temperature, and oxygenation changes following resection. Such conditions lead to a rapid shift (on the order of minutes)[187] of tissue metabolism towards anaerobic respiration,[188] and rapid cell death,[188] which will manifest with changes in tissue autofluorescence properties following excision. It has also been established that the molecular changes induced during and after tumor resection are heteromorphic (exhibiting unique differences among patients),[186,187] while also demonstrating dependence on the anatomical tissue resected.[186] The healthy tissue surrounding the periphery of a surgical resection bed also changes as a result of the procedure, where surgery introduces a cascade of biological responses due to injury.[189] In particular, surgery creates a hypermetabolic response, induces catabolic metabolism changes, creates local vasodilation, and initiates other inflammation-mediated biochemical changes.[189]

The results demonstrate that intensity ratios are more likely to vary with imaging context. With respect to average lifetime, channel 1 was most affected by the imaging context, whereas the lifetime parameters from CH2 and CH3 (associated with metabolic changes) were less affected. In particular, no major differences were observed for measurements performed *in vivo*

pre- and post-resection. However, changes were observed for surgically excised specimens. These findings suggest a potential recovery of metabolic features of the epithelial tissue at the periphery of the tumor bed, but as expected, irreversible changes take place in the excised tissue specimens.

Although CH3 intensity ratio overall enabled the best separation of cancer vs. healthy tissue for this dataset, it is important to note that lifetimes were still very informative in distinguishing healthy tissue from cancer and in some cases, offered the best tumor vs. healthy contrast on a patient-by patient basis. For example, for Patient 2, CH1 lifetime provided the strongest contrast between healthy tissue and cancer. When coupled with LDA, even if intensity ratio enabled the best data class separation, lifetimes bolstered the overall cancer vs. healthy tissue discrimination capacity for all patients.

In clinical practice, we envision that FLIm will leverage weighed combinations of all channels, using both intensity and lifetime data, to detect cancer. Having at least one channel which provides adequate tumor vs. healthy contrast is not required for cancer delineation; based on the results of this study, there is no single FLIm parameter that can distinguish healthy tissue from cancer in all contexts, therefore a multiparameter approach is required. For example, in *figure 30*, *in vivo* and *ex vivo* for Patient 7, there is no single metric from one channel that gives a significant difference, however after using weighted combinations of the FLIm metrics in an LDA, adequate tumor vs healthy contrast is achieved. This result again highlights the need for classification algorithms to identify patterns within complex multivariate FLIm data to identify consistent and reliable patters across patients for diagnostic decision-making.

This manuscript demonstrates that a set of FLIm parameters can always achieve contrast between healthy and tumor tissue for a 10-patient cohort. This is an important first step towards training a general classifier since discrimination is only possible if the FLIm method itself can provide adequate healthy vs. tumor contrast. Having used this work as a baseline to

demonstrate the feasibility of FLIm for intraoperative cancer detection, training a general classifier is the focus of our next work. In training a general classifier, our goal will be to incorporate a larger data population (after performing further clinical studies) which accounts for the diverse range of head and neck anatomic sites, cancer types, and inherent tissue differences across patients. Future work will also seek to evaluate how FLIm parameters are specifically affected by the presence of more granular features, such as the presence of ulceration, necrosis, low-grade and high-grade dysplasia.

5.6 | Conclusion

The results of this study suggest that Fluorescence Lifetime Imaging (FLIm) has the potential to be developed into a diagnostic tool for clinical cancer applications of the oropharynx. Once such a system is implemented and extensively validated, this technique can help to circumvent the issues posed by the lack of tactile feedback associated with robotic surgical platforms and assist in cancer delineation. For FLIm to be used as a universal transoral diagnostic standard, the biological complexity of cancer and the fundamental biochemical variability across patients need to be considered to develop a generalized combination of signal parameters which can be utilized for diagnostic decision-making. Machine learning methods will be investigated as means to produce such a generalized model and define the fluorescence decay signatures of specific conditions. We anticipate that continued rigorous research in this area will enable the generation of larger and more robust data sets to better elucidate the extent of interpatient variability and identify common autofluorescence properties which can be leveraged for pathology contrast.

CHAPTER 6 | Intraoperative Label-Free Fluorescence Lifetime Imaging for Real-Time Delineation of p16+ Oropharyngeal Carcinoma of Unknown Primary Origin: An 8-Patient Cohort Preliminary Investigation

This chapter evaluates whether label-free Fluorescence Lifetime Imaging (FLIm), coupled with standard diagnostic workups, could enhance primary lesion detection of the oropharynx in patients with p16+ head and neck squamous cell carcinoma of the unknown primary origin (HNSCCUP). Herein, FLIm was integrated with the da Vinci SP transoral robotic surgical platform (TORS) to acquire optical datapoints and display results. To our knowledge, this is one of the earliest studies to integrate a supplemental imaging approach with TORS to enhance occult primary tumor detection. One other group has made notable progress in this area using narrowband imaging (NBI) on an 8-patient HNSCCUP cohort.[190]

Over a 2-year period, FLIm data was acquired using TORS on 61 head & neck cancer patients presenting to *University of California, Davis Health*. Among these subjects, 55 patients comprised conventional primary tumors of the oropharynx, whereas the other 6 patients were classified with p16+ HNSCCUP after exhaustive preoperative diagnostic workup. HNSCCUP are uncommon tumors (~2,600 annual United States cases), therefore the potential for further HNSCCUP patient recruitment in this single-institution study was limited. A random forest machine learning classifier was trained on FLIm optical parameters derived from the larger independent 55-patient dataset and leveraged to investigate HNSCCUP discriminatory performance in the 6-patient cohort. Results were validated by histopathology.

Among the 6 HNSCCUP patients, p16+ occult primary was surgically identified in 3 patients, whereas 3 patients ultimately had no identifiable primary site in the oropharynx (i.e., no carcinoma beyond the cervical lymph nodes). FLIm correctly detected HNSCCUP in all 3 patients (ROC-AUC: 0.90 ± 0.06), and correctly predicted benign oropharyngeal tissue for the remaining 3 patients. The mean sensitivity was $95 \pm 3.5\%$, and specificity $89 \pm 12.7\%$.

The preliminary results demonstrate the potential for FLIm to facilitate intraoperative delineation of mucosa-presenting p16+ HNSCCUP. Ultimately, these initial results suggest the potential for FLIm to reduce surgical procedure times, preserve functional healthy tissue, and enable enhanced intraoperative decision-making for the benefit of the patient.

6.2 | Abstract

Background: This study evaluated whether Fluorescence Lifetime Imaging (FLIm), coupled with standard diagnostic workups, could enhance primary lesion detection in patients with p16+ head and neck squamous cell carcinoma of the unknown primary (HNSCCUP).

Methods: FLIm was integrated into transoral robotic surgery to acquire optical data on 6 HNSCCUP patients' oropharyngeal tissues. An additional 55-patient FLIm dataset, comprising conventional primary tumors, trained a machine learning classifier; the output predicted the presence and location of HNSCCUP for the 6 patients. Validation was performed using histopathology.

Results: Among the 6 HNSCCUP patients, p16+ occult primary was surgically identified in 3 patients, whereas 3 patients ultimately had no identifiable primary site in the oropharynx. FLIm correctly detected HNSCCUP in all 3 patients (ROC-AUC: 0.90 ± 0.06), and correctly predicted benign oropharyngeal tissue for the remaining 3 patients. The mean sensitivity was 95 ± 3.5%, and specificity 89 ± 12.7%.

Conclusions: FLIm may be a useful diagnostic adjunct for detecting HNSCCUP.

6.3 | Introduction

Head and neck squamous cell carcinoma of unknown primary origin (HNSCCUP), also known as occult primary, is defined as the occurrence of squamous cell carcinoma in cervical lymph nodes with no primary site identified.[191] These cases (~2,600 annually in the United States) represent approximately 3-5% of all new cases of head and neck squamous cell carcinoma, and are considered unknown after exhaustive clinical, radiographic, and surgical evaluation.[192–196] HNSCCUP is disproportionately correlated to positive human papillomavirus

(HPV) status and exhibits weaker association to tobacco and alcohol abuse.[197,198] Statistically, most HPV+ HNSCCUP patients are male, White, non-smokers, and non-drinkers.[194,199] HPV-mediated tumors aberrantly overexpress p16 biomarkers, thus p16 immunohistochemistry is recommended for determining HNSCCUP etiology.[23]

It is critically important to locate the primary site in these patients to reduce treatment-related morbidity via more anatomically-focused interventions.[197,200] Most HNSCCUP cancers are eventually located in the cryptic lymphoepithelium of the palatine tonsils and the lingual tonsils of the base of tongue.[194,195,198] Traditional surgical assessments of these cases included bilateral tonsillectomy and base of tongue biopsies in efforts to locate the primary tumor.[198,201] Recent publications in the HPV era, have suggested the appropriateness of only performing an ipsilateral tonsillectomy in the workup of these patients.[202] The adoption of transoral robotic surgical platforms (TORS) is increasingly being utilized in the workup of HNSCCUP and has facilitated improved HNSCCUP detection rates[194,203–205]; however, depending on the diagnostic and clinical capabilities of different medical institutions, more than 50% of primary tumors may remain undiscovered for patients with HNSCCUP.[201] To improve intraoperative decision-making and enhance the detection of these elusive tumors, new diagnostic technologies compatible with TORS are needed.

While FLIm has not been specifically developed as a tool for identifying unknown primary tumors, the recent success of this technology for demarcating conventional primary oropharyngeal tumors[2,168,169] has motivated the present investigation of discriminatory performance in HNSCCUP patients. Specifically, we investigated whether the addition of FLIm to standard diagnostic workups could enhance the detection of primary lesions within p16+ HNSCCUP patients. To our knowledge, this is one of the earliest studies to integrate a supplemental imaging approach with TORS to enhance occult primary tumor detection. One

other group has made notable progress in this area using narrowband imaging (NBI) on an 8-patient HNSCCUP cohort.[190]

This study aimed to conduct intraoperative FLIm measurements on patients with TORS-facilitated extirpation of HNSCCUP to identify the presence of occult primary tumors not identified by standard-of-care workup. FLIm was integrated into the da Vinci SP and deployed for acquiring measurements on oropharyngeal tissues with a high propensity for harboring the primary tumor (i.e., palatine and lingual tonsils).[194,195,198] We sought to test the hypothesis that intraoperatively acquired FLIm measurements output from a machine learning classifier can successfully detect p16+ occult primaries presenting in the mucosa (<250 μm from tissue surface) and differentiate such malignancies from healthy tissue.

6.4 | Materials and Methods

This study comprises an N=61 patient dataset evaluating FLIm for diagnosis and surgical guidance of oral cavity and oropharyngeal cancers. Of the 61-patients, 55 comprised conventional primary tumors of the oropharynx, whereas the other 6 patients were classified with p16+ HNSCCUP after exhaustive diagnostic workup. Procedures were approved by the *University of California, Davis Institutional Review Board* (IRB ID#800853) and conducted in accordance with the *Code of Ethics of the World Medical Association* for experiments involving humans.

6.4.1 Study Design and Inclusion/Exclusion Criteria of Patients

Eligible patients presenting to *UC Davis Otolaryngology – Head & Neck Surgery* department were recruited in the study over a 2-year period from May 2019 – April 2021 without demographic or prognostic consideration. Patients with a preoperative diagnosis of HNSCCUP were eligible for this study. Patients were classified as presenting with HNSCCUP after an exhaustive clinical, radiographic, and surgical evaluation did not identify the primary tumor site;

this includes negative PET and CT findings, absence of tactile cues when palpating tissue, lack of visual identification by endoscopy, and negative directed biopsies at suspicious areas.

Exclusion criteria consisted of: (1) pediatric patients based on IRB considerations, (2) patients with HIV+ status from a safety standpoint for research personnel, (3) individuals with previous major head & neck surgery where extensive scarring may be present, and (4) patients with known use of orally administered crack-cocaine or methamphetamine (MA), which imparts severe adverse effects on oral tissues and confounds FLIm measurements.[206] HNSCCUP patients with p16- cancer were not assessed within the scope of this manuscript (as HPV-negative disease represents a different entity).

One prospective p16+ HNSCCUP patient resided within the study's exclusion criteria, and therefore was not analyzed (see discussion) due to their known recurring use of orally administered methamphetamine (MA). In total, N=6 p16+ HNSCCUP patients met the inclusion criteria for the study and provided their informed consent to participate in this research.

6.4.2 Instrumentation & Data Collection

Figure 5 of *section 1.3* illustrates the custom-built, fiber-based, point-scanning FLIm system with corresponding integration into the da Vinci SP surgical system. In-depth characterizations of this instrument and specifications are detailed in the previous section. The optical fiber's distal end features a 3D printed stainless steel grasper, which is held and maneuvered by the da Vinci SP robotic system's instruments (*figure 5*).

As this technology is a point-scanning technique, the field-of-view can be as large as the entire visualized surgical area (multiple centimeter scale) from the da Vinci SP. When scanning directly adjacent to tissue, the spatial resolution of the device is determined by the fiber core size (365 μm) and the probe-to-tissue distance, yielding a resolution between 0.6 ± 0.2 mm depending on the distance of the probe to the tissue surface. The peritumoral region has many morphologic and phenotypic distinctions from non-tumor-bearing healthy tissue, including altered pH levels, metabolic characteristics, and oxygenation gradients, extending up to 1 cm from the margins of tumor tissue.[207] Correspondingly, although the penetration depth of the UV laser is approximately 250 μm, the secondary tissue effects from neoplasms extend multiple millimeters beyond the cancer site, potentially allowing FLIm to detect cancers beyond the absolute penetration depth of the UV laser; this has yet to be formally evaluated.

6.4.3 Data Collection

FLIm scanning was conducted after patients were anesthetized, intubated, and prepared for TORS. Intraoperative biopsies were conducted after FLIm scanning to mitigate any potential confounding effect on the data. The da Vinci SP was introduced into the patient's oral cavity and the sterile optical fiber's distal end was grasped and actuated by the robot's Maryland graspers (*figure 5*). In vivo scans of approximately 90 seconds in duration were conducted bilaterally over palatine tonsils and the base of tongue regions to generate spectroscopic data overlaid over white light images. An example of this spectroscopic data overlay on a patient's tongue tissue (used in the classifier training dataset) is illustrated in *figure 17* (*section 3.3*). The fiber optic probe was then removed from the patient, and the surgeon proceeded with *en bloc* excision of tissues suspected of occult primary. This typically included a bilateral tonsillectomy followed by biopsies and/or lingual tonsillectomy depending on the surgeon's discretion. Excised specimens were sectioned in a pathology grossing room to generate multiple sequential H&E slides for

pathologic interpretation; these slides included a combination of both frozen and permanent sections. HPV status was assessed by using p16 immunohistochemistry.

6.4.4 Calculations and Analysis of Data

Average lifetime estimation for each spectral band was performed using constrained least square deconvolution with Laguerre expansion. This fast and robust technique has been detailed extensively.[153] Briefly, the pulsed UV laser repetition rate of 120 Hz determines the FLIm measurement speed. The FLIm waveforms which originate from each spectral measurement are averaged four times before further processing, leading to 30 averaged spectroscopic datapoints acquired each second. For each of the four spectral bands of the instrument, the average lifetime value, spectral intensity, and 12 fitting coefficients of the Laguerre expansion are computed (*figure 17 - section 3.3*). Spectral properties of the fluorescence emission are also estimated by computing the relative intensity of each spectral channel of the instrument. This leads to a total of 56 parameters (4 time-resolved average lifetimes, 4 spectral intensity ratios, and 48 expansion metrics).

A random forest machine learning classifier estimated the probability of healthy vs. cancer for each point-measurement.[170] This classifier was trained on the larger 55-patient cohort of known primary oropharyngeal tumors (38 palatine tonsil and 17 base of tongue patients) and then applied to make predictions on the measurements obtained from HNSCCUP patients. Sensitivity and specificity were calculated by standard convention. ROC-AUC quantified the true positive rate vs. false positive rate of individual spectroscopic point-measurements based on histological findings. This approach builds up on the development of predictors previously described elsewhere (*figure 19 – section 3.3*).[169] The unit of analysis for statistical evaluation consists of binary predictors (i.e., cancer vs. healthy) output from machine learning classification for individual spectroscopic datapoints acquired over a surgical region of interest. This type of analysis is distinct from region/lesion-based assessment, where multiple measurements are

combined to predict the nature of a preidentified region. This approach typically leads to better sensitivity and specificity numbers, however, requires *a priori* knowledge of the extent of the lesions.

6.4.5 Coregistration and Histopathological Validation of Data

Registration of data to histopathology is detailed in our prior work, and in *chapter 4* .[168] In brief, a pathologist (DG) digitally annotated H&E slides using *Aperio (Leica) Imagescope* viewing software. Features within 250 μm of the tissue's mucosal surface were annotated, corresponding approximately to the maximum penetration depth of the laser. The following annotation labels were used: (1) carcinoma, (2) lymphoid tissue, and (3) benign tissue. Label 1 was treated as the positive class (i.e., cancer) and labels 2 & 3 were treated as the negative class (i.e., benign) from an analysis standpoint. Histopathology sections were overlaid onto a high-resolution image of the excised specimen, accounting for compression and expansion registration artifacts between histology and the excised specimen. An in vivo recording of the surgical excision process was used to facilitate registration of the excised specimen to the original in vivo environment. This histopathological data was then overlaid onto a reference image in vivo. To account for motion between the TORS surgical camera and the evaluated tissue, a novel motion compensation algorithm was applied.[166] Quantification of performance was based only on regions with coregistered histopathology.

6.5 | Results

Table 6 depicts all patient demographics, pertinent clinical characteristics, and surgical outcomes of the enrolled patient population. An average of 2,355 FLIm spectroscopic datapoints (ranging between 1,393 and 4,793) were acquired from each of the 6 patients. 3 patients (Patients 1-3) presented with HNSCCUP (all p16+) within the regions where FLIm scans were performed. Patient 6 did have p16+ HNSCCUP near the FLIm scan area, however the region of cancer was outside the area of the research scan, thus only FLIm data for benign tissue was acquired. All other patients enrolled in the study presented with HNSCCUP, however no

oropharyngeal primary was identified with TORS. Each patient had multiple tissues excised where some of these tissues contained the occult primary and others were benign, as presented in *table 6*. Patients 4-6 only had benign tissue imaged in the FLIm scan area, thus only specificity is calculated for these patients due to the absence of the positive data class (i.e., cancer). Only tissue areas validated with histopathology were used to calculate ROC-AUC, sensitivity, and specificity.

Table 7 presents ROC-AUC, sensitivity, and specificity calculations for each patient. FLIm correctly detected the presence of the occult primary in all 3 patients (Patients 1-3), yielding a mean ROC-AUC score of 0.90 ± 0.06. The extent of the cancer (quantified by sensitivity) was detected with a mean of $95 \pm 3.5\%$. The method however demonstrated mixed specificity results for these patients. Patients 4-6 comprised data from benign tissues only, where the FLIm classifier correctly demarcated the entire extent of all tissues as benign and output a mean specificity of $99 \pm 1\%$. All 6 patients together, which includes the 3 patients with p16+ SCC within the FLIm scan area and the 3 patients with only benign tissue evaluated, resulted in a classification specificity of $89 \pm 12.7\%$.

Table 6. Demographics, Clinical Characteristics, and Surgical Outcomes of the Study Population.

		Patient 1	Patient 2	Patient 3	Patient 4	Patient 5	Patient 6
Demo-graphics	**Gender**	Male	Male	Male	Male	Male	Male
	Age at Surgery	63	74	59	62	77	69
	Race	White	White	White	White	White	White
	Ethnicity	Not Hispanic	Not Hispanic	Not Hispanic	Not Hispanic	Not Hispanic	Not Hispanic
Pertinent Clinical Characte	**Alcohol Use**	2 DPD	3 DPD	Infrequent	Infrequent	1 DPD	3 DPD
	Tobacco Use	Never Smoker	0.25 PPD (Quit 2011)	Never Smoker	Never Smoker	0.5 PPD (Current)	0.5 PPD (Quit 2014)
	Illicit Drug Use	No	No	No	No	No	Cannabis (Daily)
Surgical Outcomes	**Post-Operative Occult Primary Diagnosis**	p16+ SCC	p16+ SCC	p16+ SCC	p16+ SCC	p16+ SCC	p16+ SCC
	Occult Primary Tissue Imaged in Area of FLIm Scan Region? [a]	Yes *R*-PT	Yes *L*-BOT	Yes *R*-BOT	No	No	No
	Occult Primary Tissue Ultimately Found in Oropharynx? [a]	Yes *R*-PT	Yes *L*-BOT	Yes *R*-BOT	No	No	Yes Superior *R*-PT
	Other Benign Excised Tissues [a]	*L*-PT *R*-BOT *R*-GTS	*R*-BOT *L*-BOT	*L*-PT	*L*-PT *L*-BOT *L*-GTS	*R*-BOT *R*-GTS	*L*-PT *R*-BOT *R*-GTS

Abbreviations: *DPD* = Drinks Per Day, *PPD* = Cigarette Packs Per Day, *MA*= Methamphetamine, *SCC* = Squamous Cell Carcinoma, *p16+ SCC*= HPV Positive & HPV Mediated Squamous Cell Carcinoma, BOT = Base of Tongue, *PT*= Palatine Tonsil, *GTS*= Glossotonsillar Sulcus.
[a] "R" and "L" designate "Right" or "Left" respectively with anatomy (e.g., R-PT refers to Right Palatine Tonsil).

Table 7. FLIm Performance on Occult Primary Cancer: ROC-AUC, Sensitivity, and Specificity.

		ROC-AUC	Sensitivity	Specificity
p16+ SCC Within FLIm Scan Area	Patient 1	0.97	92%	87%
	Patient 2	0.90	96%	81%
	Patient 3	0.82	99%	68%
No Carcinoma Within FLIm Scan Area	Patient 4	-	-	100%
	Patient 5	-	-	98%
	Patient 6	-	-	99%
	Mean	**0.90±0.06**	**96±3.5%**	**89±12.7%**

Abbreviations: p16+ SCC = HPV-Positive Squamous Cell Carcinoma

Figure 33 presents case studies for all 3 patients with p16+ HNSCCUP imaged by FLIm. Each patient case study displays both the binary probability of cancer for each acquired spectral point-measurement and the patient's corresponding registered histopathology *in vivo*.

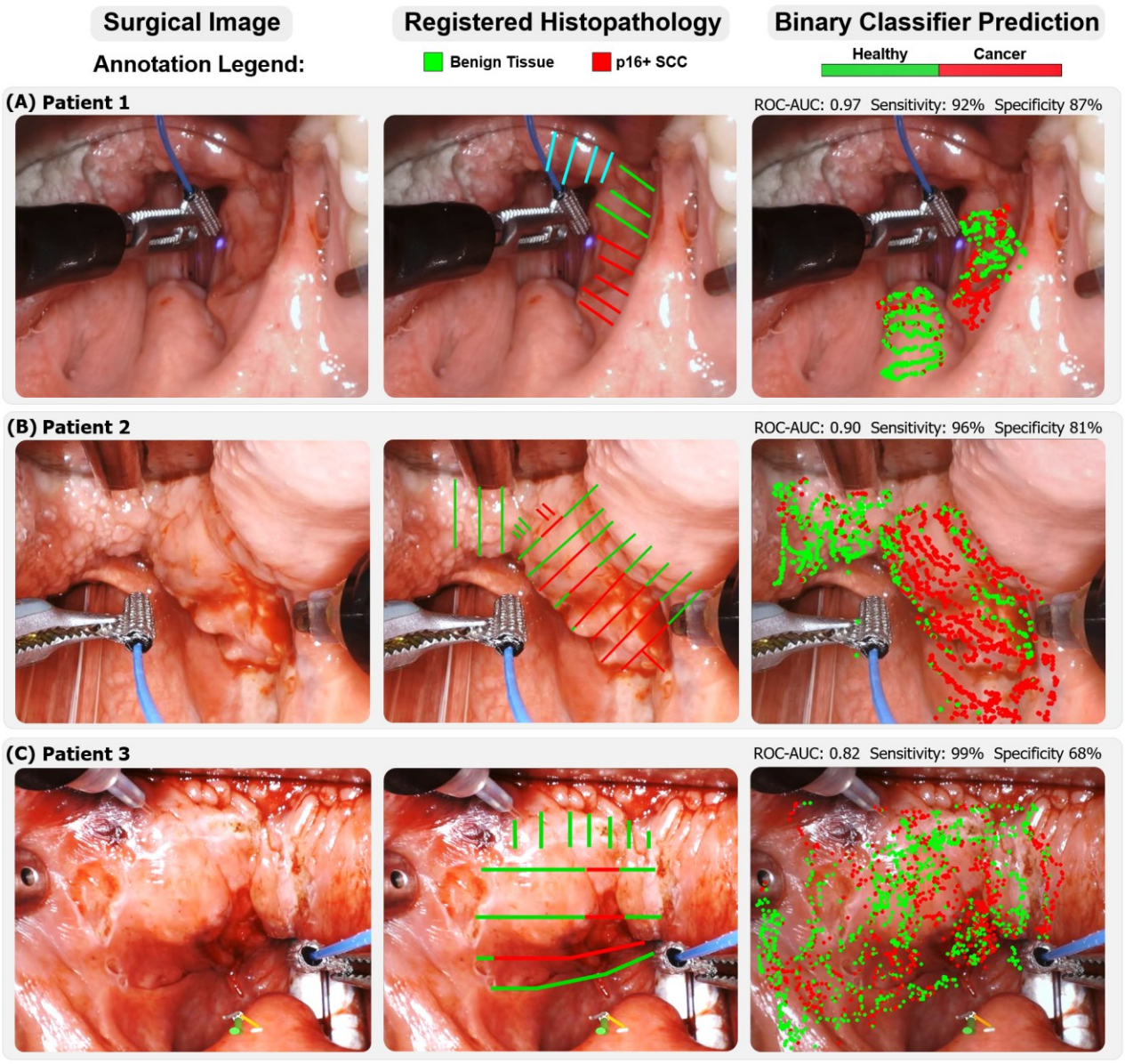

Figure 33: Patients with p16+ SCC within the imaged FLIm area. Each patient case study displays three tiles: (1) the original photograph of the surgical white light image, (2) the histopathology of the excised specimen registered in vivo, and (3) an overlay of the binary probability of cancer for each acquired spectral point-measurement. (A) Patient 1 with p16+ SCC of the right palatine tonsil. (B) Patient 2 with p16+ SCC of the left base of tongue. (C) Patient 3 with p16+ SCC of right base of tongue.

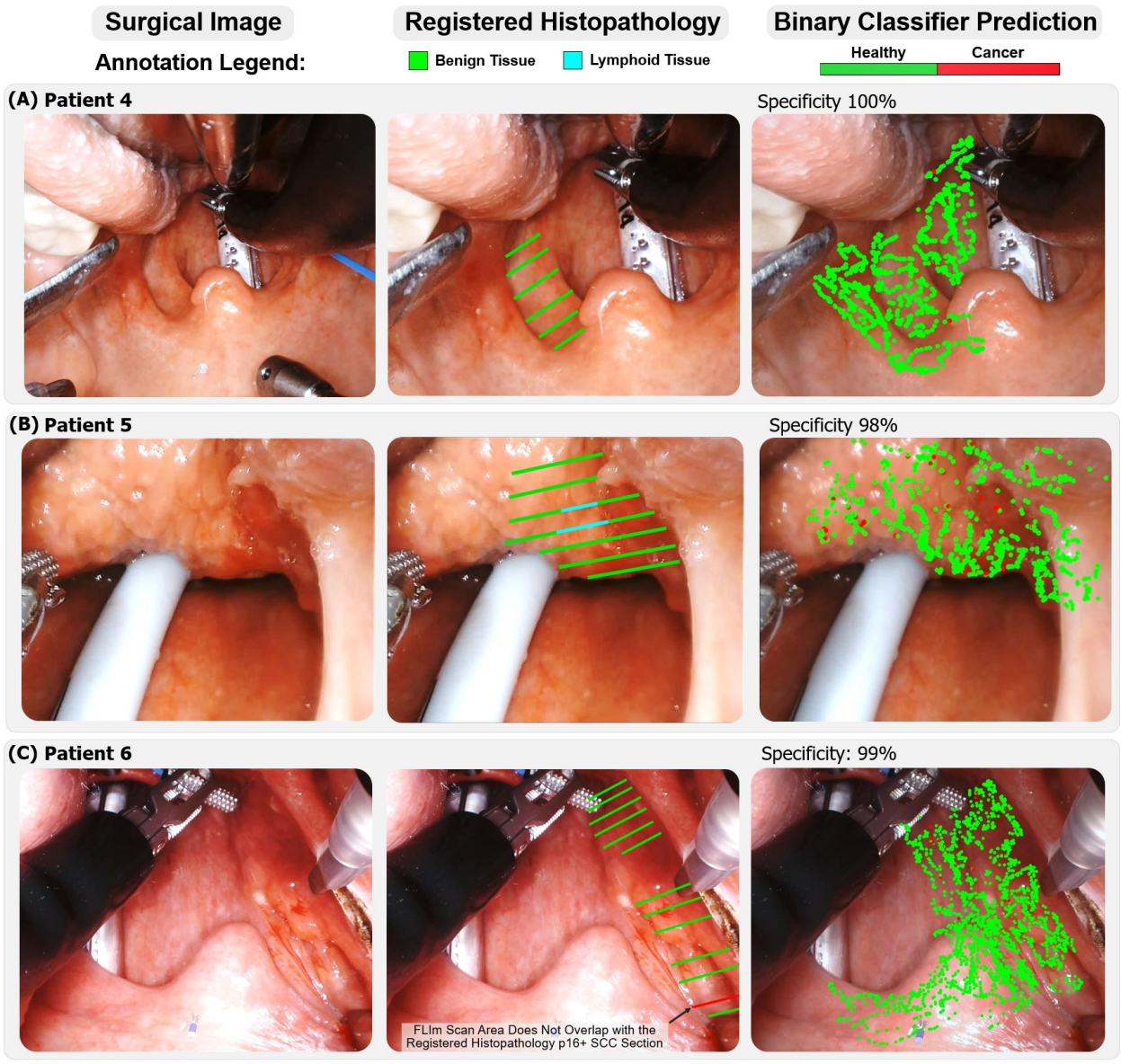

Figure 34: Patients with benign tissue only within the imaged FLIm area. Each patient case study displays three tiles: (1) the original photograph of the surgical white light image, (2) the histopathology of the excised specimen registered in vivo, and (3) an overlay of the binary probability of cancer for each acquired spectral point-measurement. (A) FLIm scan for Patient 4 of a benign left palatine tonsil. (B) FLIm scan for Patient 5 of a benign right base of tongue tissue. (C) Patient 6 case study illustrative of a challenging scenario where the FLIm scan area does not overlap with the area of cancer. For this patient with cancer of the right palatine tonsil, all benign tissue areas are correctly marked as healthy with 99% sensitivity, however the FLIm scan was not performed on the small area of the palatine tonsil where the occult primary p16+ SCC occurred. This case is illustrative of the importance of fully scanning an entire surgical region of interest with the FLIm technique to avoid missing a potential occult primary area.

Figure 34 presents case studies for all 3 patients who did not have cancer imaged within the FLIm scan area (i.e., only benign tissue evaluated). Like *figure 33*, this figure displays the

binary probability of cancer classifier output and the patient's corresponding registered histopathology *in vivo*.

6.6 | Discussion

Collectively, the results demonstrate FLIm's clinical value in the surgical management of p16+ HNSCCUP in two key areas: (1) differentiation between oropharyngeal tissues that are benign versus those involved with p16+ SCC, and (2) demarcation of the extent of cancer.

The ability to correctly identify benign tissues uninvolved with HNSCCUP was demonstrated with the 3-patient cohort who had only benign tissues imaged in the FLIm scan region. Among these patients, the FLIm classifier yielded exceptionally high specificities, averaging 99 ± 1% and correctly delineated the entire scanned regions of these tissues as benign. Ultimately, these patients each had multiple benign tissues of their oropharynx excised, which comprised palatine tonsils, base of tongue tissues, and glossotonsillar sulcus regions (*table 6*). Due to the increased intraoperative procedure times, costs, pain, and functional implications from resection of patient's healthy tissue, there is strong motivation to prevent the unnecessary excision of benign tissues.

FLIm's ability to identify oropharyngeal tissues harboring HNSCCUP, as well as demarcate associated cancer margins, was demonstrated for the 3-patient cohort presenting with p16+ HNSCCUP tissue within the FLIm scan region. For these patients, HNSCCUP was successfully detected using the FLIm classifier method. The best classifier results were observed for Patient 1, where healthy tissue and cancer were comprehensively differentiated. The classifier for Patient 2 performed well overall and fully demarcated the extent of the tumor. Cancer was successfully detected for Patient 3 presenting with p16+ HNSCCUP of the right base of tongue, however there was a low specificity (68%). Close inspection of *figure 33C* reveals that the borders of the specimen were pre-marked with the da Vinci SP monopolar electrocautery tool prior to FLIm scanning, which is typically performed after the FLIm scan. In

our previous work, we found that our FLIm signal is disrupted and altered by electrocautery, where effects on the FLIm signal extend many millimeters beyond the electrocautery site.[131] *Figure 33C* illustrates that many of the false positives occur around the cautery outline, thus offering a potential explanation for the low specificity. We hypothesize that FLIm could potentially differentiate between cancer and healthy tissue with accuracy on electrocauterized surfaces, however this has yet to be tested, and electrocauterized data was not included in the classifier training model.

6.6.1 Exclusion Criteria Remarks

One HNSCCUP patient was not analyzed due to their medical history which designated this patient in the study's exclusion criteria. This patient routinely orally self-administered MA, which like crack-cocaine, is associated with severe oral health complications.[206] In brief, MA itself is acidic and when smoked or inhaled, has been linked to direct corrosive effects on oral tissues.[208,209] It has been found that MA is linked to increased expression of proinflammatory factors,[210] cellular senescence,[210] reduced oral tissue wound healing,[211] and reduced saliva pH and buffering capacity.[212] Additionally, in murine models, MA has been found to facilitate host-mediated collagen degradation by increased expression and production of matrix metalloproteinases (MMPs).[211] Collectively, the effects of MA on oral cavity tissues demonstrates conserved properties to many cancer hallmarks,[114] therefore motivating this patient's exclusion from analysis due to confounding effects on the data. It is conceivable that with a large enough training dataset of MA patients, FLIm can differentiate benign MA-affected tissue from cancer, however this has yet to be tested.

Unlike the effect of MA, patient tobacco and ethanol (EtOH) use has not demonstrated apparent challenges in distinguishing benign tissue from cancer in our prior work.[168,169] One potential explanation for the classifier's resilience to this medical history may stem from the

magnitude of patient data available (i.e., varied patient tobacco and EtOH use habits) to train the classifier's algorithm in predicting cancer probability.

6.6.2 Study Limitations & Collective Dataset Remarks

Although the results obtained from this study are promising, the N=6 HNSCCUP patient sample size is a key limitation; however, it should be emphasized that the rare nature of HNSCCUP makes the potential for patient recruitment in this single institution study limited. Like most high-volume head and neck cancer centers, we were stringent in our definition of HNSCCUP and only assigned patients to this designation after comprehensive preoperative workup were performed, including visual and endoscopic inspection, palpation, and comprehensive imaging. While validation was performed on 6 HNSCCUP patients, it is emphasized that training data in the classifier was developed using the larger 55-patient conventional SCC dataset, enabling the extrapolation of classification results on pilot study cohorts reliable. Along these lines, future investigation for the diagnostic utility of FLIm as a diagnostic adjunct for HNSCC should place emphasis on multi-institutional studies to obtain larger sample sizes.

A limitation of FLIm is demonstrated in patient 6, where cancer only presented in a subtle area of the superior right palatine tonsil and resided outside of the FLIm scan. This case study is illustrative of the importance of thoroughly scanning the entire region of interest to assess the presence of tumor.

TORS has been incorporated as a successful strategy to detect unknown primary carcinoma of the oropharynx.[194,203–205] Several authors have demonstrated detection rates averaging as high as 80%.[213–215] While our study had a pathologic detection rate lower than those studies (50%), our practice is to aggressively look for the primary site with physical examination, imaging, and only consider the diagnosis of unknown primary if there is no suspicion of location based on preoperative and intraoperative findings. This difference in

approach, and the size of our data sample, might explain the detection success discrepancy between our institution and the literature.

Collectively, these results, although preliminary, are promising for the potential identification of cancer of the unknown primary. These findings demonstrate potential to enhance surgical decision-making by aiding a surgeon in identifying candidate tissues of the oropharynx involved with carcinoma and in establishing the extent of cancer. If this potential to detect subtle mucosal-presenting carcinomas is confirmed in larger studies, FLIm could have dramatic impacts on radiation field reduction, or even the elimination of radiation therapy, in patients adequately treated with surgery alone. Along these lines, potential for FLIm to potentially guide initial biopsies and margins, which can reduce morbidity of unnecessary tonsillectomies/biopsies on oropharyngeal tissues that do not harbor malignancy.

6.7 | Conclusion

FLIm, in combination with the conventional diagnostic workup for HNSCCUP, may be a useful adjunctive modality for detecting primary tumors. This preliminary investigation demonstrated that FLIm, integrated with TORS, may aid a surgeon in rapidly and non-invasively screening patients for mucosa-presenting (<250 μm from tissue surface) p16+ HNSCCUP. The results suggest that FLIm can correctly demarcate entire benign tissues of the oropharynx and thus indicate to a surgeon that tissues suspected of occult primary are uninvolved with carcinoma. For all patients presenting with p16+ HNSCCUP in the FLIm scan region, the method correctly identified the presence and location of the occult primary with overall strong performance, in addition to accurately identifying uninvolved healthy functional tissue. Ultimately, these results demonstrate potential to reduce surgical procedure times, preserve functional healthy tissue, and enable enhanced intraoperative decision-making for the benefit of the patient.

CHAPTER 7 | 100-Patient Dataset Evaluation: Collective LDA Classification, Effect of Biological Variables, Patient Demographics, and Surgical Characteristics, and Preliminary Analysis of *In Vivo* Positive Surgical Margins

This final chapter is dedicated to drawing conclusions on the 100-patient dataset acquired over the five-year period from 2017 – 2021. The major findings based on linear discriminant analysis and univariate analysis are presented. *Chapter 8.1* details the composition of the 100-patient oral cavity and oropharyngeal cancer database. *Chapter 8.2* presents the collective FLIm-based patient-level performance evaluation through LDA resubstitution validation. *Chapter 8.3* investigates the influence of local anesthetic use, patient demographics, and biological variables on FLIm data; this includes: (1) evaluating the effect of lidocaine and epinephrine injection on patient oral tongue and tonsil data *in vivo*, (2) demonstrating the effect of patient age on FLIm data, and (3) assessing the impact of deeply embedded tumor (>0.5 mm from epithelium), lymphoid tissue, and high-grade dysplasia on FLIm data. *Chapter 8.4* investigates overall univariate data trends and uses Pearson's Chi Square analysis to investigate correlations between FLIm data and anatomic, patient, and tumor characteristics. Lastly, *chapter 8.5* demonstrates two *in vivo* case studies demonstrating the use of FLIm time-resolved features to identify positive surgical margins in a patient's electrocauterized surgical cavity.

7.1 | Composition of the 100-Patient Oral Cavity and Oropharyngeal Cancer Database

Figure 35 visually presents the 100-patient H&N database composition in a tree diagram format. One hundred patients of age 18+ were recruited and participated in the FLIm research study upon obtaining their informed consent. Of the 100 patients consented, 92 patients were satisfactory for data analysis. Eight patients were not analyzed due to complications in data collection, such as hardware issues (e.g., laser misalignment, video signal loss, poor signal-to-noise-ratio) or insufficient datapoint samples to approximate a standard normal distribution.

For the 92 patients analyzed, data was obtained from N=34 patients undergoing palatine tonsil resection, N=16 base of tongue, N=27 oral tongue, and N=15 patients with cancer distributed elsewhere within either the oral cavity or oropharynx. For the purposes of classifying non-smoking vs. smoking patients, the *U.S. Centers for Disease Control* defines a non-smoker as a patients who has smoked less than 100 cigarettes per lifetime.[216] Accordingly, this designation was used in the classification of patient tobacco status using reported patent medical history records. Within this analyzed dataset, 35 patients were classified as non-smoking patients, and 57 patients were classified as smokers. Seventy-two patients were male, and 20 patients were female.

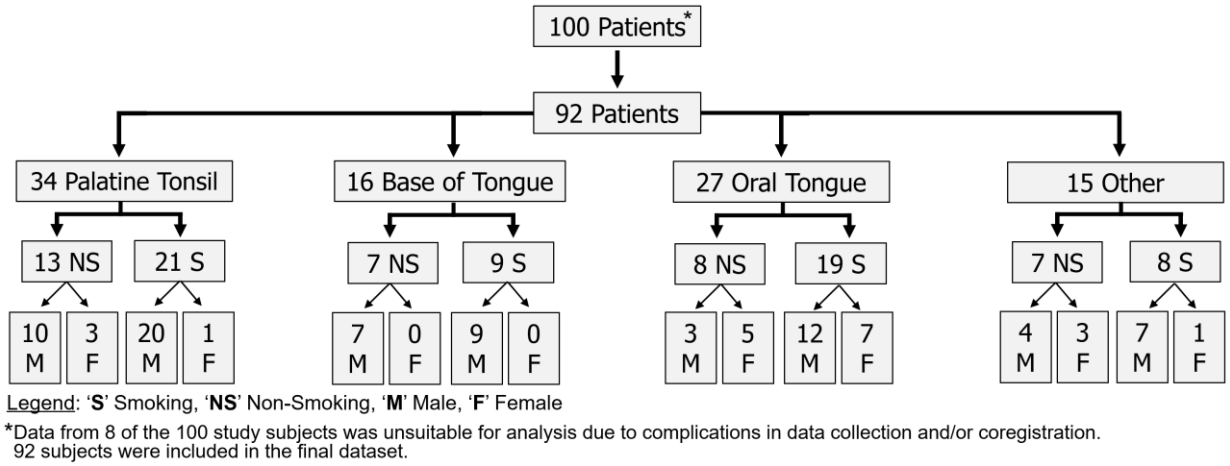

Figure 35: Tree diagram illustrating the composition of the 100-patient H&N dataset.

Appendix tables A9-A12 enumerate the patient-specific demographic details, clinical characteristics, and surgical outcomes for the tonsil, base of tongue, 'other anatomy', and oral tongue patients, respectively. Patient ID is listed to the right of the anatomical designation in parentheses. HPV status indicates the status of the patient's surgically excised tissue(s) when tested for HPV using a p16 antibody probe.

Based on the final interpretation of tissue pathology provided by patients' surgical grossing laboratory reports, six numeric classes of cancer were established to designate the level of cancer malignancy according to the following pathologist descriptors of final pathology

status: (1) benign tissue or low-grade dysplasia [malignancy N/A], (2) polymorphous adenocarcinoma or condyloma [lowest malignancy], (3) squamous cell carcinoma (SCC) *in situ* and non-invasive SCC [low malignancy], (4) verrucous SCC [medium malignancy], (5) SCC and invasive SCC [high malignancy], and (6) basaloid SCC [very high malignancy].

Figure 36 reports a summary of how the patient dataset was distributed in terms of anatomy, p16 status, and cancer malignancy. The results demonstrate that squamous cell carcinoma comprised most of the database (N=73, 79.3%). As expected of tumors of the oropharynx (tonsil & base of tongue), N=33 of N=38 (86.8%) of the tumors were associated with positive p16 status, whereas all tumors of the oral cavity were HPV negative (except for a single patient that had composite oropharyngeal tissue resected during a total glossectomy procedure).

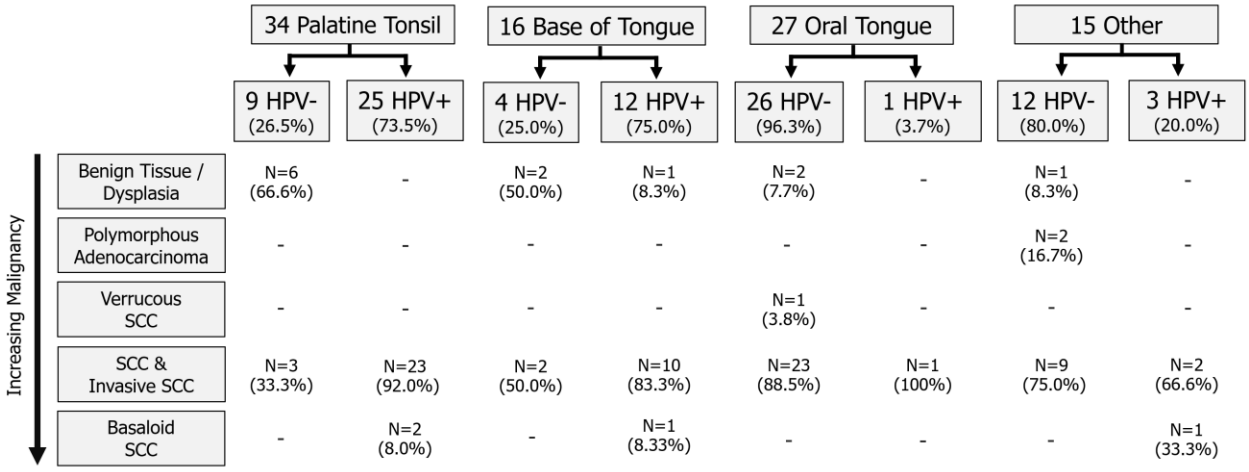

Figure 36: Composition of the 92-patient dataset based on cancer malignancy and p16 status. Results were bifurcated based on patient anatomy, HPV (p16) diagnosis, and pathologist-indicated cancer designation.

7.2 | Collective Database Linear Discriminant Analysis (LDA)

LDA is used as a tool for classification, dimensionality reduction, and data visualization. Within the scope of this H&N FLIm investigation, LDA provides robust class separability between benign and cancer data by drawing an optimized decision region between the two data classes. This analysis seeks to maximize the variance between healthy tissue and cancer, while

minimizing within-class variance. LDA is a powerful analytical tool since the optimization of the decision region, which separates the healthy and cancer data classes, provides quantitation of the extent of overlap between the two data classes. For this analysis, once a linear boundary is established which maximizes the separation of the two data classes, receiver-operator-characteristic area-under-the-curve (ROC-AUC) classification performance can then be evaluated as a function of the true positive rate (TPR) vs. false positive rate (FPR) of the data, expressed by *equation 12* and *equation 14* respectively.

Herein, LDA was leveraged to investigate the H&N patient dataset to explore what FLIm parameters and analytical methods (i.e., computed average lifetime vs. phasor harmonic analysis) gives rise to the best discrimination potential from both an intra- and inter-patient standpoint. Patients eligible for LDA analysis consisted of those who had both benign tissue and cancer imaged by FLIm. Patients with occult primary tumor where the primary was not located, and patients without a cancer diagnosis (e.g., high grade dysplasia, leukoplakia) were not assessed in this section. To be eligible for analysis within this section, a minimum of 30 datapoints corresponding to both cancer and benign tissue was required. Thirty datapoints correspond to 1 second of data acquisition (corresponding to 120 Hz laser repetition rate averaged 4 times to give 30 measurements per second); 30 datapoints additionally represents the minimum number of samples needed to create a standard normal distribution according to the *central limit theorem*. Among the 92 patients available for analysis, 71 patients met these criteria.

Figure 37 demonstrates the summary of LDA performance achieved across all patients, bifurcated based on 4 anatomical groupings: oral tongue (N=26), tonsil (N=21), base of tongue (N=10), and 'other' (N=14). Appendix *figures A54 – A57* depict the patient-level LDA. Linear combinations of univariate parameters were computed, designated by '*Collective LDA*'. '*M.R.*' corresponds to *metabolic ratio* computed by taking the intensity of [CH2] and dividing by the

intensity of [CH2 + CH3]. CH1, CH2, and CH3 phasors represents the highest LDA achieved when evaluating the phasors across each of their first five harmonics: (1) $\omega = \omega_0$, (2) $\omega = 2\omega_0$, (3) $\omega = 3\omega_0$, (4) $\omega = 4\omega_0$, and (5) $\omega = 5\omega_0$. '*Phasor LDA*' corresponds to the ROC-AUC obtained from LDA when linearly combining the first phasor harmonic of CH1, CH2, and CH3. '*LT LDA*' corresponds to the use of CH1-3 lifetime (3 univariate parameters) in the weighted linear combination computation of ROC-AUC arising from LDA. Analogously, ROC-AUC of '*IR LDA*' was computed with the variables IR CH1-3 and M.R. (4 variables in total). Finally, '*LT & IR LDA*' was computed using lifetime parameters from channels 1-3, intensity ratio from channels 1-3, and M.R. (7 variables total). From *section 3.1*, the expectation is that the weighted linear combination of FLIm parameters should provide better discrimination of benign vs. cancer tissue than individual FLIm parameters.

	Lifetime			Intensity Ratio				Best Harmonic Phasor Contrast			Collective LDA			
	LT CH1	LT CH2	LT CH3	IR CH1	IR CH2	IR CH3	M.R.	CH1 Phasor	CH2 Phasor	CH3 Phasor	Phasor LDA	LT LDA	IR LDA	LT&IR LDA
Tongue N=26	**0.67** ±0.09	**0.72** ±0.15	**0.72** ±0.15	**0.76** ±0.11	**0.66** ±0.14	**0.81** ±0.12	**0.75** ±0.13	**0.74** ±0.08	**0.78** ±0.11	**0.72** ±0.13	**0.89** ±0.06	**0.82** ±0.13	**0.84** ±0.10	**0.89** ±0.10
Tonsil N=21	**0.62** ±0.08	**0.69** ±0.14	**0.66** ±0.12	**0.76** ±0.11	**0.72** ±0.11	**0.76** ±0.10	**0.68** ±0.09	**0.63** ±0.06	**0.71** ±0.12	**0.71** ±0.11	**0.79** ±0.11	**0.77** ±0.12	**0.79** ±0.08	**0.84** ±0.09
Base of Tongue N=10	**0.66** ±0.14	**0.64** ±0.13	**0.64** ±0.14	**0.78** ±0.13	**0.77** ±0.12	**0.76** ±0.13	**0.66** ±0.12	**0.79** ±0.09	**0.71** ±0.08	**0.65** ±0.10	**0.83** ±0.09	**0.77** ±0.13	**0.78** ±0.12	**0.85** ±0.12
Other N=14	**0.64** ±0.13	**0.69** ±0.12	**0.74** ±0.12	**0.70** ±0.14	**0.69** ±0.13	**0.77** ±0.11	**0.75** ±0.11	**0.67** ±0.11	**0.73** ±0.10	**0.73** ±0.08	**0.87** ±0.06	**0.84** ±0.10	**0.79** ±0.12	**0.88** ±0.09
Weighted Average N=71	**0.65** ±0.11	**0.69** ±0.14	**0.70** ±0.14	**0.75** ±0.12	**0.70** ±0.13	**0.78** ±0.11	**0.72** ±0.12	**0.68** ±0.10	**0.74** ±0.11	**0.71** ±0.12	**0.84** ±0.09	**0.80** ±0.12	**0.80** ±0.10	**0.87** ±0.10

ROC-AUC: 1.00 – 0.50

Figure 37: Summary of oral cavity and oropharynx linear discriminant analysis performance. '*M.R.*' corresponds to metabolic ratio defined as [CH2] / ([CH2]+[CH3]). The AUC reported within '*Best Harmonic Phasor Contrast*' represents the phasor between the first and fifth harmonic giving rise to the highest AUC value. '*Phasor LDA*' involved the weighted linear combination of CH1, CH2, & CH3 phasor's first harmonic. '*LT LDA*' is the result of the weighted linear combination of CH1-3 lifetime. *'IR LDA'* is defined as the combination if CH1-3 intensity ratio and M.R. and '*LT & IR* LDA' reports the AUC from the combination of all seven parameters: CH1-3 lifetime, CH1-3 IR, and M.R.

As demonstrated by *figure 37*, CH1 lifetime collectively provided lower AUC-based discrimination of benign tissue vs. cancer compared to CH2 & CH3 lifetime (at the intrapatient level). CH1-3 phasor AUC was higher for each anatomy than CH1-3 lifetime AUC, suggesting

additional contrast can be leveraged through phasor analysis to substantiate more conventional computed average lifetime based on Laguerre features alone. CH3 IR provided the highest healthy vs. cancer LDA contrast, which continues to corroborate previous findings from *chapter 5*. CH1 IR provided similarly high AUC to CH3 IR. The weighted linear combination of phasors resulted in higher AUC than the weighted linear combination of lifetime, as well as intensity ratio. The weighted linear combination of all lifetime and intensity ratio parameters (designated by *'LT&IR LDA*') resulted in the highest AUC, suggesting the importance of using the weighted linear combination of multiple parameters in benign vs. cancer decision-making, further substantiating conclusions drawn from *section 3.1*. The best collective weighted LDA AUC was achieved for oral tongue (0.89 ± 0.10), and the lowest for tonsil (0.84 ± 0.09).

7.3 | Influence of Biological Variables, Patient Demographics, and Local Anesthetic Use on FLIm Data

This section investigates the influence of surgical characteristics (i.e., local anesthetic use), biological variables, and other patient demographics on FLIm data. The first part, *section 7.3.1*, explores if the surgical use of local anesthetics (lidocaine mixed with epinephrine) alters native tissue FLIm properties. To perform this investigation, a FLIm scan was performed immediately prior to the injection of local anesthetic, followed by a repeat scan of the tissue immediately after injection. This procedure was performed on both oral tongue and tonsil tissue; FLIm lifetime and intensity ratio parameters were subsequently analyzed to assess differences between the pre- and post-injection of the anesthetic. *Section 7.3.2* investigates the influence of patient age on FLIm data using a cohort of non-smoking palatine tonsil patients. *Section 7.3.3* explores if FLIm can detect deep tumor embedded beneath the mucosa ($0.5\ \text{mm} < x < 5\ \text{mm}$). This investigation is motivated by the understanding that FLIm's penetration depth is limited to ~250 μm from tissue surfaces, however changes pH, stromal behavior, metabolic characteristics, and transcriptomic aberrations may extend 'secondary tissue effects' of a neoplasms millimeters beyond a cancer site.[207] With the understanding that the anatomical

composition of tissue between the oral cavity and oropharynx differs, especially with the presence of lymphoid tissue comprising tissues of the oropharynx (e.g., base of tongue, palatine tonsil, and lingual tonsil), *section 7.3.4* investigates the effect of lymphoid tissue on FLIm data, relative to standard epithelized mucosa. Lastly, *section 7.3.5* evaluates the FLIm properties associated to high-grade dysplasia, relative to benign tissue and cancer.

7.3.1 Effect of Lidocaine & Epinephrine Injection on *In Vivo* FLIm - Case Study on Tongue (N=1) and Tonsil (N=1)

During oral surgery, some surgeons opt to use local anesthetics, where lidocaine mixed with epinephrine is commonly used. While lidocaine has a vasodilatory effect on tissue, when mixed with epinephrine, it has an overall vasoconstriction effect, enabling hemostatic properties to help control surgically-induced local bleeding.[217]

In order assess if lidocaine injection has any measurable effect on FLIm lifetime and intensity ratio parameters, an initial study was conducted *in vivo* on standard oral cavity and oropharyngeal mucosa. In this study, a pre- and post-lidocaine FLIm scan was conducted on two tissues – dorsal tongue and palatine tonsil (*figure 38*). First, as demonstrated in *figure 38A*, a pre-lidocaine FLIm scan of an approximate 1-minute duration was acquired. Next, lidocaine mixed with epinephrine was injected by the surgeon; the injection was performed in a manner to distribute the local anesthetic as uniformly as possible within the area of the FLIm scan. Thereafter, a post-lidocaine FLIm scan was immediately performed, where the imaging area and density of datapoints were made to be as close as possible to replicate the pre-lidocaine scan. This procedure was performed on both dorsal tongue and palatine tonsil.

Figure 38B demonstrates a representative surgical image acquired during each scan, followed by augmentation of channel 1 fluorescence lifetime, which was output from the spectral measurements originating from the FLIm scan. Qualitatively, juxtaposing the pre- and post-lidocaine scans for both dorsal tongue and palatine tonsil demonstrates a red-shift in the collective datapoints of the scan; the red-shift is indicative of longer average fluorescence

lifetime because of lidocaine injection. *Figure 38C* supports this finding in channel 1 quantitatively with the increase in median lifetime of post-injection (gray) vs. pre-injection (slate blue). *Figure 38C* also demonstrates significant differences pre- and post-lidocaine injection for channel 2 in both oral tongue and tonsil, and in channel 3 for tonsil.

Figure 38D demonstrates differences pre- and post-lidocaine injection for dorsal tongue and palatine tonsil. Relative to pre-lidocaine tissue, post-lidocaine FLIm scans demonstrated an increase in channel 1 intensity ratio and metabolic ratio for both tongue and tonsil, an increase in channel 2 intensity ratio for tongue, and a decrease in channel 3 intensity ratio.

Collectively, these initial results suggest that lidocaine use may impact intrinsic tissue fluorescence lifetime and intensity properties. This is an important consideration since the initial results show that lidocaine increased channel 1 intensity ratio, and decreased channel 3 intensity ratio.

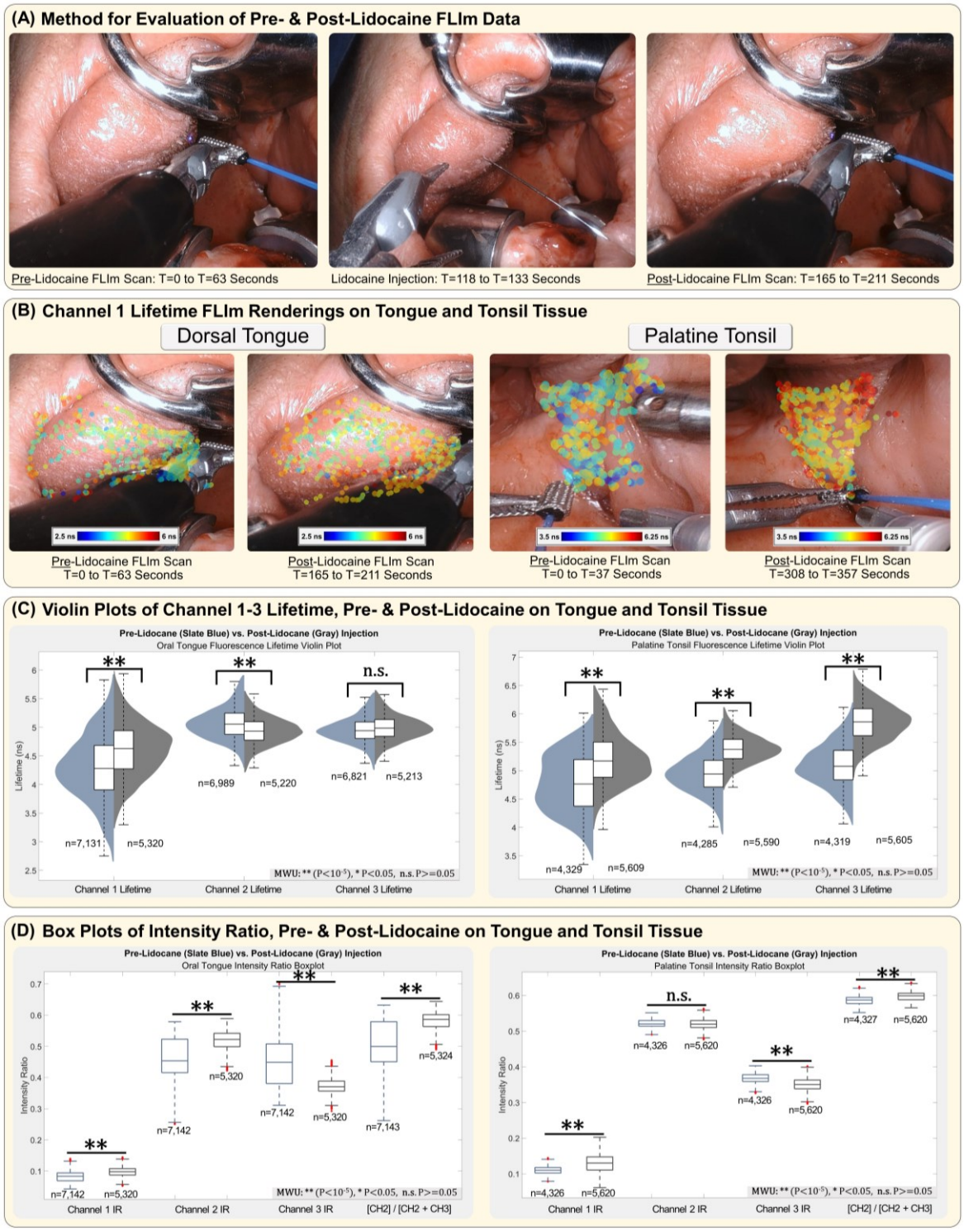

Figure 38: Evaluation of FLIm data pre- and post- injection of lidocaine with epinephrine. (A) A preliminary pre-lidocaine injection FLIm scan was performed, followed by immediate lidocaine injection, and a subsequent post-lidocaine scan. (B) Channel 1 lifetime FLIm renderings augmented on white-light surgical images of tongue and tonsil tissue pre- and post-lidocaine injection. (C) Violin plots of pre- and post-lidocaine injection on oral tongue and palatine tonsil, where slate blue denotes the pre-lidocaine FLIm distribution, and gray designates the post-lidocaine FLIm distribution. (D) Boxplots of pre- and post-lidocaine FLIm intensity ratio and CH2 / [CH2+CH3] data. Statistical significance of (C) and (D) designed by Mann-Whitney U significance testing.

7.3.2 Effect of Age on FLIm Data

The clinical appearance of oral cavity and oropharyngeal mucosa in healthy older populations is akin to that of young populations;[218] histologic examination however demonstrates evidence of patient age resulting in various degrees of epithelial thinning, decreased cellular proliferation, loss of submucosal elastin and fat, and increased fibrotic connective tissues, and degenerative alterations in collagen.[218] Along these lines, patient age is recognized as a biological consideration that may play affect fluorescence lifetime and intensity properties.

A challenge with the present human dataset is the potential sources of variability arising from both genetic and environmental factors. For example, when considering identifying the impact of patient age on FLIm properties, factors such as tobacco use, gender, and anatomic site, among other factors, must be accounted for so they do not confound analysis. Patient tobacco history is variable across patients, and the severity of impact to oral health is dependent on a variety of factors, including longevity of smoking and packs per day. While not formally evaluated, patient gender in theory should present some differences in FLIm characteristics between men and women; the rationale for this stems from gender-specific differences in epithelial thickness.[219] Through investigations of gender specific epithelial thickness using optical coherence tomography (OCT), men were found to present with thicker epithelium (30 μm on average) compared to women.[219] In the oral cavity and oropharynx, most epithelial thicknesses range from 100 μm to 250 μm depending on the anatomic site (e.g., soft palate, tonsil, tongue, hard palate, etc.). Due to FLIm's shallow penetration depth (~250 μm), and provided that the average epithelial thickness is correlated to patient gender, women with thinner epithelium in principle have higher autofluorescence contribution from the underlying lamina propria than men with thicker epithelium. Since the epithelium and lamina propria differ considerably from both a biochemistry and histologic standpoint, gender, alongside tobacco use and anatomic site, must be considered when evaluating the effect of patient age on FLIm data.

As previously mentioned in *chapter 7.1*, 92 patients were entered into analysis, with imaging data conducted from the following patient composition: 34 palatine tonsil patients, 16 base of tongue, 27 oral tongue, and 15 patients with the “other” anatomic designation. Considering the effect of FLIm on patient age, only patients with non-smoking history were analyzed within an anatomic cohort, leaving the following patient breakdown: 13 non-smoking palatine tonsil patients (10 men, 3 women), 7 base of tongue patients (7 men, 0 women), and 8 non-smoking oral tongue patients (3 men, 5 women). The 10-palatine tonsil male patients were selected for investigation on patient age since these patients comprised the largest cohort based on the bifurcation of the dataset.

The effect of patient age on FLIm properties was assessed on benign tissue of the palatine tonsil and not on cancer. The rational for this stems from the marked heterogeneity of the tumors arising in the oral cavity and oropharynx,[20,26] attributed to the complex interplay of etiologies and significant extent of molecular changes driving carcinogenesis.[20] The high degree of HNSCC cellular heterogeneity enables tumor cells to reverse lineage commitment to either proliferative or quiescent stages due to complex cell populations with various stages of differentiation.[27] In order to assess the effect of patient age on FLIm properties, benign tissue served as the better candidate for analysis due to the more homogenous profile of the tissue across patients.

FLIm lifetime and intensity ratio parameters for the cohort of 10 male palatine tonsil patients were thereby evaluated on benign tissue as a function of patient age. *MATLAB’s* built-in function ‘*corrplot*’ was used to create a matrix of plots showing correlations among FLIm optical parameters and patient age. Histograms of the variables appeared along the matrix diagonal, with scatter plots of variable pairs appearing in the off diagonal. The slopes of the least-squares reference lines in the scatter plots were equal to the displayed correlation coefficients. No linear or quadratic correlation, defined as $R^2 > 0.20$, was identified from the correlation plots, except for

channel 1 lifetime, which demonstrated a high linear correlation (R^2=0.81) between increasing patient age and decreasing channel 1 lifetime. These results are demonstrated in *figure 39*.

Within *figure 39*, each boxplot designates and individual patient and their corresponding age, whereas the y-axis designates the range of channel 1 lifetime data associated to the patient's benign tonsillar tissue. One patient of ten was omitted due to no benign tissue of the palatine tonsil available for analysis (i.e., all imaged regions of that patient's palatine tonsil were cancer). The results demonstrate a linear relationship with a computed linear regression R^2 value of 0.81.

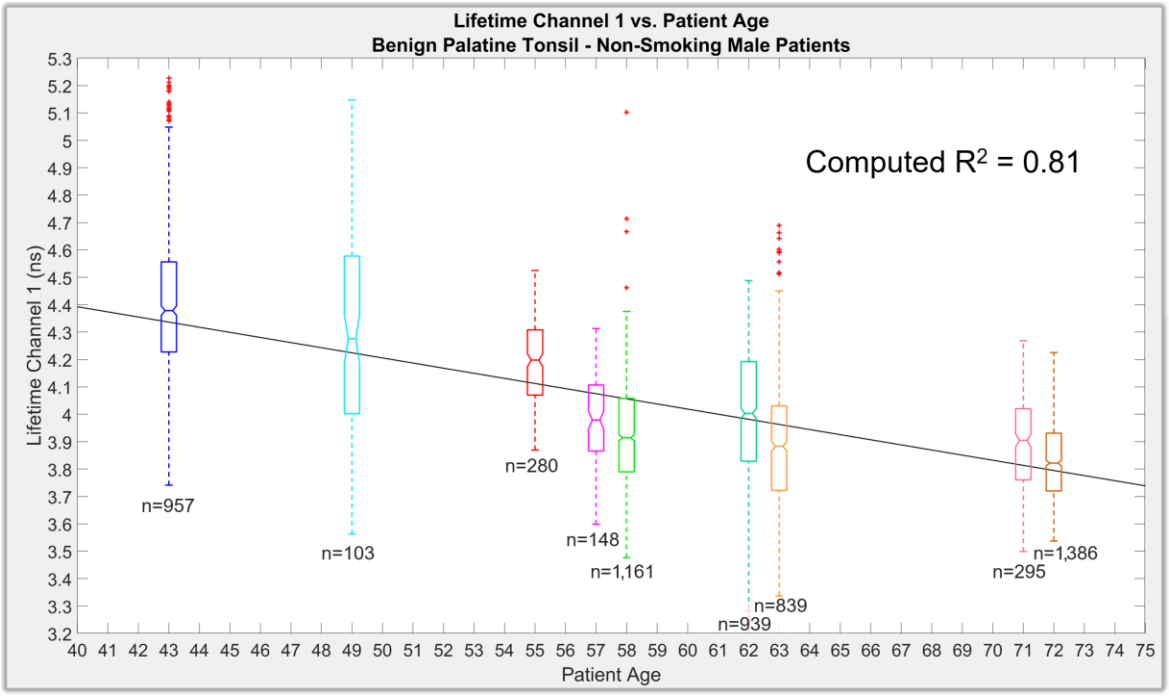

Figure 39: Influence of patient age on channel 1 lifetime, investigated on *in vivo* benign palatine tonsil tissue for N=9 patients. The figure illustrates computed average lifetime boxplots and the associated number of datapoints, in addition to the linear regression R^2 value.

7.3.3 FLIm Investigated on Deep Tumor Embedded Under Epithelium (0.5 mm < x < 5 mm)

The shallow penetration depth associated (~250 μm) with FLIm due to the inherent optical properties of UV laser excitation is a key limitation of the technique. However, because greater than 90% of all H&N cancers present as mucosa-presenting SCC,[3,4] and since the range of epithelial thickness of the H&N anatomy is on average between 100 to 200 μm,[219] FLIm is well-suited for interrogation these surface-presenting tumors for diagnosis and surgical guidance.

Despite most H&N tumors demonstrating superficial presentation within the mucosa of tissues, it is important to understand if FLIm has an ability to identify deeper tumor (0.5 mm < x < 5mm) extending beyond the penetration depth of the laser; such an ability would play an important role in the broader clinical adoption and universal utilization of this technique for oncologic procedures of the oral cavity and oropharynx. Although FLIm's UV laser would not directly penetrate to deeper tumor depths (0.5 mm < x < 5mm), it is conceivable that the technique can pick up on "secondary tumor tissue effects" imparted by cancer.

Histologically, *normal tissue adjacent to tumor* (NAT) is used as controls in oncology studies, however the biochemical and transcriptomic profile of NAT is influenced by the tumor, exhibiting different properties from non-tumor bearing benign tissue.[207] It has been demonstrated that NAT presents a unique intermediate state, disparate from conventional cancer and benign tissue from both morphologic and phenotypic distinctions.[207] This includes altered pH levels,[220] allelic imbalance,[221] stromal behavior,[222] epigenetic aberrations,[223] and altered transcriptomic behavior. These biochemical, phenotypic, and genetic changes are found to take effect as far as 10 millimeters beyond the site of tumor (depending on tumor size and characteristics).[207] Suitably, the sensitivity of endogenous fluorophores to numerous biochemical factors (pH, oxygenation, temperature, solvent polarity, and binding to macromolecules)[108] may enable FLIm to detect deep cancer through unique spectral signatures imparted from NAT.

FLIm's ability to detect deep tumor through intermediate normal tissue adjacent to tumor was formally assessed in a patient case study, presented in *figure 40*. In this case study, deep tumor was defined as the histologic delineation of cancer by our pathologist (Dr. Dorina Gui) within 500 μm to 5,000 μm of the tissue epithelium. 500 μm was chosen based on double the approximate FLIm penetration depth through tissue, and 5,000 μm as half of the maximum distance which "secondary tumor tissue effects" are reported to extend into adjacent benign tissue beyond solid tumor margins.

The case study in *figure 40A* first demonstrates representative H&E sections of palatine tonsil tissue where the pathologist identified both superficial (< 500 μm from surface) and deep tumor (500 μm $\leq$ x < 5,000 μm). *Figure 40B* presents the LDA evaluation of benign tissue vs. cancer, and benign tissue vs. deep cancer. Lifetime, intensity ratio, and phasors were assessed using LDA. The LDA ROC-AUC performance of multi-parameter lifetime, lifetime & intensity ratio, and phasor analysis demonstrated comparable performance; these incudes an ROC-AUC of 0.85 for the multi-parametric benign vs. cancer LDA (using both lifetimes and intensity ratio), and an ROC-AUC of 0.87 for benign vs. deep cancer. The combined channel phasor LDA ROC-AUC performances exceeded 0.70 for all assessed harmonics. Channel 1 and 2 intensity ratios provided the best discriminative performance from univariate LDA analysis.

The multiparametric LDA analysis of *figure 40B* showed that benign tissue vs. deep cancer was resolved with adequate (>0.70) ROC-AUC, demonstrating FLIm's ability to detect differences between NAT tissue and standard benign tissue far from tumor sites. This finding suggests that although FLIm's limited penetration depth cannot directly image cancer cells, deeper tumor, which imparts secondary tissue effects in adjacent benign tissue, may enable FLIm to identify the presence of deep (>500 μm from tissue surface) tumor tissue. From both patients, intensity ratio LDA outperformed lifetime LDA, suggesting FLIm intensity ratios serve as the most significant parameters enabling benign vs. deep cancer discrimination.

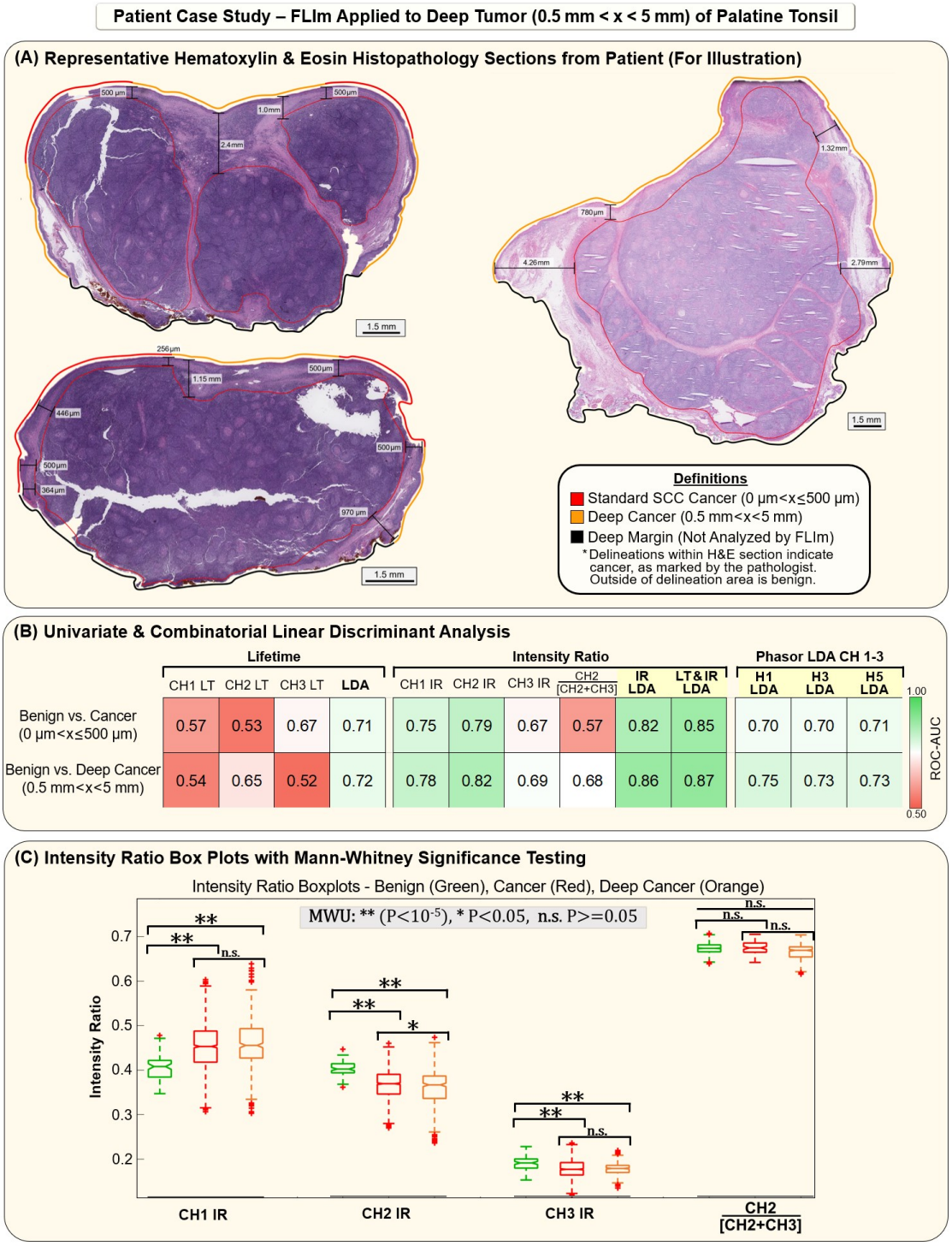

Figure 40: Investigation of FLIm properties on deep tumor (0.5 mm < x < 5mm) palatine tonsil case study. (A) Representative H&E sections with pathologist annotations. Scale bar corresponds to 2.0 mm. (B) Univariate and multivariate linear discriminant analysis (LDA) for benign tissue vs. standard cancer (0 µm < x ≤ 500µm) and benign tissue vs. deep tumor (0.5 mm < x ≤ 5 mm). (C) Box plots of intensity ratio and CH2 / [CH2+CH3] with Mann-Whitney U significance testing denoted.

Figures 40C demonstrates boxplots of FLIm intensity ratio parameters for benign tissue (indicated as green), cancer (red), and deep cancer (orange). Mann-Whitney U significance testing was performed to evaluate across the boxplots for significant differences. As demonstrated in *figure 40C*, epithelial cancer and deep cancer presented with statistically equal medians for channel 1 and 3 intensity ratio. For this patient, the median channel 1 and 3 intensity ratio values for benign tissue vs. cancer and benign tissue vs. deep cancer were statistically different. For channel 2 intensity ratio, benign tissue vs. cancer and benign tissue vs. deep cancer were statistically different, however the medians between cancer and deep cancer were not statistically equal. The results support the hypothesis that FLIm can detect deep tumor through secondary tissue effects imparted in the NAT space.

7.3.4 Effect of Lymphoid Tissue on FLIm Data

The effect of lymphoid tissue on FLIm optical signatures is an important consideration due to the disparate histological and physiological composition of this tissue relative to standard epithelized tissues and lamina propria of the head and neck anatomy. At the present, no current published studies have investigated the impact of lymphoid tissue on FLIm lifetime and intensity ratio parameters.

The lymphatic tissues of the oropharynx are composed of a circumferential tonsillar ring, known as Waldeyer's ring; this region comprises the palatine tonsils, nasopharyngeal tonsils, lingual tonsils, and tubal tonsils.[224] Lymphoid tissue typically resides in the lamina propria (beneath the epithelium) and contains high concentrations of lymphocytes. After detecting an antigen, these lymphocytes switch from a quiescent state to a more metabolically active state of proliferation.[225] Upon activation, lymphocytes conform to meet the bioenergetic and biosynthetic demands of increased cell proliferation, demonstrating an intrinsic link between metabolic reprogramming and lymphocyte activation.[225] Lymphoid tissue contains B, T, and M-cells. During the resting (quiescent) state, naïve T cells undergo low levels of glycolysis while deriving

most of their energy via oxidative phosphorylation or fatty acid oxidation.[225] When activated, naïve T cells must switch to a metabolic program that can sustain anabolic growth to generate progeny known as effector T cells (T_{EFF}). This program looks very similar to the Warburg Effect described in cancer cells where glucose-derived pyruvate is converted to lactate in glycolysis despite aerobic conditions.[225] After the pathogen or other source of antigen is cleared, most T_{EFF} cells die leaving behind a population of longer-living memory T cells (T_M). T_M cells have a metabolic profile akin to naïve T cells whereby energy is derived predominantly from oxidative phosphorylation. However, T_M cells differ from naïve T cells in that they have greater mitochondrial mass. This allows T_M cells with tremendous capacity for mitochondrial-derived ATP generation necessary for a rapid immunologic response to re-exposure of the antigen.

Collectively, this background serves to demonstrate that lymphoid tissue presents with unique and variable metabolic profiles. Additionally, the collagen surrounding the lymphoid tissue architecture features type III collagen fibrils, which is in contrast to the predominant type I collagen found elsewhere in H&N anatomy.[226] Accordingly, it is conceivable that the different structural protein composition would play a role in altering channel 1 (collagen) FLIm signal, and the metabolic effects would have some effect on channel 2 (NADPH) and channel 3 (FAD) FLIm parameters.

Figure 41 features representative histology acquired from benign tissue, lymphoid tissue, and cancer from 4 base of tongue patients (Patient A-D). The scale bar corresponds to 300 μm for all figures. From the histology, it is apparent that all benign tissues have a highly organized and well-defined epithelial structure, basement membrane, and underlying lamina propria. From the histology, the increased hematoxylin component (darker purple from staining more cellular nuclear material) demonstrates a substantial increase in cellular density when compared to the histology of benign tissue. The lymphoid tissue aggregates in the example primarily reside

directly beneath the basement membrane. Cancer demonstrates the most histologic variability, due to cancer's inherent histology variability.

An important consideration in evaluating the effect of lymphoid tissue on FLIm data, relative to benign tissue, is the observed histologic variability across patients. For example, in *figure 41,* lymphoid tissue for the base of tongue appears quite variable across patient A, B, C, and D, where all histology is from base of tongue patient. For these patients, the density of diffuse lymphatic tissue which accumulates in the lamina propria has variability, which in turn can affect optical scattering and absorption properties. Suitably, understanding this variation can help put FLIm results in context with more dynamic histopathologic corroboration.

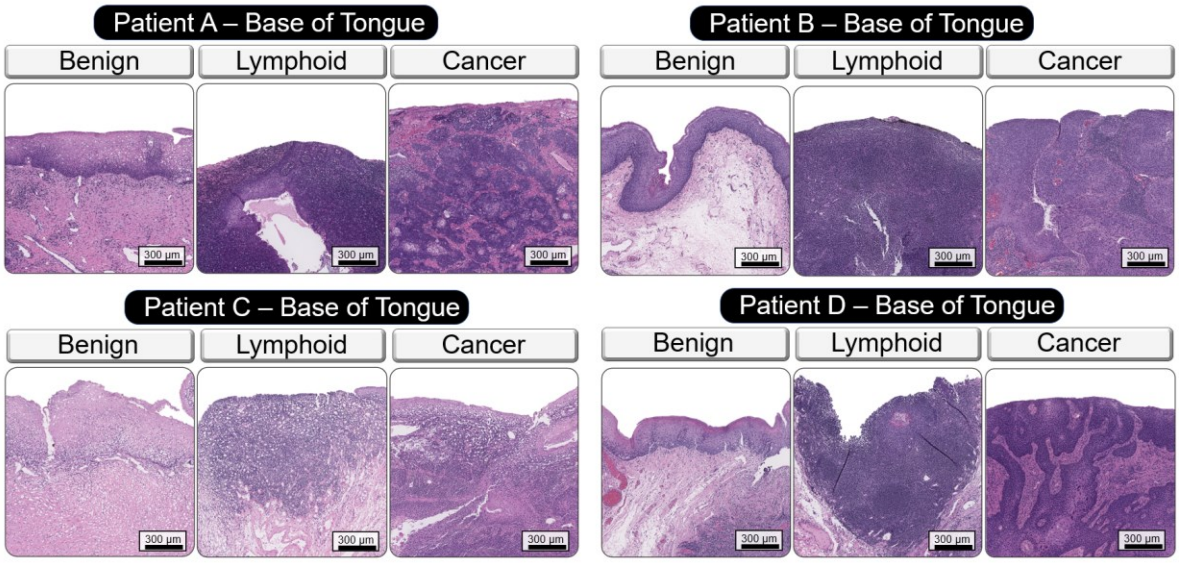

Figure 41: Illustrative histopathology for an eight-patient cohort comprising benign tissue, lymphoid tissue, and cancer. Base of tongue H&E represented in patients 'A-D.' Scale bar corresponds to 300 µm.

Figure 42 depicts the results of FLIm lifetime and intensity ratio parameters derived from two representative base of togue patients (Patient A & B). All results relate to measurements acquired *in vivo*, with an assignment of benign tissue, lymphoid tissue, or cancer based on the coregistered histopathology derived from the surgically excised specimen. The data is plotted in terms of boxplot graphs, where green boxplots correspond to benign tissue, purple to lymphoid tissue, and red to cancer.

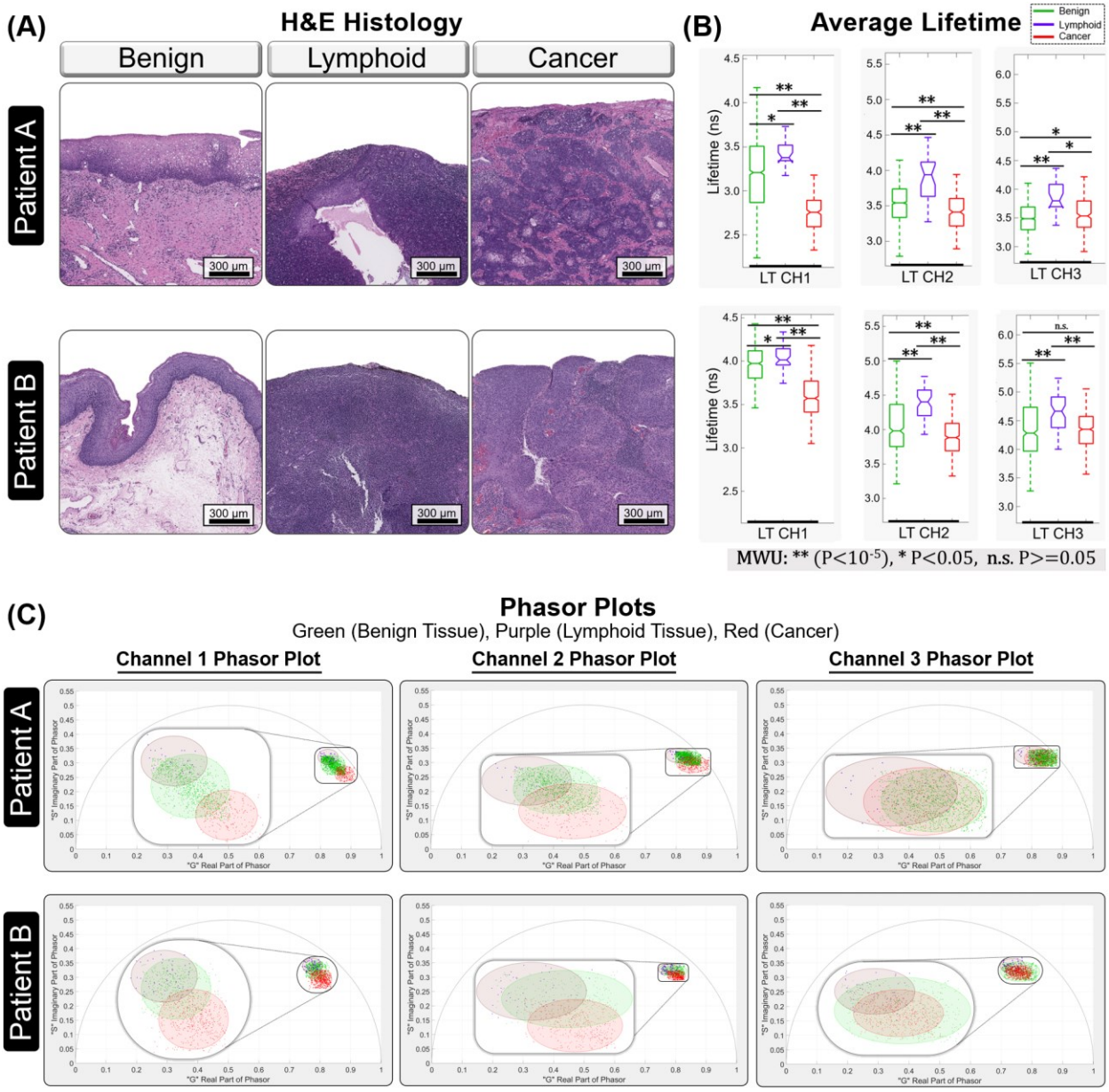

Figure 42: Evaluation of lymphoid tissue's influence on FLIm lifetime and intensity ratio for base of tongue tissue. Benign tissue indicated in green, lymphoid tissue in purple, and cancer in red. (A) Representative histology sections for benign tissue, cancer, and lymphoid tissue. (B) Boxplots of the distributions of lifetimes for benign tissue (green), lymphoid tissue (purple), and cancer (red) for the two patient case studies. (C) Phasor plots for benign tissue (green), lymphoid tissue (purple), and cancer (red). Mann-Whitney U test significance indicated by '**' for $P<10^{-5}$, '*' for $P<0.05$, and 'n.s.' as not significant for $P>=0.05$.

These results suggest that lymphoid tissue shifts fluorescence lifetime in all channels towards longer values, relative to benign tissue and cancer. This is observed from both computed average lifetime (*figure 42B*) and phasor analysis (*figure 42C*).

7.3.5 Effect of High-Grade Dysplasia on FLIm Data

From a surgical standpoint, dysplasia is a subjective and difficult diagnosis, and is considered a precancerous lesion. In otolaryngology, historically, low-grade dysplasia is observed closely, whereas high-grade dysplasia (HGD) is resected due to risk of cancer progression. Suitably, the ability for FLIm to confer discrimination between benign tissue, HGD, and cancer would be advantageous in a surgical capacity, better enabling decision-making as to which lesions may become problematic. *Figure 43* features histology derived from N=4 patients presenting with HGD at final pathology. Significant histologic differences within the mucosa between benign tissue and HGD is observed, visualized by an increase in nuclear crowding and the apparent disruption of the basement membrane for HGD.

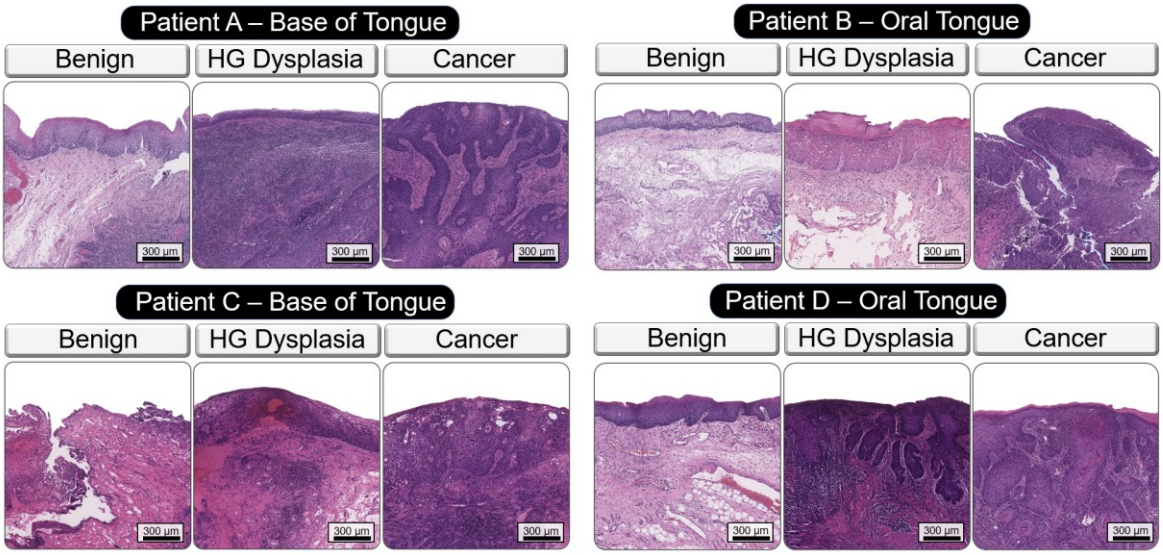

Figure 43: Illustrative histopathology of benign tissue, high-grade dysplasia, and cancer. Base of tongue and oral tongue H&E is represented. Scale bar corresponds to 300 µm.

From the N=4 patients featured in *figure 43*, one base of tongue patient (Patient A) and one oral tongue patient (Patient B) are featured in the case study demonstrated in *figure 44*, which investigates the effect of HGD on FLIm parameters. All results reported pertain to FLIm measurements acquired *in vivo*, where green boxplots pertain to the data associated to benign tissue, orange boxplots to dysplasia, and red to cancer. In general, HGD more closely represented FLIm lifetime and intensity ratio characteristics to cancer than benign tissue.

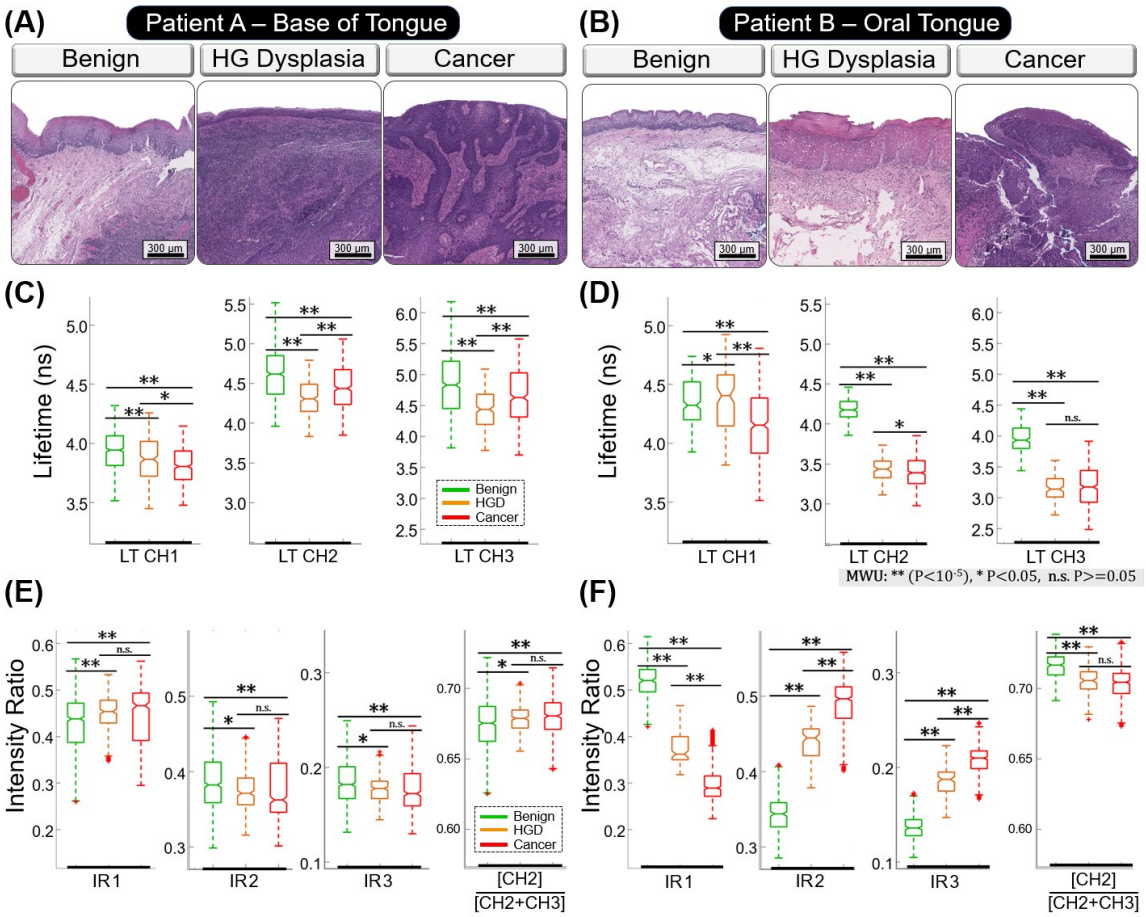

Figure 44: Evaluation of high-grade dysplasia's influence on FLIm lifetime and intensity ratio parameters for base of tongue (Patient A) and oral tongue (Patient B). Benign tissue indicated in green, high-grade dysplasia in orange, and cancer in red. (A & B) Representative histopathology from Patient A and B respectively. (C & D) Lifetime channel 1-3 for Patient A & B, where green boxplots correspond to benign tissue, orange to high-grade dysplasia, and red to cancer. (E & F) Intensity ratio channels 1-3 for Patient A & B. Mann-Whitney U test significance indicated by '**' for $P<10^{-5}$, '*' for $P<0.05$, and 'n.s.' as not significant for $P>=0.05$.

7.4 | Evaluation of Univariate Data Trends (Δ) Between Benign Tissue vs. Cancer

Prior research investigating the effects of cancer on fluorescence lifetime and intensity parameters have been documented for oral cavity tissues in various studies.[59,129,130,145,146] These studies preclude the investigation of these trends in the oropharynx as this anatomical region is accessed through TORS, which in the field of fluorescence lifetime imagine, has been unique to our laboratory group (Marcu Lab at UC Davis). Relative to baseline collagen intensity, the literature demonstrates that cancer is associated with reduced collagen intensity.[59,129,145] This trend of reduced intensity of collagen autofluorescence is the method by which the commercially available technology *VELscope* and *Identafi* operate by for contrast between pathological and

benign tissue. Cancer is recognized to increase NAD(P)H[59,145] and FAD[129,146] intensity, while decreasing NAD(P)H[129,130] and FAD[130] lifetime relative to benign tissue. Another study has documented reduced optical redox ratio (CH2/[CH2+CH3]) for oral cancer relative to benign tissue.[145] A graphical illustration which summarizes these previously reported trends is demonstrated in *figure 45*.

Autofluorescence loss attributed to collagen with cancer progression is a well-established phenomenon. When cancer progresses, the tumor microenvironment is altered in favor of enabling tumor invasion and intravasation as a factor of the metastatic niche.[113] It is well known that HNSCC tumors mediate the activity of collagenases, such as matrix metalloproteinase 1, 9, 13, and 18, which unwind triple-helical collagen and hydrolyzes the peptide bonds of fibrillar collagen type I, III, and IV.[115] Because approximately 50% of autofluorescent constituents are located within the peptide bond crosslinks of collagenous molecules, cancer-associated collagen crosslink degradation reduces autofluorescence intensity attributed to collagen.[107] This property is the phenomenon by which commercially available technologies such as VELscope operate, where autofluorescence loss enables the identification of neoplastic tissue.

FLIm channel 2 and 3 capitalize on the autofluorescence maxima of NAD(P)H and FAD respectively. Chance et al. in 1976[227] and 1979[228] coined “redox ratio” as a direct indicator of the amount of oxygen used in the mitochondria of cells, where the collective ratio of NAD(P)H and FAD fluorescence ties closely to the cellular oxygenation state; suitably, NAD(P)H and FAD are frequently analyzed together in a ratio, named redox or metabolic ratio. Together, these metabolic cofactors together provide useful information about the metabolic status of cells.

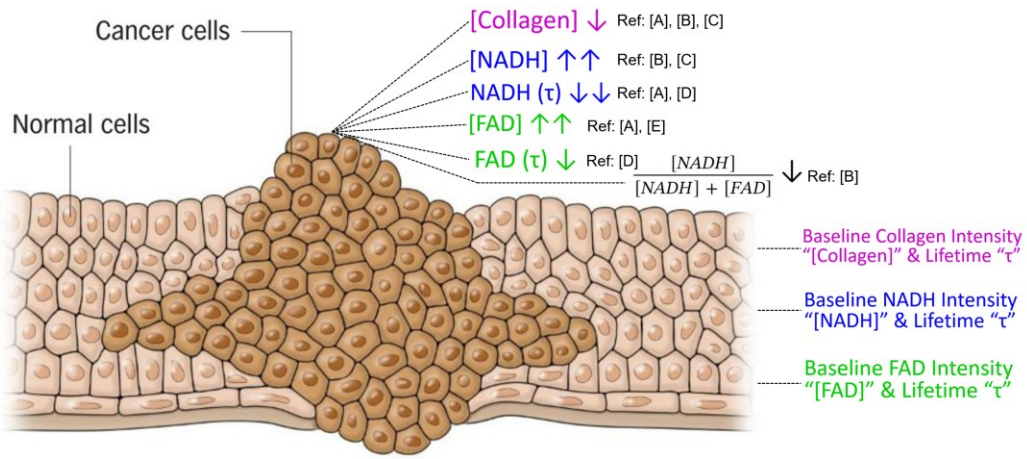

[A] Malik, B. H. et al. Objective Detection of Oral Carcinoma with Multispectral Fluorescence Lifetime Imaging In Vivo. *Photochem. Photobiol.* 92, 694–701 (2016).

[B] Wu, Y. & Qu, J. Y. Autofluorescence spectroscopy of epithelial tissues. *J. Biomed. Opt.* 11, 054023 (2006).

[C] Pavlova, I., Williams, M., El-Naggar, A., Richards-Kortum, R. & Gillenwater, A. Understanding the biological basis of autofluorescence imaging for oral cancer detection: High-resolution fluorescence microscopy in viable tissue. *Clin. Cancer Res.* 14, 2396–2404 (2008).

[D] Gorpas, D. et al. Time-resolved fluorescence spectroscopy for the diagnosis of oral lichen planus. *Clin. Exp. Dermatol.* 43, 546–552 (2018).

[E] Duran, E. et al. In vivo metabolic imaging of early-stage oral cancer and dysplasia based on autofluorescence lifetime endoscopy. *Med Img.* doi:10.1117/12.2293794.

Figure 45: Autofluorescence lifetime and intensity ratio trends for oral cancer. Compared to baseline autofluorescence intensity and lifetime properties for benign tissue, cancer has been demonstrated to exhibit the following properties in oral epithelium: (1) decreased collagen intensity,[59,129,145] (2) increased NAD(P)H intensity,[59,145] (3) increased FAD intensity,[129,146] (4) decreased NAD(P)H lifetime,[129,130] (5) decreased FAD lifetime,[130] & (6) decreased optical metabolic ratio defined as NADPH / [NADPH + FAD].[146]

Herein, this section investigates if the results from the 92-patient dataset conform to the previously reported results from other researchers. The sign (+/-) of the Δ value between benign tissue and cancer is assessed, as well as magnitude of the differences. Relationships between the magnitudes and FLIm trends with respect to patient clinical cancer characteristics and medical history are elucidated; this evaluation is performed to better understand inherent patient characteristics that affect FLIm lifetime and intensity parameters. This understanding can help better shape the development and input training data considered in creating robust classification algorithms using the data.

7.4.1 Methods: Kruskal-Wallis U Test and Evaluation of Benign Tissue vs. Cancer Trends

Differences in univariate FLIm lifetime and intensity ratio parameters were assessed using the methods demonstrated in *figure 46*. First, the Mann-Whitney U significance test was used to evaluate distributions of the data from benign tissue and cancer for a given patient. For a given patient, this test evaluated the null hypothesis that the data in benign (blue) and cancer (red) are samples from a continuous distribution (i.e., 30+ datapoints according to the central limit theorem with no apparent skew between the median and quartiles) with equal medians, against the alternative that the medians are not equal. The test assumes the two samples (benign and cancer) are independent, and the sample may have different numbers of datapoints. P-values less than 0.05 are significant, and values less than 0.0001 exhibit a high significance level. *Figure 46A* demonstrates 3 benign tissues (blue) vs. cancer (red) violin plot distributions, acquired from 3 different patients for demonstration. The left-most distribution quantitatively does not have any significance, corroborated quantitatively with a P value greater than 0.05. The middle distribution of *figure 46A* is significant at the $P < 0.05$ level, indicating that the medians between benign tissue and cancer are not equal. The right-most benign (blue) vs. cancer (red) distribution is significant at the $P < 0.0001$ level.

For data derived from a given patient, if statistical significance was computed to be $P<0.05$ or less, an assignment of sign (+/-) for the difference, denoted as Δ, between benign tissue and cancer was computed (*Figure 46B*). Distributions where values for benign tissue were greater than cancer gave a +Δ, and where cancer values were higher than benign tissue, gave a -Δ.

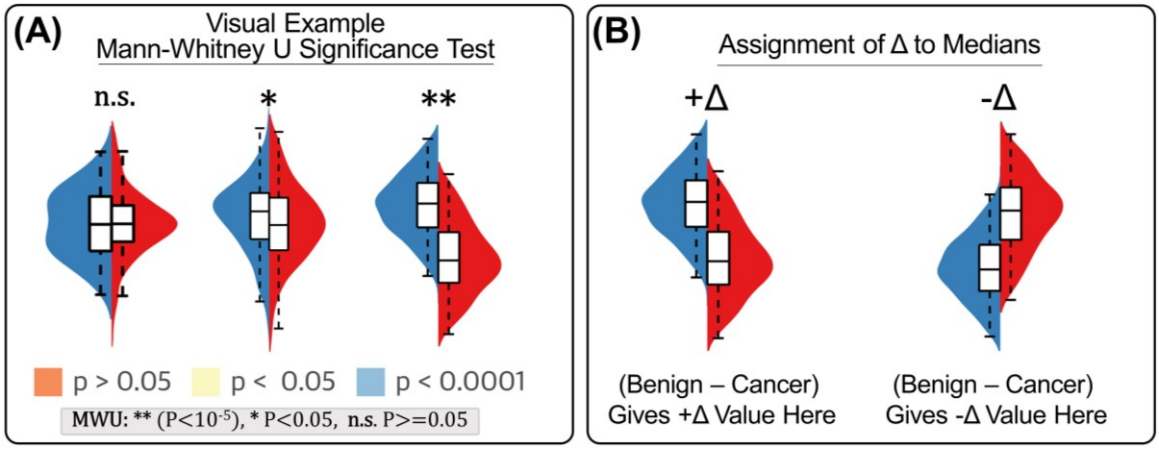

Figure 46**:** Method for assigning deltas (Δ) between benign tissue and cancer, and application of significance testing to the FLIm data. (A) Visual example of violin plot distributions between benign tissue (blue) and cancer (red) obtained from a given patient. The violin plots enable qualitative comparison through visual assessment, and quantitative statistical evaluation testing the null hypothesis that the medians are equal between the benign and cancer distribution; statistical evaluation was performed with Mann-Whitney U significance testing. (B) Where differences in the median were at a significance of $p<0.05$, the difference (Δ) between benign tissue (blue) and cancer (red) were computed. +Δ indicates that the median FLIm parameter of the benign distribution was greater than cancer. -Δ indicated the median FLIm parameter of the cancer distribution was greater than benign.

7.3.2 Pearson's Chi Square Analysis of FLIm Trends vs. Clinical Characteristics

As demonstrated in the appendix data for *figures A58 – A60*, the majority of the FLIm data trends from the 88-patients analyzed correlate to the autofluorescence lifetime and intensity ratio trends expected for oral cancer. To understand potential sources of variability in the FLIm data for the minority of patients who do not conform to the typical trends, a Pearson's Chi Square Test was performed to investigate if any apparent correlation exists between clinical characteristics (patient gender, ethnicity, race, p16/HPV status, tobacco use, anatomic site, and cancer class) and FLIm data trends. FLIm trends were evaluated based on the sign (+/- Δ) of the difference between benign tissue and cancer. This non-parametric statistical test is well-suited for evaluating whether there is an association between categorical variables and to understand whether the variables are independent or related.

CH1 – CH3 intensity ratio, CH2 and CH3 lifetime, and metabolic ratio [CH2] / [CH2+CH3] was assessed. The following subdivisions of clinical characteristics were made: (1) *Gender* as 'male' and 'female'; (2) *Ethnicity* as 'Not Hispanic or Latino,' 'Hispanic or Latino', and 'Unknown'; (3) *Race* as 'White', "Hispanic or Latino', 'Asian', 'Indian', and 'Unknown'; (4) *HPV*

Status as 'positive' or 'negative'; (5) *Tobacco Use* as either 'lifelong non-smoker (<100 cigarettes in lifetime)' or 'smoker (≥ 100 cigarettes in lifetime)', (6) *Anatomy* as 'oral cavity' and 'oropharynx', and (7) *Cancer Class* as 'other,' 'verrucous SCC', 'SCC and invasive SCC', and 'Basaloid SCC.'

Computations for Pearson's Chi Square test were performed in *IBM SPSS*. As demonstrated from *figure 46*, the sign of delta values (+/-) between benign tissue and cancer were evaluated where the difference was statistically significant at the patient level ($p < 0.05$) when all patient-level data was compared by Mann-Whitney U Significance testing. The summary of the results for all assessed analytical variables and patient clinical characteristics is featured in *table 12*.

Table 8. Pearson's Chi Square Analysis of FLIm Data Trends vs. Clinical Patient Characteristics.

		Analytical Variables Δ (+/-) Cancer - Benign Tissue							
		Intensity Ratio					**Lifetime**		
		Δ CH1 IR	Δ CH2 IR	Δ CH3 IR	$\frac{[CH2]}{[CH2+CH3]}$	Δ IR CH2 & Δ IR CH3	Δ CH2 LT	Δ CH3 LT	Δ LT CH2 & Δ LT CH3
Clinical Characteristics	Gender	0.151	0.243	0.052	0.504	0.078	0.852	0.475	0.761
	Ethnicity	0.619	0.825	0.795	0.805	0.806	0.606	0.719	0.632
	Race	0.69	0.281	0.951	0.651	0.771	0.257	0.346	0.345
	HPV Status	**0.006***	**0.096**	**0.004***	**0.002***	**0.071**	**0.092**	**0.015***	0.108
	Tobacco User	0.221	0.526	0.365	0.446	0.614	0.79	0.529	0.878
	Anatomy	**0.09**	0.764	0.301	**0.023***	0.335	0.14	**0.041***	0.39
	Cancer Class	0.764	0.572	0.933	0.307	0.868	0.557	0.514	0.245

Statistical significance achieved where $p < 0.05$ and identified by bolding and denoted by asterisks. Potentially significant results ($0.05 \leq p < 0.10$), which may become significant with greater sample size, identified by bolding.

The results of *table 8* demonstrate a few important concepts. First, the analysis demonstrates minimal to no correlation of patient gender, ethnicity, race, tobacco use, and cancer malignancy to the sign (+/-) of the median difference between benign tissue and cancer. Anatomic site and HPV status both appeared to play the most significant role in the outcome of

the sign of the FLIm data trends. For anatomy, two analytical variables (Δ [CH2]/[CH2+CH3] & Δ CH3 LT) were significant from the test, and for HPV/p16 status, 4 analytical variables were significant (ΔCH1 IR, ΔCH3 IR, Δ [CH2]/[CH2+CH3] & Δ CH3 LT).

From the statistical test, since p16 status was determined as the most informative of differences observed for FLIm benign vs. cancer data trends; correspondingly, the distribution of patient data trends for channel 1 intensity ratio, channel 2 & 3 intensity ratio, and channel 2 & 3 average lifetime as a function of tumor p16 status was investigated. The median of the difference between cancer – benign for the investigated FLIm metrics are reported in terms of magnitude and sign within *figure 52*.

Figure 47 A&B demonstrates that IR CH1 for cancer is less than benign tissue for all N=20 patients with p16- tumors, as anticipated by data trends reported in the literature (*figure 45*). While most p16+ tumors also correspond to this trend (N=20,76.9%), a few p16+ patient tumors demonstrate the reverse trend, where IR CH1 cancer > benign (N=6, 23.1%). *Figure 47 C&D* demonstrates that the majority of p16- patient data corresponds to IR CH2 cancer > benign and IR CH3 cancer > benign (N=18, 90%), as expected by the literature (*figure 50*). For the p16- tumor patient cohort, no p16- tumors present as IR CH2 cancer < benign and IR CH3 cancer < benign (N=0, 0%). For p16+ tumors however, multiple patients demonstrate IR CH2 cancer < benign and IR CH3 cancer < benign (N=7, 25.9%), and the rest of these p16+ tumors group in the expected result: IR CH2 cancer > benign and IR CH3 cancer > benign (N=20, 74.1%). No significant correlation to p16 status was found for Δ CH2 & Δ CH3 lifetime, as assessed by *figure 47 E&F*, however it is noted that the magnitude of the Δ between channel 2 and 3 are linearly correlated (R^2 = 0.89 for p16+ tumors and R^2 = 0.91 for p16- tumors).

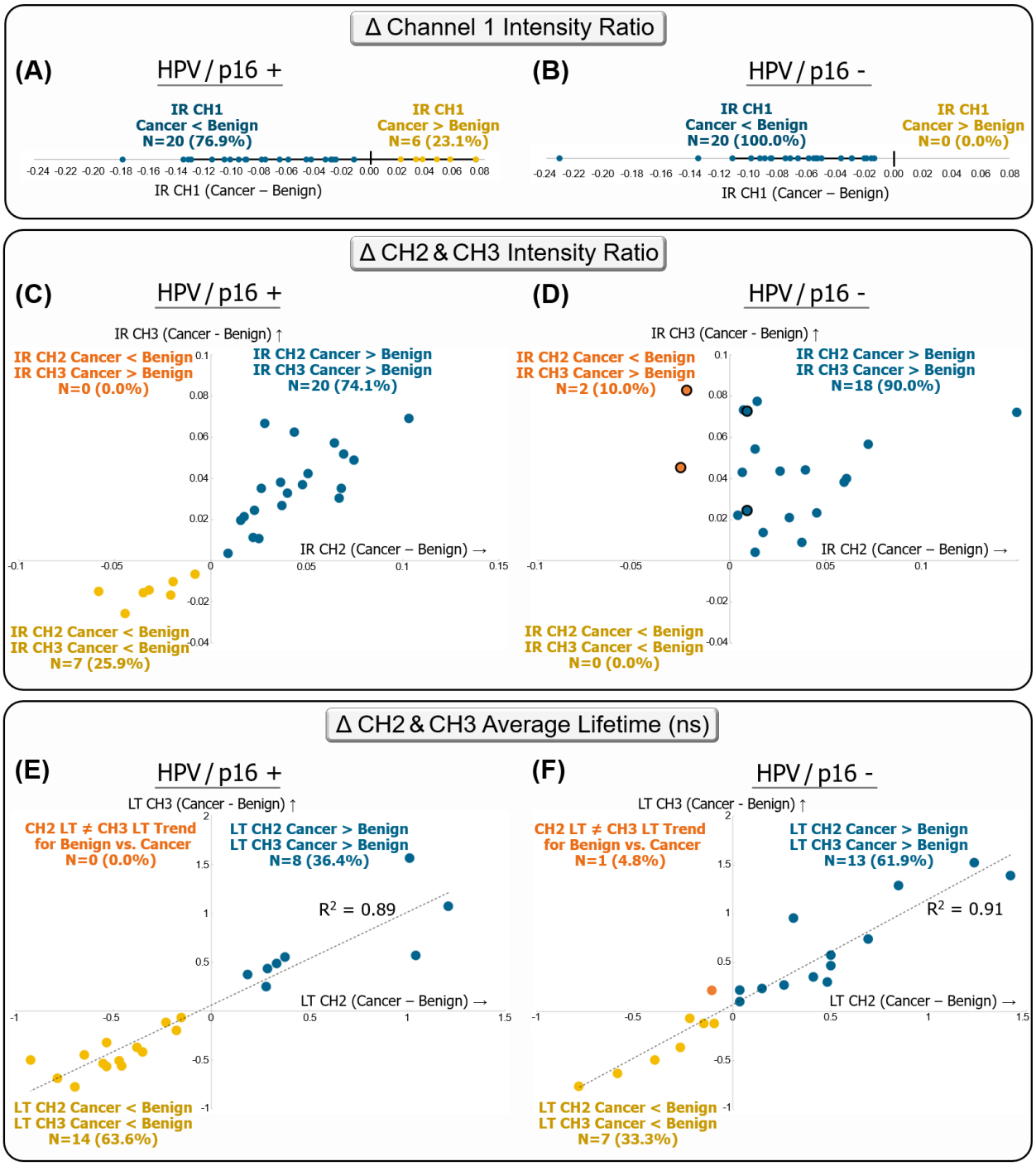

Figure 47: Evaluation of average lifetime and spectral intensity ratio vs. tumor p16 status. All values correspond to the medians at the patient-level for (cancer – benign) data. Each datapoint corresponds to the magnitude and sign of a single-patient's FLIm data result. (A) Δ Channel 1 intensity ratio for p16+ and (B) p16- tumors, (C) Δ Channel 2 & Δ Channel 3 intensity ratio for p16+ and (D) p16- tumors, and (E) Δ Channel 2 & Δ Channel 3 average lifetime for p16+ and (F) p16- tumors.

Collectively, the results suggest that HPV+/p16+ status may mediate unique characteristics of the tumor, which FLIm may be able to detect. For the p16+ tumors which behaved differently than p16- tumors from a FLIm data trend standpoint, it may be worth investigating the reasons for the observed discrepancies as this may have clinical implications and potential value. Future investigation may consider additional histologic review and molecular analysis as alternative methods to further explore the inherent properties of the observed p16+ tumor outliers, and if any relationship can be linked to the apparent differences in FLIm properties for this tumor cohort. Additionally, this result is important within the scope of developing machine learning algorithms, as the inclusion of pathology-derived tumor characteristics in the classifier may better refine the training data set and potentially lead to enhanced classification accuracy.

7.5 | Evaluation of Residual Tumor in Electrocauterized Surgical Cavity

Within the 100-patient data collection, 8 patients in total presented with positive surgical margins (PSMs) after initial *en bloc* surgical excision of tumor. Among these 8 patients, only N=2 patients were possible for PSM analysis due to either one, or a combination of the following reasons: (1) coregistration was not clear, (2) PSM area was not visible based on the angle of the visualizing camera during the FLIm scan, (3) the PSM area was microscopic and therefore the remaining cancer area was too small for analysis (> 0.25 mm^2), or (4) the PSM area was not scanned, and was therefore missed within the FLIm data acquisition.

The two *in vivo* case studies available for analysis are presented in *figure* 48, where patient case study A corresponds to lingual tonsil (n=29 cancer and n=507 benign electrocautery datapoints) and patient case study B corresponds to palatine tonsil (n=27 cancer and n=1,032 benign electrocautery datapoints). As performed with the full dataset, all PSM areas were determined by conventional histopathology interpreted by pathology derived from the deep margin of the *en bloc* excised specimen.

For the two case studies, *figure 48 A&C* illustrates the registration of deep margin histopathology on the surgical cavity, whereas *figure 48 B&D* demonstrates boxplots of the computed average lifetime for benign vs. cancer surgical cavity tissue for case study A and B respectively. *Figure 48 E* demonstrates average lifetime augmented for channels 1-3 for case study B.

The two case studies illustrate higher average lifetime ($P<0.05$) across all three channels for positive surgical margin tissue compared to benign electrocauterized tissue. This is also visualized within the augmented lifetime plots. While preliminary, these results are encouraging of FLIm's ability to demarcate PSMs. Due to the small sample size of residual tumor patients possible for analysis, it was not possible to apply ensemble-based classification for cancer probability prediction. Future work may benefit from investigating the use of classification algorithms in the PSM identification process, once a suitable dataset size is available for analysis.

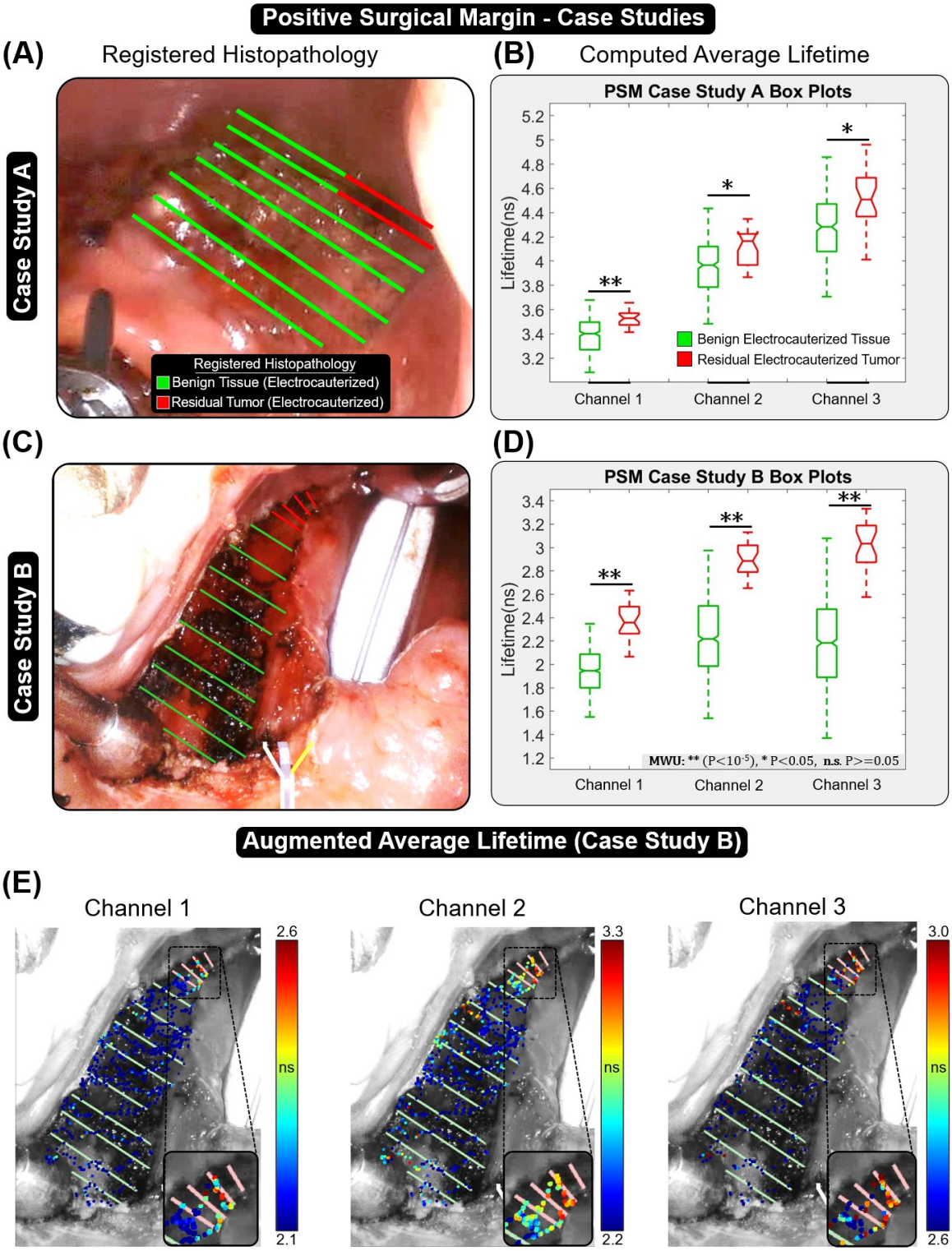

Figure 48: Evaluation of residual tumor in vivo for lingual tonsil (Patient A) and palatine tonsil (Patient B). (A) Registered histopathology and (B) boxplot diagram of channel 1-3 average lifetime for Patient A. (C) Registered histopathology and (D) boxplots of average lifetime for Patient B. (E) Computed average lifetime augmented over surgical image with registered histopathology for channels 1-3.

CHAPTER 8 | Conclusion: Summary of Research and Next Steps

8.1 | Summary of The Clinical Problem & Six Major Research Objectives Addressed

Surgeons across oncology disciplines need novel technologies which enhance their ability to determine tumor margins in real-time. A balance in the extent of tissue removed must be carefully considered; if too conservative with tissue resection, cancer may remain in the patient and reoccur, whereas if too aggressive, benign functional tissue may be lost and result in poor cosmesis. Certain tumor cohorts, such as occult (i.e., unknown primary) tumors, may evade detection all together despite exhaustive radiographic, surgical, and clinical workups. Within the scope of head and neck cancer, positive surgical margins are found in up to 30% of patients at final histopathology approximately 1 week after the surgery, which is a percentage that has not changed over the past 30 years.[36–39] Accordingly, surgeons need new technologies which enable the full extent of cancer to be identified to optimize patient surgeries and enhance clinical outcomes.

This original work investigated the ability of FLIm to aid in the intraoperative tumor margin evaluation of H&N cancer by addressing six research objectives, where objectives 1-4 were investigated in detail, and objectives 5-6 through preliminary feasibility/case studies. These objectives include: (1) In order to benchmark FLIm results against the gold standard of H&E histopathology, a series of custom-developed tools, methodologies, and techniques were developed to correlate ground truth histopathology to optical FLIm datapoints acquired over entire surgical regions. This was an essential first step in order to develop the appropriate validation to pathology status for measurements conducted *in vivo* and *ex vivo*. (2) Through univariate statistical analysis and multivariate linear discriminant analysis, it was demonstrated that FLIm can differentiate healthy tissue from cancer across a range of anatomies of the oral cavity oropharynx. The FLIm parameters which provided the best benign tissue vs. tumor contrast were identified. This was the first demonstration of FLIm for surgical guidance of

oropharyngeal cancer; this work correspondingly motivated a transition to classification-based analysis to leverage multivariate FLIm data and enhance cancer probability assessments. (3) For rare tumor cohorts which evade surgical detection (i.e., unknown primary tumors) after exhaustive clinical (absence of visual cues and palpation), radiographic (negative PET, CT, MRI findings), and surgical evaluation (directed biopsies of suspicious lesions), the results demonstrated that FLIm can support the localization of the primary tumor side and correctly identify uninvolved benign functional tissue. (4) In a collaborative approach integrating an expert in machine learning from our laboratory group, FLIm lifetime, intensity ratio, phasor analytical parameters, and Laguerre coefficients were systematically integrated into classification algorithms to predict cancer probability. The classifier which integrated multivariate FLIm data enhanced tumor demarcation, compared to previous approaches that relied on single FLIm parameters for benign vs. cancer contrast. (5) The effect of surgical conditions (e.g., local anesthetic use), patient demographic characteristics (e.g., patient age), biological tissue characteristics (lymphoid tissue, high-grade dysplasia), and cancer characteristics (e.g., HPV-mediated vs. non-HPV associated cancer) on FLIm data trends was investigated. Finally (6) two preliminary *in vivo* case studies demonstrated FLIm's ability to detect residual tumor presenting in electrocauterized deep margin tissue, therefore showing potential to demarcate residual tumor.

8.2 | Review of the Key Scientific Research Findings & Contributions

The following sections summarize the original contributions and scientific findings established in this research effort. *Chapter 4*, presented as a study protocol, contributed novel tools, methodologies, and techniques developed for the coregistration of histopathology to intraoperative optical imaging measurements *in vivo*. This included: (1) procedures for digital annotation of histologic grossing processes, (2) a customized tool for pathologists to digitally annotate histopathology sections, (3) processes to account for tissue deformation, (4) denoting

tissue labels on ex vivo specimen images, (5) demarcating tissue excision margins on in vivo reference images, (6) identifying and matching of anatomical landmarks of reference images between ex vivo tissue and in vivo pre-resected tissue, (7) methodology for transferring ex vivo tissue labels to in vivo pre-resected tissue, and (8) a custom-developed MATLAB tool to perform histologic labeling of surgical images, and subsequent extraction of labeled data.

This chapter focused on a key limitation in clinical optical research, which is the accurate association of optical measurements to tissue labels (e.g., benign tissue, dysplasia, cancer) as determined by ground-truth histopathology. This chapter communicated that registration errors between optical measurements and histopathology negatively affects the accuracy and validation of these technologies. Registration errors in turn become even more detrimental when developing classification algorithms where adding the correct histopathology label to each spectroscopic measurement is essential for developing training data and evaluating performance. It was articulated that despite the importance of mitigating registration error, many studies in the optical research space are unclear as to how they perform histopathology registration and account for tissue deformation between the evaluated tissue and H&E sections. These limitations accordingly impact the reproducibility of such research and devalues the accuracy of the optical technique's performance.

Suitably, this work strived to facilitate reproducibility by clearly articulating methods used in the clinical validation of FLIm using H&E histology. Due to the paucity of published methods in the optical research space for robust clinical histopathologic validation, this work aimed to provide ideas, methodologies, and tools to the scientific community to improve on current approaches. This chapter also conveyed the importance of mitigating registration errors to accurately vet optics technology and develop classification algorithms in the clinical research

space. These contributions were designed to be extrapolatable to other optical research technologies in the clinical space, therefore extending to broader optical research applications beyond FLIm.

Chapter 5 featured the first intraoperative FLIm study conducted *in vivo* for surgical guidance of oropharyngeal cancer. This work demonstrated FLIm's ability to differentiate benign tissue from cancer of the oropharynx (on palatine tonsil tumors) using both univariate and multivariate FLIm parameters. It was established that all patients presented with at least one FLIm parameter (e.g., channel 3 lifetime) that enabled benign tissue to be differentiated from cancer ($P<0.001$). The results showed that leveraging all FLIm parameters together, through linear discriminant analysis, enabled the best healthy vs. tumor contrast; this finding underscored the importance of exploring classification algorithms which integrate all FLIm lifetime and intensity ratio parameters in diagnostic decision-making, due to the enhanced discrimination capacity. The FLIm parameters which provided the best contrast across patients was variable. For example, in some patients, channel 3 intensity ratio enabled the best benign vs. tumor contrast, while for other patients, channel 1 lifetime provided the best differentiation between benign tissue and cancer. Close investigation of these results demonstrated that the parameters imparting the best FLIm-based contrast appear to bear some relationship to inherent patient tumor characteristics (e.g., p16 status) and potentially the patient's medical (i.e., age, cancer type, tobacco use, etc.). Finally, this section discovered that FLIm better identified cancer *in vivo* compared to *ex vivo*. This was observed due to the loss in metabolic-associated contrast in FLIm's spectral channels associated to metabolism (CH2: NAD(P)H & CH3: FAD). This result was anticipated due to the loss of vasculature and impeded cellular energetics of tissue imparted through the surgical excision process.

Chapter 6 evaluated whether fluorescence lifetime imaging (FLIm), coupled with standard diagnostic workups, could enhance primary lesion detection in patients with head and

neck squamous cell carcinoma of the unknown primary (HNSCCUP). These tumors represent approximately 3-5% of all new cases of head and neck squamous cell carcinoma (SCC), and are considered unknown after exhaustive clinical, radiographic, and surgical evaluation.[192–196] To conduct this study, FLIm was integrated into transoral robotic surgery to acquire optical data from 6 HNSCCUP patient's oropharyngeal tissues. An additional 55-patient FLIm dataset, comprising conventional primary tumors, trained a machine learning classifier; the output predicted the presence and location of HNSCCUP for the 6 patients. Among the 6 HNSCCUP patients, p16+ occult primary was surgically identified in 3 patients, whereas 3 patients ultimately had no identifiable primary site in the oropharynx. FLIm correctly detected HNSCCUP in all 3 patients (ROC-AUC: 0.90±0.06), and correctly predicted benign oropharyngeal tissue for the remaining 3 patients. The mean sensitivity was 95 ± 3.5%, and specificity 89 ± 12.7%. The results demonstrated that for mucosa-presenting p16+ HNSCCUP, FLIm holds great promise in aiding the surgeon, as an adjunctive technology, to screen, intraoperatively delineate, and excise these elusive tumor cohorts. Ultimately, these initial results indicated FLIm's potential to reduce surgical procedure times, preserve functional healthy tissue, and enable enhanced intraoperative decision-making for the benefit of the patient.

Chapter 7 presented various results and case studies pertaining to the collective 100-patient database analysis. *Section 7.1* outlined the composition of the 100-patient dataset with respect to anatomic sites assessed, patient characteristics, and cancer characteristics (e.g., p16 status). *Chapter 7.2* performed a full-database linear discriminant analysis (LDA) evaluation. They key findings were that phasor analysis resulted in slightly better benign vs. cancer discrimination than Laguerre-derived lifetime metrics alone, both from individual channels and through combined LDA analysis, indicating the importance of considering phasor analysis in this research effort, both in classification algorithms and in database analysis. For all patients, the univariate metrics which provided the best contrast in order were: CH3 IR > CH1 IR > CH3 LT >

CH2 IR > CH 2 LT > CH 1 LT. Combining both lifetime and intensity parameters together led to the best discrimination. Oral tongue achieved the best LDA-derived ROC-AUC (0.89±0.10). Channel 1 and 2 lifetimes did not discriminate cancer well (ROC-AUC < 0.70) in the oropharynx, however did much better at classification on oral cavity tongue (ROC-AUC > 0.70), indicating that the FLIm parameters giving rise to the best contrast may exhibit dependence on the evaluated anatomy; this result makes sense in context of the underlying physiologic and histologic differences between the oral cavity and oropharynx.

Chapter 7.3.1 investigated if the surgical use of local anesthetics in the surgical field affects FLIm properties. In the study, local anesthetics (lidocaine and epinephrine solution) were found to increase channel 1 lifetime and intensity ratio in back-to-back pre- and post-lidocaine FLIm scans, conducted on a patient's oral tongue and palatine tonsil. *Chapter 7.3.2* discovered a linear inverse relationship (R^2=0.81) between increasing patient age and decreasing channel 1 lifetime. *Chapter 7.3.3* demonstrated FLIm's potential to detect deep tumor tissue (in the range of 0.5 mm to 5 mm) through indirect imaging of biochemical alterations imparted within normal tissue adjacent to tumor. *Chapter 7.3.4* demonstrated that lymphoid tissue, which is predominantly distributed in varied proportions of oropharyngeal tissues within the lamina propria, results in increased fluorescence lifetime in all channels. *Chapter 7.3.5* assessed the univariate FLIm trends associated with high-grade dysplasia. In these case studies, FLIm properties (lifetime and intensity ratio) of HGD more closely followed cancer than benign tissue.

C*hapter 7.4* evaluated demonstrated the tendency of FLIm data (evaluated through deltas of [Δ cancer – benign]) to understand if cancer imparts a systemic and consistent shift in fluorescence lifetime and autofluorescence properties, or if more nuanced trends were identified pertaining to cancer characteristics and patient demographics. Pearson's Chi Square statistical analysis was used to explore correlated in the data. It was observed that anatomic site and tumors mediated by HPV were the most significant predictor of data trends, and that patient demographic characteristics and medical history were weakly correlated to the observed trends.

Lastly *chapter 7.5* demonstrated FLIm's ability to resolve positive surgical margins (also known as residual tumor), *in vivo* (N=2) based on univariate analysis of FLIm lifetime.

8.3 | Perspective on Next Steps to Prepare FLIm for Intraoperative Surgical Guidance

FLIm represents a promising modality for intraoperative use. Some of the major advantages of this technique includes the ability to acquire measurements while operating room lights are on, the real-time implementation, endogenous-based contrast, and point-scanning implementation which facilitates the optical interrogation of complex and tortuous anatomies of the head & neck. The collective original research established FLIm's ability to diagnose a wide variety of tumors of the oral cavity and oropharynx both through classification algorithms and resubstitution-based analysis of univariate and multivariate FLIm data. While promising, these research findings are the product of retrospective data optimization, which would need to be accounted for in real time for actual diagnosis and intraoperative decision-making. This optimization includes: (1) accounting for surgical motion in real-time to maintain accurate augmentation of acquired FLIm datapoints to the location acquired on tissue, (2) correcting incorrect localization, and thereby augmentation, of the FLIm data, and (3) real-time machine learning outputs, which integrate all FLIm analytical metrics, to predict cancer probability. While still under development, our group's ongoing research seeks to have solutions for this in the near future, with feasibility recently demonstrated.[166]

Two central limitations of the present study exist, both being based on the reliance of histopathology for validation. First, as *chapter 4* addressed, the incorrect registration of histopathology to optical imaging measurements affects the validation efforts of this project. While registration error is unavoidable, the proposed schema introduced in *chapter 4* sought to mitigate potential for error. The second, arguably most significant limitation, is the reliance on hematoxylin and eosin-stained slides to provide the "ground truth" in this study. While pathologist interpreted H&E slides are the gold standard for identifying pathologic tissue in this

field, H&E is acknowledged as an imperfect standard; this is due to H&E reporting on structural stained cellular characteristics, rather than on genetic and biochemical characteristics. Along these lines, FLIm may exhibit sensitivity to tumor biochemistry (e.g., pH, metabolic gradients, etc.), however such characteristics cannot be corroborated against FLIm's optical measurements since such information is absent in H&E. To this end, approaches which perform molecular analysis on small regions of tissue, obtained through laser microdissection, as well as alternate stains, such as trichrome, have been proposed to enhance the input data available to be associated to optical measurements.

The use of genomic analysis to characterize FLIm data is currently under investigation by our group. For this research, protocols to spatially resolve gene expression in formalin-fixed paraffin-embedded (FFPE) tissue sections have been obtained from 10x Genomics. This protocol allows for FFPE tissue sections to be obtained through laser microdissection of tissue microarrays and correspondingly evaluated for gene expression. The protocol uses RNA-templated ligation, where pairs of probes specific to genes in the protein-coding transcriptome are hybridized to their gene targets and ligated to one another. The tissue thereafter is permeabilized to release ligated probe pairs to bind to capture probes on the side, thereby enabling the evaluation of gene expression. The complete protocol is available at 10xgenomics.com, protocol CG000240, revision C.

For robust clinical diagnosis, FLIm is trending towards the direction of machine learning, both to assist with data visualization and in data analysis (due to the complex multiparametric nature of FLIm data). There is still significant progress to be made in the classification aspect of this project. This includes further investigating deep learning and central neural network approaches, exploring alternate decision-tree optimization approaches (e.g., XGBoost), inclusion of other FLIm parameters (e.g., multiexponential fitting, phasors, etc.), and incorporation of patient metadata (e.g., tobacco use, p16 status, age, etc.).

Recent technical and methodological advancements are rapidly facilitating FLIm hardware towards clinical adoption.[2] Zhou X. et al. recently (2021) demonstrated new FLIm hardware[229] which improves upon the FLIm system used in the course of this original research. This new FLIm system has up to a 5-fold reduction in measurement variability, independent gain adjustment of spectral bands, up to 4-times faster imaging speed, and increased signal-to-noise ratio. It is anticipated that the incorporation of these hardware improvements will improve upon current sensitivity and specificity results; these improvements are expected due to the reduced measurement variability and density of acquired datapoints, which would better enable statistical rigor and improvements to data used for training and evaluation of classifiers.

Under a R01 renewal, 200 additional patients are to be enrolled and investigated within targeted 4-year period, which began July 2021. The additional patient enrollment with the revised FLIm system developed by Zhou X. et al[229] will further enhance the available data for classification algorithms and accounting for patient medical histories and demographic information.

Other ongoing intraoperative investigation using FLIm in the head & neck oncology includes the investigation of FLIm for identifying lymph node metastases. For patients with HNSCC, there is up to a 30% chance of occult nodal metastasis at the time of surgery.[230] This finding is despite negative clinical and radiographic evidence of neck lymph node metastasis. Accordingly, it is routine for patients to undergo a preemptive elective neck dissection in search of lymph node metastases.[230] Identification of metastatic lymph nodes remains a challenge, and is critical for accurate staging and guides the extent of adjuvant therapy and prognosis.[230] Current ongoing work by our group is investigating the optical evaluation of surgically excised and bisected lymph nodes in a surgical grossing room environment to see if benign vs. cancer-associated lymph nodes can be detected. If working, this finding can enhance surgical decision-making and patient treatment at the point-of-care during surgery.

Collectively, this original research demonstrates the feasibility for FLIm to intraoperatively demarcate carcinoma during upper aerodigestive oncology procedures, therefore motivating ongoing investigation to materialize this technology towards an intraoperative diagnostic modality. If real-time intraoperative use proves to be as efficacious as the current retrospective analysis demonstrates, this technology can have dramatic impacts in clinical practice through enabling rapid identification of neoplastic tissue and the confirmation of negative surgical margins.

8.4 | The Big Picture – Towards Clinical Adoption

While the widespread clinical adoption of optical technology (such as FLIm) is still far from the status achieved by radiology and nuclear-based imaging methods, intraoperative tissue assessments based on optical methods have gained significant ground. A paramount example of this is optical coherence tomography (OCT), which is currently the standard-of-care in ophthalmology.[231] In general, optical imaging techniques are well suited for providing clinicians with real-time feedback at the point-of-care. Optical technologies are non-ionizing (unlike X-ray & positron emission tomography modalities), can be designed to be portable, are cost-effective, and many can be integrated into clinical workflows. A key advantage of FLIm, which is shared across most implementations of optical technology, is the ability to interrogate tissue for information without administering exogenous contrast, which facilitates the ease to implement these devices in real-time within clinical settings. When external contrast needs to be applied, additional time needs to be expended to prepare and administer the contrast agent, in addition to considering pharmacokinetic and pharmacodynamic properties.

As discussed by Gioux et al.,[232] there are three general criteria which serve as prerequisites to adopt novel clinical technologies: (1) the existence of a clinical need, (2) the ability of the technology to solve or ameliorate challenges pertaining to the clinical need, and (3) the ability for the proposed technology to integrate seamlessly into existing clinical workflows

without impeding the surgical procedure. The work herein has articulated FLIm's ability to address criteria 1 & 2 in detail, whereas the focus of this remaining section is to address FLIm's ability to fulfill criteria 3.

Gorpas et al. in 2019 demonstrated FLIm's ability to integrate into transoral robotic surgery using the da Vinci Si platform without impeding the surgical workflow,[134] whereas Weyers et al. demonstrated this integration into the da Vinci SP in 2022.[233] A key advantage of FLIm is the ability to conduct measurements in the presence of any operating room lighting conditions; the dynamics of FLIm instrumentation permit imaging irrespective of tissue illumination. The point-scanning implementation of FLIm is well-suited for both small (sub-centimeter) and large (centimeter scale) tumor volumes within complex anatomy (i.e., anatomy with uneven surfaces, flaps, ceases), enabling versatile interrogation of tumors in a variety of conformations. This ability to rapidly evaluate tissue over large scales is a significant advantage which helps mitigate the potential for sampling error and increases the breadth of applications. For example, with respect to intraoperative tumor resection, it is required to first locate relatively large tumor masses (millimeters to centimeters), particularly for occult primary tumors. To achieve impactful outcomes which has a direct impact on patient survival rates, it becomes necessary to directly identify regions of infiltrating cells, as such cells are often responsible for cancer recurrence. This is where the ability to interrogate large tissue areas using FLIm's point-scanning implementation becomes beneficial.

FLIm's ability to be transported in and out of the operating room, like ultrasound, is significant. Consider CT, MRI, and PET - for these modalities, a patient must be brought to the imaging device, time must be expended to position and situate the patient for scanning, and in many cases, contrast agents need to be prepared (e.g., iodine for CT, radiotracers for PET) and systemically injected. FLIm alternatively is setup at the point-of-care, where the device can be brought to the patient during surgery and manipulated to conduct measurements on demand.

Safety is an important factor to fulfill criteria 3. The emission of the clinical FLIm instrument reported herein is categorized under class 2 of 21 CFR 1040.10, and operates at energy levels well below the limits for eye/skin exposure stipulated by ANSI Z136.1, therefore being considered safe for standard operation without specific eye protection from system operators or personnel within the vicinity of the instrument.

Beyond otolaryngology, FLIm is able to be deployed for oncology investigation in other areas, such as in brain tumors, breast cancer, prostate cancer, atherosclerosis, among others.[2] While the magnitude of spectral intensities and trends corresponding to time-resolved characteristics between benign tissue and cancer may change depending on the oncology application (e.g., absence of collagen in normal brain tissue), our group has experienced success deploying this technology across oncology disciplines due to the general conservation of fluorophores (e.g., NAD(P)H, FAD) and cancer vs. benign tissue properties (i.e., Warburg effect) across various anatomies.[2]

From a surgeon's perspective, the clinical adoption of FLIm requires clear, interpretable outputs which is generalizable and understandable across healthcare professionals. FLIm data is complicated, with multivariate time-resolved and spectral-intensity parameters. Designing FLIm outputs which seamlessly synthesize the complexity of FLIm data into clear outputs (such as probability of cancer) which aid in surgical decision-making will remain imperative.

Medical device technology transfer remains a complex process, but ultimately needs to be addressed thoroughly through both the invention and implementation stages to achieve clinical adoption. Clark D. et al. in 2019 characterized the medical technology pathway as follows: (1) *conception* – intent & definition, (2) *creation* – design & development, (3) *confirmation* – verification and validation, (4) *realization* – processes and information, (5) *production* – product and services, (6) *provision* – supply and diffusion, and (7) *improvement* – safety and effectivness.[234] 1-4 correspond to the invention stages, whereas 5-7 correlate to

implementation stages.[234] FLIm is currently in the *confirmation* stage 3, which comprises verification and validation processes. Key next steps towards clinical trials should focus on a study design with the following characteristics as suggested by Clark D. et al.[234] – the study should be simple, tailored to a patient group, designed to address clear questions of clinical importance, and appropriately blinded outcomes assessments and controls. During design transfer, the healthcare environment will need to be carefully considered in the development of the final prototype. This requires clear communication between engineering teams and clinicians to ensure clinical/user needs are being addressed, that the FLIm system is ergonomically favorable to the clinician, and that the technology does not impede any current health management workflows.

While the future for FLIm is promising, there is still significant ground to cover to achieve clinical adoption. This includes but is not limited to preparation for clinical trials, continued successful multi-institutional clinical outcomes, consideration of human factors, design transfer, production processes, regulatory evidence, GMP manufacturing, training, logistics, distribution, marketing, deployment, adoption, post-marketing surveillance, impact assessments, etc.[234] While the process appears complex, the path to success that other prominent optical modalities took towards clinical adoption (i.e., OCT) can be evaluated and leveraged to improve the current technology translation pathway for FLIm.

Despite significant ground to still cover, FLIm holds great promise in aiding surgeons in their goal of balancing aggressiveness in tumor extirpation and conservation of benign functional tissue. By providing surgeons with accurate tools to intraoperatively quantify the extent of tumor, the time to complete the surgical procedure will be accelerated and the potential for positive surgical margins will be reduced; this will undeniably support the healthcare industry by allowing clinicians to treat more patients, to enhance the precision and accuracy of

surgical treatment, and will reduce risk to the patient with decreased time under anesthesia and enhanced accuracy of tumor removal through the optimization of the surgical procedure.

APPENDIX | Supplementary Data (Reference Only)

Table A9. Tonsil (N=34) Demographics, Clinical Characteristics, and Surgical Outcomes.

Anatomy & ID	Cancer Class	Gender	Race	HPV Status	Tobacco Use	Age at Surgery
Tonsil (6)	5	M	White	Negative	Non-Smoker	55
Tonsil (48)	1	M	White	Negative	Smoker	51
Tonsil (66)	1	M	White	Negative	Smoker	67
Tonsil (51)	5	M	White	Negative	Smoker	68
Tonsil (71)	1	M	White	Negative	Non-Smoker	62
Tonsil (29)	1	M	White	Negative	Smoker	58
Tonsil (2)	1	M	White	Negative	Smoker	77
Tonsil (14)	6	M	White	Positive	Non-Smoker	54
Tonsil (37)	5	M	White	Positive	Non-Smoker	57
Tonsil (26)	5	M	White	Positive	Non-Smoker	58
Tonsil (44)	5	M	White	Positive	Non-Smoker	63
Tonsil (81)	5	M	White	Positive	Non-Smoker	71
Tonsil (59)	5	M	White	Positive	Non-Smoker	72
Tonsil (60)	5	M	White	Positive	Smoker	47
Tonsil (7)	5	M	White	Positive	Smoker	57
Tonsil (41)	5	M	White	Positive	Smoker	58
Tonsil (24)	5	M	White	Positive	Smoker	64
Tonsil (5)	6	M	White	Positive	Smoker	65
Tonsil (92)	5	M	White	Positive	Smoker	66
Tonsil (52)	5	M	White	Positive	Smoker	69
Tonsil (16)	5	M	White	Positive	Smoker	70
Tonsil (13)	5	M	White	Positive	Smoker	71
Tonsil (99)	5	M	White	Positive	Smoker	71
Tonsil (31)	5	M	White	Positive	Smoker	73
Tonsil (94)	5	M	White	Positive	Smoker	81
Tonsil (12)	5	M	Hispanic/Latino	Negative	Smoker	49
Tonsil (33)	5	M	Hispanic/Latino	Positive	Non-Smoker	43
Tonsil (90)	5	M	Hispanic/Latino	Positive	Non-Smoker	49
Tonsil (82)	5	M	Hispanic/Latino	Positive	Smoker	43
Tonsil (97)	5	M	Hispanic/Latino	Positive	Smoker	57
Tonsil (35)	1	F	White	Negative	Non-Smoker	75
Tonsil (30)	5	F	White	Positive	Non-Smoker	57
Tonsil (36)	5	F	White	Positive	Non-Smoker	64
Tonsil (31)	5	F	White	Positive	Smoker	73

Pathology Report Cancer Class Designations: (1) Benign tissue or low-grade dysplasia, (2) Polymorphous adenocarcinoma or condyloma, (3) Squamous Cell Carcinoma (SCC) in situ and non-invasive SCC, (4) Verrucous SCC, (5) SCC and Invasive SCC, (6) Basaloid SCC. '*Non-Smoker'* defined as a patient with a reported use of less than 100 total cigarettes in entire lifespan.

Table A10. Base of Tongue (N=16) Demographics, Clinical Characteristics, and Surgical Outcomes.

Anatomy & ID	Cancer Class	Gender	Race	HPV Status	Tobacco Use	Age at Surgery
BOT (4)	1	M	White	Negative	Non-Smoker	54
BOT (58)	5	M	White	Negative	Smoker	64
BOT (84)	5	M	White	Positive	Non-Smoker	51
BOT (45)	5	M	White	Positive	Non-Smoker	54
BOT (70)	5	M	White	Positive	Non-Smoker	59
BOT (18)	1	M	White	Positive	Non-Smoker	75
BOT (83)	5	M	White	Positive	Smoker	66
BOT (80)	5	M	White	Positive	Smoker	66
BOT (28)	6	M	White	Positive	Smoker	71
BOT (47)	5	M	White	Positive	Smoker	71
BOT (63)	5	M	White	Positive	Smoker	74
BOT (87)	5	M	White	Positive	Smoker	77
BOT (100)	5	M	White	Positive	Smoker	78
BOT (64)	5	M	White	Positive	Smoker	79
BOT (69)	5	M	Hispanic/Latino	Negative	Non-Smoker	66
BOT (93)	1	M	Hispanic/Latino	Negative	Non-Smoker	66

Pathology Report Cancer Class Designations: (1) Benign tissue or low-grade dysplasia, (2) Polymorphous adenocarcinoma or condyloma, (3) Squamous Cell Carcinoma (SCC) in situ and non-invasive SCC, (4) Verrucous SCC, (5) SCC and Invasive SCC, (6) Basaloid SCC. '*Non-Smoker'* defined as a patient with a reported use of less than 100 total cigarettes in entire lifespan.

Table A11. 'Other' Anatomy (N=15) Demographics, Clinical Characteristics, and Surgical Outcomes.

Anatomy & ID	Cancer Class	Gender	Race	HPV Status	Tobacco Use	Age at Surgery
Glossotonsillar Sulcus (67)	5	M	White	Negative	Non-Smoker	50
Pharynx (95)	5	M	White	Negative	Smoker	54
Pharynx (15)	6	M	White	Positive	Smoker	66
Floor of Mouth (17)	5	M	White	Negative	Smoker	78
Floor of Mouth (96)	5	F	White	Unknown	Smoker	60
Lip (57)	2	M	White	Negative	Smoker	82
Retromolar Trigone (72)	5	M	Asian	Positive	Non-Smoker	48
Gingiva (76)	5	M	White	Unknown	Smoker	62
Gingiva (38)	5	M	White	Unknown	Smoker	72
Gingiva (88)	5	F	White	Negative	Non-Smoker	63
Gingiva (79)	1	F	White	Unknown	Non-Smoker	90
Palate (91)	5	M	White	Unknown	Smoker	83
Palate (56)	2	F	Hispanic/Latino	Negative	Non-Smoker	54
Vallecula (98)	5	M	White	Positive	Non-Smoker	51
Vallecula (85)	5	M	White	Unknown	Non-Smoker	63

Pathology Report Cancer Class Designations: (1) Benign tissue or low-grade dysplasia, (2) Polymorphous adenocarcinoma or condyloma, (3) Squamous Cell Carcinoma (SCC) in situ and non-invasive SCC, (4) Verrucous SCC, (5) SCC and Invasive SCC, (6) Basaloid SCC. '*Non-Smoker'* defined as a patient with a reported use of less than 100 total cigarettes in entire lifespan.

Table A12. Oral Tongue (N=27) Demographics, Clinical Characteristics, and Surgical Outcomes.

Anatomy & ID	Cancer Class	Gender	Race	HPV Status	Tobacco Use	Age at Surgery
Oral Tongue (68)	5	M	White	Negative	Non-Smoker	57
Oral Tongue (50)	1	M	White	Negative	Smoker	53
Oral Tongue (65)	1	M	White	Negative	Smoker	69
Oral Tongue (62)	5	M	White	Negative	Smoker	71
Oral Tongue (73)	5	M	White	Positive	Smoker	54
Oral Tongue (55)	5	M	White	Unknown	Non-Smoker	69
Oral Tongue (27)	5	M	White	Unknown	Smoker	40
Oral Tongue (77)	5	M	White	Unknown	Smoker	63
Oral Tongue (34)	5	M	White	Unknown	Smoker	66
Oral Tongue (25)	5	M	White	Unknown	Smoker	68
Oral Tongue (74)	5	M	White	Unknown	Smoker	73
Oral Tongue (43)	5	M	White	Unknown	Smoker	76
Oral Tongue (32)	5	M	Hispanic/Latino	Unknown	Smoker	73
Oral Tongue (61)	5	M	Indian (India)	Negative	Non-Smoker	23
Oral Tongue (46)	5	M	Unknown	Unknown	Smoker	76
Oral Tongue (75)	5	F	White	Negative	Smoker	62
Oral Tongue (89)	5	F	White	Negative	Smoker	76
Oral Tongue (20)	5	F	White	Negative	Non-Smoker	64
Oral Tongue (39)	4	F	White	Unknown	Non-Smoker	69
Oral Tongue (49)	5	F	White	Unknown	Non-Smoker	81
Oral Tongue (53)	5	F	White	Unknown	Smoker	60
Oral Tongue (86)	5	F	White	Unknown	Smoker	73
Oral Tongue (23)	5	F	White	Unknown	Smoker	75
Oral Tongue (22)	5	F	White	Unknown	Smoker	82
Oral Tongue (78)	5	F	Asian	Negative	Non-Smoker	75
Oral Tongue (54)	5	F	Asian	Unknown	Non-Smoker	66
Oral Tongue (42)	5	F	Asian	Unknown	Smoker	62

Pathology Report Cancer Class Designations: (1) Benign tissue or low-grade dysplasia, (2) Polymorphous adenocarcinoma or condyloma, (3) Squamous Cell Carcinoma (SCC) in situ and non-invasive SCC, (4) Verrucous SCC, (5) SCC and Invasive SCC, (6) Basaloid SCC. '*Non-Smoker'* defined as a patient with a reported use of less than 100 total cigarettes in entire lifespan.

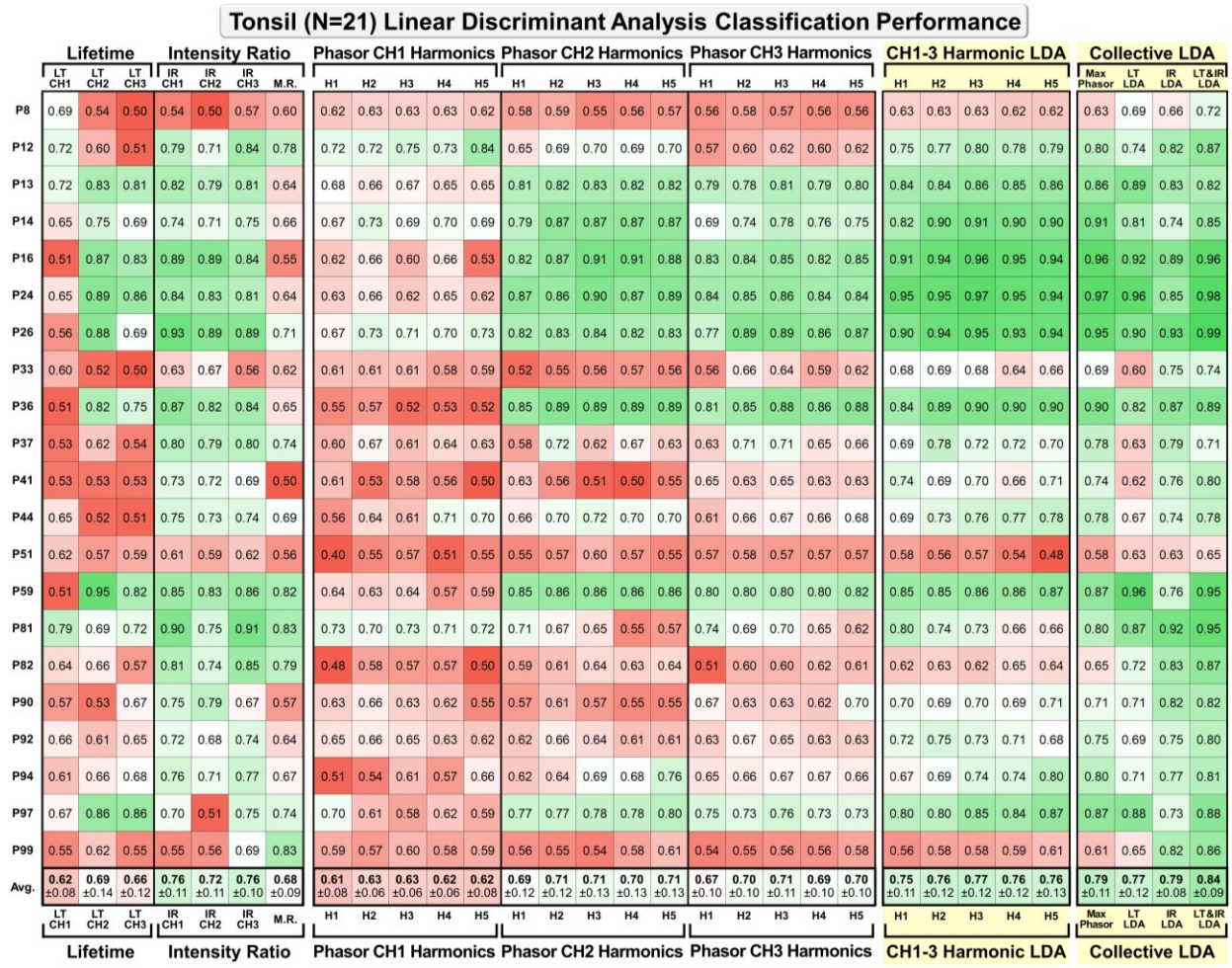

Figure A54: Tonsil (N=21) linear discriminant analysis classification performance. '*M.R.*' corresponds to metabolic ratio defined as [CH2] / ([CH2]+[CH3]). '*H1-H5*' represent the first harmonic (ω= ω0) to fifth harmonic (ω= 5ω0) of a given phasor channel. '*CH1-3 Harmonic LDA*' reports the AUC arising from the weighted linear combination of CH1, CH2, and CH3 phasors evaluated at each of the five harmonics. '*Max Phasor*' reports the highest AUC arising from a given patient from the best CH1-3 weighted linear phasor harmonic combination. '*LT LDA*' is the result of the weighted linear combination of CH1-3 lifetime. *'IR LDA'* is defined as the combination if CH1-3 intensity ratio and M.R. and '*LT & IR* LDA' reports the AUC from the combination of all seven parameters: CH1-3 lifetime, CH1-3 IR, and M.R.

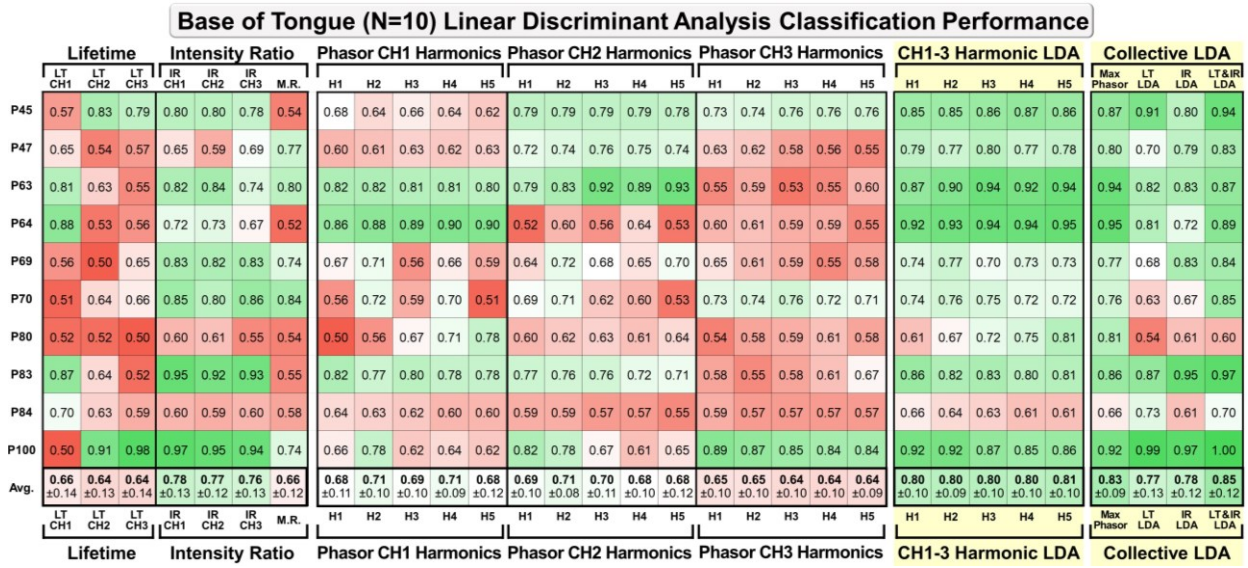

Figure A55: Base of tongue (N=10) linear discriminant analysis classification performance. '*M.R.*' corresponds to metabolic ratio defined as [CH2] / ([CH2]+[CH3]). '*H1-H5*' represent the first harmonic (ω= ω0) to fifth harmonic (ω= 5ω0) of a given phasor channel. '*CH1-3 Harmonic LDA*' reports the AUC arising from the weighted linear combination of CH1, CH2, and CH3 phasors evaluated at each of the five harmonics. '*Max Phasor*' reports the highest AUC arising from a given patient from the best CH1-3 weighted linear phasor harmonic combination. '*LT LDA*' is the result of the weighted linear combination of CH1-3 lifetime. *'IR LDA'* is defined as the combination if CH1-3 intensity ratio and M.R. and '*LT & IR* LDA' reports the AUC from the combination of all seven parameters: CH1-3 lifetime, CH1-3 IR, and M.R.

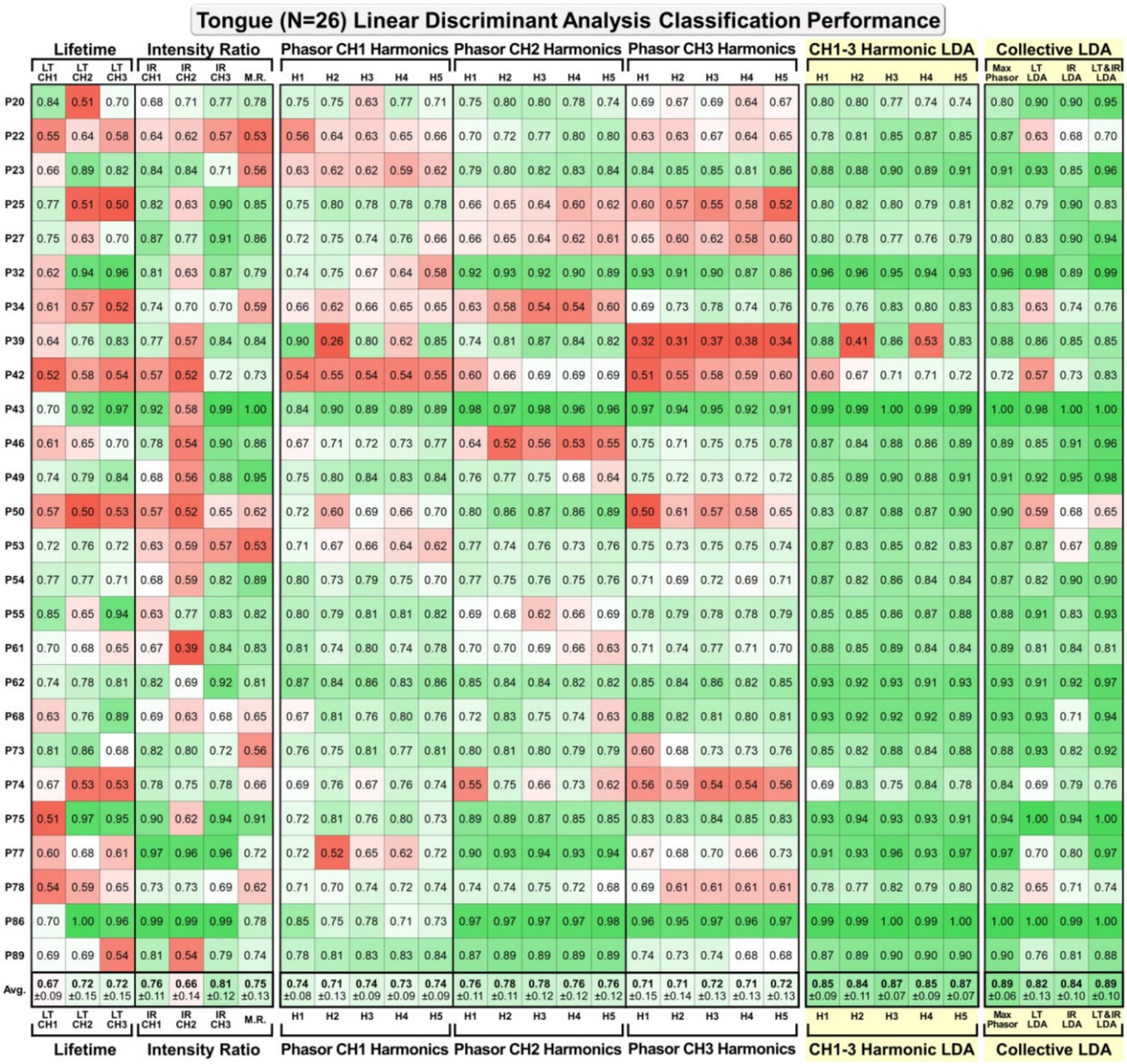

Figure A56: Oral tongue (N=26) linear discriminant analysis classification performance. '*M.R.*' corresponds to metabolic ratio defined as [CH2] / ([CH2]+[CH3]). '*H1-H5*' represent the first harmonic (ω= ω0) to fifth harmonic (ω= 5ω0) of a given phasor channel. '*CH1-3 Harmonic LDA*' reports the AUC arising from the weighted linear combination of CH1, CH2, and CH3 phasors evaluated at each of the five harmonics. '*Max Phasor*' reports the highest AUC arising from a given patient from the best CH1-3 weighted linear phasor harmonic combination. '*LT LDA*' is the result of the weighted linear combination of CH1-3 lifetime. *'IR LDA'* is defined as the combination if CH1-3 intensity ratio and M.R. and '*LT & IR* LDA' reports the AUC from the combination of all seven parameters: CH1-3 lifetime, CH1-3 IR, and M.R.

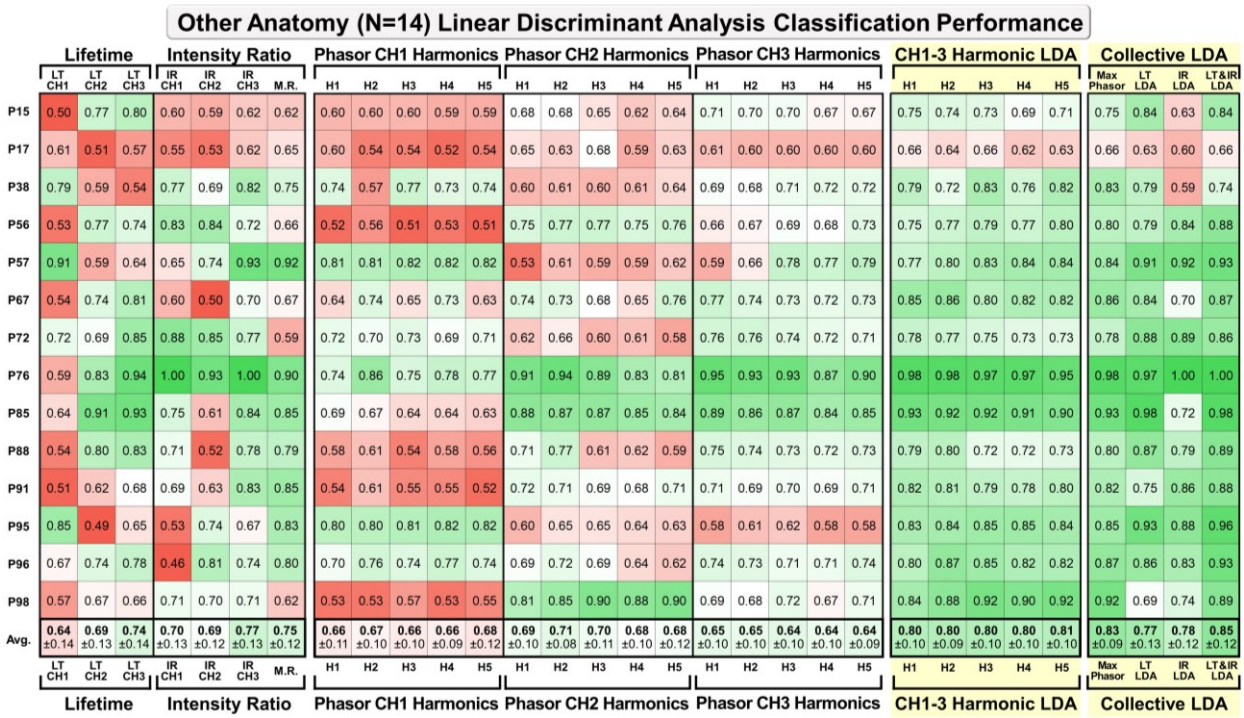

Figure A57: 'Other Anatomy' (N=14) linear discriminant analysis classification performance. '*M.R.*' corresponds to metabolic ratio defined as [CH2] / ([CH2]+[CH3]). '*H1-H5*' represent the first harmonic (ω= ω0) to fifth harmonic (ω= 5ω0) of a given phasor channel. '*CH1-3 Harmonic LDA*' reports the AUC arising from the weighted linear combination of CH1, CH2, and CH3 phasors evaluated at each of the five harmonics. '*Max Phasor*' reports the highest AUC arising from a given patient from the best CH1-3 weighted linear phasor harmonic combination. '*LT LDA*' is the result of the weighted linear combination of CH1-3 lifetime. *'IR LDA'* is defined as the combination if CH1-3 intensity ratio and M.R. and '*LT & IR* LDA' reports the AUC from the combination of all seven parameters: CH1-3 lifetime, CH1-3 IR, and M.R.

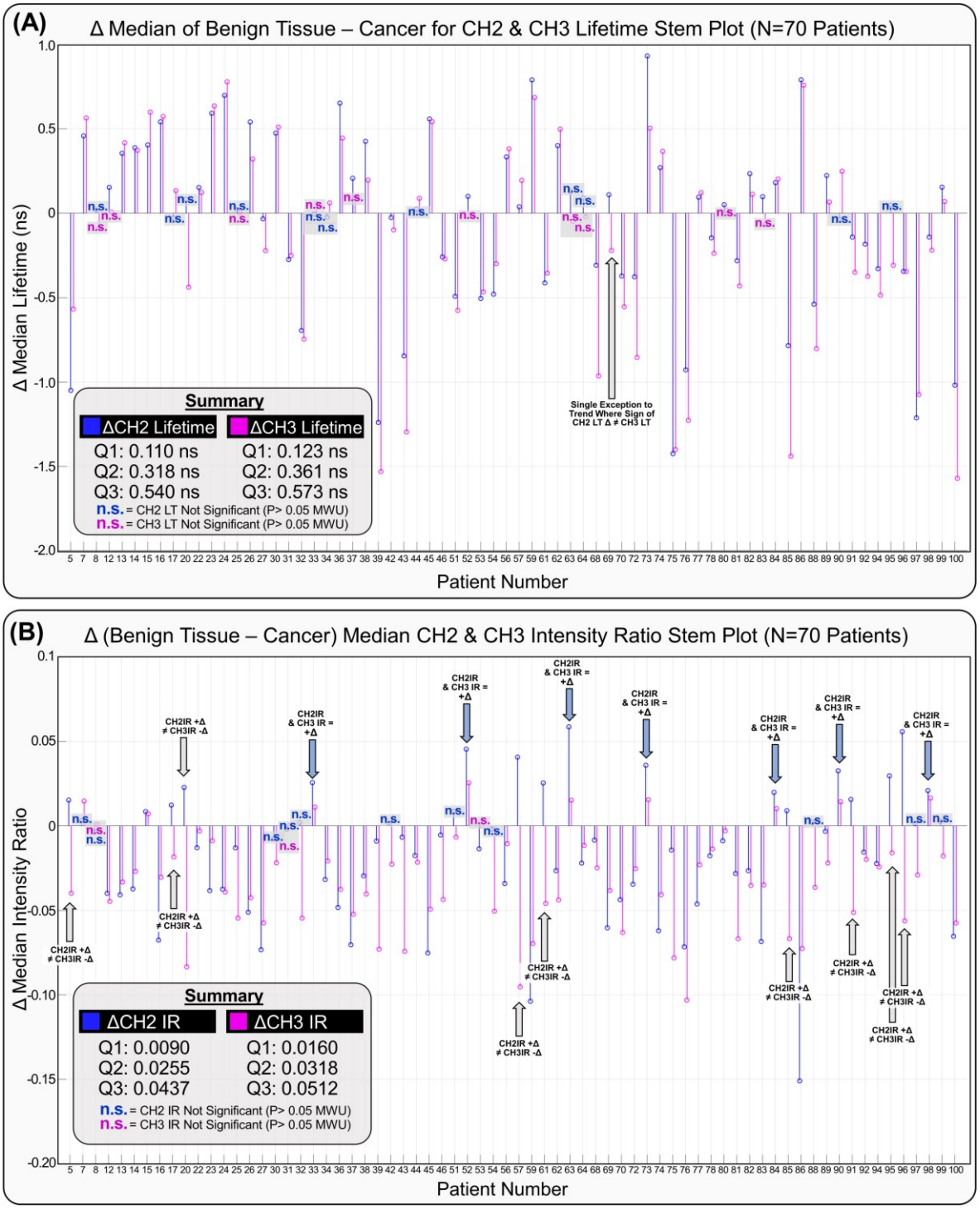

Figure A58: *In vivo* evaluation of CH2 (NADPH) & CH3 (FAD) lifetime and intensity ratio cancer trends. (A) Median of patient-level benign tissue vs. cancer lifetime for channel 2 & 3. (B) Median of patient-level benign tissue vs. cancer intensity ratio for channel 2 & 3. Positive Δ value indicates FLIm-parameter for benign tissue is higher than cancer, and vice versa for negative Δ value. All values expressed as the difference (Δ) in median optical metabolic ratio for a given patient between benign tissue and cancer. Medians were only computed if at least 30 FLIm datapoints registered to both benign tissue and cancer were obtained. Values expressed as a stem plot, where 'n.s.' indicates the median between patient-level benign tissue vs. cancer were not significant by Mann-Whitney U significance testing.

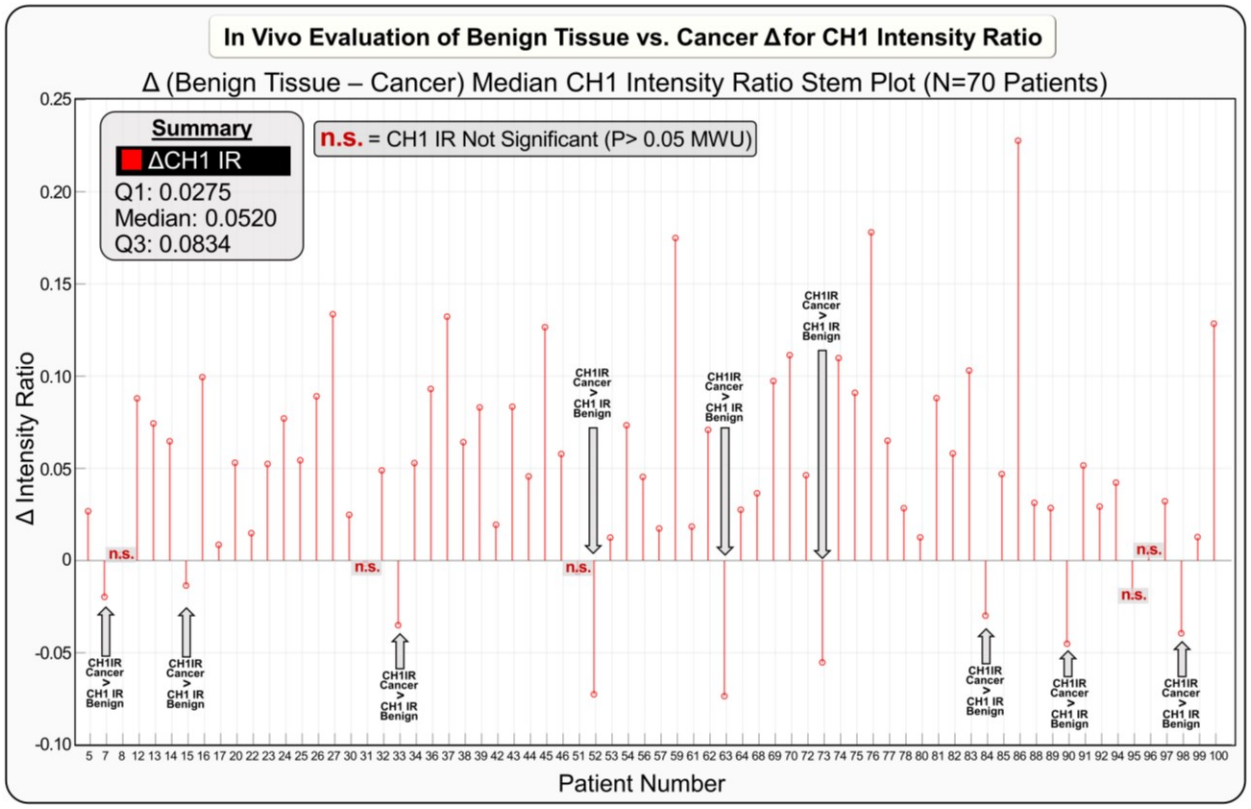

Figure A59: In Vivo Evaluation of Benign Tissue vs. Cancer Trends for CH1 (collagen) Intensity Ratio between benign tissue and cancer. Positive Δ value indicates CH1 intensity ratio for benign tissue is higher than cancer, and vice versa for negative Δ value. All values expressed as the difference (Δ) in median optical metabolic ratio for a given patient between benign tissue and cancer. Medians were only computed if at least 30 FLIm datapoints registered to both benign tissue and cancer were obtained. Values expressed as a stem plot, where 'n.s.' indicates the difference between patient-level benign vs. cancer CH1 IR datapoints were not significant by Mann-Whitney U significance testing.

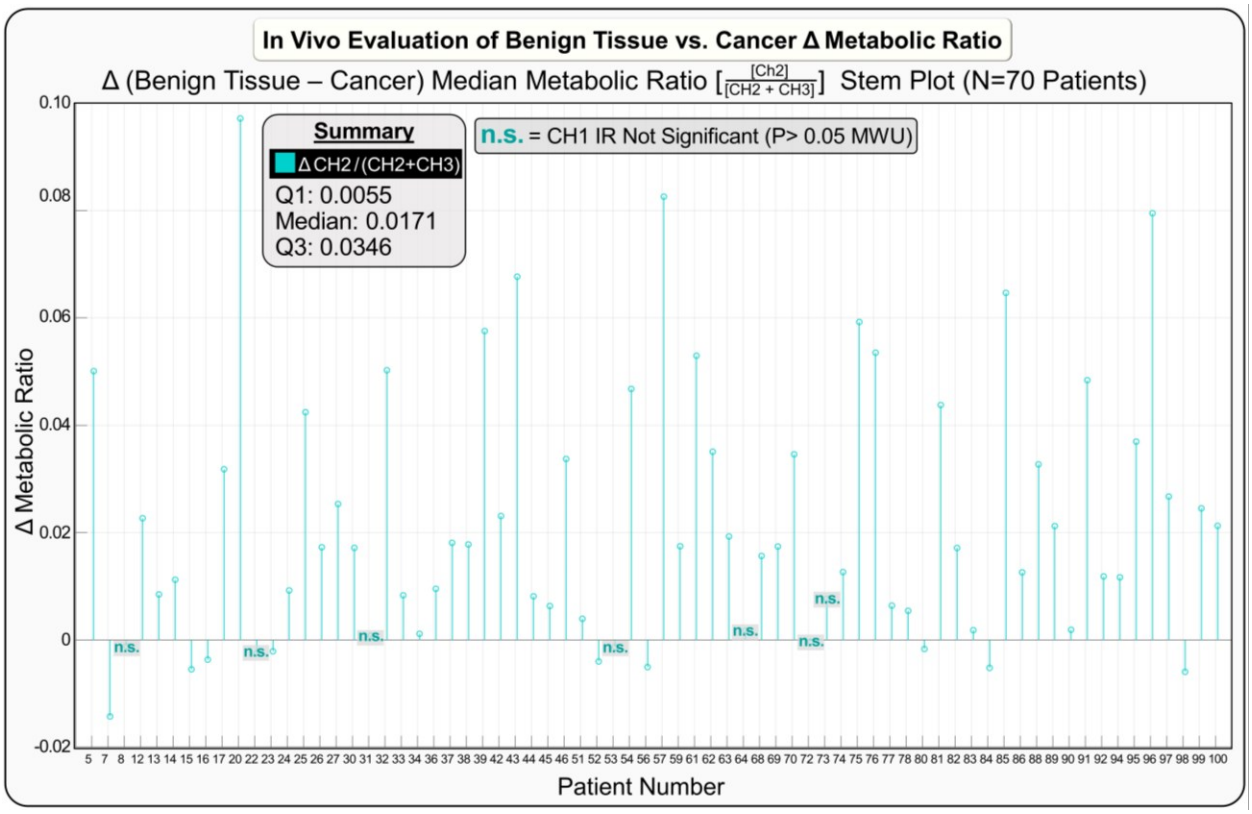

Figure A60: In Vivo Evaluation of Benign Tissue vs. Cancer Δs for Metabolic Ratio CH2/(CH2+CH3) trends between benign tissue and cancer. Positive Δ value indicates the ratio of CH2 / [CH2+CH3] for benign tissue is higher than cancer, and vice versa for negative Δ value. All values expressed as the difference (Δ) in median optical metabolic ratio for a given patient between benign tissue and cancer. Medians were only computed if at least 30 FLIm datapoints registered to both benign tissue and cancer were obtained. Values expressed as a stem plot, where 'n.s.' indicates the difference between patient-level benign vs. cancer optical metabolic ratio datapoints were not significant by Mann-Whitney U significance testing.

LIST OF ABBREVIATIONS

AUC – Area Under the Curve
BOT – Base of Tongue
CDC – Centers for Disease Control
CH – Channel (In Reference to FLIm Spectral Channels 1, 2, 3, or 4)
CLS – Constrained Least Squares (Deconvolution Method)
CNN – Convolutional Neural Network
ECM – Extracellular Matrix
FAD – Flavin Adenine Dinucleotide
FLIm – Fluorescence Lifetime Imaging
FLIM – Fluorescence Lifetime Microscopy
FN – False Negative
FOV – Field of View
FP – False Positive
FPR – False Positive Rate (FP/[TN+FP])
FPS – Frames Per Second
FWHM – Full Width at Half Maximum
GTS – Glossotonsillar Sulcus
GUI – Graphical User Interface
H&E – Hematoxylin and Eosin
H&N – Head and Neck
HGD – High Grade Dysplasia
HIPPA – Health Insurance Portability and Accountability Act
HIV – Human Immunodeficiency Virus
HNSCCUP – Head and Neck Squamous Cell Carcinoma of Unknown Primary Origin
HPV – Human Papilloma Virus
HRME – High Resolution Microendoscopy
HSV – Hue Saturation Value
IR – Intensity Ratio (FLIm Univariate Parameter)
IRB – Institutional Review Board
IRF – Impulse Response Function
LDA – Linear Discriminant Analysis
LGD – Low Grade Dysplasia
LT – Lifetime (FLIm Univariate Parameter)
LT – Lingual Tonsil
MA – Methamphetamine
MAD – Median Absolute Deviation
MATLAB – Matrix Laboratory Software (Release R2018b)
MMP – Matrix Metalloproteinase
MRI – Magnetic Resonance Imaging
NAD(P)H – Nicotinamide Adenine (Phosphate) Dinucleotide
NAS – Nasopharynx
NAT – Normal Tissue Adjacent to Tumor

NBI – Narrow Band Imaging
OCT – Optical Coherence Tomography
OLP – Oral Lichen Planus
p16- – HPV Negative (Determined by no P16 Protein Antibody Binding)
p16+ – HPV Positive (Determined by P16 Protein Antibody Binding)
PAI – Photoacoustic Imaging
PET – Positron Emission Tomography
PPIX – Protoporphyrin IX
PSM – Positive Surgical Margin
PSM – Positive Surgical Margin
PT – Palatine Tonsil
RF – Random Forrest (Classifier)
ROC-AUC – Receiver Operator Characteristic Area Under the Curve
SCC – Squamous Cell Carcinoma
SNR – Signal to Noise Ratio
SVM – Support Vector Machine
TCSPC – Time Correlated Single Photon Counting
TN – True Negative
TORS – Transoral Robotic Surgery
TP – True Positive
TPR – True Positive Rate (TP/[TP+FN])
TRFS – Time Resolved Fluorescence Spectroscopy
UBM – Ultrasound Backscatter Microscopy
US – Ultrasound
UV – Ultraviolet
WSM – Wavelength Selection Module

COPYWRITE PERMISSIONS

Chapter 2.2 | Figure 3

Figure Reproduced From**:** Alfonso-Garcia A, Bec J, **Weyers BW**, Marsden M, Zhou X, Li C, Marcu L. Mesoscopic fluorescence lifetime imaging: fundamental principles, clinical applications, and future directions. *J. Biophotonics* e202000472 (2021) doi:10.1002/jbio.202000472.

Reproduced in thesis/dissertation with permission from John Wiley and Sons - *Journal of Biophotonics*. Licensed Content Title *Mesoscopic fluorescence lifetime imaging: Fundamental principles, clinical applications and future directions*. Type of use: Dissertation/Thesis; Requestor type: Author of this Wiley article; Format: Electronic; Portion: Figure/table, Number of figures/tables: 1. Order placed through the Copyright Clearance Center's RightsLink® service. Order Date: Aug 12, 2021. Order Number: 5126650051626.

Chapter 5 | Application of FLIm for Intraoperative Delineation of Primary Tumors of the Oropharynx: An Initial 10-Patient Feasibility Study

Chapter Reproduced with Modifications From: **Weyers BW**, Marsden M, Sun T, Bec J, Bewley AF, Gandour-Edwards RF, Moore MG, Farwell DG, Marcu L. Fluorescence lifetime imaging for intraoperative cancer delineation in transoral robotic surgery. *Transl. Biophotonics* (2019) doi:10.1002/tbio.201900017.

Text and figures reproduced with permission from Wiley Online Library - *Translational Biophotonics* under the creative commons attribution license. Per the permissions: "All articles published in this journal are made available under the terms of the Creative Commons Attribution License. Permission is therefore not required for academic or commercial reuse, provided that full attribution is included in the new work." Type of use: Dissertation/Thesis; Requestor type: Article 1st Author; Format: Electronic; Portion: Entire Manuscript with Modifications, Permissions Verification Date: Aug 12, 2021.

Chapter 6 | Intraoperative Label-Free FLIm for Real-Time Delineation of p16+ Oropharyngeal Carcinoma of Unknown Primary Origin: An 8-Patient Preliminary Investigation

Chapter Reproduced with Modifications From: **Weyers BW**, Birkeland AC, Marsden MA, Tam AJ, Bec J, Frusciante RP, Gui D, Bewley AF, Abouyared MA, Marcu L, and Farwell DG. Intraoperative delineation of p16+ oropharyngeal carcinoma of unknown primary origin with fluorescence lifetime imaging: Preliminary report. *Head & Neck* (2022) https://doi.org/10.1002/hed.27078.

Per the permissions: "If you are the author of a published Wiley article, you have the right to reuse the full text of your published article as part of your thesis or dissertation. In this situation, you do not need to request permission from Wiley for this use." Type of use: Dissertation/Thesis; Requestor type: Article 1st Author; Format: Electronic; Portion: Entire Manuscript with Modifications, Permissions Verification Date: May 7, 2022.

DATA AVALIABILITY STATEMENT

HARDWARE

Characteristics of FLIm hardware and the design of the instrumentation have been previously reported and described extensively within the following publications:

Yankelevich, D. R. et al. Design and evaluation of a device for fast multispectral time-resolved fluorescence spectroscopy and imaging. *Rev. Sci. Instrum.* 85, (2014).

Ma, D., Bec, J., Gorpas, D., Yankelevich, D. & Marcu, L. Technique for real-time tissue characterization based on scanning multispectral fluorescence lifetime spectroscopy (ms-TRFS). Biomed. *Opt. Express* 6, 987 (2015).

Gorpas, D., Ma, D., Bec, J., Yankelevich, D. R. & Marcu, L. Real-Time Visualization of Tissue Surface Biochemical Features Derived from Fluorescence Lifetime Measurements. *IEEE Trans.* Med. Imaging 35, 1802–1811 (2016).

Lagarto, J. L. et al. Autofluorescence lifetime imaging during transoral robotic surgery: a clinical validation study of tumor detection. *SPIE Digital Library.* https://doi.org/10.1117/12.2253226 10039, 43–43 (2017).

Gorpas, D. et al. Autofluorescence lifetime augmented reality as a means for real-time robotic surgery guidance in human patients. *Sci. Rep.* 9, (2019).

ESTIMATION OF FLUORESCENCE DECAY DYNAMICS

Liu, J., Sun, Y., Qi, J. & Marcu, L. A novel method for fast and robust estimation of fluorescence decay dynamics using constrained least-squares deconvolution with Laguerre expansion. *Phys. Med. Biol.* 57, 843–865 (2012).

HISTOPATHOLOGY ANNOTATION

Software for the histopathology annotation and labeled data extraction (described in Chapter 4) is provided at the following GitHub repository: https://github.com/bwweyers/Histopathology-Annotation-Tool.git

ANALYSIS SOFTWARE, RAW DATA, AND MEDIA

A request to obtain analysis software, raw data, and media corresponding to any chapter in this dissertation can be made available by first initiating a reasonable written request to Laura Marcu, Principal Investigator of the Marcu Laboratory at the University of California, Davis. The request may be sent by mail to GBSF 2303, 451 Health Sciences Drive, Davis CA 95618, or email to lmarcu@ucdavis.edu.

All analysis software, raw data, and media provided must be in concordance with the governing policies of the UC Davis Office of Research (1850 Research Park Drive, Suite 300, Davis CA 95618-6153). All provided materials must agree with IRB (800853) and all *Health Insurance Portability and Accountability Act* (HIPPA), including deidentification of all patient data and omission of private health information.

REFERENCES

1. Marcu, L., French, P. M. W. & Elson, D. S. *Fluorescence lifetime spectroscopy and imaging : principles and applications in biomedical diagnostics*.
2. Alfonso-Garcia, A. *et al.* Mesoscopic fluorescence lifetime imaging: Fundamental principles, clinical applications and future directions. *J. Biophotonics* **14**, e202000472 (2021).
3. Sanderson, R. J., Ironside, J. A. D. & Wei, W. I. Squamous cell carcinomas of the head and neck - Clinical review. *BMJ* **325**, 822 (2002).
4. Tandon, P., Dadhich, A., Saluja, H., Bawane, S. & Sachdeva, S. The prevalence of squamous cell carcinoma in different sites of oral cavity at our Rural Health Care Centre in Loni, Maharashtra – a retrospective 10-year study. *Współczesna Onkol.* **2**, 178–183 (2017).
5. Cancer Statistics - National Cancer Institute. https://www.cancer.gov/about-cancer/understanding/statistics.
6. Surgery for Cancer - National Cancer Institute. https://www.cancer.gov/about-cancer/treatment/types/surgery.
7. Intuitive | Surgeons | da Vinci Robotic Assisted Surgery. https://www.intuitive.com/en-us/healthcare-professionals/surgeons.
8. Tringale, K. R., Pang, J. & Nguyen, Q. T. Image-guided surgery in cancer: A strategy to reduce incidence of positive surgical margins. *Wiley Interdisciplinary Reviews: Systems Biology and Medicine* vol. 10 (2018).
9. Orosco, R. K. *et al.* Positive Surgical Margins in the 10 Most Common Solid Cancers. *Sci. Reports 2018 81* **8**, 1–9 (2018).
10. Health, N. I. of. Anatomy of the Head & Neck | SEER Training. https://training.seer.cancer.gov/head-neck/anatomy/.
11. Oral Cancers ▸ THANC Guide. https://thancguide.org/cancer-types/oral/.
12. Sung, H. *et al.* Global Cancer Statistics 2020: GLOBOCAN Estimates of Incidence and Mortality Worldwide for 36 Cancers in 185 Countries. *CA. Cancer J. Clin.* **71**, 209–249 (2021).
13. Chandel, V. *et al.* Metabolic regulation in HPV associated head and neck squamous cell carcinoma. *Life Sci.* **258**, 118236 (2020).
14. Oral Cavity and Pharynx Cancer — Cancer Stat Facts. *NIH National Cancer Institute, Surveillance, Epidemiology, and End Results Program (SEER)* https://seer.cancer.gov/statfacts/html/oralcav.html (2021).
15. Head and Neck Cancer: Risk Factors and Prevention | Cancer.Net. https://www.cancer.net/cancer-types/head-and-neck-cancer/risk-factors-and-prevention.
16. Jethwa, A. R. & Khariwala, S. S. Tobacco-related carcinogenesis in head and neck cancer. *Cancer Metastasis Rev.* **36**, 411–423 (2017).
17. Rettig, E. M. & D'Souza, G. Epidemiology of Head and Neck Cancer. *Surgical Oncology Clinics of North America* vol. 24 379–396 (2015).
18. Fitzmaurice, C. *et al.* Global, regional, and national cancer incidence, mortality, years of life lost, years lived with disability, and disability-adjusted life-years for 32 cancer groups, 1990 to 2015: A Systematic Analysis for the Global Burden of Disease Study Global Burden of Disease Cancer Collaboration. *JAMA Oncology* vol. 3 524–548 (2017).
19. Mourad, M. *et al.* Epidemiological Trends of Head and Neck Cancer in the United States: A SEER Population Study. *J. Oral Maxillofac. Surg.* **75**, 2562–2572 (2017).
20. Leemans, C. R., Snijders, P. J. F. & Brakenhoff, R. H. The molecular landscape of head and neck cancer. *Nature Reviews Cancer* vol. 18 269–282 (2018).
21. Wittekindt, C. *et al.* HPV – Das andere Kopf-Hals-Karzinom. *Laryngo- rhino- otologie* vol. 97 S48–S113 (2018).

22. Gillison, M. L., Chaturvedi, A. K., Anderson, W. F. & Fakhry, C. Epidemiology of human papillomavirus-positive head and neck squamous cell carcinoma. *Journal of Clinical Oncology* vol. 33 3235–3242 (2015).

23. Lewis, J. S., Shelton, J., Kuhs, K. L. & K. Smith, D. p16 Immunohistochemistry in Oropharyngeal Squamous Cell Carcinoma Using the E6H4 Antibody Clone: A Technical Method Study for Optimal Dilution. *Head Neck Pathol.* **12**, 440–447 (2018).

24. Brouns, E. *et al.* Malignant transformation of oral leukoplakia in a well-defined cohort of 144 patients. *Oral Dis.* **20**, (2014).

25. Definition of squamous cell carcinoma - NCI Dictionary of Cancer Terms - National Cancer Institute. https://www.cancer.gov/publications/dictionaries/cancer-terms/def/squamous-cell-carcinoma.

26. Chow, L. Q. M. Head and Neck Cancer. *N. Engl. J. Med.* **382**, 60–72 (2020).

27. Dotto, G. P. & Rustgi, A. K. Squamous cell cancers: a unified perspective on biology and genetics. doi:10.1016/j.ccell.2016.04.004.

28. Head and Neck: Squamous cell carcinoma: an overview. http://atlasgeneticsoncology.org/Tumors/HeadNeckSCCID5078.html.

29. Eldeeb, H., Macmillan, C., Elwell, C. & Hammod, A. The effect of the surgical margins on the outcome of patients with head and neck squamous cell carcinoma: single institution experience. *Cancer Biol. Med.* **9**, 29–33 (2012).

30. Tandon, S. *et al.* Fine-needle aspiration cytology in a regional head and neck cancer center: Comparison with a systematic review and meta-analysis. *Head Neck* **30**, 1246–1252 (2008).

31. Yee, S. Transoral Robotic Surgery. *AORN J.* **105**, 73–84 (2017).

32. Lingen, M. W. *et al.* Evidence-based clinical practice guideline for the evaluation of potentially malignant disorders in the oral cavity: A report of the American Dental Association. *J. Am. Dent. Assoc.* **148**, 712-727.e10 (2017).

33. Jaafar, H. Intra-operative frozen section consultation: Concepts, applications and limitations. *Malaysian Journal of Medical Sciences* vol. 13 4–12 (2006).

34. Okamura, A. M. Haptic feedback in robot-assisted minimally invasive surgery. *Current Opinion in Urology* vol. 19 102–107 (2009).

35. Wedmid, A., Llukani, E. & Lee, D. I. Future perspectives in robotic surgery. *BJU Int.* **108**, 1028–1036 (2011).

36. van Keulen, S. *et al.* Intraoperative Tumor Assessment Using Real-Time Molecular Imaging in Head and Neck Cancer Patients. *J. Am. Coll. Surg.* **229**, 560-567.e1 (2019).

37. Ravasz, L. A., Slootweg, P. J., Hordijk, G. J., Smit, F. & van der Tweel, I. The status of the resection margin as a prognostic factor in the treatment of head and neck carcinoma. *J. Cranio-Maxillofacial Surg.* **19**, 314–318 (1991).

38. Woolgar, J. A. & Triantafyllou, A. A histopathological appraisal of surgical margins in oral and oropharyngeal cancer resection specimens. *Oral Oncol.* **41**, 1034–1043 (2005).

39. McMahon, J. *et al.* Influence of condition of surgical margins on local recurrence and disease-specific survival in oral and oropharyngeal cancer. *Br. J. Oral Maxillofac. Surg.* **41**, 224–231 (2003).

40. Zhang, L. *et al.* Toluidine blue staining identifies high-risk primary oral premalignant lesions with poor outcome. *Cancer Res.* **65**, 8017–8021 (2005).

41. Güneri, P. *et al.* The utility of toluidine blue staining and brush cytology as adjuncts in clinical examination of suspicious oral mucosal lesions. *Int. J. Oral Maxillofac. Surg.* **40**, 155–161 (2011).

42. Arantes, L. M. R. B., De Carvalho, A. C., Melendez, M. E. & Lopes Carvalho, A. Serum, plasma and saliva biomarkers for head and neck cancer. *Expert Rev. Mol. Diagn.* **18**, 85–112 (2018).

43. Wilder-Smith, P., Holtzman, J., Epstein, J. & Le, A. Optical diagnostics in the oral cavity: an

overview. *Oral Dis.* **16**, 717–728 (2010).

44. Protano, M. A. *et al.* Low-cost high-resolution microendoscopy for the detection of esophageal squamous cell neoplasia: An international trial. *Gastroenterology* **149**, 321–329 (2015).
45. Wu, C., Gleysteen, J., Teraphongphom, N. T., Li, Y. & Rosenthal, E. In-vivo optical imaging in head and neck oncology: Basic principles, clinical applications and future directions review-Article. *International Journal of Oral Science* vol. 10 (2018).
46. Vila, P. M. *et al.* Discrimination of benign and neoplastic mucosa with a High-Resolution Microendoscope (HRME) in head and neck cancer. *Ann. Surg. Oncol.* **19**, 3534–3539 (2012).
47. Pierce, M., Yu, D. & Richards-Kortum, R. High-resolution Fiber-optic Microendoscopy for in situ Cellular Imaging. *J. Vis. Exp* 2306 (2011) doi:10.3791/2306.
48. Barbeiro, S., Libânio, D., Castro, R., Dinis-Ribeiro, M. & Pimentel-Nunes, P. Narrow-Band Imaging: Clinical Application in Gastrointestinal Endoscopy. *Rev. Artic. GE Port J Gastroenterol* **26**, 40–53 (2019).
49. Messadi, D. V. Diagnostic aids for detection of oral precancerous conditions. *International Journal of Oral Science* vol. 5 59–65 (2013).
50. Lloyd, G. R. *et al.* Discrimination between benign, primary and secondary malignancies in lymph nodes from the head and neck utilising Raman spectroscopy and multivariate analysis. *Analyst* **138**, 3900–3908 (2013).
51. Fercher, A. F. Optical coherence tomography – development, principles, applications. *Z. Med. Phys.* **20**, 251–276 (2010).
52. De Boer, E. *et al.* Optical innovations in surgery. *British Journal of Surgery* vol. 102 (2015).
53. Keereweer, S. *et al.* Image-guided surgery in head and neck cancer: Current practice and future directions of optical imaging. *Head and Neck* vol. 34 120–126 (2012).
54. Kimmig, R., Aktas, B., Buderath, P., Rusch, P. & Heubner, M. Intraoperative navigation in robotically assisted compartmental surgery of uterine cancer by visualisation of embryologically derived lymphatic networks with indocyanine-green (ICG). *J. Surg. Oncol.* **113**, 554–559 (2016).
55. Schaafsma, B. E. *et al.* The clinical use of indocyanine green as a near-infrared fluorescent contrast agent for image-guided oncologic surgery. *J. Surg. Oncol.* **104**, 323–332 (2011).
56. Regula, J. *et al. Photosensitisation and photodynamic therapy of oesophageal, duodenal, and colorectal tumours using 5 aminolaevulinic acid induced protoporphyrin IX a pilot study*. *Gut* vol. 36 (1995).
57. Zhang, R. R. *et al.* Beyond the margins: Real-time detection of cancer using targeted fluorophores. *Nature Reviews Clinical Oncology* vol. 14 347–364 (2017).
58. Marcu, L. Fluorescence lifetime techniques in medical applications. *Ann. Biomed. Eng.* **40**, 304–331 (2012).
59. Pavlova, I., Williams, M., El-Naggar, A., Richards-Kortum, R. & Gillenwater, A. Understanding the biological basis of autofluorescence imaging for oral cancer detection: High-resolution fluorescence microscopy in viable tissue. *Clin. Cancer Res.* **14**, 2396–2404 (2008).
60. Muldoon, T. J. *et al. Subcellular-resolution molecular imaging within living tissue by fiber microendoscopy*.
61. Protano, M.-A. *et al.* Low-Cost High Resolution Microendoscopy for the Detection of Esophageal Squamous Cell Neoplasia: An International Trial: High Resolution Microendoscopy for ESCN Detection HHS Public Access. *Gastroenterology* **149**, 321–329 (2015).
62. Louie Medical Student, J. S. *et al.* 'High-resolution microendoscopy in differentiating neoplastic from non-neoplastic colorectal polyps' HHS Public Access. *Best Pr. Res Clin Gastroenterol* **29**, 663–673 (2015).
63. Chang, S. S. *et al.* High resolution microendoscopy for classification of colorectal polyps. doi:10.1055/s-0032-1326502.

64. Yen, C. T., Lai, Z. W., Lin, Y. T. & Cheng, H. C. Optical Design with Narrow-Band Imaging for a Capsule Endoscope. *J. Healthc. Eng.* **2018**, (2018).

65. Ash, C., Dubec, M., Donne, K. & Bashford, T. Effect of wavelength and beam width on penetration in light-tissue interaction using computational methods. doi:10.1007/s10103-017-2317-4.

66. Lin, Y. C., Wang, W. H., Lee, K. F., Tsai, W. C. & Weng, H. H. Value of narrow band imaging endoscopy in early mucosal head and neck cancer. *Head and Neck* vol. 34 1574–1579 (2012).

67. Chu, P. Y., Tsai, T. L., Tai, S. K. & Chang, S. Y. Effectiveness of narrow band imaging in patients with oral squamous cell carcinoma after treatment. *Head Neck* **34**, 155–161 (2012).

68. Moester, M. J. B., Zada, L., Fokker, B., Ariese, F. & Boer, J. F. Stimulated Raman scattering microscopy with long wavelengths for improved imaging depth. *J. Raman Spectrosc.* **50**, 1321–1328 (2019).

69. Li, Y. *et al.* Research on the Raman spectral character and diagnostic value of squamous cell carcinoma of oral mucosa. *J. Raman Spectrosc.* **41**, n/a-n/a (2009).

70. Santos, I. P. *et al.* Raman spectroscopy for cancer detection and cancer surgery guidance: Translation to the clinics. *Analyst* vol. 142 3025–3047 (2017).

71. What are the advantages and disadvantages of near infra-red (NIR) lasers for Raman? . *Horiba Sci.* (2021).

72. Shen, K., Lu, H., Baig, S. & Wang, M. R. Improving lateral resolution and image quality of optical coherence tomography by the multi-frame superresolution technique for 3D tissue imaging. *Biomed. Opt. Express* **8**, 4887 (2017).

73. Shu, X., Beckmann, L. & Zhang, H. F. Visible-light optical coherence tomography: a review. *J. Biomed. Opt.* **22**, 1 (2017).

74. Kraus, M. F. *et al.* Motion correction in optical coherence tomography volumes on a per A-scan basis using orthogonal scan patterns. *Biomed. Opt. Express* **3**, 1182 (2012).

75. Huang, R. *et al.* Integrin αvβ3-Targeted IRDye 800CW Near-Infrared Imaging of Glioblastoma. *Clin. Cancer Res.* **18**, 5731 (2012).

76. Warram, J. M. *et al.* Antibody-based imaging strategies for cancer. (2014) doi:10.1007/s10555-014-9505-5.

77. Keereweer, S., Van Driel, P. B. A. A., Robinson, D. J. & Lowik, C. W. G. M. Shifting focus in optical image-guided cancer therapy. *Mol. Imaging Biol.* **16**, 1–9 (2014).

78. Yu, X. *et al.* Deciphering of cerebrovasculatures via ICG-assisted NIR-II fluorescence microscopy. *J. Mater. Chem. B* **7**, 6623–6629 (2019).

79. Wei, L., Roberts, D. W., Sanai, N. & Liu, J. T. C. Visualization technologies for 5-ALA-based fluorescence-guided surgeries. *Journal of Neuro-Oncology* vol. 141 495–505 (2019).

80. Hadjipanayis, C. G. & Stummer, · Walter. 5-ALA and FDA approval for glioma surgery. *J. Neurooncol.* **141**, 479–486 (2019).

81. Zheng, C. *et al.* Indocyanine green-loaded biodegradable tumor targeting nanoprobes for in vitro and in vivo imaging. *Biomaterials* **33**, 5603–5609 (2012).

82. Alacam, B., Yazici, B., Intes, X. & Chance, B. Extended Kalman filtering for the modeling and analysis of ICG pharmacokinetics in cancerous tumors using NIR optical methods. *IEEE Trans. Biomed. Eng.* **53**, 1861–1871 (2006).

83. Sun, Y. *et al.* Fluorescence lifetime imaging microscopy: in vivo application to diagnosis of oral carcinoma. *Opt. Lett.* **34**, 2081 (2009).

84. Miles, B. A. *et al.* Operative margin control with high-resolution optical microendoscopy for head and neck squamous cell carcinoma. *Laryngoscope* **125**, 2308–2316 (2015).

85. Garofolo, S. *et al.* Intraoperative Narrow Band Imaging Better Delineates Superficial Resection Margins during Transoral Laser Microsurgery for Early Glottic Cancer. *Ann. Otol. Rhinol. Laryngol.* **124**, 294–298 (2015).

86. Tirelli, G., Piovesana, M., Gatto, A., Torelli, L. & Nata, F. B. Is NBI-Guided Resection a Breakthrough for Achieving Adequate Resection Margins in Oral and Oropharyngeal Squamous Cell Carcinoma? *Ann. Otol. Rhinol. Laryngol.* **125**, 596–601 (2016).

87. Malik, A. *et al.* In vivo Raman spectroscopy–assisted early identification of potential second primary/recurrences in oral cancers: An exploratory study. *Head Neck* **39**, 2216–2223 (2017).

88. Sunny, S. P. *et al.* Intra-operative point-of-procedure delineation of oral cancer margins using optical coherence tomography. *Oral Oncol.* **92**, 12–19 (2019).

89. van Keulen, S. *et al.* The Clinical Application of Fluorescence-Guided Surgery in Head and Neck Cancer. *J. Nucl. Med.* **60**, 758–763 (2019).

90. Cicciù, M. *et al.* Early Diagnosis on Oral and Potentially Oral Malignant Lesions: A Systematic Review on the VELscope® Fluorescence Method. *Dent. J. 2019, Vol. 7, Page 93* **7**, 93 (2019).

91. Pan, J. *et al.* Real-time surveillance of surgical margins via ICG-based near-infrared fluorescence imaging in patients with OSCC. *World J. Surg. Oncol.* **18**, 96 (2020).

92. Lakowicz, J. R. Principles of fluorescence spectroscopy. *Princ. Fluoresc. Spectrosc.* 1–954 (2006) doi:10.1007/978-0-387-46312-4.

93. Berezin, M. Y. & Achilefu, S. Fluorescence lifetime measurements and biological imaging. *Chem. Rev.* **110**, 2641–2684 (2010).

94. Chen, Y. & Periasamy, A. Characterization of Two-photon Excitation Fluorescence Lifetime Imaging Microscopy for Protein Localization. *Microsc. Res. Tech.* **63**, 72–80 (2004).

95. McGown, L. B. & Nithipahkom, K. Molecular fluorescence and phosphorescence. *Applied Spectroscopy Reviews* vol. 35 353–393 (2000).

96. Lakowicz, J. R. Introduction to Fluorescence. in *Principles of Fluorescence Spectroscopy - Section 1.2. JABLONSKI DIAGRAM* 1–26 (Springer US, 2006). doi:10.1007/978-0-387-46312-4_1.

97. Suhling, K. *et al.* Fluorescence Lifetime Imaging. in *Handbook of Photonics for Biomedical Engineering* 1–50 (Springer Netherlands, 2014). doi:10.1007/978-94-007-6174-2_13-1.

98. Richards-Kortum, R. & Sevick-Muraca, E. Quantitative optical spectroscopy for tissue diagnosis. *Annu. Rev. Phys. Chem.* **47**, 555–606 (1996).

99. Datta, R., Heaster, T. M., Sharick, J. T., Gillette, A. A. & Skala, M. C. Fluorescence lifetime imaging microscopy: fundamentals and advances in instrumentation, analysis, and applications. *J. Biomed. Opt.* **25**, 1 (2020).

100. Sherwood, L. *Human Physiology: From Cells to Systems*. (2013).

101. Kamath, V. The nature of collagen in oral submucous fibrosis: A systematic review of the literature. *Saudi J. Oral Sci.* **1**, 57 (2014).

102. Maarek, J.-M. I., Marcu, L., Snyder, W. J. & Grundfest, W. S. Time-resolved Fluorescence Spectra of Arterial Fluorescent Compounds: Reconstruction with the Laguerre Expansion Technique. *Photochem. Photobiol.* **71**, 178–187 (2007).

103. König, K. Clinical multiphoton tomography. *Journal of Biophotonics* vol. 1 13–23 (2008).

104. Koziol, B., Markowicz, M., Kruk, J. & Plytycz, B. Riboflavin as a Source of Autofluorescence in Eisenia fetida Coelomocytes. *Photochem. Photobiol.* **82**, 570 (2006).

105. Schweitzer, D. *et al.* Towards metabolic mapping of the human retina. in *Microscopy Research and Technique* vol. 70 410–419 (John Wiley & Sons, Ltd, 2007).

106. Glanzmann, T., Ballini, J. P., Van Den Bergh, H. & Wagnières, G. Time-resolved spectrofluorometer for clinical tissue characterization during endoscopy. *Rev. Sci. Instrum.* **70**, 4067–4077 (1999).

107. Lutz, V. *et al.* Impact of collagen crosslinking on the second harmonic generation signal and the fluorescence lifetime of collagen autofluorescence. *Ski. Res. Technol.* **18**, 168–179 (2012).

108. Lakowicz, J. R., Szmacinski, H., Nowaczyk, K. & Johnson, M. L. Fluorescence lifetime imaging of

free and protein-bound NADH. *Proc. Natl. Acad. Sci. U. S. A.* **89**, 1271–1275 (1992).

109. Blinova, K. *et al.* Distribution of mitochondrial NADH fluorescence lifetimes: Steady-state kinetics of matrix NADH interactions. *Biochemistry* **44**, 2585–2594 (2005).
110. Warburg, O. On the Origin of Cancer Cells. *Science (80-.).* **123**, 309–314 (1956).
111. WARBURG, O. On respiratory impairment in cancer cells. *Science* **124**, 269–70 (1956).
112. Lukina, M. M. *et al.* Interrogation of tumor metabolism in tissue samples ex vivo using fluorescence lifetime imaging of NAD(P)H. *Methods Appl. Fluoresc.* **8**, 014002 (2020).
113. Kessenbrock, K., Plaks, V. & Werb, Z. Matrix Metalloproteinases: Regulators of the Tumor Microenvironment. *Cell* vol. 141 52–67 (2010).
114. Hanahan, D. & Weinberg, R. A. Hallmarks of cancer: The next generation. *Cell* vol. 144 646–674 (2011).
115. Cui, N., Hu, M. & Khalil, R. A. Biochemical and Biological Attributes of Matrix Metalloproteinases. in *Progress in Molecular Biology and Translational Science* vol. 147 1–73 (Elsevier B.V., 2017).
116. Pankova, D. *et al.* Cancer-associated fibroblasts induce a collagen cross-link switch in tumor stroma. *Mol. Cancer Res.* **14**, 287–295 (2016).
117. Lee, S. H. & Griffiths, J. R. How and why are cancers acidic? Carbonic anhydrase ix and the homeostatic control of tumour extracellular ph. *Cancers* vol. 12 1–23 (2020).
118. Islam, M. S., Honma, M., Nakabayashi, T., Kinjo, M. & Ohta, N. pH dependence of the fluorescence lifetime of FAD in solution and in cells. *Int. J. Mol. Sci.* **14**, 1952–1963 (2013).
119. Hu, Y. *et al.* Dynamic optical contrast imaging for real-time delineation of tumor resection margins using head and neck cancer as a model. (2022) doi:10.48550/arxiv.2202.07108.
120. Chang, C. L. *et al.* Autofluorescence lifetime measurement on oral carcinogenesis. in *Annual International Conference of the IEEE Engineering in Medicine and Biology - Proceedings* vol. 26 IV 2349–2351 (2004).
121. Chen, H. M., Chiang, C. P., You, C., Hsiao, T. C. & Wang, C. Y. Time-resolved autofluorescence spectroscopy for classifying normal and premalignant oral tissues. *Lasers Surg. Med.* **37**, 37–45 (2005).
122. Farwell, D. G. *et al.* Time-resolved fluorescence spectroscopy as a diagnostic technique of oral carcinoma: Validation in the hamster buccal pouch model. *Arch. Otolaryngol. - Head Neck Surg.* **136**, 126–133 (2010).
123. Jo, J. A. *et al.* In Vivo simultaneous morphological and biochemical optical imaging of oral epithelial cancer. *IEEE Trans. Biomed. Eng.* **57**, 2596–2599 (2010).
124. Shrestha, S., Park, J., Pande, P., Applegate, B. E. & Jo, J. A. Multimodal optical imaging for simultaneous in-vivo morphological and biochemical characterization of oral epithelial cancer. in *2010 Annual International Conference of the IEEE Engineering in Medicine and Biology Society, EMBC'10* 1970–1973 (2010). doi:10.1109/IEMBS.2010.5627569.
125. Shrestha, S. *et al.* High-speed multispectral fluorescence lifetime imaging implementation for in vivo applications. *Opt. Lett.* **35**, 2558 (2010).
126. Sun, Y. *et al.* Endoscopic fluorescence lifetime imaging for in vivo intraoperative diagnosis of oral carcinoma. in *Microscopy and Microanalysis* vol. 19 791–798 (NIH Public Access, 2013).
127. Fatakdawala, H. *et al.* Multimodal in vivo imaging of oral cancer using fluorescence lifetime, photoacoustic and ultrasound techniques. *Biomed. Opt. Express* **4**, 1724 (2013).
128. Pande, P. *et al.* Automated analysis of multimodal fluorescence lifetime imaging and optical coherence tomography data for the diagnosis of oral cancer in the hamster cheek pouch model. *Biomed. Opt. Express* **7**, 2000 (2016).
129. Malik, B. H. *et al.* Objective Detection of Oral Carcinoma with Multispectral Fluorescence Lifetime Imaging In Vivo. *Photochem. Photobiol.* **92**, 694–701 (2016).

130. Gorpas, D. *et al.* Time-resolved fluorescence spectroscopy for the diagnosis of oral lichen planus. *Clin. Exp. Dermatol.* **43**, 546–552 (2018).

131. Lagarto, J. L. *et al.* Electrocautery effects on fluorescence lifetime measurements: An in vivo study in the oral cavity. *J. Photochem. Photobiol. B Biol.* **185**, 90–99 (2018).

132. Jo, J. A. *et al.* Endogenous Fluorescence Lifetime Imaging (FLIM) Endoscopy for Early Detection of Oral Cancer and Dysplasia∗. in *Proceedings of the Annual International Conference of the IEEE Engineering in Medicine and Biology Society, EMBS* vols 2018-July 3009–3012 (Institute of Electrical and Electronics Engineers Inc., 2018).

133. Jo, J. A. *et al.* Autofluorescence lifetime endoscopy for early detection of oral dysplasia and cancer. in *Optics InfoBase Conference Papers* vol. Part F123-LAOP 2018 (OSA - The Optical Society, 2018).

134. Gorpas, D. *et al.* Autofluorescence lifetime augmented reality as a means for real-time robotic surgery guidance in human patients. *Sci. Rep.* **9**, (2019).

135. Gorpas, D., Ma, D., Bec, J., Yankelevich, D. R. & Marcu, L. Real-Time Visualization of Tissue Surface Biochemical Features Derived from Fluorescence Lifetime Measurements. *IEEE Trans. Med. Imaging* **35**, 1802–1811 (2016).

136. Taybos, G. Oral Changes Associated with Tobacco Use. in *American Journal of the Medical Sciences* vol. 326 179–182 (Lippincott Williams and Wilkins, 2003).

137. Boyle, J. O. *et al.* Effects of cigarette smoke on the human oral mucosal transcriptome. *Cancer Prev. Res.* **3**, 266–278 (2010).

138. Hamam Dalia, G. G. & Aly El-Waseef, A. E.-D. Effect of Cigarette Smoking on Human Gingival Mucosa-Histological and Morphometric Study. *J. Cytol. Histol.* **09**, (2018).

139. Khowal, S. & Wajid, S. Role of Smoking-Mediated molecular events in the genesis of oral cancers. *Toxicol. Mech. Methods* **29**, 665–685 (2019).

140. Prestin, S., Rothschild, S. I., Betz, C. S. & Kraft, M. Measurement of epithelial thickness within the oral cavity using optical coherence tomography. *Head Neck* **34**, 1777–1781 (2012).

141. Chang, C. H. *et al.* Significant association of high-grade inflammation and thick lining epithelium with the increased number of Langerhans cells in dentigerous cysts. *J. Formos. Med. Assoc.* **116**, 837–843 (2017).

142. Speight, P. M. Update on oral epithelial dysplasia and progression to cancer. *Head Neck Pathol.* **1**, 61–66 (2007).

143. Pai, S. I. & Westra, W. H. Molecular pathology of head and neck cancer: Implications for diagnosis, prognosis, and treatment. *Annual Review of Pathology: Mechanisms of Disease* vol. 4 49–70 (2009).

144. Ciano, J. & Beatty, B. L. Regional Quantitative Histological Variations in Human Oral Mucosa. *Anat. Rec.* **298**, 562–578 (2015).

145. Wu, Y. & Qu, J. Y. Autofluorescence spectroscopy of epithelial tissues. *J. Biomed. Opt.* **11**, 054023 (2006).

146. Duran, E. *et al.* In vivo metabolic imaging of early stage oral cancer and dysplasia based on autofluorescence lifetime endoscopy (Conference Presentation). in *Medical Imaging 2018: Biomedical Applications in Molecular, Structural, and Functional Imaging* (eds. Gimi, B. & Krol, A.) 27 (SPIE, 2018). doi:10.1117/12.2293794.

147. Pitts, J. D. & Mycek, M. A. Design and development of a rapid acquisition laser-based fluorometer with simultaneous spectral and temporal resolution. *Rev. Sci. Instrum.* **72**, 3061–3072 (2001).

148. Fang, Q. *et al.* Time-domain laser-induced fluorescence spectroscopy apparatus for clinical diagnostics. *Rev. Sci. Instrum.* **75**, 151–162 (2004).

149. Yankelevich, D. R. *et al.* Design and evaluation of a device for fast multispectral time-resolved fluorescence spectroscopy and imaging. *Rev. Sci. Instrum.* **85**, (2014).

150. Nam, H. S. *et al.* Multispectral analog-mean-delay fluorescence lifetime imaging combined with optical coherence tomography. *Biomed. Opt. Express* **9**, 1930 (2018).

151. Kittle, D. S. *et al.* Real time optical Biopsy: Time-resolved Fluorescence Spectroscopy instrumentation and validation. *Sci. Rep.* **6**, 1–9 (2016).

152. Cheng, S. *et al.* Handheld multispectral fluorescence lifetime imaging system for in vivo applications. *Biomed. Opt. Express* **5**, 921 (2014).

153. Liu, J., Sun, Y., Qi, J. & Marcu, L. A novel method for fast and robust estimation of fluorescence decay dynamics using constrained least-squares deconvolution with Laguerre expansion. *Phys. Med. Biol.* **57**, 843–865 (2012).

154. Sanchez, S., Bakás, L., Gratton, E. & Herlax, V. Alpha Hemolysin Induces an Increase of Erythrocytes Calcium: A FLIM 2-Photon Phasor Analysis Approach. *PLoS One* **6**, e21127 (2011).

155. Celli, A. *et al.* The Epidermal Ca2+ Gradient: Measurement Using the Phasor Representation of Fluorescent Lifetime Imaging. *Biophys. J.* **98**, 911 (2010).

156. Ranjit, S., Malacrida, L., Jameson, D. M. & Gratton, E. Fit-free analysis of fluorescence lifetime imaging data using the phasor approach. *Nat. Protoc. 2018 139* **13**, 1979–2004 (2018).

157. Digman, M. A., Caiolfa, V. R., Zamai, M. & Gratton, E. The phasor approach to fluorescence lifetime imaging analysis. *Biophys. J.* **94**, L14–L16 (2008).

158. Franssen, W. M. J., Vergeldt, F. J., Bader, A. N., Van Amerongen, H. & Terenzi, C. Full-Harmonics Phasor Analysis: Unravelling Multiexponential Trends in Magnetic Resonance Imaging Data. *J. Phys. Chem. Lett.* **10**, 9152–9158 (2020).

159. Liao, S.-C., Sun, Y. & Coskun, U. FLIM Analysis using the Phasor Plots.

160. Sun, Y. & Liao, S.-C. The Ultimate Phasor Plot and beyond.

161. Fukazawa, T. *et al.* Head and neck cancer visualization using deep learning combined with fluorescence lifetime imaging and white light imaging. *https://doi.org/10.1117/12.2581449* **11631**, 116310O (2021).

162. Nie, Y. & Ma, K.-K. Adaptive Rood Pattern Search for Fast Block-Matching Motion Estimation. *IEEE Trans. IMAGE Process.* **11**, (2002).

163. Lowe, D. G. Distinctive image features from scale-invariant keypoints. *Int. J. Comput. Vis.* **60**, 91–110 (2004).

164. Bay, H., Ess, A., Tuytelaars, T. & Van Gool, L. Speeded-Up Robust Features (SURF). *Comput. Vis. Image Underst.* **110**, 346–359 (2008).

165. Ronneberger, O., Fischer, P. & Brox, T. U-net: Convolutional networks for biomedical image segmentation. in *Lecture Notes in Computer Science (including subseries Lecture Notes in Artificial Intelligence and Lecture Notes in Bioinformatics)* vol. 9351 234–241 (Springer Verlag, 2015).

166. Marsden, M. *et al.* FLImBrush: dynamic visualization of intraoperative free-hand fiber-based fluorescence lifetime imaging. *Biomed. Opt. Express* **11**, 5166 (2020).

167. Shvets, A. A., Rakhlin, A., Kalinin, A. A. & Iglovikov, V. I. Automatic Instrument Segmentation in Robot-Assisted Surgery using Deep Learning. in *Proceedings - 17th IEEE International Conference on Machine Learning and Applications, ICMLA 2018* 624–628 (Institute of Electrical and Electronics Engineers Inc., 2019). doi:10.1109/ICMLA.2018.00100.

168. Weyers, B. W. *et al.* Fluorescence lifetime imaging for intraoperative cancer delineation in transoral robotic surgery. *Transl. Biophotonics* (2019) doi:10.1002/tbio.201900017.

169. Marsden, M. *et al.* Intraoperative Margin Assessment in Oral and Oropharyngeal Cancer Using Label-Free Fluorescence Lifetime Imaging and Machine Learning. *IEEE Trans. Biomed. Eng.* **68**, 857–868 (2021).

170. Breiman, L. Random forests. *Mach. Learn.* **45**, 5–32 (2001).

171. Bakshi, C. Random Forest Regression. Random Forest Regression is a… | by Chaya Bakshi |

Level Up Coding. https://levelup.gitconnected.com/random-forest-regression-209c0f354c84.

172. de Boer, L. L. *et al.* Method for coregistration of optical measurements of breast tissue with histopathology: the importance of accounting for tissue deformations. *J. Biomed. Opt.* **24**, 1 (2019).

173. Unger, J., Sun, T., Chen, Y.-L., Phipps, J. E. & Bold, R. J. Method for accurate registration of tissue autofluorescence imaging data with corresponding histology: a means for enhanced tumor margin assessment. *J. Biomed. Opt.* **23**, 1 (2018).

174. Alyami, W., Kyme, A. & Bourne, R. Histological Validation of MRI: A Review of Challenges in Registration of Imaging and Whole-Mount Histopathology. *J. Magn. Reson. Imaging* jmri.27409 (2020) doi:10.1002/jmri.27409.

175. Park, H. *et al.* Registration Methodology for Histological Sections and In Vivo Imaging of Human Prostate. *Acad. Radiol.* **15**, 1027–1039 (2008).

176. Wildeboer, R. R. *et al.* Accurate validation of ultrasound imaging of prostate cancer: a review of challenges in registration of imaging and histopathology. *Journal of Ultrasound* vol. 21 197–207 (2018).

177. Kerawala, C. J. & Ong, T. K. *RELOCATING THE SITE OF FROZEN SECTIONS-IS THERE ROOM FOR IMPROVEMENT?* (2001) doi:10.1002/1097-0347.

178. Bulbul, M. G. *et al.* Margin Practices in Oral Cavity Cancer Resections: Survey of American Head and Neck Society Members. *Laryngoscope* **131**, 782–787 (2021).

179. Alfonso-Garcia, A. *et al.* Real-time augmented reality for delineation of surgical margins during neurosurgery using autofluorescence lifetime contrast. *J. Biophotonics* (2019) doi:10.1002/jbio.201900108.

180. Pichat, J., Iglesias, J. E., Yousry, T., Ourselin, S. & Modat, M. A Survey of Methods for 3D Histology Reconstruction. *Med. Image Anal.* **46**, 73–105 (2018).

181. Leys, C., Ley, C., Klein, O., Bernard, P. & Licata, L. Detecting outliers: Do not use standard deviation around the mean, use absolute deviation around the median. *J. Exp. Soc. Psychol.* **49**, 764–766 (2013).

182. Siegel, S. & Castellan, N. *Nonparametric Statistics for the Behavioral Sciences*. (McGraw-Hill, 1956).

183. Hogg, R. & E, T. *Probability and Statistical Inference*. (Macmillan, 1977).

184. Lin, M., Lucas, H. C. & Shmueli, G. Too big to fail: Large samples and the p-value problem. *Inf. Syst. Res.* **24**, 906–917 (2013).

185. Cohen, J. *Statistical Power Analysis for the Behavioral Sciences Second Edition*.

186. Juhl, H. Preanalytical aspects: A neglected issue. *Scand. J. Clin. Lab. Invest.* **70**, 63–65 (2010).

187. David, K. A. *et al.* Surgical procedures and postsurgical tissue processing significantly affect expression of genes and EGFR-pathway proteins in colorectal cancer tissue. *Oncotarget* **5**, 11017–11028 (2014).

188. verre Grimnes, Ø. G. M. Tissue Metabolism - an overview | ScienceDirect Topics • Passive Tissue Electrical Properties 4.2.8 Postexcision Changes and the Death Process.

189. Kohl, B. A. & Deutschman, C. S. The inflammatory response to surgery and trauma. *Current Opinion in Critical Care* vol. 12 325–332 (2006).

190. Al-Mulki, K. *et al.* Narrowband Imaging for p16+ Unknown Primary Squamous Cell Carcinoma Prior to Transoral Robotic Surgery. *Otolaryngol. - Head Neck Surg. (United States)* **163**, 1198–1201 (2020).

191. Mackenzie, K., Watson, M., Jankowska, P., Bhide, S. & Simo, R. Investigation and management of the unknown primary with metastatic neck disease: United Kingdom National Multidisciplinary Guidelines. *J. Laryngol. Otol.* **130**, S170–S175 (2016).

192. Pavlidis, N., Khaled, H. & Gaafar, R. A mini review on cancer of unknown primary site: A clinical

puzzle for the oncologists. *J. Adv. Res.* **6**, 375–382 (2015).

193. Pavlidis, N. & Pentheroudakis, G. Cancer of unknown primary site. in *The Lancet* vol. 379 1428–1435 (Elsevier, 2012).

194. Motz, K. *et al.* Changes in unknown primary squamous cell carcinoma of the head and neck at initial presentation in the era of human papillomavirus. *JAMA Otolaryngol. - Head Neck Surg.* **142**, 223–228 (2016).

195. Ofo, E., Spiers, H., Kim, D. & Duvvuri, U. Transoral Robotic Surgery and the Unknown Primary. *ORL* **80**, 148–155 (2018).

196. Strojan, P. *et al.* Contemporary management of lymph node metastases from an unknown primary to the neck: I. A review of diagnostic approaches. *Head and Neck* vol. 35 123–132 (2013).

197. Rassy, E., Nicolai, P. & Pavlidis, N. Comprehensive management of HPV-related squamous cell carcinoma of the head and neck of unknown primary. *Head Neck* **41**, 3700–3711 (2019).

198. Zengel, P. *et al.* Cancer of unknown primary originating from oropharyngeal carcinomas are strongly correlated to HPV positivity. *Virchows Arch.* **461**, 283–290 (2012).

199. O'Rorke, M. A. *et al.* Human papillomavirus related head and neck cancer survival: A systematic review and meta-analysis. *Oral Oncology* vol. 48 1191–1201 (2012).

200. Dhere, V. R. *et al.* The omission of intentional primary site radiation following transoral robotic surgery in 59 patients: No local-regional failures. *Head Neck* **44**, 382–390 (2022).

201. Fu, T. S., Foreman, A., Goldstein, D. P. & De Almeida, J. R. The role of transoral robotic surgery, transoral laser microsurgery, and lingual tonsillectomy in the identification of head and neck squamous cell carcinoma of unknown primary origin: A systematic review. *Journal of Otolaryngology - Head and Neck Surgery* vol. 45 (2016).

202. Parhar, H. S. *et al.* Revisiting the Recommendation for Contralateral Tonsillectomy in HPV-Associated Tonsillar Carcinoma. *Otolaryngol. - Head Neck Surg. (United States)* **164**, 1222–1229 (2021).

203. Channir, H. I. *et al.* Transoral robotic surgery for the management of head and neck squamous cell carcinoma of unknown primary. *Acta Otolaryngol.* **135**, 1051–1057 (2015).

204. Patel, S. A. *et al.* Robotic surgery for primary head and neck squamous cell carcinoma of unknown site. *JAMA Otolaryngol. - Head Neck Surg.* **139**, 1203–1211 (2013).

205. Fu, T. S., Foreman, A., Goldstein, D. P. & De Almeida, J. R. The role of transoral robotic surgery, transoral laser microsurgery, and lingual tonsillectomy in the identification of head and neck squamous cell carcinoma of unknown primary origin: A systematic review. *Journal of Otolaryngology - Head and Neck Surgery* vol. 45 1–10 (2016).

206. Shekarchizadeh, H., Khami, M. R., Mohebbi, S. Z., Ekhtiari, H. & Virtanen, J. I. Oral health of drug abusers: A review of health effects and care. *Iranian Journal of Public Health* vol. 42 929–940 (2013).

207. Aran, D. *et al.* Comprehensive analysis of normal adjacent to tumor transcriptomes. *Nat. Commun. 2017 81* **8**, 1–14 (2017).

208. Teoh, L., Moses, G. & McCullough, M. Oral manifestations of illicit drug use. *Aust. Dent. J.* **64**, 213–222 (2019).

209. De-Carolis, C., Boyd, G. A., Mancinelli, L., Pagano, S. & Eramo, S. Methamphetamine abuse and "meth mouth" in Europe. *Medicina Oral, Patologia Oral y Cirugia Bucal* vol. 20 e205–e210 (2015).

210. Astarita, G. *et al.* Methamphetamine Accelerates Cellular Senescence through Stimulation of De Novo Ceramide Biosynthesis. (2015) doi:10.1371/journal.pone.0116961.

211. Mihu, M. R. *et al.* Methamphetamine alters the antimicrobial efficacy of phagocytic cells during methicillin-resistant staphylococcus aureus skin infection. *MBio* **6**, (2015).

212. Hamamoto, D. T. & Rhodus, N. L. Methamphetamine abuse and dentistry. *Oral Diseases* vol. 15 27–37 (2009).

213. Hatten, K. M. *et al.* Transoral robotic surgery-assisted endoscopy with primary site detection and treatment in occult mucosal primaries. *JAMA Otolaryngol. - Head Neck Surg.* **143**, 267–273 (2017).

214. Weert, S. *et al.* A systematic review on Transoral robotic surgery (TORS) for carcinoma of unknown primary origin: Has tongue base mucosectomy become indispensable? *Clin. Otolaryngol.* **45**, 732–738 (2020).

215. Geltzeiler, M. *et al.* Transoral robotic surgery for management of cervical unknown primary squamous cell carcinoma: Updates on efficacy, surgical technique and margin status. *Oral Oncol.* **66**, 9–13 (2017).

216. Pomerleau, C. S., Pomerleau, O. F., Snedecor, S. M. & Mehringer, A. M. Defining a never-smoker: results from the nonsmokers survey. *Addict. Behav.* **29**, 1149–1154 (2004).

217. Giovannitti, J. A., Rosenberg, M. B. & Phero, J. C. Pharmacology of Local Anesthetics Used in Oral Surgery. *Oral Maxillofac. Surg. Clin. North Am.* **25**, 453–465 (2013).

218. Guiglia, R. *et al.* Aging and Oral Health: Effects in Hard and Soft Tissues. *Curr. Pharm. Des.* **16**, 619–630 (2010).

219. Albrecht, M. *et al.* In Vivo Endoscopic Optical Coherence Tomography of the Healthy Human Oral Mucosa: Qualitative and Quantitative Image Analysis. *Diagnostics* **10**, (2020).

220. Gerweck, L. E. & Seetharaman, K. Cellular pH Gradient in Tumor versus Normal Tissue: Potential Exploitation for the Treatment of Cancer. *Cancer Res.* **56**, (1996).

221. Heaphy, C. M. *et al.* Telomere DNA content and allelic imbalance demonstrate field cancerization in histologically normal tissue adjacent to breast tumors. *Int. J. Cancer* **119**, 108–116 (2006).

222. Trujillo, K. A. *et al.* Markers of fibrosis and epithelial to mesenchymal transition demonstrate field cancerization in histologically normal tissue adjacent to breast tumors. *Int. J. Cancer* **129**, 1310 (2011).

223. Heaphy, C. M., Griffith, J. K. & Bisoffi, M. Mammary field cancerization: Molecular evidence and clinical importance. *Breast Cancer Res. Treat.* **118**, 229–239 (2009).

224. Masters, K. G., Zezoff, D. & Lasrado, S. Anatomy, Head and Neck, Tonsils. *StatPearls* (2021).

225. Pearce, E. L., Poffenberger, M. C., Chang, C. H. & Jones, R. G. Fueling Immunity: Insights into Metabolism and Lymphocyte Function. *Science* **342**, 1242454 (2013).

226. Michael H.Ross, P. (deceased) & Wojciech Pawlina. HISTOLOGY A TEXT AND ATLAS with Correlated Cell and Molecular Biology. *Psychol. Sci.* **25**, 1682–1690 (2014).

227. Chance, B. Pyridine nucleotide as an indicator of the oxygen requirements for energy-linked functions of mitochondria. *Circ. Res.* **38**, I31-8 (1976).

228. Chance, B., Schoener, B., Oshino, R., Itshak, F. & Nakase, Y. Oxidation-reduction ratio studies of mitochondria in freeze-trapped samples. NADH and flavoprotein fluorescence signals. *J. Biol. Chem.* **254**, 4764–4771 (1979).

229. Yankelevich, D., Bec, J., Marcu, L. & Zhou, X. Multispectral fluorescence lifetime imaging device with a silicon avalanche photodetector. *Opt. Express, Vol. 29, Issue 13, pp. 20105-20120* **29**, 20105–20120 (2021).

230. Nishio, N. *et al.* Optical molecular imaging can differentiate metastatic from benign lymph nodes in head and neck cancer. *Nat. Commun.* **10**, (2019).

231. Fujimoto, J. & Swanson, E. The development, commercialization, and impact of optical coherence tomography. *Investigative Ophthalmology and Visual Science* vol. 57 OCT1–OCT13 (2016).

232. Gioux, S., Choi, H. S. & Frangioni, J. V. Image-guided surgery using invisible near-infrared light: Fundamentals of clinical translation. *Molecular Imaging* vol. 9 237–255 (2010).

233. Weyers, B. W. *et al.* Intraoperative delineation of p16+ oropharyngeal carcinoma of unknown primary origin with fluorescence lifetime imaging: Preliminary report. *Head Neck* (2022) doi:10.1002/HED.27078.

234. Clark, D., Dean, G., Bolton, S. & Beeson, B. Bench to bedside: The technology adoption pathway in healthcare. *Health Technol. (Berl).* **10**, 537–545 (2020).